Theoretical studies of tunnel-coupled double quantum dots

Frederic William Jayatilaka
Trinity College, Oxford

A thesis submitted for the degree of
Doctor of Philosophy
at the University of Oxford, Trinity 2013

Theoretical studies of tunnel-coupled double quantum dots

Frederic William Jayatilaka
Trinity College, Oxford

A thesis submitted for the degree of
Doctor of Philosophy
at the University of Oxford, Trinity 2013

Abstract

We study the low-temperature physics arising in models of a strongly correlated, tunnel-coupled double quantum dot (DQD), particularly the two-impurity Anderson model (2AIM) and the two-impurity Kondo model (2IKM), employing a combination of physical arguments and the Numerical Renormalisation Group.

These models exhibit a rich range of Kondo physics. In the regime with essentially one electron on each dot, there is a competition between the Kondo effect and the interdot exchange interaction. This competition gives rise to a quantum phase transition (QPT) between local singlet and Kondo singlet phases in the 2IKM, which becomes a continuous crossover in the 2AIM as a result of the interlead charge transfer present. The 2IKM is known to exhibit two-channel Kondo (2CK) physics at the QPT, and we investigate whether this is also the case for the 2AIM at the crossover. We find that while in principle 2CK physics can be observed in the 2AIM, extremely low temperatures are required, such that it is unlikely that 2CK physics will be observed in an experimental DQD system in the near future.

We have studied the effect of a magnetic field on the 2AIM and the 2IKM, finding that both the zero-field QPT in the 2IKM and the zero-field crossover in the 2AIM, persist to finite field. This presents the possibility of observing 2CK physics in an experimental DQD at finite field, but we find that the temperatures required to do so are extremely low. We show that longer even-numbered chains of spins also exhibit QPTs at finite field, and argue that a $2N$-spin chain should undergo N QPTs as field is increased (starting deep in the local singlet phase at zero field).

We have also carried out a joint theoretical-experimental study of a carbon nanotube based DQD, in collaboration with Dr. Mark Buitelaar et al. The agreement between experimental and theoretical results is good, and the experiments are able to access the crossover present in the 2AIM at finite field. Furthermore, the experiments show the wide range of physics exhibited by DQD systems, and illustrate the utility of such systems in probing correlated electron physics.

Acknowledgements

I would like to thank my supervisor, David Logan, who has taught me a great deal - not all of it about physics. Martin Galpin and Andrew Mitchell have given me a lot of help and support over the past 5 years, and deserve my thanks also.

I would also like to thank Dr. Mark Buitelaar. I was very lucky to have the opportunity to collaborate with him and his group, and learned a lot about the confusing (to me at least!) world of experimental science.

The members of the Logan group, past and present, deserve my thanks, for making the last 5 years bearable. In particular, Chris's scathing judgements of his students, Adam's laddy banter, Phil's aristocratic wit, and Sam's illustrations have made the office a fun place to be. Once the "Where are the lads" app is available, I hope we can use it to stay in touch.

Finally I would like to thank my family, particularly my parents, for their unconditional support, as well as all my friends, in Trinity and beyond, for reminding me that there's more to life than two-channel Kondo physics.

Gloassary of acronyms

1AIM	Single-impurity Anderson model
(2/3/4)AIM	(Two-/three-/four-)impurity Anderson model
(2/3/4/6)IKM	(Two-/three-/four-/six-)impurity Kondo model
2CK	Two-channel Kondo
2DEG	Two-dimensional electron gas
AS	Anders-Schiller
BISEA	Bias-independent self-energies approximation
BS	Bonding singlet
CNT	Carbon nanotube
FDM	Full density matrix
FO	Free orbital
FP	Fixed point
KS	Kondo singlet
LM	Local moment
LOT	Leading-order in t
LR	left-right
LS	Local singlet
MO	molecular orbital
(N)FL	(Non-)Fermi liquid
NRG	Numerical renormalisation group
ph	particle-hole
PMS	Poor Man's Scaling
QPT	Quantum phase transition
RG	Renormalisation group
SC	Strong coupling
STM	Scanning tunneling microscope
SW	Schrieffer-Wolff
(TC)(D)QD	(Tunnel-coupled) (Double) quantum dot

Contents

1 Introduction **1**

2 Models of quantum dot systems **13**

2.1 Modelling a quantum dot device 14

2.2 The single-impurity Anderson model 15

2.3 Schrieffer-Wolff transformation and the single-impurity Kondo model 16

2.4 Poor Man's Scaling 17

2.5 The two-channel Kondo model 21

2.6 The two-impurity Anderson model 23

2.7 Schrieffer-Wolff transformation of the 2AIM 26

2.8 The two-impurity Kondo model 26

2.9 Schrieffer-Wolff transformation of the 2AIM to third order 29

2.10 The 2AIM in the atomic limit 30

2.11 The 2AIM in the non-interacting limit 33

3 The Numerical Renormalisation Group **39**

3.1 Transforming the Hamiltonian 40

3.2 Logarithmic discretisation 40

3.3 Iterative diagonalisation 44

3.4 The NRG for the 2AIM 48

3.5 NRG flows and fixed points 49

3.6 Calculating dynamical properties from the NRG 53

3.6.1 The Anders-Schiller basis set 55

3.6.2 The full density matrix method 56

3.6.3 Self-energy method of calculating Green's functions 59

3.7 Calculating the conductance of the 2AIM 60

3.7.1 Meir-Wingreen approach 60

3.7.2 Scattering approach 61

3.7.3 Linear-response approach 63
3.7.4 Finite-bias conductance 64

4 Kondo physics in the 2AIM **67**
4.1 Self-energies and Friedel Sum Rule 68
4.2 Particle-hole symmetry 72
4.2.1 Phase shifts 74
4.2.2 Thermodynamics 75
4.2.3 Spectra 78
4.2.4 Conductance 80
4.2.5 Effect of interdot repulsion 84
4.2.6 Unequal dot-lead couplings 86
4.3 Results for equal dot level energies ($\epsilon_1 = \epsilon_2$) 88
4.3.1 Conductance 92
4.3.2 Unequal dot-lead couplings 95
4.4 Results for unequal dot level energies ($\epsilon_1 \neq \epsilon_2$) 96
4.5 Finite-bias conductance of the 2AIM 102
4.5.1 Bias-independent self-energy approximation 102
4.5.2 Conductance in the limit of weakly-coupled dots 102

5 Two-channel Kondo physics in the 2AIM **107**
5.1 Two-impurity Kondo model 109
5.2 Effect of charge transfer 111
5.3 Interdot repulsion 119
5.4 The 2AIM away from ph symmetry 122
5.5 Two-channel Kondo physics in longer quantum dot chains 125

6 Magnetic field effects in even-impurity models **129**
6.1 Two-impurity Kondo model 130
6.1.1 Staggered field 136
6.2 Four-impurity Kondo model 141
6.3 Two-impurity Anderson model 149
6.3.1 Unequal dot-lead couplings 154
6.3.2 Away from ph symmetry 157

7 Experimental realisation of the 2AIM **163**
7.1 Stability diagram 166
7.2 Varying dot energy levels 173
7.3 Varying dot-lead and interdot couplings 176

7.4 Behaviour upon application of a magnetic field 179

8 Summary **183**

A Outline of the third-order Schrieffer-Wolff transformation of the 2AIM **189**

B Generalised self-energy method for calculating the Green's functions of multi-impurity systems **193**

C Derivation of the linear-response formula for the finite-temperature, zero-bias conductance of the 2AIM **195**

D Derivation of the current of the 2AIM to leading order in the interdot tunnel-coupling **203**

E Outline of first-order perturbation theory for the 2IKM in a field **209**

Bibliography **213**

CHAPTER 1

Introduction

Strongly correlated systems present a great theoretical challenge. In such systems the interactions are too strong to be simply neglected, and in many cases the interactions cannot even be taken into account perturbatively. Single-particle descriptions of such systems are therefore often precluded. In addition, these systems may contain a macroscopically large number of particles, rendering ab initio methods completely unfeasible. In spite of these difficulties, there has been long-standing interest in such systems, and in particular in the emergent phenomena to which the strong correlations can give rise. Such phenomena are neatly described in terms of *collective* excitations, meaning that strongly correlated systems can exhibit fundamentally different behaviour to analogous non-interacting systems [1]. Understanding such fascinating phenomena, examples of which include high-temperature superconductivity [2, 3], colossal magnetoresistance [4] and metal-insulator transitions [5], is one of the main goals of modern condensed matter science.

The Kondo effect [3], which plays a dominant role in the low-temperature physics of the systems discussed in this thesis, is another such phenomenon, and remains one of the enduring paradigms of many-body physics. It has been studied for over 40 years and was first observed in metal samples containing magnetic impurities [6]. At high temperatures these systems obey the Curie law for magnetic susceptibility, implying the existence of local moments – an interesting finding in itself. The resistivity of these systems may also be measured, and at high temperature it is dominated by electron-phonon scattering, as expected. Such scattering decays rapidly with temperature, so the resistivity of the metal is expected to decrease as the temperature is decreased. Surprisingly however, a resistance minimum is observed, with the resistivity beginning to *increase* as temperature is lowered sufficiently. This unexpected increase in resistivity was discovered to be due to scattering by the magnetic impurity atoms present in the metal. Such scattering causes the magnetic moment of the impurity to be screened by the delocalised electrons in the

metal, with the impurity forming a many-body spin singlet state with the conduction electrons of the host metal. This was later named the Kondo effect [7], of which such a screening (or "quenching") of impurity degrees of freedom (such as spin) is characteristic. Since its first observation, theorists have spent much effort trying to understand the nature of the Kondo effect, and the simplest variant of the effect, as exhibited by the single-impurity Anderson model [8] (1AIM, see below) is now rather well understood.[1]

The 1AIM was devised as a model for a metal containing *dilute* magnetic impurities, which are approximately independent of each other. Thus, only one impurity is accounted for in the model. Specifically, the 1AIM describes a single localised electron level, representing the impurity, with energy ϵ and on-site repulsion U, tunnel-coupled to a non-interacting continuum of levels, representing the metallic conduction band, by matrix elements $V_{\mathbf{k}}$. In the regime $-U \ll \epsilon \ll 0$ (where the Fermi level of the metal is taken as the zero of energy), and provided the correlations are strong enough (*i.e.*, U is sufficiently large), for temperatures $T \ll U$ there is a essentially a single electron on the localised level. As such, the level behaves effectively as a local moment in this regime. The 1AIM is therefore successful in showing that strong correlations can lead to the existence of an effective local moment in a metallic medium. It is this local moment which is quenched at low temperature in the 1AIM by the Kondo effect.

Studying the 1AIM has proven a real challenge for theorists ever since it was first devised in the 1960s [8]. The local correlation (U) renders the 1AIM non-trivial, and the large number of particles in the metallic band rules out ab initio methods. Approximate solutions to the problem were therefore sought. Anderson initially tried a mean-field, Hartree-Fock approach [8], which suggested there may be a phase transition between magnetic and non-magnetic ground states upon varying U. However, this is incorrect: the ground state of the system is always non-magnetic, as shown by more recent work [11, 12]. Mean-field theory is therefore not sufficient to capture the low-temperature physics of quantum impurity systems such as the 1AIM, and more sophisticated techniques are required.

Finite-order perturbation theory in U has also been applied to the 1AIM [13–15], with some success. This method is however not feasible for *strongly* correlated systems, which are of most interest as they support local moment formation. Perturbation theory in the $V_{\mathbf{k}}$ matrix elements is also problematic, as it must done about an inherently correlated state, so Wick's theorem cannot be used, and the standard diagrammatic techniques cannot be applied. Many other techniques have been used to study the 1AIM, such as the so-called $1/N$ expansion [3]. This method is exact in the limit $N \to \infty$, where N is the spin degeneracy of the impurity. As $N = 2$

[1] Although fundamental questions still remain over the behaviour of the 1AIM out of equilibrium for instance (see, *e.g.*, Refs. [9, 10]).

for the 1AIM it is not clear whether the approximations involved are justified for this model. Non-crossing approximations and slave-boson methods have also been used, and some useful results thereby obtained, but these methods fail to capture the essential physics of the 1AIM fully [3].

One way of making progress in studying the 1AIM is to consider a simplified model, which *presupposes* the existence of a local moment. The Kondo model is such a model, to which the strongly correlated 1AIM is intimately related. The Kondo model consists of a spin-$\frac{1}{2}$ impurity, antiferromagnetically coupled to a metallic conduction band. Such a model can be derived perturbatively from the 1AIM in the regime where there is essentially one electron on the localised impurity level. The method of doing this is known as a Schrieffer-Wolff transformation [16] (as discussed further in section 2.3). As such, the physics exhibited by the Kondo model can also be accessed in the 1AIM.

In the 1960s, Jun Kondo made a major breakthrough when he applied third-order perturbation theory in the antiferromagnetic coupling to the Kondo model [3, 7], and derived the following expression for the resistivity of the model as a function of temperature, $R(T)$,

$$R(T) = a + bT^5 + c\ln\left(\frac{k_B T}{D}\right) \ , \tag{1.1}$$

where D is the half-bandwidth of the conduction band. The first term is a temperature-independent constant associated with electrons in the metal scattering off the impurity spins, while the second term is due to electron-phonon scattering. It is the third term that is most interesting, diverging as $T \to 0$. When taken with the other terms, this anomalous contribution gives rise to a resistivity minimum, as indeed observed experimentally in metal-impurity systems. This explanation of the resistivity minimum was of major importance, but questions still remained. Particularly, the above equation gives rise to an unphysical, divergent resistivity as $T \to 0$, indicating that the perturbation theory breaks down at sufficiently low temperatures. The physics of the Kondo model and the 1AIM on the lowest energy scales was therefore still not clear. This issue became known as the "Kondo problem".

An important step in solving the Kondo problem was provided by Anderson in 1970 [17]. Anderson treated the Kondo model with a perturbative renormalisation group (RG) technique, known as Poor Man's Scaling (PMS). RG approaches essentially consist of successively coarse graining the system of interest by integrating out certain degrees of freedom – in the cases we consider, those corresponding to high energy excitations. One then examines the successive coarse-grained systems in order to determine the behaviour on progressively lower energy scales. Within the PMS approach, the effective coupling between the spin-$\frac{1}{2}$ impurity and the conduction band in the Kondo model increases without limit as the temperature goes to zero. Due to the perturbative nature of PMS however, the results are only valid

when the effective coupling is small, and so PMS is unable to deal with the Kondo model at very low temperature. The so-called Kondo scale (or Kondo temperature), T_{K}, is the temperature for which the dimensionless effective coupling, ρJ (with ρ the density of states per orbital of the conduction band at the Fermi level), becomes $\sim \mathcal{O}(1)$, and T_{K} therefore sets the scale for the breakdown of PMS. The existence of the Kondo scale was however to prove an important part in understanding the Kondo effect.

It was clear that a non-perturbative approach to the problem, lacking unphysical divergences, was required. This was provided by Wilson, who built on the scaling ideas of Anderson [17], to develop a novel RG approach to the problem. The inherently non-perturbative RG technique devised by Wilson was the Numerical Renormalisation Group (NRG) [18]. This technique takes into account energy scales from the bandwidth of the conduction band down to arbitrarily small energies. It does this by discretising the conduction band logarithmically, thereby sampling all energy scales equally. The NRG shows that at low temperature the impurity spin in the Kondo model is screened by the conduction electrons, so that the ground state of the system is non-magnetic. The NRG also shows that at low energies the system behaves as though it were non-interacting, albeit with renormalised parameters, such that the Kondo model is a Fermi liquid at low energies [19–21]. Another result definitively confirmed by the NRG was the existence of the low-energy Kondo scale, and all low-energy properties of the Kondo model can be shown to exhibit universal scaling in terms of T_{K}. As the NRG is non-perturbative it is not limited to any particular set of parameters. Furthermore, the NRG provides a novel way of understanding these systems, in terms of RG flows and fixed points. The NRG method, used extensively in this thesis, will be described in detail in chapter 3.

Wilson's solution of the Kondo model paved the way for the use of the NRG to solve other impurity systems, particularly the 1AIM, to which the NRG was applied by Krishnamurthy et al. in 1980 [11, 12]. These NRG results, showing that the ground state of the 1AIM is non-magnetic for all U, contrary to the result of the Hartree-Fock approach [8], were later confirmed by exact solutions to both the Kondo model and the 1AIM via the so-called Bethe Ansatz [22, 23]. Since the 1980s, and aided by advances in computing technology, the NRG has become the tool of choice to study quantum impurity models, and is now widely used [3, 24]. Many new techniques have also been developed to study these models, including conformal field theory methods [25], a local moment approach [26], and renormalised perturbation theory [27, 28]. Recently a method was developed to obtain comprehensive and highly accurate dynamics from the NRG using the full density matrix [29, 30]. The results satisfy all the necessary Fermi liquid relations, and we discuss this method in section 3.6.2.

We have seen that the Kondo effect arises in both the 1AIM and the Kondo

model, and these are now reasonably well understood. However Kondo physics can also arise in more complicated quantum impurity models. Understanding the Kondo physics in these systems, examples of which include the two-channel Kondo (2CK) model, proposed by Nozieres and Blandin [31, 32], the gapped [33] and pseudo-gapped [34] Anderson models, and three-impurity models [35–38], remains a major challenge for theorists. In this thesis we study an important example of a complex quantum impurity system: the two-impurity Anderson model (2AIM) [39–42]. The 2AIM describes a system of two localised electron levels, each with on-site repulsion, and each tunnel-coupled to separate metallic conduction bands, with a tunnel-coupling between the two localised levels. The 2AIM will be discussed in more detail in chapter 2. Just as the 1AIM is related to the Kondo model by a Schrieffer-Wolff transformation, the 2AIM is likewise related to the two-impurity Kondo model (2IKM). The 2IKM consists of two spins, coupled via an antiferromagnetic exchange coupling, and each coupled antiferromagnetically to separate metallic conduction bands. The 2IKM has been studied in some detail [25, 43–49], in part as a minimal model for a Kondo lattice – a system comprised of a lattice of spins within a metallic host, in which the Kondo effect competes with the interimpurity coupling. In the 2IKM (as in the Kondo lattice) this competition gives rise to a quantum phase transition (QPT), occurring for a critical value of the interimpurity coupling.

This QPT is particularly interesting as it gives rise to so-called two-channel Kondo (2CK) physics [25, 45, 46, 49–51] and the 2IKM behaves as a non-Fermi liquid (NFL) at the QPT. Such behaviour was first observed theoretically in the 2CK model [31], in which a single spin-$\frac{1}{2}$ is coupled to two separate metallic conduction bands. In this model, both conduction bands attempt to quench the spin at low energies, and provided the spin is equally coupled to the conduction bands, an "overscreening" occurs, giving rise to a NFL state, with an unusual $\frac{1}{2}\ln 2$ residual entropy[2] [52, 53]. This ground state, which is not continuously connected to the ground state of the non-interacting system, can be described in terms of Majorana fermions [54], exotic quasiparticles which are their own antiparticles [50, 51, 53, 55]. In this description, just one type of conduction Majorana fermion (out of the eight in total) is involved in screening the impurity degree of freedom, leading to the residual entropy observed[3].

The NFL state arising in the 2CK model is rather delicate [57–60] – any deviation from equal couplings to the two bands (or if there is cotunneling charge transfer between the two conduction bands, discussed in more detail later) causes

[2]Strictly this is the residual impurity contribution to the entropy of the system. Also note that we set $k_B = 1$ throughout this work.

[3]Recently Majorana fermions have been observed in superconductor-semiconductor nanowires [56], systems with proposed applications in the field of quantum computing. Consideration of such is however beyond the scope of this thesis.

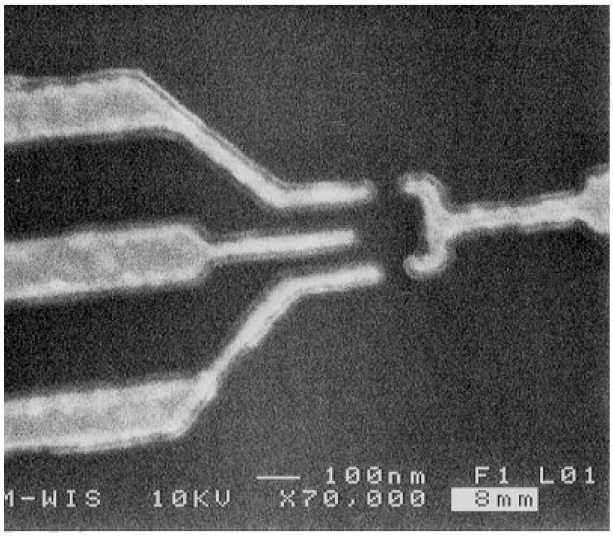


Figure 1.1: Electron micrograph image of a quantum dot device in a semiconductor. Dark colours represent high electron density in the 2DEG, whereas light colours represent regions of the 2DEG where the electrodes have excluded electron density. The quantum dot itself is the small enclosed dark region roughly in the centre of the image. The two metallic leads are the large dark areas at the top and bottom of the image. A voltage can be applied between the two leads, leading to current flow from one lead to the other, via the quantum dot. Reproduced from Ref. [62]

Fermi liquid physics to be recovered on the lowest energy scales. As a result of this delicacy, 2CK physics is believed to have been observed experimentally only once [61]. The NFL state in the 2IKM is similarly delicate, and has been studied previously by conformal field theory methods [25, 49–51] and via the NRG [44, 46]. Given that it can occur in the 2IKM, the question naturally arises: does 2CK physics occur in the (related) 2AIM, and if so, under what circumstances? Answering this question will be one of the major themes of chapter 5.

Parallel to the theoretical progress in understanding the physics of quantum impurity systems, there has been rapid progress in the experimental field, particularly in the last two decades. As discussed, the 1AIM was originally devised to explain the physics of a localised magnetic impurity in a metal sample. However, thanks to recent advances in nanofabrication techniques, the 1AIM has been realised experimentally in a new way; in so-called quantum dot (QD) systems [63]. A QD is simply a small region of a medium in which electrons are trapped. QDs have been created in semiconductors, graphene and carbon nanotubes (see, for example, Refs. [62, 64, 65]).

In semiconductors the method of manufacture of a QD device is as follows. Two wafers of doped semiconductor are placed together, forming a two-dimensional electron gas (2DEG) at the interface [66]. Electrodes can then be placed on the outer

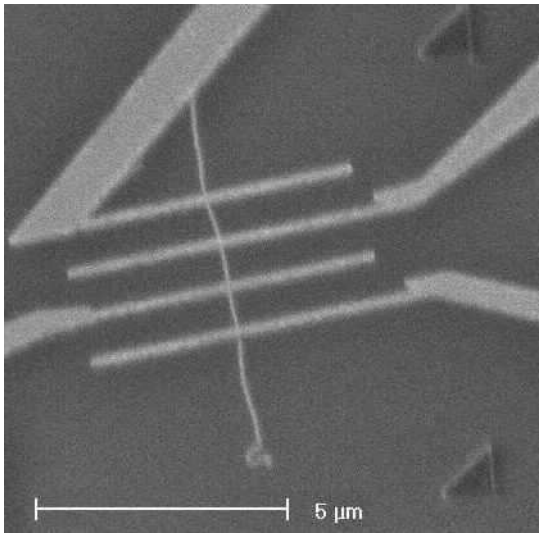


Figure 1.2: Electron microscope image of a quantum dot in a carbon nanotube. The nanotube is the line running almost vertically. The nearly horizontal straight lines are metallic electrodes which define the QD and control its parameters. Reproduced from Ref. [70]

surface of one of the semiconductor wafers. Applying negative voltages to these electrodes repels the electrons in the 2DEG, thereby restricting them to certain regions, separating out the QD from larger areas of electron density which form metallic (source and drain) leads. One such semiconductor-based QD device is shown in Fig. 1.1. A carbon nanotube (CNT) based QD [64, 67–69] is created by depositing a CNT on a silicon surface by chemical vapour deposition, and then laying metallic electrodes over the tube – two of these electrodes serve as the source and drain leads, and others act as gate electrodes, causing confinement of electrons by dragging the CNT band energies down in their vicinity[4]. An example of a CNT-based QD device is shown in Fig. 1.2.

Isolated QDs naturally have discrete single-particle energy levels, and, provided the energy level spacing is large enough, one can in practice consider only one such level (as all other levels will be either essentially empty or full, and so will not affect the properties of the system)[5]. The single active dot level then corresponds to the localised level of the 1AIM, and it has an on-site repulsion – the electrons in the QD are confined to a small region of space and so interact with each other strongly. Such a QD is generally coupled to two macroscopic metallic leads in experiment, so that electrons from the leads can tunnel into the QD and vice versa. The metallic leads, taken together, therefore act as the conduction band in the 1AIM[6]. As a single QD

[4] A voltage may also be applied to the silicon wafer on which the CNT sits in order to define the QD – this is known as a back gate.

[5] This is only true provided there is no degeneracy in the dot levels, as can arise for instance in CNT QDs [71–73].

[6] Although there are two leads in the experimental QD system, provided they have the same

corresponds closely to the 1AIM, it too exhibits the Kondo effect [62, 74].

Experimentalists have exquisite control over the parameters of the system, such as the tunnel-couplings and dot energy levels, allowing the predictions of theorists to be put to the test. In QD experiments, the Fermi levels of the two leads can also be adjusted via application of a voltage bias, so that current flows from one lead to the other through the QD [63]. This current, and therefore the conductance, can be measured, and it serves as an excellent probe of the underlying physics of the QD system. So-called Coulomb blockade peaks are clearly visible in the zero-bias conductance, arising at points in parameter space for which an electron can be added to, or removed from, the dot with little energy cost [75–80]. At these points there is strong sequential one-electron tunneling leading to strongly enhanced zero-bias conductance. Kondo physics is also manifest in the zero-bias conductance [62, 64, 74], as the Kondo effect involves strong scattering of conduction band / metallic lead electrons off the impurity / dot. In an impure metal sample this causes an increase in resistivity [6, 7], whereas by contrast in a QD system, where scattering is essential to current flow *through* the dot, this leads to a strong enhancement of the zero-bias conductance – often referred to as the zero-bias "anomaly".

Recent advances have allowed experimentalists to create systems involving more than one quantum dot. One such system is a tunnel-coupled double quantum dot (TCDQD) [67, 81–85]. In a TCDQD, two quantum dots are connected in series between two metallic leads. Each dot is tunnel-coupled to one of the leads, and the two dots are themselves tunnel-coupled. With each quantum dot treated as a single correlated level, a TCDQD therefore corresponds to the 2AIM. TCDQDs can be made in semiconductors [83] as well as in CNTs [67, 68, 82][7]. QD devices in CNTs have an additional complexity: it is well known that a (defect-free) CNT has orbitally degenerate levels [88], arising from its cylindrical symmetry. When a TCDQD is created in a CNT, the orbital degeneracy may be preserved (see Refs. [89, 90]), but often mixing between the K and K' CNT bands causes the degeneracy to be broken (see Refs. [67, 82]). In Ref. [68], both kinds of behaviour are observed as the gate voltages are varied. Clearly if orbital degeneracy exists then the 2AIM, containing only singly-degenerate dot levels, is not an appropriate model for a CNT-based TCDQD.

Fermi level, *i.e.*, there is no voltage bias across the device, the leads can be combined into a single, effective lead in the model. As such, the 1AIM is sufficient to model the experimental system. This will be discussed in more detail in section 2.2.

[7] A related system has also been manufactured in a scanning tunneling microscope (STM) device [86]. In this system a STM with an impurity Co atom on the tip is brought near to a Co impurity atom sitting on a surface, such that electrons can tunnel between the two impurity atoms. In this system however, electrons may also tunnel directly between the STM tip and the surface, without going via the impurities, such that the experimental system corresponds to the 2AIM with an additional direct, interlead charge-transfer term [87]. Whilst this system is interesting in its own right, its study is beyond the scope of this thesis.

The aim of this work is to gain a comprehensive understanding of the low-temperature behaviour of the 2AIM and related models, such as the 2IKM, over a wide range of parameter regimes. We focus in particular on the possibility of observing 2CK physics in these systems, and the effect of a magnetic field on the Kondo physics arising in these models. We use the knowledge gained to understand some recent experiments on a non-orbitally degenerate CNT-based TCDQD [67]. We note that previous theoretical work on the 2AIM has been carried out in a particular parameter regime (left-right and particle-hole symmetry, see section 2.6) [91–95] in the absence of a magnetic field. The 2IKM has also been studied previously, as mentioned above, but the effect of a magnetic field has not been fully elucidated. As TCDQD experiments are able to probe many different parameter regimes, and as a magnetic field may be applied, we wish to understand these models rather generally.

We conclude this introduction with a brief outline of the rest of this thesis. In chapter 2 the theoretical models describing quantum dot systems are discussed, beginning with the 1AIM (relevant to the case of a single quantum dot). We show how the 1AIM is related to the Kondo model via the Schrieffer-Wolff transformation. The perturbative Poor Man's Scaling method of treating the Kondo model is then looked at briefly, as this gives important physical insight into the Kondo effect. We also discuss the 2CK model, some understanding of which is important in interpreting the results given later in the thesis, before going on to look at the 2AIM. Performing the standard Schrieffer-Wolff transformation on the 2AIM in a certain parameter regime gives rise to the 2IKM, and a brief introduction to the physics of this well-known model is given. The Schrieffer-Wolff transformation on the 2AIM to higher (third) order gives rise to additional terms; the existence of such terms accounting for the differences between the 2AIM and the 2IKM, as we discuss in later chapters. The chapter is concluded by looking at the physics of the 2AIM in two simple limits: the atomic limit and the non-interacting limit. These results form an important basis for understanding the full 2AIM system, as well as indicating the rich behaviour exhibited by the model.

In chapter 3, the NRG, the method used to obtain many of the results in this thesis, is outlined. We describe and discuss the NRG procedure as applied to the 1AIM, explaining how thermodynamic properties of quantum impurity systems can be calculated. The conceptual framework provided by the NRG is described. This allows one to understand quantum impurity systems in terms of renormalisation group flows and fixed points. Having looked at the NRG as applied to the 1AIM, we discuss briefly how it can be extended to the models studied in this work, such as the 2AIM and the 2IKM. The full density matrix method [29, 30] for obtaining dynamical information from the NRG, of which we make extensive use in the following chapters, is then discussed. The chapter ends with a discussion of how

the conductance of the 2AIM can be calculated from the NRG. The zero-bias conductance may be calculated exactly via scattering and linear-response approaches, whereas the conductance can only be calculated approximately at finite bias, when the system is not in equilibrium.

In chapter 4, results for the 2AIM across a wide range of parameter regimes are presented. We begin by deriving some analytic relations involving the self-energies of the system via Fermi liquid theory. The system at so-called particle-hole symmetry is then studied, and NRG results for the thermodynamics of the system are presented, which illustrate the underlying Kondo physics. We look at the dynamics of the system as well, particularly the conductance, which gives additional insight into the physics of the 2AIM. The effect of adding an interdot Coulomb repulsion to the model, as well as taking the dot-lead couplings to be unequal is studied. We go on to consider the system away from particle-hole symmetry, at first keeping the two dot level energies equal, concentrating mainly on the zero-bias conductance, before looking at the 2AIM more generally, with arbitrary dot energy levels, presenting results for the zero-bias conductance. The chapter concludes with a brief study of the finite-bias conductance of the 2AIM at particle-hole symmetry, including a comparison of two different methods for calculating this quantity.

In chapter 5 the possibility of observing 2CK physics in a TCDQD, as modelled by the 2AIM, is investigated. We begin by looking at the 2IKM, for which 2CK physics arises at a critical value of interdot coupling. The effect of introducing charge transfer between the leads, as contained in the 2AIM, is then looked at. Though charge transfer ultimately destroys the 2CK physics on the lowest energy scales, for sufficiently high correlation strength there is an intermediate temperature range in which 2CK physics can be observed. The temperatures are however much too low to be experimentally accessible in a TCDQD at the current time. We go on to look at whether introducing an interdot repulsion, or particle-hole asymmetry to the model can increase the temperatures at which 2CK physics can be observed. This is not however the case. We finish by discussing the possibility of observing 2CK physics in longer quantum dot chains, explaining that it is theoretically possible to do so, although realising these systems experimentally would be a real challenge.

In chapter 6 we look at the effect of applying a magnetic field to the models previously discussed, beginning with the 2IKM, for which we find that the zero-field QPT persists at finite field, provided the system possesses left-right mirror symmetry. More generally it is shown that any even-impurity spin chain has a number of QPTs at finite field, and that all these QPTs exhibit 2CK physics. It is also shown that 2CK physics can be observed in a left-right *asymmetric* 2IKM, provided that the field applied is also left-right asymmetric. Moving on to the 2AIM, we show that the finite-field QPT present in the 2IKM is smeared into a continuous crossover by the interlead charge transfer present, just as at zero field, and 2CK

physics cannot be observed at experimentally feasible temperatures. Interesting behaviour is found in the zero-bias conductance of the 2AIM as a function of field, which is sensitive to the presence of left-right asymmetry.

In chapter 7, we discuss results obtained by our collaborators [67] in experiments on a CNT-based TCDQD, comparing them to NRG results for the 2AIM and using the insight developed over the previous chapters to understand the underlying physics in these experiments. Kondo physics is probed in all charge regimes of the TCDQD and interesting asymmetry is observed in the conductance behaviour, resulting from the fact that the dots are not equally coupled to the leads. Near to particle-hole symmetry, one may attempt to access the crossover from a local singlet to a Kondo singlet regime, but sufficiently low values of interdot tunnel-coupling were not reached in the experiment. The crossover was however accessed at finite field, and enhanced zero-bias conductance observed as an indicator of such, confirming the results of chapter 6.

Finally, in chapter 8, we conclude with a summary of our findings. We note that much of the work in chapters 5 and 6 has been published in Ref. [96], and much of the work in chapter 7 has been published in Ref. [67].

CHAPTER 2

Models of quantum dot systems

In this chapter the models commonly used to study quantum dot (QD) systems theoretically are discussed, including those studied in this thesis. We begin with the models describing single QDs, namely the single-impurity Anderson model (1AIM) [8] and the Kondo model [7]. These two models are intimately related via the Schrieffer-Wolff (SW) transformation [16], a perturbative technique which maps the 1AIM onto the Kondo model at low energies in a certain parameter regime. Having discussed these single-impurity models, we take the opportunity to include a brief discussion of the Poor Man's Scaling (PMS) technique [17], discussed briefly in chapter 1. Whilst PMS is not able to deal fully with the 1AIM or the Kondo model, it does illustrate some of the scaling ideas that play a central role in this work, and provides necessary background for an understanding of the Numerical Renormalisation Group (NRG) [11, 12, 18, 24] – the subject of chapter 3. A brief discussion of the two-channel Kondo (2CK) model [31], a single-impurity model which will prove relevant to the work in this thesis, is also included.

We go on to discuss two-impurity models describing tunnel-coupled double quantum dots (TCDQDs), which form the main focus of our work, starting with the two-impurity Anderson model (2AIM) [91–93], the most comprehensive model used, and an extension of the 1AIM discussed previously. As for the 1AIM, one can perform a SW transformation on the 2AIM to obtain simpler effective models at low energies. A second-order SW transformation gives the well-known two-impurity Kondo model (2IKM) [25, 43–49], and we give a brief discussion of its physics. The SW transformation to *third* order gives rise to additional terms in the low-energy effective model [96]. As we will see in later chapters, these terms are what distinguishes the physics of the 2AIM from that of the 2IKM and they are of great importance. We conclude the chapter by carrying out a preliminary study of the 2AIM in two simple limits: the atomic limit, in which the QDs are completely decoupled from the metallic leads; and the non-interacting limit, in which electron repulsion is ignored. The 2AIM is

trivially soluble in both these limits, and a knowledge of these solutions is useful in understanding the full 2AIM, the subject of chapter 4.

2.1 Modelling a quantum dot device

As discussed in the previous chapter, a single QD device consists of a QD tunnel-coupled to two metallic leads. The isolated QD (that is, the dot completely decoupled from the leads, known as the QD in the "atomic limit") is essentially a potential well in which electrons can be trapped, and as such it has a series of quantised energy levels. An isolated metallic lead has an effectively continuous band of energy levels, which are filled up to the Fermi level. Upon coupling a QD to one or more metallic leads, any QD levels which are sufficiently far below the Fermi level will be essentially filled (doubly occupied, with an $\uparrow$-spin and a $\downarrow$-spin electron), and any levels sufficiently far above the Fermi level will be essentially unoccupied. These high and low QD levels will not contribute to the low-energy physics of the system, so they may be neglected. In some instances there may be more than one QD level near to the Fermi level, for instance if there is orbital degeneracy in the QD, and an appropriate model must take into account all of these levels [72, 97]. The simplest case, however, and the one which we consider exclusively, is the case where there is only one QD level sufficiently close to the Fermi level to contribute to the low-energy physics. In this case we may treat the QD simply as a single level, which may contain zero, one or two electrons. Clearly, due to the tight spatial confinement, electrons in the QD will repel each other strongly. This is taken into account by including an onsite Coulomb repulsion for the dot level. As the QD is tunnel-coupled to two leads, we must include electron hopping terms between the dot level and all the lead levels in our model.

In the case of a single QD with only one active level, a further simplification may be achieved provided there is no bias voltage between the two leads, *i.e.*, the Fermi levels of the two leads are equal. The dot-lead tunnel-coupling term is given by

$$\sum_{\nu\sigma\mathbf{k}} V_\nu (c^\dagger_{\nu\mathbf{k}\sigma} d_\sigma + d^\dagger_\sigma c_{\nu\mathbf{k}\sigma}) \ , \tag{2.1}$$

where $\nu = 1, 2$ labels the leads, $c^\dagger_{\nu\mathbf{k}\sigma}$ creates a σ-spin electron ($\sigma = \uparrow, \downarrow$) in lead ν with wavevector $\mathbf{k}$, while $d^\dagger_\sigma$ creates a σ-spin electron on the dot level. V_ν is the matrix element for electron hopping between the dot level and lead ν, which we take to be real, as well as independent of wavevector or spin. We may perform a canonical transformation of the lead operators via

$$\begin{aligned} c^\dagger_{1\mathbf{k}\sigma} &= c^\dagger_{a\mathbf{k}\sigma} \cos\theta + c^\dagger_{b\mathbf{k}\sigma} \sin\theta \ , \\ c^\dagger_{2\mathbf{k}\sigma} &= c^\dagger_{a\mathbf{k}\sigma} \sin\theta - c^\dagger_{b\mathbf{k}\sigma} \cos\theta \ , \end{aligned} \tag{2.2}$$

taking $\tan\theta = V_1/V_2$. Under this transformation the dot-lead coupling term becomes simply

$$\sqrt{V_1^2 + V_2^2}\sum_{\sigma\mathbf{k}}(c^\dagger_{a\mathbf{k}\sigma}d_\sigma + d^\dagger_\sigma c_{a\mathbf{k}\sigma}) \ , \tag{2.3}$$

so that the dot decouples from the "b" lead and couples only to a *single* lead. In order to model a single QD, we therefore need to take into account only one lead. [This is not however the case for TCDQDs, as we will see in section 2.6.]

2.2 The single-impurity Anderson model

We are now in a position to discuss the standard model for a single QD, the 1AIM. The Hamiltonian for the 1AIM is [3, 8]

$$\hat{H}_{1\mathrm{AIM}} = \sum_{\mathbf{k}\sigma}\epsilon_{\mathbf{k}}c^\dagger_{\mathbf{k}\sigma}c_{\mathbf{k}\sigma} + \sum_\sigma \epsilon\ d^\dagger_\sigma d_\sigma + U\hat{n}_\uparrow\hat{n}_\downarrow + V\sum_{\mathbf{k}\sigma}(c^\dagger_{\mathbf{k}\sigma}d_\sigma + d^\dagger_\sigma c_{\mathbf{k}\sigma}). \tag{2.4}$$

where $c^\dagger_{\mathbf{k}\sigma}$ creates a lead electron with wavevector $\mathbf{k}$ and spin $\sigma = \uparrow, \downarrow$. $\epsilon_{\mathbf{k}}$ is the energy of a lead electron with wavevector $\mathbf{k}$. $\hat{n}_\sigma = d^\dagger_\sigma d_\sigma$ is the number operator for σ-spin electrons on the dot level, ϵ is the energy of the dot level, U is the Coulomb repulsion between electrons on the dot level and V is the hopping matrix element between the dot level and the lead states. The first term in the Hamiltonian describes the metallic lead, which consists of a continuum of uncorrelated energy levels. The second and third terms describe the isolated dot, consisting of a single correlated level. The final term is the dot-lead tunnel coupling. Throughout this work, we consider only metallic leads with a uniform density of states per lead orbital, denoted ρ. We label the half-bandwidth D, such that $\rho = \frac{1}{2D}$. The strength of the dot-lead coupling is usually expressed in terms of the so-called dot-lead hybridisation strength, $\Gamma = \pi\rho_T V^2$, where $\rho_T = N\rho$ is the total lead density of states, with $N \to \infty$ the number of orbitals in the lead.

The bandwidth of the 1AIM is taken to be much larger than any other energy scale, as is relevant to QD experiments, such that its precise value has no bearing on the low-energy physics of the model. Taking Γ as the unit of energy, the 1AIM therefore has just two independent parameters: U/Γ and ϵ/Γ. If $\epsilon = -U/2$, then the 1AIM Hamiltonian is invariant to the particle-hole (ph) transformation:

$$d^\dagger_\sigma \leftrightarrow -\ d_\sigma, \quad c^\dagger_{\mathbf{k}\sigma} \leftrightarrow\ c_{-\mathbf{k}\sigma} \ , \tag{2.5}$$

so long as $\epsilon_{\mathbf{k}} = -\epsilon_{-\mathbf{k}}$, as is the case for the flat bands considered here. This property is known as ph symmetry. When the 1AIM is near to ph symmetry ($\epsilon \simeq -\frac{U}{2}$), the low-energy states contain a single electron on the dot level (provided $U/\Gamma \gg 1$); states with zero or two electrons on the dot level being $\sim U$ higher in energy. In this

case the system may be mapped onto the Kondo model via a SW transformation, to which we now turn our attention.

2.3 Schrieffer-Wolff transformation and the single-impurity Kondo model

The ph-symmetric Anderson model with $U/\Gamma \gg 1$ has essentially one electron on the dot level, in the sense that fluctuations in the dot charge away from its expectation value ($\langle \sum_\sigma \hat{n}_\sigma \rangle = 1$ precisely at ph symmetry) are small. When the dot level is singly occupied the dot electron can have either up or down spin, such that the dot level behaves effectively as a single spin-$\frac{1}{2}$, provided one is interested only in properties at sufficiently low energies that charge excitations are not significant.

The mapping of this dot level onto a spin can be formalised via the SW transformation [3, 16]. This involves perturbation theory in the dot-lead tunnel coupling, in order to derive an effective model valid only at low energies. The unoccupied and doubly-occupied atomic-limit ($V = 0$) dot states are projected out, such that the low-energy effective model (valid for energies $\ll U$) can be written as a single spin-$\frac{1}{2}$ antiferromagnetically coupled to the metallic lead. This is nothing more than the Kondo model, discussed in chapter 1.

We now outline the SW transformation. The first step is to partition the Hamiltonian into two parts, $\hat{H}_{1\mathrm{AIM}} = \hat{H}_0 + \hat{H}_1$, where $\hat{H}_1$ is the perturbation. For the 1AIM, $\hat{H}_1$ is taken to be the dot-lead tunnel coupling (the final term in Eqn. (2.4)). One then assumes that the eigenstates of $\hat{H}_0$ can be cleanly separated into a low-energy and a high-energy manifold. This is evidently the case for the ph-symmetric 1AIM, where the unoccupied and doubly-occupied atomic-limit dot states have an energy U greater than the singly-occupied ground states. $\hat{1}'$ is defined to be the unity operator for the low-energy manifold, and $\hat{P} = \hat{1} - \hat{1}'$ to be the operator which projects into the high-energy manifold. We then wish to project the full Hamiltonian into the low-energy manifold, perturbatively eliminating virtual excitations to the high-energy manifold. By using Brillouin-Wigner perturbation theory [98], it can be shown that to second order in $\hat{H}_1$, the effective Hamiltonian that arises from carrying out such a procedure is

$$\hat{H}_{\mathrm{eff}} = \hat{1}'\hat{H}_0\hat{1}' + \hat{1}'\hat{H}_1\hat{1}' + \hat{1}'\hat{H}_1(\epsilon_0 - \hat{H}_0)^{-1}\hat{P}\hat{H}_1\hat{1}' \ , \tag{2.6}$$

with ϵ_0 the ground state energy of $\hat{H}_0$, and the three separate terms being the zeroth, first and second order contributions respectively. For the 1AIM, the projection operators are given by $\hat{1}' = |\uparrow\rangle\langle\uparrow| + |\downarrow\rangle\langle\downarrow|$ and $\hat{P} = |\uparrow\downarrow\rangle\langle\uparrow\downarrow| + |-\rangle\langle -|$, with $|\uparrow\downarrow\rangle$ and $|-\rangle$ the doubly-occupied and unoccupied dot states respectively, and $|\uparrow\rangle$ and $|\downarrow\rangle$ the singly-occupied dot states. The effective Hamiltonian is then found to be of

Kondo form,

$$\hat{H}_{\text{eff}} = \hat{H}_{\text{Kondo}} = \sum_{\mathbf{k}\sigma} \epsilon_{\mathbf{k}} c^{\dagger}_{\mathbf{k}\sigma} c_{\mathbf{k}\sigma} + J_K \hat{\mathbf{S}}_{\mathbf{0}} \cdot \hat{\mathbf{S}} \ , \tag{2.7}$$

where $\hat{\mathbf{S}}$ is the localised spin-$\frac{1}{2}$ representing the dot level, and $\hat{\mathbf{S}}_{\mathbf{0}}$ is the local spin density of lead electrons at the impurity site given by

$$\begin{aligned} \hat{\mathbf{S}}_{\mathbf{0}} &= \sum_{\sigma,\sigma'} f^{\dagger}_{0\sigma} \boldsymbol{\sigma}_{\sigma\sigma'} f_{0\sigma'} \ , \\ f^{\dagger}_{0\sigma} &= \frac{1}{\sqrt{N}} \sum_{\mathbf{k}} c^{\dagger}_{\mathbf{k}\sigma} \ , \end{aligned} \tag{2.8}$$

where $\boldsymbol{\sigma}$ is a vector of the Pauli matrices, with

$$\sigma^z = \begin{pmatrix} \frac{1}{2} & 0 \\ 0 & -\frac{1}{2} \end{pmatrix} \quad \sigma^x = \begin{pmatrix} 0 & -\frac{i}{2} \\ \frac{i}{2} & 0 \end{pmatrix} \quad \sigma^y = \begin{pmatrix} 0 & \frac{1}{2} \\ \frac{1}{2} & 0 \end{pmatrix} \ , \tag{2.9}$$

and $f^{\dagger}_{0\sigma}$ is the creation operator for what is known as the zero-orbital of the Wilson chain of the lead (see chapter 3 for more details). For the ph-symmetric 1AIM, the effective exchange coupling J_K is given by $J_K = 8NV^2/U$, such that $\rho J_K = 8\Gamma/\pi U$. J_K is always positive, so the dot-lead coupling is always *antiferromagnetic*.

We now look at the PMS approach, as applied to the Kondo model (Eqn. (2.7)). Apart from giving an insight into the physics of the Kondo model (and other impurity models), it is useful for introducing some of the scaling ideas which will be key to an understanding of the NRG, discussed in the next chapter.

2.4 Poor Man's Scaling

To deal fully with complex many-body systems such as the 1AIM and Kondo models, rather sophisticated calculations, such as the NRG, are required. However, simpler approaches are still able to give some physical insight into the problem at hand. PMS [3, 17] is one such approach. The method can be applied directly to the 1AIM [3, 99], but in the ph-symmetric case it is simpler to work with the low-energy effective Kondo model described above.

We have seen that in the SW transformation of the 1AIM, excitations from the atomic-limit ($V = 0$) ground states (which contain a single-electron on the dot level) to excited states with either zero or two electrons on the dot level, are eliminated perturbatively to give an effective model valid at low energies. The basic principle of PMS as applied to the Kondo model is somewhat similar. In this case, excitations which involve creating an electron near the top of the lead conduction band, or creating a hole near the bottom of the lead conduction band, processes which are of energy $\sim D$, are perturbatively eliminated. By doing so, one is left with an effective

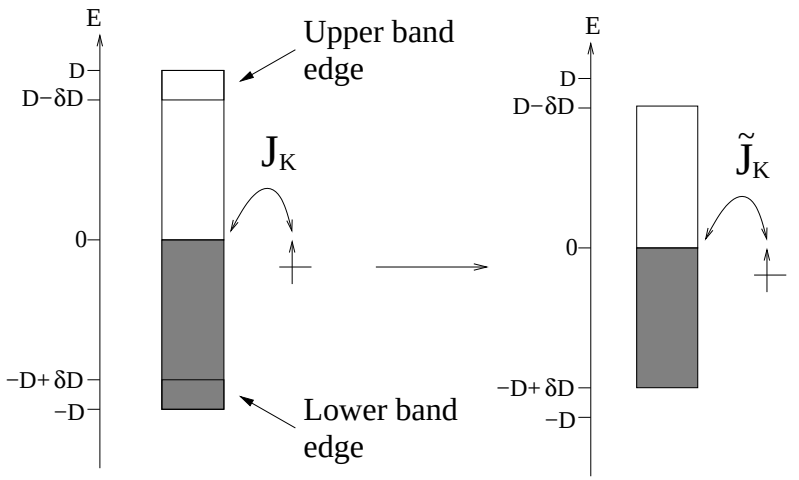


Figure 2.1: Diagram illustrating the PMS procedure for the Kondo model. The lead conduction band, represented by the half shaded rectangle, is coupled to a single spin-$\frac{1}{2}$. D is the initial half-bandwidth of the conduction band of the leads and δD is the width of the band edges. The bandwidth is reduced from $2D \to 2D - 2\delta D$, and to account for this the coupling constant is renormalised from $J \to \tilde{J}$.

model with a reduced bandwidth and a *renormalised* dot-lead coupling, $\tilde{J}_K$. One significant difference from the SW transformation is that in PMS, the effective model derived is of the same *form* as the original model, but with different parameters.

The first step in the PMS process is to partition the lead conduction band into three sections: a pair of "band edges" at $D - \delta D < |E| < D$, and the remaining bulk section in between (see Fig. 2.1). One then considers scattering involving the band edges (*i.e.*, the creation of electrons in the upper band edge, and the creation of holes in the lower band edge) as a perturbation to a new Hamiltonian with a reduced half-bandwidth of $(D - \delta D)$. Brillouin-Wigner perturbation theory to second order (although it is possible to go to higher order) in J_K is then used to derive the new effective Hamiltonian. The second-order terms which arise from such a process are illustrated in Fig. 2.2: the horizontal line represents the dot spin, whilst the incoming and outgoing lines represent conduction band states in the bulk of the conduction band. The dashed lines represent states in the conduction band edges. We will concentrate on the results of carrying out the PMS procedure and will not discuss the full mathematical details; these can be found in the original paper by Anderson [17], as well as in the monograph by Hewson [3].

The effective Hamiltonian that is derived by the PMS process has the same (Kondo) form as the original, but with a *different* coupling constant, $\tilde{J}_K$, and a smaller half-bandwidth, $\tilde{D} = D - \delta D$. This is illustrated schematically in Fig. 2.1. The "bare" coupling constant, J_K, is said to have been renormalised, and this renormalisation of the Hamiltonian can be considered as an example of a renormalisation group transformation (see section 3.5). One can then take the limit $\delta D \to 0$, and

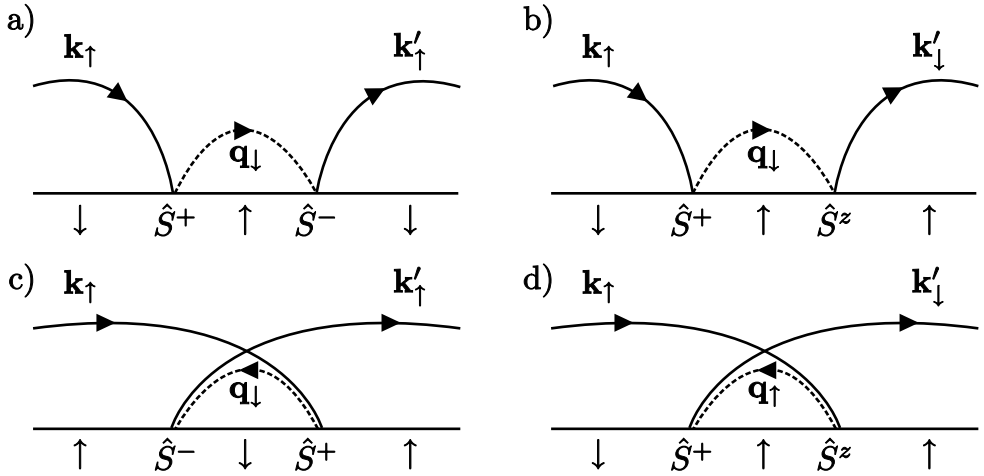


Figure 2.2: Illustration of the second-order diagrams that arise in PMS for the Kondo model. The horizontal line describes the state of the impurity. Diagrams a) and c) involve scattering of a particle/hole from the bulk (with wavevector $\mathbf{k}$) to the band edge (with wavevector $\mathbf{q}$) and back to the bulk (with wavevector $\mathbf{k}'$). Diagrams b) and d) involve spin-flip scattering of a particle/hole. Reproduced from Ref. [100].

furthermore one can repeat the elimination process many times. This means that a differential equation can be obtained, describing how $\tilde{J}_K$ changes as the bandwidth decreases. To second order, the result is [3, 17]

$$\frac{d\tilde{J}_K}{d\ln\tilde{D}} = -\rho\tilde{J}_K^2 \ , \tag{2.10}$$

an example of a scaling equation. Such an equation states how parameters must be renormalised to account for a change in some scale, in this case, D. We can solve this simple differential equation to give

$$\tilde{J}_K = \frac{1}{\rho\ln\frac{\tilde{D}}{T_\mathrm{K}}}, \tag{2.11}$$

where T_K is the so-called Kondo temperature/scale; an example of a scaling invariant, a quantity which remains constant as the scale is successively changed (*i.e.*, the bandwidth is reduced). Rearranging Eqn. (2.11) and using the boundary condition $\tilde{J}_K(D) = J_K$ gives

$$T_\mathrm{K} = D\exp\left(\frac{-1}{\rho J_K}\right). \tag{2.12}$$

For physical systems, $\rho J_K \ll 1$ [3], and hence T_K/D is exponentially small[1]. The existence of a scaling invariant implies that all low-energy properties of the model

[1]This expression for the Kondo scale is naturally approximate, as illustrated for instance by going to third order in PMS, which gives $T_\mathrm{K} = D\sqrt{\rho J_K}\exp\left(\frac{-1}{\rho J_K}\right)$. The exponential dependence of the Kondo scale on ρJ_K is however correct, as has been confirmed by NRG calculations.

must be universal functions of T_{K}, such that systems with the same T_{K} have the same low-energy physics [18].

If the initial $\tilde{J}_K = 0$, decreasing $\tilde{D}$ will cause no change in $\tilde{J}_K$ (as is obvious from Eqn. (2.10)). The point $\tilde{J}_K = 0$ is therefore known as a "fixed point" – a point at which further transformations of the Hamiltonian have no effect. Fixed points will be discussed in more detail in section 3.5. If the initial $\tilde{J}_K > 0$, Eqn. (2.10) shows that as $\tilde{D}$ is decreased, $\tilde{J}_K$ increases. Therefore if $\tilde{J}_K$ is near to zero (but not precisely at it), then reducing the bandwidth will move the system away from this fixed point, so we say this is an unstable fixed point (reducing the energy scale when the system is close to a *stable* fixed point moves the system closer to that fixed point). The $\tilde{J}_K = 0$ situation corresponds to a free spin completely decoupled from the band, and this is thus known as the local moment (LM) fixed point (reflecting the localised magnetic moment of the free spin).

A key point to note is that decreasing $\tilde{D}$ by eliminating excitations to the band edges, is equivalent to reducing the temperature, as excitations of successively lower energy are eliminated [11]. The result derived therefore effectively implies that as temperature is decreased to around T_{K}, the effective coupling between the impurity and the metallic band becomes large (provided the initial J_K is not zero). One can say that strong coupling between the impurity and the conduction electrons occurs on the scale of T_{K}.

The main limitation of PMS is that it relies on perturbation theory in the exchange coupling $\tilde{J}_K$. This means it is only truly valid when $\tilde{J}_K$ is small (relative to $\tilde{D}$), and we cannot rely on the results when $\tilde{J}_K$ becomes large, namely at low temperature. However, PMS does serve as a very neat introduction to the concepts of renormalisation by introducing the ideas of scaling and scaling invariants – ideas which are key to the NRG (see chapter 3). It also suggests the existence of strong coupling behaviour at low temperatures. Although PMS breaks down when $\tilde{J}_K$ becomes large, the results do lead one to suspect that a stable fixed point may exist for infinitely strong effective impurity-lead coupling, a so-called strong coupling (SC) fixed point. Indeed, this is the case, as can be shown by the NRG [18, 24], discussed further in chapter 3. At the SC fixed point, the impurity spin forms a spin singlet state with the conduction electrons, known as a Kondo singlet, and its magnetic moment is said to be "quenched" or "screened".

Having looked at PMS, we now briefly discuss another single-impurity model that will be relevant to the work in this thesis – the 2CK model – before going on to look at the two-impurity models that will be the main focus of this thesis.

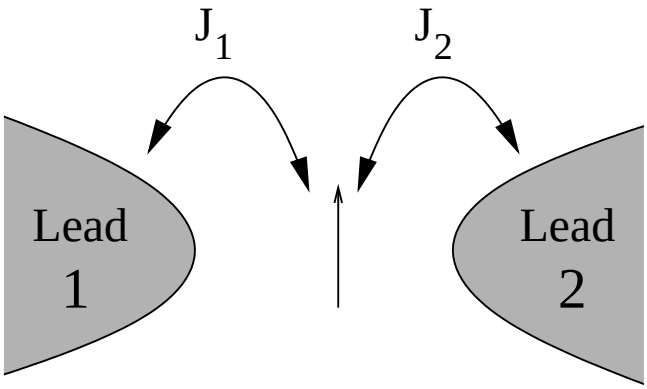


Figure 2.3: Illustration of the 2CK model. A single spin-$\frac{1}{2}$ is coupled to two separate metallic leads/conduction bands, with antiferromagnetic exchange couplings J_1 and J_2.

2.5 The two-channel Kondo model

The 2CK model, illustrated in Fig. 2.5, consists of a spin-$\frac{1}{2}$ coupled to *two* separate but equivalent metallic leads, with antiferromagnetic exchange couplings J_1 and J_2. The Hamiltonian is

$$\hat{H}_{\rm 2CK} = J_1 \hat{\mathbf{S}} \cdot \hat{\mathbf{S}}_{\mathbf{01}} + J_2 \hat{\mathbf{S}} \cdot \hat{\mathbf{S}}_{\mathbf{02}} + \hat{H}_{\rm leads} \ , \tag{2.13}$$

where $\mathbf{S}$ represents the localised impurity spin-$\frac{1}{2}$ and $\hat{\mathbf{S}}_{\mathbf{0}\nu}$ is the local spin density of lead ν ($\nu = 1, 2$) given by

$$\begin{aligned} \hat{\mathbf{S}}_{\mathbf{0}\nu} &= \sum_{\sigma,\sigma'} f^\dagger_{\nu\sigma} \boldsymbol{\sigma}_{\sigma\sigma'} f_{\nu\sigma'} \ , \\ f^\dagger_{\nu\sigma} &= \frac{1}{\sqrt{N}} \sum_{\mathbf{k}} c^\dagger_{\nu\mathbf{k}\sigma} \ , \end{aligned} \tag{2.14}$$

where $f^\dagger_{\nu\sigma}$ is the creation operator for the zero-orbital of lead ν and $c^\dagger_{\nu\mathbf{k}\sigma}$ creates an electron with spin σ and wavevector $\mathbf{k}$ in lead ν. $\hat{H}_{\rm leads}$ is given by

$$\hat{H}_{\rm leads} = \sum_{\nu\mathbf{k}\sigma} \epsilon_{\mathbf{k}} c^\dagger_{\nu\mathbf{k}\sigma} c_{\nu\mathbf{k}\sigma} \ . \tag{2.15}$$

It is straightforward to establish that no canonical transformation of the lead operators can eliminate the coupling between the spin and one of the leads. This is markedly different from the case of a single *level* coupled to two leads, as discussed in section 2.1.

The 2CK model was first proposed by Nozieres and Blandin [31], and is of great interest as it is known to exhibit exotic non-Fermi liquid (NFL) physics in the case of left-right (LR) symmetry ($J_1 = J_2$). Whilst Landau's Fermi liquid theory [19, 20]

has been incredibly successful in explaining the physics of a wide range of systems, NFLs, by definition, do not fit into this paradigm. The physics of the 2CK model has however been established definitively [31, 101–104], and can be summarised as follows[2]. If $J_{1(2)} > J_{2(1)}$, then the spin undergoes a Kondo effect with lead 1 (2), and becomes effectively decoupled from lead 2 (1) at low temperature. The system therefore flows to a fixed point where the effective coupling to lead 1 (2) is infinite, whereas the effective coupling to lead 2 (1) is zero. However, if the spin is equally coupled to both leads, then instead of one or the other lead screening the spin, the so-called 2CK effect occurs. This can be thought of as both leads trying to screen the spin, resulting in what is often referred to as "overscreening". In the usual (single-channel) Kondo effect the $\ln 2$ contribution to the entropy of the system arising from a free spin at high temperature is reduced to zero as the temperature is lowered, due to the spin being quenched by the Kondo effect. In the 2CK effect however, the entropy does not vanish as the temperature is reduced, rather there is a residual $\frac{1}{2}\ln 2$ impurity contribution to the entropy [52, 53]. The system flows to the so-called 2CK fixed point, which has equal, intermediate effective couplings to the leads [111]. The scale on which it flows to this fixed point, the two-channel Kondo scale, T_{K}^{2CK}, is essentially the same as the equivalent single-channel Kondo scale for the Kondo model which would arise if one of the leads were completely decoupled, *i.e.*, if J_2 or J_1 were set to zero[3].

The 2CK effect is however rather delicate. In the pristine LR-symmetric case discussed above, the 2CK fixed point is stable, so that once the system has flowed to this fixed point, it remains there, and the system is a NFL on the lowest energy scales. Whilst the inclusion of spin anisotropy in the impurity-lead couplings does not change this [49, 57, 113], addition of a magnetic field or cotunneling interlead charge transfer (that is, interlead charge transfer mediated by the spin) renders the 2CK FP unstable [25, 49, 57, 114, 115]. The system thus flows away from the 2CK FP and toward the stable SC fixed point, below some energy scale, denoted T^*. This means that the system behaves as a Fermi liquid on the lowest energy scales. Provided $T^* \ll T_{\mathrm{K}}^{2CK}$ however, NFL, 2CK physics can still be observed for temperatures $T^* \ll T \ll T_{\mathrm{K}}^{2CK}$. Achieving such separation of energy scales depends on minimising interlead charge transfer (and thereby minimising T^*), which is extremely difficult in single QD experiments. As a result of this, 2CK physics is only believed to have been observed once [61], in a single QD system where one of the metallic leads was made interacting (a so-called quantum box) and tuned

[2] We note also that the 2CK model can be shown to be identical to a "compactified" 1AIM in the high U limit, and work on this model has helped elucidate the physics of the 2CK model [55, 105–110].

[3] PMS to second order gives $T_{\mathrm{K}}^{2CK} \sim \exp(-1/\rho J_1)$, just as for the single-channel Kondo scale, T_{K}, arising in the Kondo model. Going to third order, however, gives rise to different pre-exponential factors for the two models, $T_{\mathrm{K}}^{2CK} \sim \rho J_1 \exp(-1/\rho J_1)$, whereas $T_{\mathrm{K}} \sim \sqrt{\rho J_1}\exp(-1/\rho J_1)$ [31, 112].

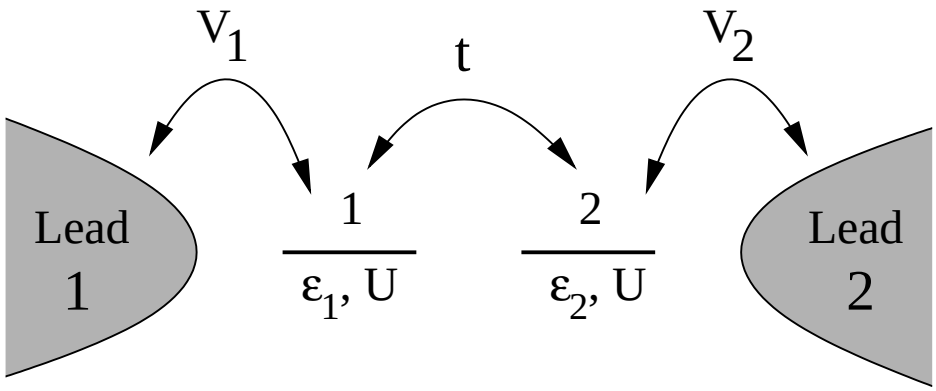


Figure 2.4: Schematic of the 2AIM, consisting of two dot levels (1 and 2) with equal onsite Coulomb repulsion, U, and level energies ϵ_1 and ϵ_2. The two dot levels are coupled by the hopping matrix element, t, and each is coupled to a metallic lead conduction band by the hopping matrix elements, V_1 and V_2.

to a "Coulomb blockade valley", at which adding or removing electrons from the interacting lead is energetically unfavourable. In consequence, electrons could not easily be added to or removed from the interacting lead, thereby strongly suppressing interlead charge transfer at low temperature. We will see later that the physics of the 2CK model, described above, is closely related to that of the 2IKM, discussed in section 2.8.

Having discussed the relevant single-impurity models, we now go on to look at the two-impurity models which will be the main focus of this thesis, beginning with the 2AIM.

2.6 The two-impurity Anderson model

The 2AIM, illustrated in Fig. 2.4, is the canonical model for a TCDQD. It consists of two levels, labeled 1 and 2 (corresponding to the two quantum dots of the TCDQD) with equal on-site Coulomb repulsion (U) coupled by a hopping matrix element (t) to each other, and each coupled to its own metallic lead (labeled 1 and 2) by hopping matrix elements, V_1 and V_2. The full 2AIM Hamiltonian comprises terms for the isolated leads and dots, $\hat{H}_{\rm leads}$ and $\hat{H}_{\rm dots}$, and a hybridisation term involving electron hopping between the two, $\hat{H}_{\rm hyb}$:

$$\hat{H}_{\rm 2AIM} = \hat{H}_{\rm leads} + \hat{H}_{\rm dots} + \hat{H}_{\rm hyb} \ , \tag{2.16}$$

where

$$\hat{H}_{\rm leads} = \sum_{\nu \mathbf{k}\sigma} \epsilon_{\mathbf{k}} c^{\dagger}_{\nu \mathbf{k}\sigma} c_{\nu \mathbf{k}\sigma} \ , \tag{2.17}$$

$$\begin{aligned}\hat{H}_{\rm dots} &= \hat{H}_\epsilon + \hat{H}_t + \hat{H}_U \\ &= \sum_{\nu\sigma} \epsilon_\nu \hat{n}_{\nu\sigma} + t \sum_\sigma \left(d^\dagger_{1\sigma} d_{2\sigma} + h.c. \right) \\ &\quad + U \sum_\nu \hat{n}_{\nu\uparrow} \hat{n}_{\nu\downarrow} \ ,\end{aligned} \tag{2.18}$$

$$\hat{H}_{\rm hyb} = \sum_{\nu\mathbf{k}\sigma} V_\nu \left(d^\dagger_{\nu\sigma} c_{\nu\mathbf{k}\sigma} + h.c. \right) \ , \tag{2.19}$$

with $\nu = 1, 2$ and $\sigma = \uparrow, \downarrow$. $\epsilon_\nu(\epsilon_{\mathbf{k}})$ is the level energy for dot ν (lead state with wavevector $\mathbf{k}$), $c^\dagger_{\nu\mathbf{k}\sigma}$ creates an electron on lead ν with spin σ and wavevector $\mathbf{k}$. $\hat{n}_{\nu\sigma} = d^\dagger_{\nu\sigma} d_{\nu\sigma}$ is the number operator for electrons on dot ν with spin σ. The hybridisation to lead 1(2) is $\Gamma_{1(2)} = \pi \rho_T V^2_{1(2)}$. t is the tunnel-coupling matrix element between the two dot levels. U, the onsite Coulomb repulsion, is taken to be equal for the two dot levels.

The application of a local (dot) magnetic field, which we consider in later chapters, is given by the additional term

$$\hat{H}_B = -g\mu_B B \hat{S}_z = -h\hat{S}_z, \tag{2.20}$$

where $\hat{S}_z$ is the operator for the total z-component of spin on the dots, g is the electron g factor, B is the magnetic field strength and μ_B is the Bohr magneton. We also consider an interdot Coulomb repulsion term, which we would expect to arise in an experimental TCDQD system, given by

$$\hat{H}_{U'} = U' \hat{n}_1 \hat{n}_2 \ , \tag{2.21}$$

where $\hat{n}_\nu = \sum_\sigma \hat{n}_{\nu\sigma}$ is the total number operator for dot ν.

Symmetries of the Hamiltonian

If $\epsilon_1 = \epsilon_2$ and $\Gamma_1 = \Gamma_2$ then the system is invariant to transforming the operator labels as follows: $1 \leftrightarrow 2$, *i.e.*, the system is left-right (LR) symmetric. Further, if $\epsilon_1 = \epsilon_2 = -U/2$ (but regardless of whether or not $\Gamma_1 = \Gamma_2$), then the model is invariant to the particle-hole (ph) transformation

$$d^\dagger_{1\sigma} \leftrightarrow - \, d_{1\bar{\sigma}}, \ \ d^\dagger_{2\sigma} \leftrightarrow \ d_{2\bar{\sigma}}, \ \ c^\dagger_{\mathbf{1k}\sigma} \leftrightarrow \ c_{1-\mathbf{k}\bar{\sigma}}, \ \ c^\dagger_{\mathbf{2k}\sigma} \leftrightarrow - \, c_{2-\mathbf{k}\bar{\sigma}} \ , \tag{2.22}$$

with $\bar{\sigma}$ the opposite spin to σ, and we say the system is ph symmetric. [In the case of finite interdot Coulomb repulsion, the condition for ph symmetry becomes $\epsilon_1 = \epsilon_2 = -U/2 - U'$.]

Parity basis

In the LR-symmetric case it proves useful (as we will see in later chapters) to transform the Hamiltonian into the so-called parity basis, where symmetric and antisymmetric combinations of 1 and 2 orbitals are taken to form even (e) and odd (o) orbitals, *i.e.*,

$$d_{e\sigma} = \frac{1}{\sqrt{2}}(d_{1\sigma} + d_{2\sigma}) \ , \quad d_{o\sigma} = \frac{1}{\sqrt{2}}(d_{1\sigma} - d_{2\sigma}) \ , \tag{2.23}$$

and

$$c_{e\mathbf{k}\sigma} = \frac{1}{\sqrt{2}}(c_{1\mathbf{k}\sigma} + c_{2\mathbf{k}\sigma}) \ , \quad c_{o\mathbf{k}\sigma} = \frac{1}{\sqrt{2}}(c_{1\mathbf{k}\sigma} - c_{2\mathbf{k}\sigma}) \ . \tag{2.24}$$

The Hamiltonian for the LR-symmetric 2AIM ($\epsilon_1 = \epsilon_2 = \epsilon$, $V_1 = V_2 = V$) in the parity basis is

$$\begin{aligned}
\hat{H}_{\text{leads}} &= \sum_{\alpha\mathbf{k}\sigma} \epsilon_{\mathbf{k}} c^{\dagger}_{\alpha\mathbf{k}\sigma} c_{\alpha\mathbf{k}\sigma} \\
\hat{H}_{\text{dots}} &= (\epsilon - t)\hat{n}_o + (\epsilon + t)\hat{n}_e \\
&\quad + \frac{U}{2}\left[(\hat{n}_{e\uparrow} + \hat{n}_{o\uparrow})(\hat{n}_{e\downarrow} + \hat{n}_{o\downarrow}) + (d^{\dagger}_{o\uparrow} d_{e\uparrow} + d^{\dagger}_{e\uparrow} d_{o\uparrow})(d^{\dagger}_{o\downarrow} d_{e\downarrow} + d^{\dagger}_{e\downarrow} d_{o\downarrow})\right] \\
\hat{H}_{\text{hyb}} &= V \sum_{\alpha\mathbf{k}\sigma} \left(d^{\dagger}_{\alpha\sigma} c_{\alpha\mathbf{k}\sigma} + h.c. \right) \ ,
\end{aligned} \tag{2.25}$$

with $\alpha = e, o$, $\hat{n}_{\alpha\sigma} = d^{\dagger}_{\alpha\sigma} d_{\alpha\sigma}$ and $\hat{n}_{\alpha} = \sum_{\sigma} \hat{n}_{\alpha\sigma}$. The only terms which involve charge transfer between even and odd orbitals are those in $\hat{H}_{\text{dots}}$, which transfer two electrons between the orbitals. This means that the parity (P) of the system, defined to be the number of electrons in odd orbitals modulo 2, is conserved. The Hamiltonian is therefore block diagonal in the parity basis, with no mixing between $P = 0, 1$ subspaces. This proves very useful in reducing the computational cost of NRG calculations (see chapter 3)[4].

In the limit of $\frac{t}{U} \gg 1$, a case considered at various points throughout this work, the even and odd dot orbitals are very far apart in energy, such that at least one of them must be either very far above the leads' Fermi levels (and therefore essentially unoccupied) or very far below the leads' Fermi levels (and therefore essentially doubly occupied). In the case where only one dot level is near the Fermi level, the system reduces to an *effective* single-level model, with the unoccupied or doubly-occupied level playing no role in the low-temperature physics. By projecting the Hamiltonian (Eqn. (2.25)) into the manifold with one of the (parity basis) dot orbitals either unoccupied or doubly-occupied, one can show that the effective onsite Coulomb repulsion of the remaining active level is $\frac{U}{2}$, reflecting the fact that electrons in the even and odd orbitals are delocalised across both of the original dot 1 and dot 2 lev-

[4] Useful and interesting analytic relations may also be derived for the LR-symmetric 2AIM in the parity basis, as detailed in section 4.1.

els. The effect of this reduced Coulomb repulsion in the effective single-level model arising for $\frac{t}{U} \gg 1$ will be seen in later chapters.

We now return to the 2AIM in the original, "1,2" basis. Clearly it is a rather complicated model, but just as for the 1AIM, we may carry out a SW transformation to derive a somewhat simpler low-energy effective model, valid in the regime in which the dots are essentially singly occupied. This is detailed in the next section.

2.7 Schrieffer-Wolff transformation of the 2AIM

If each dot level in the 2AIM is essentially singly occupied, as is the case for the system at ph symmetry with $U \gg t, \Gamma_1, \Gamma_2$, we may carry out a SW transformation [16] to derive a simpler, effective model, valid on temperature/energy scales $\ll U$. The perturbing Hamiltonian is taken to be $\hat{H}_1 = \hat{H}_{\rm hyb} + \hat{H}_t$ (see Eqns. (2.16) – (2.19)), and only eigenstates of $\hat{H}_0 = \hat{H} - \hat{H}_1$ in the low-energy manifold of states with one electron on each dot level are retained.

The low-energy effective model resulting from performing a *second*-order SW transformation on the 2AIM is the much-studied two-impurity Kondo model (2IKM) [25, 44–48], illustrated in Fig. 2.5, which has the Hamiltonian,

$$\hat{H}_{\rm 2IKM} = J_1 \hat{\mathbf{S}}_1 \cdot \hat{\mathbf{S}}_{01} + J_2 \hat{\mathbf{S}}_2 \cdot \hat{\mathbf{S}}_{02} + J \hat{\mathbf{S}}_1 \cdot \hat{\mathbf{S}}_2 + \hat{H}_{\rm leads}, \tag{2.26}$$

where $\hat{\mathbf{S}}_\nu$ is a spin-$\frac{1}{2}$ representing dot ν, and $\hat{\mathbf{S}}_{0\nu}$ is the local spin density of lead ν. From the SW transformation we find that $\rho J_\nu = 8\Gamma_\nu/\pi U$ and $J = 4t^2/U$. Note that J is always positive, such that the exchange coupling between the two spins is always *antiferromagnetic*. In the following section we give an introduction to the physics of this model. This will be useful background for the results presented in the later chapters. An important feature of this model, and one which distinguishes it from the related 2AIM, is that there can be no charge transfer between the two leads. As we will see, particularly in chapter 5, this accounts for some fundamental differences between the low-temperature physics of the 2AIM and the 2IKM.

2.8 The two-impurity Kondo model

In the 2IKM there is a competition between the Kondo effects which may arise between the impurity spins and the leads, and the antiferromagnetic exchange coupling, J. This gives rise to two phases in the model as J is varied. We begin by considering the LR-symmetric 2IKM, *i.e.*, the 2IKM with $J_1 = J_2$. First let us consider the low-energy physics of the system in the limit of small interdot antiferromagnetic exchange coupling, *i.e.*, the limit of small J (in practice, $J \ll T_{\rm K}$, with $T_{\rm K}$ the Kondo scale for each dot in the absence of interdot coupling, *i.e.*, with $J = 0$). In this case,

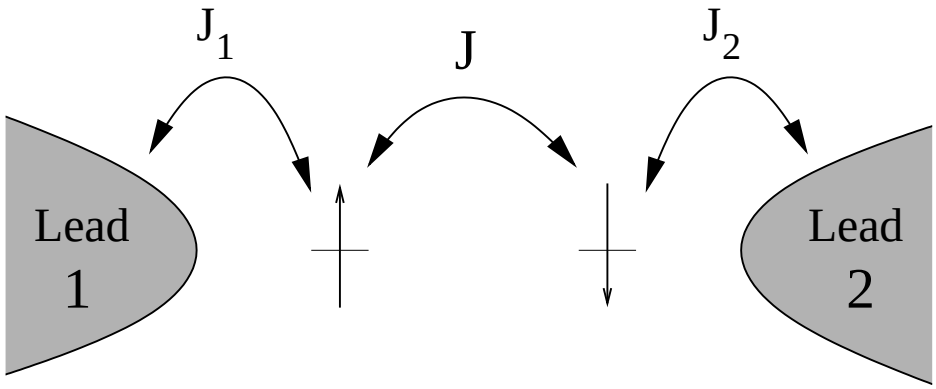


Figure 2.5: Schematic of the 2IKM, containing two spin-$\frac{1}{2}$'s coupled by the antiferromagnetic exchange coupling J, and each is antiferromagnetically coupled to a metallic lead conduction band by the exchange couplings, J_1 and J_2.

the system effectively comprises two separate Kondo models (Eqn. (2.7)) with each spin being quenched by its associated lead when the temperature is reduced below T_{K}. The ground state therefore consists of two decoupled Kondo singlets, and this phase is referred to as the Kondo singlet (KS) phase. Conversely, in the limit of high J ($J \gg T_{\mathrm{K}}$), as the temperature is reduced from the high-temperature limit the two spins lock up into a singlet state when $T \sim J$. This singlet is then effectively decoupled from the leads. This phase is referred to as the local singlet (LS) phase. The KS and LS phases are separated by a second-order quantum phase transition (QPT), which occurs when $J = J_c \sim T_{\mathrm{K}}$ [45]. Whilst in the two separate phases the system flows to the LS or KS fixed point as the temperature is decreased, exactly at the critical point $J = J_c$ the system flows to the 2CK fixed point – the same fixed point that occurs in the 2CK model [114, 116]. The ground state of the system at the critical point is therefore a NFL.

Signatures of the underlying physics are visible in the phase shifts (defined in section 4.1) experienced by the lead electrons due to scattering off the impurities. In the LS phase the spins are effectively decoupled from the leads, so the lead electrons do not scatter off the impurities and experience zero phase shift. In the KS phase, the spins are strongly coupled to the leads, and the lead electrons experience a phase shift of $\frac{\pi}{2}$ due to scattering off the impurities, as is characteristic of strong coupling to the leads [11, 46]. As well as the discontinuous change in phase shift, the QPT between the two phases is also heralded by the divergence of the staggered magnetic susceptibility (see Refs. [25, 49] for details).

The physics of the 2IKM is also clearly displayed in the impurity contribution to the entropy of the system, S_{imp}, the difference in the entropy of the system with and without the impurities present (see section 3.3 for more details). NRG results for S_{imp} are shown in Fig. 2.6 (see chapter 3 for details of the calculation). In

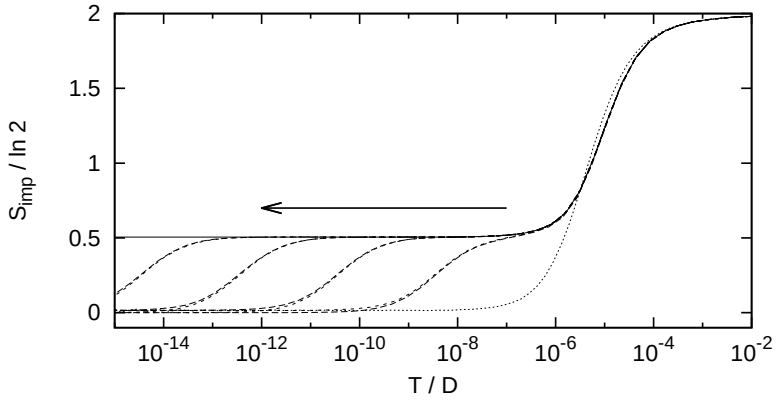


Figure 2.6: The impurity contribution to the entropy ($S_{\rm imp}$) of the LR-symmetric 2IKM as a function of temperature for various values of J with $\rho J_1 = \rho J_2 = 0.093$. The solid line is $J = J_c \simeq 3 \times 10^{-5} D$, the dotted line is for $J = 0$, the short-dashed (long-dashed) lines are $J - J_c = \pm 10^{-n} D$ with $n = 1, 2, 3, 4$. The lines for equal $|J - J_c|$ are essentially indistinguishable. The arrow indicates decreasing $|J - J_c|$. At high temperature $S_{\rm imp} = \ln 4$ in all cases. For $J = 0$ it decreases to zero on the scale of $T_{\rm K} \sim 10^{-5} D$. For $J = J_c$ the entropy instead falls to $\frac{1}{2} \ln 2$ when the system flows to the 2CK fixed point, *i.e.*, on the scale of $T_{\rm K}^{2CK}$ which can be seen to be $\sim T_{\rm K}$. For $J \simeq J_c$ the system flows near to the 2CK fixed point, indicated by a $\frac{1}{2} \ln 2$ plateau in $S_{\rm imp}$, before flowing on to either the KS or LS fixed points, with zero residual entropy.

the limit of high temperature, $S_{\rm imp} = \ln 4$, regardless of the value of J, as there are four possible configurations of the two spins. At high temperature the system is close to a local moment fixed point, and the two spins are essentially free local moments. As the temperature is reduced deep in the LS phase ($J \gg T_{\rm K}$), the two dot spins form a singlet on the scale of J, and $S_{\rm imp}$ therefore falls to zero on this scale. As the temperature is reduced deep in the KS phase ($J \ll T_{\rm K}$) the spins are Kondo screened by the leads on the scale of $T_{\rm K}$, and $S_{\rm imp}$ falls to zero on this scale. Exactly at the critical point ($J = J_c$) the entropy does not go to zero as temperature is reduced, rather it falls to $S_{\rm imp} = \frac{1}{2} \ln 2$, characteristic of the 2CK fixed point [52, 53]. If the system is close to, but not precisely at, the critical point, then as the temperature is reduced it flows near to the 2CK fixed point for some range of temperature, but ultimately flows onwards to either the LS or KS fixed points as the temperature is reduced[5]. Therefore, as the QPT is approached from either side ($|J - J_c| \to 0$) a plateau of $S_{\rm imp} = \frac{1}{2} \ln 2$ develops. The plateau starts at $T \simeq T_{\rm K}^{2CK}$, with $T_{\rm K}^{2CK}$ the scale on which the system flows to the 2CK fixed point. For the LR-symmetric 2IKM, $T_{\rm K}^{2CK} \sim T_{\rm K}$, as can be seen in Fig. 2.6. The entropy then goes to zero on a scale dependent on $|J - J_c|$, labeled T^*. T^* therefore vanishes as the QPT is approached from either side, and it has been established numerically that $T^* \sim \frac{|J - J_c|^2}{T_{\rm K}}$ as $|J - J_c| \to 0$ [59].

[5]This low temperature crossover was studied in detail in Ref. [114].

The behaviour of the LR-asymmetric 2IKM ($J_1 \neq J_2$) is rather similar. Without going into details here (these can be found in section 5.1, as well as in Refs. [112, 116, 117]), we merely state that the QPT remains but J_c is now dependent on both $T_{\rm K}^{(1)}$ and $T_{\rm K}^{(2)}$; the Kondo scales for the two dots in the absence of any interdot exchange coupling ($J = 0$). In the limit $J_1 \gg J_2$, J_c is given by [112, 117]

$$J_c \sim \left(\frac{1}{\rho J_2} - \frac{1}{\rho J_1} \right)^{-1} T_{\rm K}^{(1)} \ . \tag{2.27}$$

2.9 Schrieffer-Wolff transformation of the 2AIM to third order

As discussed above, carrying out the SW transformation on the 2AIM to second order yields the 2IKM. But the SW transformation can of course be carried out to higher orders. In fact, to capture interlead charge-transfer processes, which one must in order to understand fully the 2CK physics in the 2AIM, one must go to third order (as discussed further in chapter 5). Calculation of the third-order terms is a rather lengthy, although straightforward, procedure, which we outline in appendix A. Here we merely state the result, which is that the third-order term arising from a SW transformation of the ph-symmetric 2AIM is [96]

$$\begin{aligned} \hat{H}_3 &= \hat{1}' \hat{H}_1 (\epsilon_0 - \hat{H}_0)^{-1} \hat{P} \hat{H}_1 (\epsilon_0 - \hat{H}_0)^{-1} \hat{P} \hat{H}_1 \hat{1}' \\ &= V_{LR} \left[\sum_\sigma (f_{1\sigma}^\dagger f_{2\sigma} + f_{2\sigma}^\dagger f_{1\sigma}) \hat{\mathbf{S}}_1 \cdot \hat{\mathbf{S}}_2 + 2 \hat{\mathbf{A}} \cdot (\hat{\mathbf{S}}_1 \times \hat{\mathbf{S}}_2) \right] \ , \end{aligned} \tag{2.28}$$

where $\epsilon_0 = -U$ is the ground state energy of $\hat{H}_0$ and $V_{LR} = \frac{16NtV_1V_2}{U^2} = \sqrt{\frac{JJ_1J_2}{U}}$. $\hat{\mathbf{A}}$ is a vector operator given by

$$\hat{\mathbf{A}} = i \sum_{\sigma,\sigma'} \left(f_{1\sigma}^\dagger \boldsymbol{\sigma}_{\sigma\sigma'} f_{2\sigma'} - f_{2\sigma}^\dagger \boldsymbol{\sigma}_{\sigma\sigma'} f_{1\sigma'} \right) \ . \tag{2.29}$$

Note that $\hat{\mathbf{A}}$, which is self-adjoint and odd under $1 \leftrightarrow 2$ exchange, is not a spin operator; its components satisfying the commutation relations $[\hat{A}^\alpha, \hat{A}^\beta] = i\epsilon_{\alpha\beta\gamma} \hat{S}_0^\gamma$, where $\hat{\mathbf{S}}_0 = \hat{\mathbf{S}}_{01} + \hat{\mathbf{S}}_{02}$ (with $\alpha, \beta, \gamma \in (x, y, z)$ and $\epsilon_{\alpha\beta\gamma}$ the Levi-Civita symbol). $\hat{H}_3$ is clearly a rather complicated object, involving charge transfer between the leads mediated by the dot spins (we note that this term was derived previously in Ref. [118] but subsequently neglected). We refer to the third-order low-energy effective model specified by $\hat{H}_{\rm 2IKM} + \hat{H}_3$ as the H_3 model.

It is crucial to understand that the interlead charge-transfer processes in the 2AIM are *mediated* by the dots (and as such are referred to as "cotunneling" processes). In recent work [59, 60, 119], the 2IKM with an additional *direct* interlead hopping term was studied as a model for a TCDQD. The Hamiltonian used in this

work was $\hat{H}_{\mathrm{2IKM}}$ with the following additional charge-transfer term:

$$\hat{H}_3' = V_{LR}' \sum_{\sigma} (f_{1\sigma}^{\dagger} f_{2\sigma} + f_{2\sigma}^{\dagger} f_{1\sigma}) \ , \tag{2.30}$$

with $V_{LR}' = \frac{V_{LR}}{4}$. We refer to this as the H_3' model. As this model differs somewhat from the low-energy effective model for the 2AIM derived via SW transformation (the H_3 model), we should not expect the H_3' model to exhibit precisely the same physics as the 2AIM even at low energies [59, 60, 96]. We will discuss the behaviour of the H_3' model in chapter 5.

Having discussed the models relevant to this work, we now go on to study the 2AIM in two simple limits, beginning with the atomic limit, *i.e.*, the system with the two dots completely decoupled from the leads, $V_1 = V_2 = 0$. In this limit the system is trivially soluble. We then go on to look at the non-interacting limit of the 2AIM. In this limit too, the system is easy to solve, using, for example, equation-of-motion methods [3, 120, 121]. Studying the 2AIM in these two limits is a useful basis for understanding the results for the full system presented in the later chapters of this thesis, as well as giving an insight into the complex behaviour of the 2AIM.

2.10 The 2AIM in the atomic limit

In the atomic limit, the Hamiltonian for the 2AIM may be diagonalised straightforwardly. The quantum numbers used to classify the dot eigenstates are N, S and S_z: respectively, the total charge on the dots, the total spin of the dots, and the z-component of the total spin. For simplicity we begin by concentrating on the case of LR symmetry ($\epsilon_1 = \epsilon_2 = \epsilon$), the eigenstates for which are given in Table 2.10. [When the system is not LR symmetric the eigenstates have the same quantum numbers and the eigenenergies may be calculated numerically.]

Clearly there is only one $N = 0$ state and only one $N = 4$ state – these are states with either zero or two electrons on each dot, configurations denoted (0,0) and (2,2). There are four $N = 1$ and four $N = 3$ states, reflecting the spin and orbital degrees of freedom present in the system, and there are six $N = 2$ (two-electron) states, which form a triplet ($S = 1$) and three singlets ($S = 0$). Much of the work in this thesis will be concerned with the two-electron states of the 2AIM, so we now discuss these in a little more detail. We consider separately the cases of large ($\frac{t}{U} \gg 1$) and small ($\frac{t}{U} \ll 1$) interdot coupling.

In the case where $\frac{t}{U} \ll 1$, the number of electrons on *each* dot is essentially integer in the two-electron sector, and as such the eigenstates may then be approximately classified by the number of electrons on each dot, (n, m). Two of the two-electron eigenstates are singlets with dominant (0,2) and (0,2) configurations,

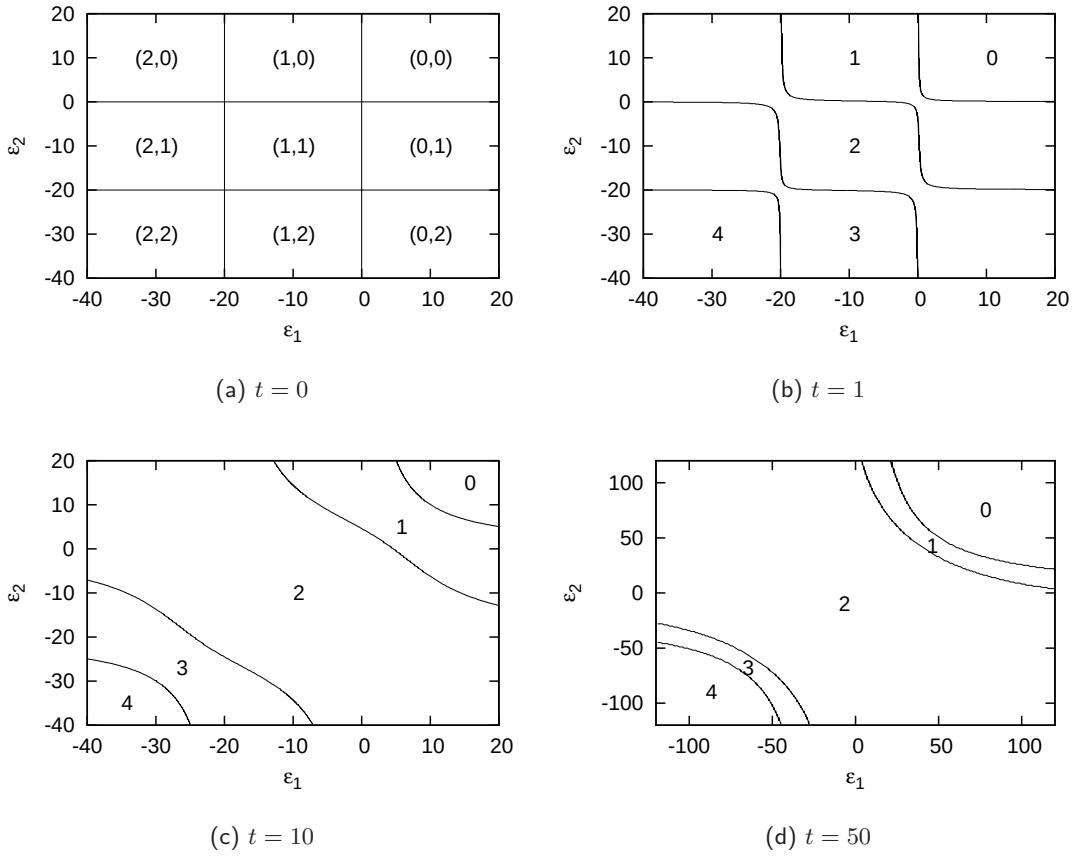
Energy	N	S_z	S
0	0	0	0
$\epsilon + t$	1	$\frac{1}{2}$	$\frac{1}{2}$
$\epsilon - t$	1	$\frac{1}{2}$	$\frac{1}{2}$
$\epsilon + t$	1	$-\frac{1}{2}$	$\frac{1}{2}$
$\epsilon - t$	1	$-\frac{1}{2}$	$\frac{1}{2}$
2ϵ	2	1	1
2ϵ	2	-1	1
2ϵ	2	0	1
$2\epsilon - \delta E$	2	0	0
$2\epsilon + U + \delta E$	2	0	0
$2\epsilon + U$	2	0	0
$3\epsilon + U + t$	3	$\frac{1}{2}$	$\frac{1}{2}$
$3\epsilon + U - t$	3	$\frac{1}{2}$	$\frac{1}{2}$
$3\epsilon + U + t$	3	$-\frac{1}{2}$	$\frac{1}{2}$
$3\epsilon + U - t$	3	$-\frac{1}{2}$	$\frac{1}{2}$
$4\epsilon + 2U$	4	0	0

Table 2.1: Energies and quantum numbers of the eigenstates of the LR-symmetric, atomic-limit 2AIM. $\delta E = -\frac{U}{2} + \frac{U}{2}\sqrt{1 + \frac{16t^2}{U^2}}$.

and energies $\simeq 2\epsilon + U$. The other four eigenstates have a (1,1) configuration. These form a degenerate triplet with energy 2ϵ, and a singlet with energy $2\epsilon - \delta E$, where $\delta E = -\frac{U}{2} + \frac{U}{2}\sqrt{1 + \frac{16t^2}{U^2}} \simeq \frac{4t^2}{U}$. The lowest energy two-electron state (provided $t \neq 0$) is therefore the (1,1) singlet state, with the (1,1) triplet states having an energy δE higher, and the (2,0) and (0,2) singlets having an energy $\sim U$ higher.

In the opposite limit, $\frac{t}{U} \gg 1$, the number of electrons on each dot is not well defined, and $\delta E \simeq 2t - \frac{U}{2}$. One may think of the two dot levels as being strongly hybridised, forming bonding and antibonding molecular orbitals (MOs). For the case of LR symmetry, the MOs are simply the even and odd orbitals described in section 2.6, which have onsite repulsion of $\frac{U}{2}$ and energies of $\epsilon \pm t$. The lowest energy two-electron state is a singlet with both electrons in the bonding orbital. There are four excited states with one electron in the bonding level and one in the antibonding level, forming a triplet and a singlet, and also an excited singlet with both electrons in the antibonding level. We note that regardless of the values of the parameters, the lowest two-electron state in the atomic limit is always a singlet with energy $2\epsilon - \delta E$ (provided $t \neq 0$).

As we can calculate the energies of the atomic-limit eigenstates for any values of the parameters, we can find the ground state of the system as a function of the dot level energies, which we plot as a phase diagram. For a fixed value of U, we show the phase diagrams for the atomic-limit 2AIM for various values of t and as a function of ϵ_1 and ϵ_2 in Fig. 2.7. For $t = 0$ (Fig. 2.7 (a)) the eigenstates may be



(a) $t = 0$ (b) $t = 1$

(c) $t = 10$ (d) $t = 50$

Figure 2.7: Phase diagrams for the atomic-limit 2AIM with $U = 20$, $U' = 0$ and various values of t (in arbitrary units). For $t = 0$, the different phases are labeled by charges on each dot, (n_1, n_2). For $t \neq 0$, the phases are labeled by N, the total number of electrons on the dots. ph symmetry occurs at $\epsilon_1 = \epsilon_2 = -10$. Note the change of scale in (d).

classified by the number of electrons on each dot, and the number of electrons on each dot is dependent only upon the energy level for that dot. For instance, there are no electrons on dot 1 for $\epsilon_1 > 0$, there is one electron on dot 1 for $-U < \epsilon_1 < 0$, and there are two electrons on dot 1 for $\epsilon_1 < -U$. Notice that at ph symmetry ($\epsilon_1 = \epsilon_2 = -\frac{U}{2}$) the ground state has a (1,1) configuration. When $0 < t \ll U$, as in Fig. 2.7 (b), the phase boundaries are only slightly altered from the $t = 0$ case (Fig. 2.7 (a)), although the sectors with the same N are now continuously connected.

Increasing t further causes the phase boundaries to shift, as illustrated in Figs. 2.7 (c), (d). As discussed, in the limit of strong interdot coupling, $t \gg U$, we may view the system in terms of MOs. In this limit, at LR symmetry ($\epsilon_1 = \epsilon_2 = \epsilon$, corresponding to the secondary diagonal (bottom left to top right) in Fig. 2.7), the boundary between the zero and one electron sector occurs at $\epsilon = t$ and the boundary between the one and two electron sectors occurs at $\epsilon \simeq t - U/2$, such that the width of the one electron sector is $\delta\epsilon \simeq U/2$ (as seen in Fig. 2.7 (d)) – equal to the onsite

repulsion for the MOs. The width of the three-electron sector is likewise $\delta\epsilon \simeq U/2$. Note that at ph symmetry, the ground state has $N = 2$ for any value of t.

So far we have considered the 2AIM without an interdot repulsion, *i.e.*, with $U' = 0$, but it is interesting to consider the effect of a finite U' (as would be expected to arise in an experimental TCDQD system) on the 2AIM in the atomic limit. Clearly, an interdot repulsion has no effect on the zero and one-electron eigenstates, whereas all the three-electron states are raised in energy by $2U'$, and the energy of the four-electron state increases by $4U'$. Whilst the effect on the above-mentioned states is straightforward, we concentrate on the more subtle effect of an interdot repulsion on the two-electron states. Provided $\frac{t}{U} \ll 1$, the two-electron eigenstates of the $U' = 0$, atomic-limit 2AIM have essentially (1,1) or (2,0)/(0,2) configurations. Upon addition of a finite but small $U' \ll U$, the (1,1) states increase in energy by $\simeq U'$, whereas the (2,0)/(0,2) states are unaffected. In this case of $\frac{t}{U} \ll 1$ then, a finite U' has the effect of increasing the amount of (2,0)/(0,2) character of the singlet ground state of the system in the two-electron sector. The important point to note is that provided $U' \ll U$, as one expects in experimental systems, the interdot repulsion does not significantly change the dot configuration, although the boundaries in the phase diagram are somewhat shifted. This will prove relevant to the results in chapter 7.

2.11 The 2AIM in the non-interacting limit

We now consider the full 2AIM system, including the two leads, but with no interactions on the dots, *i.e.*, Eqns. (2.16) – (2.19) with $U = 0$. In this section we concentrate on developing a physical understanding of the problem. We note that the ph-symmetric point of the model in the non-interacting case is $\epsilon_1 = \epsilon_2 = 0$.

In the non-interacting limit, one may consider the two dot levels to be strongly hybridised, forming bonding and antibonding MOs, for any value of t (as discussed, this picture remains valid in the interacting case provided $\frac{t}{U} \gg 1$). The operators for the bonding (labeled by subscript b) and antibonding (labeled by subscript a) orbitals are given generally by

$$d_{a\sigma} = c_{1a}d_{1\sigma} + c_{2a}d_{2\sigma}, \tag{2.31}$$

$$d_{b\sigma} = c_{1b}d_{1\sigma} + c_{2b}d_{2\sigma}, \tag{2.32}$$

where the coefficients $c_{1a}, c_{2a}, c_{1b} = (1/\sqrt{2}), c_{2b} = -(1/\sqrt{2})$ if $\epsilon_1 = \epsilon_2$. Note that in this case, the MOs are just the even and odd orbitals discussed in section 2.6. By contrast, in the limit $\epsilon_1 - \epsilon_2 \to \infty$, $c_{1a}, -c_{2b} \to 1$, $c_{2a}, c_{1b} \to 0$, corresponding to MOs localised entirely on one or the other dot. The energies of the two MOs are

$\epsilon_{a,b} = \frac{(\epsilon_1+\epsilon_2)}{2} \pm \frac{1}{2}\sqrt{(\epsilon_1-\epsilon_2)^2+4t^2}$ (with the + sign corresponding to the antibonding orbital), such that the energy separation between them is $2t$ if $\epsilon_1 = \epsilon_2$. Writing the non-interacting 2AIM Hamiltonian in terms of these MOs shows that each MO is coupled to *both* lead 1 and lead 2, with hopping matrix elements given by

$$V_{\nu\mu} = c_{\nu\mu} V_\nu, \tag{2.33}$$

where $V_{\nu\mu}$ is the hopping matrix element between the μ MO and lead ν, with $\mu = a, b$; $\nu = 1, 2$.

One of the quantities we will be concentrating on particularly in our study of the full 2AIM is the zero-temperature, zero-bias conductance, denoted $G_c(0,0)$. In section 3.7 we discuss how this quantity can be expressed in terms of the Green's functions of the system (discussed in detail in section 3.6). In the non-interacting case these Green's functions may be calculated exactly using equation-of-motion methods [3, 120, 122] (as detailed in section 4.1, the results of which we use here), and we may therefore obtain an exact expression for $G_c(0,0)$ in terms of the model parameters. Combining Eqns. (3.54), (4.5) – (4.7) yields

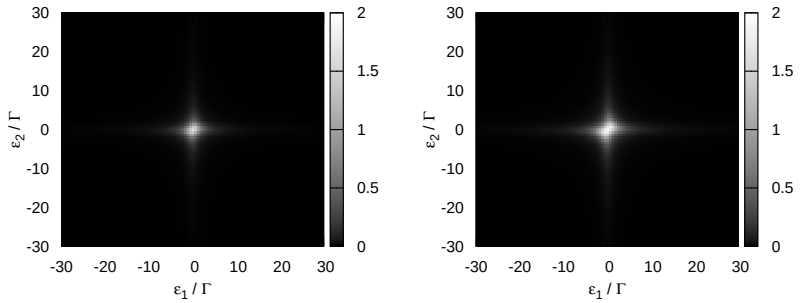
$$G_c(0,0) = \frac{8e^2}{h} \frac{\tilde{t}^2}{[(\tilde{\epsilon_1}\tilde{\epsilon_2} - \tilde{t}^2 - 1)^2 + (\tilde{\epsilon_1} + \tilde{\epsilon_2})^2]}\ , \tag{2.34}$$

where $\tilde{x} = x/\Gamma$, and we have taken $\Gamma_1 = \Gamma_2 = \Gamma$ for simplicity. From this equation we may calculate $G_c(0,0)$ as a function of t, ϵ_1 and ϵ_2 exactly, and results are shown in Fig. 2.8. The conductance behaviour shown is rather intricate, showing that even in the non-interacting limit, the 2AIM exhibits interesting physics.

This behaviour can be understood physically in terms of the MO picture of the dots. If an MO is very far from the zero-bias Fermi level of the leads (in practice if $|\epsilon_i| \gg \Gamma$; $i = a, b$, where the zero-bias Fermi level is taken as the zero of energy) then it is essentially unoccupied or doubly occupied. Adding or removing an electron to the MO incurs a large energy penalty (relative to Γ), and current flow via the MO is suppressed at low temperatures. Only MOs which are near (within Γ in energy) to the Fermi level, therefore contribute significantly to the zero-temperature, zero-bias conductance. When both MOs are far from the Fermi level, $G_c(0,0)$ is therefore very low (relative to the maximum possible conductance of $2e^2/h$, the unitary limit, with the factor of 2 arising from spin degeneracy.).

If $t \gg \Gamma$, the energy difference between bonding and antibonding orbitals is large, so only one MO can be near the Fermi level of the leads for any values of ϵ_1 and ϵ_2, so at least one of the MOs will be either essentially full or empty and will not affect the physics of the system greatly. In this case the system reduces effectively to a single-level problem at low energies.

It is well-known [123, 124], that for a single, non-interacting level coupled two



(a) $t/\Gamma = 0.7$ (b) $t/\Gamma = 1$

(c) $t/\Gamma = 2$ (d) $t/\Gamma = 5$

(e) $t/\Gamma = 8$ (f) $t/\Gamma = 10$

Figure 2.8: Exact zero-bias conductance at zero temperature, $G_c(0,0)$, in units of e^2/h, given as a colour plot for the 2AIM with $U = 0$, $\Gamma_1 = \Gamma_2 = \Gamma$ and values of t/Γ as given.

leads, $G_c(0,0)$ is high (near the unitary limit) when the level is near the Fermi level, known as the "resonance condition" [3]. Furthermore, the value of $G_c(0,0)$ for a single, non-interacting level at the Fermi level is dependent on the ratio of the

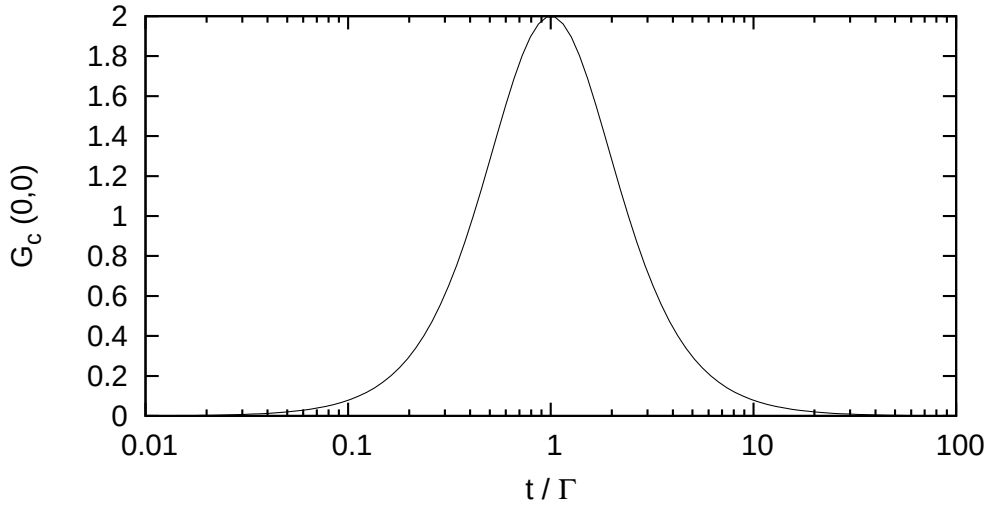


Figure 2.9: Exact, zero-bias conductance at zero temperature for the 2AIM as a function of t/Γ for $\epsilon_1 = \epsilon_2 = U = 0$ and $\Gamma_1 = \Gamma_2 = \Gamma$.

couplings of that level to each of the leads [123], according to

$$G_c(0,0) = 2G_0 = 2\frac{4V_{1\mu}^2 V_{2\mu}^2}{(V_{1\mu}^2 + V_{2\mu}^2)^2} \ , \tag{2.35}$$

where $V_{\nu\mu}$ is the coupling between the non-interacting level μ and lead ν. If the level is equally coupled to the leads ($V_{1\mu} = V_{2\mu}$) then $G_c(0,0)$ is maximal, and equal to the unitary limit, $2e^2/h$. As the asymmetry in the couplings to the leads increases, $G_c(0,0)$ decreases, going asymptotically to zero in the limit $|V_{\mu 1} - V_{\mu 2}| \to \infty$.

With $t \gg \Gamma$ then, $G_c(0,0)$ is high whenever one of the MOs is near the Fermi level. This is seen in Figs. 2.8 (c) – (f). The "boomerang-shaped" strips of enhanced conductance occur for values of ϵ_1, ϵ_2 for which one of the MOs lies near the Fermi level. As t increases, the values of ϵ_1, ϵ_2 required for a MO to be near the Fermi level change, leading to increasing separation of the strips of high conductance, as seen in Figs. 2.8 (c) – (f).

Staying within one of these strips (such that one of the MOs remains near the Fermi level), but moving away from LR symmetry[6], causes the MOs to become more localised, and their couplings to the leads to become more asymmetric (see Eqn. (2.33)). The conductance within the strips therefore decreases as one moves away from LR symmetry, as can be seen in Figs. 2.8 (c)-(f).

We look now at weak interdot coupling (*i.e.*, $t \lesssim \Gamma$). If $|\epsilon_1|, |\epsilon_2| \gg \Gamma$, then both the MOs are far from the Fermi level and $G_c(0,0)$ is low (relative to the unitary limit). If $|\epsilon_1| \gg \Gamma$ but $|\epsilon_2| \lesssim \Gamma$ (or equivalently $|\epsilon_2| \gg \Gamma$ but $|\epsilon_1| \lesssim \Gamma$), then only one

[6] LR symmetry corresponds to the secondary diagonals in Fig. 2.8, from bottom left to top right.

MO is near the Fermi level. In this case however, the MOs are essentially localised on the dots, and so are highly asymmetrically coupled to the leads, such that $G_c(0,0)$ is again low. By contrast, in the case where $|\epsilon_1|, |\epsilon_2| \lesssim \Gamma$ the problem does not reduce to an effective single-level system, as both MOs are near to the Fermi level. Significant zero-bias, zero-temperature conductance can occur in this case for weak interdot coupling ($t \lesssim \Gamma$), as seen in Figs. 2.7 (a), (b). In the case of $\epsilon_1 = \epsilon_2 = 0$ specifically, Eqn. (2.34) reduces to

$$G_c(0,0) = \frac{8e^2}{h} \frac{\tilde{t}^2}{(1+\tilde{t}^2)^2} \ , \qquad \epsilon_1 = \epsilon_2 = 0 \tag{2.36}$$

(the analogue of this result in the interacting case will be discussed in section 4.2.4). $G_c(0,0)$ therefore has a maximum at $\tilde{t} = 1$, with $G_c(0,0) = 2e^2/h$, as seen in Fig. 2.8 and (rather more clearly) in Fig. 2.9, in which we show $G_c(0,0)$ as a function of $\tilde{t}$ at the point $\epsilon_1 = \epsilon_2 = 0$.

CHAPTER 3

The Numerical Renormalisation Group

In this chapter we discuss the Numerical Renormalisation Group (NRG), of which we make extensive use to study the 2AIM and related models in the following chapters. The NRG is a powerful tool devised by Kenneth Wilson in the 1970s as a method for obtaining accurate numerical results for quantum impurity systems. It was initially applied to the Kondo model (Eqn. (2.7)) by Wilson [18], before being applied to the 1AIM (Eqn. (2.4)) by Krishna-murthy, Wilkins and Wilson [11, 12]. Since then it has been applied to many other quantum impurity systems, including capacitively-coupled QDs [125–127], orbitally-degenerate carbon nanotube QDs [72, 73], and two-level QDs [128, 129], to name but a few. The NRG, whilst building on the scaling ideas in PMS [17], is inherently non-perturbative, an essential requirement for treating strongly correlated quantum impurity systems. Whereas perturbative scaling techniques, such as PMS, break down at low energies (below the Kondo scale, T_{K}), the NRG is able to provide information about the system on all energy scales from the bandwidth of the host, down to arbitrarily small energies. Furthermore, the NRG provides not only thermodynamic information, but also dynamic information, which may be obtained via the so-called full density matrix (FDM) method [29, 30].

In this chapter we illustrate the NRG procedure for the 1AIM, beginning with some simple transformations of the Hamiltonian which yield a form amenable to discretisation. The key step of the NRG is a logarithmic discretisation of the conduction band. This involves dividing the conduction band into logarithmic intervals, and retaining only one linear combination of states in each interval. The Hamiltonian can then be written in a linear chain form, with couplings decreasing exponentially along the chain, allowing for the system to be solved numerically by so-called iterative diagonalisation (within a truncated Hilbert space, as discussed later). Although we describe the NRG procedure applied to the 1AIM for simplicity, it is straightforward to adapt it to deal with more complicated quantum impurity models, and we discuss how it can be extended to the 2AIM in section 3.4. In addition to providing a method

of solving quantum impurity Hamiltonians, the NRG also provides a framework for understanding the physics of such systems, in terms of renormalisation group flows and fixed points, as we discuss in section 3.5. We go on to outline how dynamical information, in the form of correlation functions such as the Green's functions for the system, can be calculated via the FDM method [29, 30]. We conclude this chapter by looking at how the conductance of the 2AIM can be calculated from the NRG; this being the quantity that is generally measured experimentally in TCDQD systems.

3.1 Transforming the Hamiltonian

We begin our outline of the NRG procedure with some basic transformations of the 1AIM Hamiltonian, in order to put it into a form that is amenable to logarithmic discretisation. To reiterate, the bare 1AIM Hamiltonian is (cf. Eqn. (2.4))

$$\hat{H}_{\mathrm{1AIM}} = \sum_{\mathbf{k}\sigma} \epsilon_{\mathbf{k}} c^{\dagger}_{\mathbf{k}\sigma} c_{\mathbf{k}\sigma} + \sum_{\sigma} \epsilon \; d^{\dagger}_{\sigma} d_{\sigma} + \frac{U}{2} \sum_{\sigma} \hat{n}_{\sigma} \hat{n}_{\bar{\sigma}} + V \sum_{k\sigma} (c^{\dagger}_{\mathbf{k}\sigma} d_{\sigma} + d^{\dagger}_{\sigma} c_{\mathbf{k}\sigma}) \; , \quad (3.1)$$

where $\bar{\sigma}$ is the opposite spin to σ. We take the (single) conduction band to be isotropic (so that $\epsilon_{\mathbf{k}} = \epsilon_{|\mathbf{k}|}$), flat (*i.e.*, to have a uniform density of states per orbital, ρ), and to extend in energy from $-D$ to D. This is the standard case [3] relevant to magnetic impurities in a metallic host, or single QD systems.

Under these conditions the conduction band states can then be expanded in terms of spherical harmonics centred on the dot [11]. As the conduction band is isotropic, the dot couples only to the s-wave spherical harmonics, and the Hamiltonian can be written as [11]

$$\frac{\hat{H}_{\mathrm{1AIM}}}{D} = \sum_{\sigma} \left[\int_{-1}^{+1} k a^{\dagger}_{k\sigma} a_{k\sigma} dk + \left(\frac{\epsilon}{D} + \frac{U}{2D} \hat{n}_{\bar{\sigma}} \right) \hat{n}_{\sigma} + \sqrt{\frac{\Gamma}{\pi D}} \int_{-1}^{+1} (d^{\dagger}_{\sigma} a_{k\sigma} + a^{\dagger}_{k\sigma} d_{\sigma}) dk \right] , \quad (3.2)$$

where $\Gamma = \pi \rho_T V^2$ is the dot-lead hybridisation, and the set of conduction band operators $\{a_{k\sigma}\}$ satisfy the usual fermionic commutation relations, $\{a^{\dagger}_{k\sigma}, a_{k'\sigma'}\} = \delta_{\sigma\sigma'}\delta(k-k')$. As is conventional [11], we have rescaled the Hamiltonian by the half-bandwidth, D, in order to make it dimensionless, such that the conduction band states span the energy range $k \in (-1, 1)$.

3.2 Logarithmic discretisation

Having carried out these preliminary transformations, the next step in the NRG procedure is to discretise the conduction band logarithmically, according to a parameter Λ, where $\Lambda \gtrsim 1$ [11]. The conduction band is first split into logarithmic

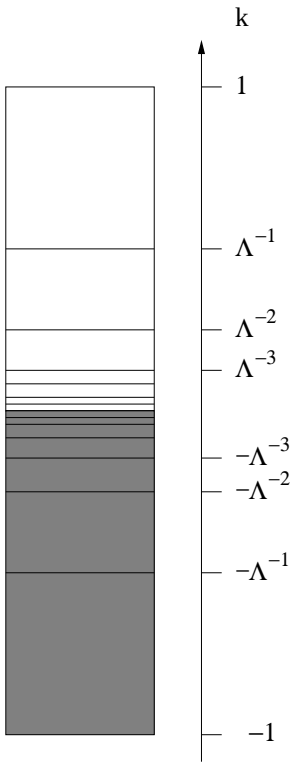


Figure 3.1: Diagram illustrating the logarithmic discretisation of the conduction band, which runs in energy from $-D$ ($k = -1$) to D ($k = 1$). As $\Lambda > 1$, the logarithmic intervals become progressively smaller nearer to the Fermi energy of the band ($k = 0$). As only one state is taken from each interval, all energy scales (up to D) are sampled. The behaviour near the Fermi level is arbitrarily finely resolved.

intervals, with the n^{th} interval for $k > 0$ defined by $\Lambda^{-(n+1)} < k < \Lambda^{-n}$, as illustrated in Figure 3.1. Within each interval, a set of orthonormal states is constructed by setting up a Fourier series:

$$\psi^{\pm}_{np}(k) = \begin{cases} \frac{\Lambda^{-n/2}}{(1-\Lambda^{-1})^{1/2}} e^{\pm i\omega_n pk} & \text{if } \Lambda^{-(n+1)} < \pm k < \Lambda^{-n} \\ 0 & \text{otherwise ,} \end{cases} \tag{3.3}$$

where $\omega_n = 2\pi\Lambda^n/(1-\Lambda^{-1})$. The $\psi^{\pm}_{np}(k)$ functions form a complete, orthogonal set, so the conduction band operators can be written as

$$a_{k\sigma} = \sum_{np} [a_{np\sigma}\psi^{+}_{np}(k) + b_{np\sigma}\psi^{-}_{np}(k)] \ . \tag{3.4}$$

The operators $a_{np\sigma}$ and $b_{np\sigma}$, which themselves form a complete set and satisfy the usual fermionic commutation rules, are then given by

$$a_{np\sigma} = \int_{-1}^{+1} \left[\psi^{+}_{np}(k)\right]^* a_{k\sigma} \mathrm{d}k \ ; \qquad b_{np\sigma} = \int_{-1}^{+1} a_{k\sigma} \left[\psi^{-}_{np}(k)\right]^* \mathrm{d}k \ . \tag{3.5}$$

The Hamiltonian, Eqn. (3.2), can then be written in terms of these operators, using [11]

$$\int_{-1}^{+1} a_{k\sigma} \mathrm{d}k = (1-\Lambda^{-1})^{1/2} \sum_n \Lambda^{-n/2} (a_{n0\sigma} + b_{n0\sigma}) \ , \tag{3.6}$$

and

$$\begin{aligned} \int_{-1}^{+1} a^\dagger_{k\sigma} a_{k\sigma} \mathrm{d}k = \tfrac{1}{2}(1+\Lambda^{-1}) \sum_{np} \Lambda^{-n} (a^\dagger_{np\sigma} a_{np\sigma} - b^\dagger_{np\sigma} b_{np\sigma}) + \\ \frac{1-\Lambda^{-1}}{2\pi i} \sum_{n, p \neq p'} \frac{\Lambda^{-n}}{p'-p} (a^\dagger_{np\sigma} a_{np'\sigma} - b^\dagger_{np\sigma} b_{np'\sigma}) \exp\left[\frac{2\pi i (p'-p)}{1-\Lambda^{-1}}\right] \ , \end{aligned} \tag{3.7}$$

which can be readily proven from Eqns. (3.3) and (3.4). It can be seen from Eqns. (3.6) and (3.2) that the dot level couples only to the $p = 0$ orbitals of the lead, and the $p > 0$ orbitals only enter into the conduction band part of the Hamiltonian, where they occur with a prefactor of $(1 - \Lambda^{-1})$. Hence if Λ is taken to be close to 1, then these terms are negligible. We therefore make the fundamental approximation of the NRG, and neglect the $p > 0$ orbitals entirely. Given that we generally work with a Λ of around 3, this approximation may appear to be rather crude. Numerical work has however shown that the results obtained are robust, even for such large values of Λ.

Having made this approximation, we make one further transformation, putting the Hamiltonian into linear chain form. The $a_{n0\sigma}$ and $b_{n0\sigma}$ operators are transformed into a new orthonormal set of $f_{N\sigma}$ operators, such that the dot level couples only to a single orbital, f_0, with

$$f_{0\sigma} = \left[\tfrac{1}{2}(1-\Lambda^{-1})\right]^{1/2} \sum_n \Lambda^{-n/2} (a_{n0\sigma} + b_{n0\sigma}) \ . \tag{3.8}$$

As the conduction band part of the Hamiltonian is diagonal in the $a_{n0\sigma}$ and $b_{n0\sigma}$ basis (Eqn. (3.7) with $p > 0$ terms neglected), we choose the $f_{N\sigma}$ operators so as to make the conduction band part of the Hamiltonian tridiagonal, *i.e.*, in the basis of the $f_{N\sigma}$ operators the conduction band forms a linear chain. The details of this transformation are rather lengthy; the reader is referred to Ref. [11] for the mathematical details. The resulting Hamiltonian in terms of these new operators

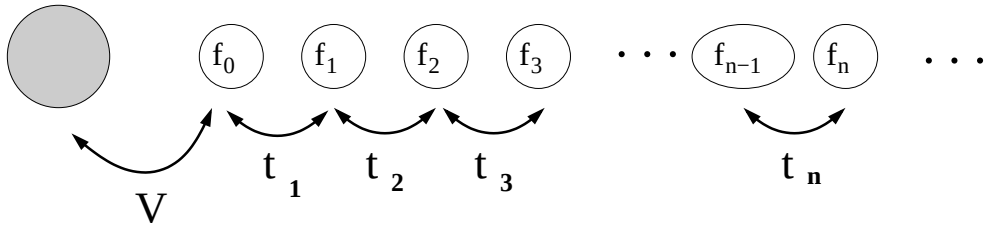


Figure 3.2: Diagram illustrating the linear chain Hamiltonian (Eqn. (3.9)) for the 1AIM. The dot level (grey circle) is coupled to the first member of a chain of orbitals (f_0), with coupling constant $\sim \sqrt{\Gamma} \sim V$. The f_n orbitals are linear combinations of band states and are coupled with coupling constants $t_n \sim \Lambda^{-n/2}\xi_n$ that decrease with n.

reads [11]

$$\begin{aligned}\frac{\hat{H}_{1AIM}}{D} = &\tfrac{1}{2}(1+\Lambda^{-1})\sum_{n=0}^{\infty}\Lambda^{-n/2}\xi_n\left(f^{\dagger}_{n\sigma}f_{(n+1)\sigma} + f^{\dagger}_{(n+1)\sigma}f_{n\sigma}\right)\\ &+\left(\frac{\epsilon}{D}+\frac{U}{2D}\hat{n}_{\bar{\sigma}}\right)\hat{n}_{\sigma}\\ &+\sqrt{\frac{2A_{\Lambda}\Gamma}{\pi D}}(f^{\dagger}_{0\sigma}d_{\sigma}+d^{\dagger}_{\sigma}f_{0\sigma}),\end{aligned} \tag{3.9}$$

where the spin index σ is summed over implicitly from now on in our discussion of the NRG, and

$$\xi_n = (1-\Lambda^{-n-1})(1-\Lambda^{-2n-1})^{-1/2}(1-\Lambda^{-2n-3})^{-1/2} \sim \mathcal{O}(1)\ , \tag{3.10}$$

$$A_{\Lambda} = \frac{\ln\Lambda}{2}\left(\frac{1+\Lambda^{-1}}{1-\Lambda^{-1}}\right)\ , \tag{3.11}$$

where A_Λ is a factor added to correct for error introduced as a result of logarithmic discretisation[1] [11] .

The final Hamiltonian, Eqn. (3.9), describes a linear chain with couplings $t_n \sim \Lambda^{-n/2}\xi_n$, coupled at one end to the dot level, as illustrated in Fig 3.2. This is known as the Wilson chain of the lead. Crucially the couplings between the orbitals in the linear chain decrease exponentially (going as $\Lambda^{-n/2}$) as one moves along the chain away from the dot level. Whilst the full linear chain system still cannot be solved exactly, arbitrarily low energies ($\sim \mathcal{O}(\Lambda^{-N/2})$) can be accessed by truncating the chain at some *finite* length, after N f-orbitals have been accounted for.

[1] Including the A_Λ factor ensures the correct result is recovered in the continuum limit ($\Lambda \to 1$) in the non-interacting case [11].

3.3 Iterative diagonalisation

The above transformations produce a Hamiltonian (Eqn. (3.9)) that contains a coupling term between the dot level and the f_0 orbital, and the sum of coupling terms between f_n and f_{n+1} orbitals, with $N \to \infty$ chain sites in total. If we truncate the chain at some finite number N, we get an approximate Hamiltonian which we shall call $\hat{H}_N$. Moreover, a recursion relation can be set up to obtain $\hat{H}_{N+1}$ from $\hat{H}_N$, and the full Hamiltonian, Eqn. (3.9), is then obtained by applying the recursion relation, and taking the limit $N \to \infty$.

The dimensionless Hamiltonian for the system with N lead orbitals in the Wilson chain is given by

$$\begin{aligned}\hat{H}_N = \Lambda^{(N-1)/2}\Bigg[&\sum_{n=0}^{N-1}\Lambda^{-n/2}\xi_n\left(f^\dagger_{n\sigma}f_{(n+1)\sigma} + f^\dagger_{(n+1)\sigma}f_{n\sigma}\right)\\ &+\left(\bar{\epsilon}+\frac{\bar{U}}{2}\hat{n}_{\bar{\sigma}}\right)\hat{n}_\sigma + \sqrt{\bar{\Gamma}}(f^\dagger_{0\sigma}d_\sigma + d^\dagger_\sigma f_{0\sigma})\Bigg],\end{aligned} \tag{3.12}$$

with the dimensionless parameters

$$\bar{\Gamma} = \left(\frac{2}{1+\Lambda^{-1}}\right)^2\frac{2A_\Lambda\Gamma}{\pi D}\ , \qquad \bar{\epsilon} = \left(\frac{2}{1+\Lambda^{-1}}\right)\frac{\epsilon}{D}\ , \qquad \bar{U} = \left(\frac{2}{1+\Lambda^{-1}}\right)\frac{U}{D}\ ,$$

such that Eqn. (3.9) is recovered on taking the limit

$$\hat{H}_{1\mathrm{AIM}} = \lim_{N\to\infty}\tfrac{1}{2}(1+\Lambda^{-1})D\Lambda^{-(N-1)/2}\hat{H}_N. \tag{3.13}$$

A factor of $\Lambda^{(N-1)/2}$ has been introduced in Eqn. (3.12) in order to make the coupling between the $N-1$ and N sites of order unity. It follows from Eqn. (3.12) that $\hat{H}_{N+1}$ may be obtained from $\hat{H}_N$ using

$$\hat{H}_{N+1} = \sqrt{\Lambda}\hat{H}_N + \xi_N\left(f^\dagger_{N\sigma}f_{(N+1)\sigma} + f^\dagger_{(N+1)\sigma}f_{N\sigma}\right) - E_{G,N+1}\ , \tag{3.14}$$

(measuring energies relative to the ground state $E_{G,N+1}$) which yields an iterative approach to calculating $\hat{H}_N$ starting from the initial Hamiltonian $\hat{H}_0$. The initial Hamiltonian itself follows from Eqn. (3.12) as

$$\hat{H}_0 = \Lambda^{-1/2}\left[\left(\bar{\epsilon}+\frac{\bar{U}}{2}\hat{n}_{\bar{\sigma}}\right)\hat{n}_\sigma + \sqrt{\bar{\Gamma}}(f^\dagger_{0\sigma}d_\sigma + d^\dagger_\sigma f_{0\sigma})\right]\ . \tag{3.15}$$

The iterative diagonalisation procedure is then as follows: $\hat{H}_0$ may be solved trivially, so this is done first and the eigenstates are found. In the basis of these eigenstates, the matrix elements of $\hat{H}_1$ are calculated using the aforementioned recursion relation,

Eqn. (3.14). This matrix is then diagonalised, and the resulting eigenstates used to find the matrix elements for $\hat{H}_2$ and so on. By this iterative procedure we can in principle build up the eigenstates for arbitrary N.

We note at this point that we can make use of any conserved quantities in order to make the numerical diagonalisation more tractable. For every conserved quantity there is a "good quantum number", and the Hamiltonian, $\hat{H}_N$, is block diagonal, with each block corresponding to a different set of these quantum numbers. Each block can then be diagonalised independently, rather than having to diagonalise the full Hamiltonian. For the 1AIM, the quantum numbers generally used are the total charge of the system (relative to half-filling), Q, and the z-component of the total spin of the system, S_z. The operators for these quantities are defined as

$$\begin{aligned} \hat{Q} &= (d_\sigma^\dagger d_\sigma - 1) + \sum_{n=0}^{N} (f_{n\sigma}^\dagger f_{n\sigma} - 1) \ , \\ \hat{S}_z &= \tfrac{1}{2}(d_\uparrow^\dagger d_\uparrow - d_\downarrow^\dagger d_\downarrow) + \sum_{n=0}^{N} \tfrac{1}{2}(f_{n\uparrow}^\dagger f_{n\uparrow} - f_{n\downarrow}^\dagger f_{n\downarrow}) \ , \end{aligned} \tag{3.16}$$

Even exploiting these quantum numbers, there is a problem with the iterative diagonalisation process in practice. At each iteration the number of eigenstates increases by a factor of four (as each f_n orbital has four basis states: unoccupied, singly-occupied with either up or down spin, and doubly-occupied), rapidly becoming intractably large. It is therefore not possible to retain all states at every iteration. The solution to this problem is simply to only retain the lowest ~ 1000 eigenstates at each iteration. All higher energy states are discarded.

This truncation of the Hilbert space may seem to invalidate the NRG procedure. However, since the couplings along the Wilson chain decrease exponentially with N, there is a "separation of energy scales" from one iteration to the next, meaning that only the low-energy states of one iteration are needed to calculate the low-energy states of the next (see Fig. 3.3 for illustration). This is at the heart of the renormalisation group concept. Consequently, we can accurately calculate the low-energy states at each iteration, even though the high-energy states of previous iterations have been discarded. The question then naturally arises, what information can be obtained from just the low-energy states?

At any given iteration, the eigenstates retained are not a good approximation to the true set of eigenstates of $\hat{H}_{\mathrm{1AIM}}$ for temperatures at which high-energy discarded states are important. If the highest energy retained state at a particular interation has an energy $E_{\max}$ above the ground state, then the retained eigenstates cannot to be used to calculate properties for $T \gtrsim E_{\max}$ (see Fig. 3.3). Because the coupling between f_N and f_{N+1} orbitals decreases as N is increased, states with ever lower energy (relative to the ground state for that particular N) are discarded as N

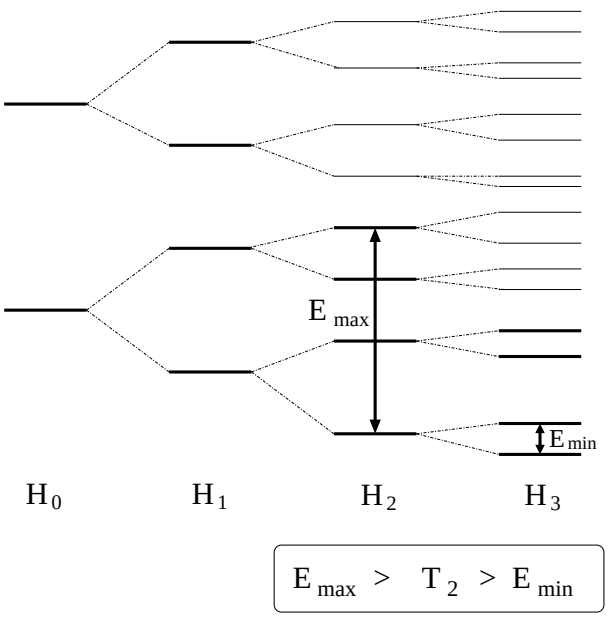


Figure 3.3: Schematic diagram illustrating the iterative procedure. Levels in bold are kept, the rest are discarded. Here only 4 states are kept at each iteration, and at every iteration the total number of states doubles. The splittings between eigenstates decrease at N increases, due to the fact that the chain couplings decrease with N. For a particular iteration (*e.g.*, $N = 2$) the results are only valid for temperatures (T_2) which are $\ll E_{\rm max}$ and $\gg E_{\rm min}$.

increases. Therefore $E_{\rm max}$ decreases as N increases.

At any value of N, the eigenstates retained are also not a good approximation to the true set of eigenstates of $\hat{H}_{\rm 1AIM}$ at temperatures for which the further splittings (caused by adding more orbitals to the chain) make a significant difference to the properties of the system. If the energy level spacings for the following iteration are $\sim E_{\rm min}$, then the eigenstates for that particular iteration cannot to be used to calculate properties for $T \lesssim E_{\rm min}$ (see Fig. 3.3). $E_{\rm min}$ also decreases as N increases and smaller and smaller splittings are accounted for. So for any given N there is a temperature range for which the thermodynamics of $\hat{H}_N$ accurately approximate those of $\hat{H}_\infty = \hat{H}_{\rm 1AIM}$. As N increases this range moves to lower temperature. As we complete more iterations, results for successively lower temperatures can be gathered. An important point to note is that increasing N is thus conceptually equivalent to decreasing T.

To calculate thermodynamic properties we then define a characteristic temperature for each iteration, T_N, for which the eigenstates at that iteration are a good approximation to the true set of eigenstates of the system ($E_{\rm min} \ll T_N \ll E_{\rm max}$)

$$\frac{T_N}{D} = \tfrac{1}{2}(1 + \Lambda^{-1})\Lambda^{-(N-1)/2}/\bar{\beta} \ , \tag{3.17}$$

where $\bar{\beta}$ is a constant of order unity (in practice many different values of $\bar{\beta}$ may be

chosen per iteration and the results combined). The Λ-dependent factors are simply those which follow from Eqn. (3.13). Using the retained states for iteration N, we can therefore calculate thermodynamic properties for $T = T_N$. To do so we start from the definition of the thermal expectation value of an operator, $\hat{O}$,

$$\langle \hat{O} \rangle = \frac{\mathrm{Tr}\, \hat{O} \exp[-\beta \hat{H}]}{\mathrm{Tr} \exp[-\beta \hat{H}]}, \tag{3.18}$$

where Tr denotes a trace over the states of the system and $\beta = 1/T$.[2] As we are usually interested in the properties of the dot(s) rather than the system as a whole, it is conventional to define "impurity" properties[3]:

$$\langle \hat{O} \rangle_{\mathrm{imp}} = \langle \hat{O} \rangle - \langle \hat{O^0} \rangle \tag{3.19a}$$

$$\simeq \frac{\mathrm{Tr}\, \hat{O} \exp[-\beta \hat{H}]}{\mathrm{Tr} \exp[-\beta \hat{H}]} - \frac{\mathrm{Tr}\, \hat{O}^0 \exp[-\beta \hat{H}^0]}{\mathrm{Tr} \exp[-\beta \hat{H}^0]}, \tag{3.19b}$$

where $\hat{H}^0$ denotes the Hamiltonian of the system with the dot removed, and $\hat{O}^0$ an operator acting on this system. Thermodynamics for $T = T_N$ are then calculated via

$$\langle \hat{O} \rangle_{\mathrm{imp}} = \langle \hat{O} \rangle - \langle \hat{O^0} \rangle \tag{3.20a}$$

$$= \frac{\mathrm{Tr}\, \hat{O} \exp[-\beta_N \hat{H}_N]}{\mathrm{Tr} \exp[-\beta_N \hat{H}_N]} - \frac{\mathrm{Tr}\, \hat{O}^0 \exp[-\beta_N \hat{H}^0_N]}{\mathrm{Tr} \exp[-\beta_N \hat{H}^0_N]} \ . \tag{3.20b}$$

In particular, in this work we concentrate largely on the impurity contribution to the entropy of the system, S_{imp}, which is given by

$$S_{\mathrm{imp}} = \bar{\beta} \langle \hat{H}_N \rangle_{\mathrm{imp}} + \ln(Z_N / Z^0_N) \ , \tag{3.21}$$

where Z_N [Z^0_N] is the partition function for the system with [without] the dot(s) present. S_{imp} is diagnostic of the renormalisation group flows and fixed points of the system (see below for discussion of these), and it also yields the energy scales (such as T_{K}) of the problem at hand. In section 4.2, we also look at the impurity contribution to the magnetic susceptibility, given by

$$\chi_{\mathrm{imp}} = \bar{\beta} \left[\langle (\hat{S}_z)^2 \rangle_{\mathrm{imp}} - (\langle \hat{S}_z \rangle_{\mathrm{imp}})^2 \right] \ , \tag{3.22}$$

[2] We set $k_B = 1$ throughout this thesis.

[3] The terminology comes from the original manifestation of the Kondo effect occurring in metals containing magnetic impurities.

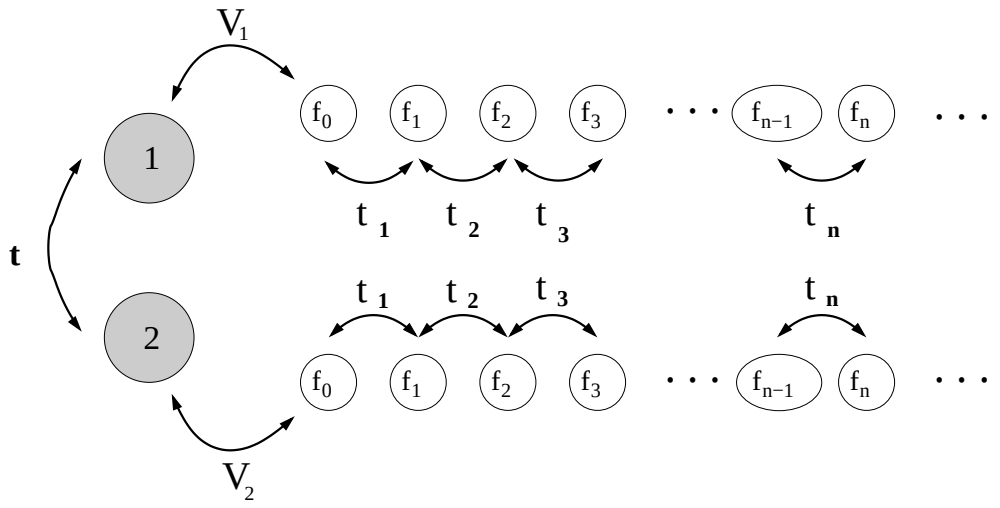


Figure 3.4: Diagram illustrating the linear chain form of the 2AIM. The two dot levels are represented by the grey circles, labelled 1 and 2, and they are mutually tunnel-coupled. Each dot level is coupled to a linear chain of non-interacting f_n orbitals, with couplings decreasing exponentially along the chain.

3.4 The NRG for the 2AIM

We have now discussed in some detail the NRG procedure as applied to the 1AIM. The NRG may be applied to the 2AIM, or indeed to any of the other models studied in this thesis, in much the same way. The main difference between the models studied in this work and the 1AIM is the presence of *two* metallic leads. For two-lead systems such as the 2AIM, the transformations and logarithmic discretisation of the Hamiltonian are carried out in the same way as for a one-lead system, giving rise to a model with *two* linear (Wilson) chains present. For the 2AIM, each of these is coupled to a dot level (see Fig. 3.4), which are themselves mutually tunnel-coupled At each iteration, an orbital of *each* chain is added, meaning that the Hilbert space for the system increases in size by a factor of 16 at every iteration – rather than the factor of 4 for one-lead systems such as the 1AIM, making the calculation rather more computationally taxing. The initial Hamiltonian for the 2AIM, $\hat{H}_0$, is also more complex as it involves two dot levels and two f_0 orbitals. This means that more states need to be retained at each iteration to obtain accurate results, again making the calculations more taxing[4]. Apart from the increase in computational demands, the NRG is carried out in much the same way for the 2AIM (and indeed for any other quantum impurity system) as for the 1AIM.

[4]In our NRG calculations for the 2AIM we generally retain around 4000 states at each iteration. One factor mitigating the high computational expense of our 2AIM NRG calculations is that in the LR-symmetric case, we can make use of the conservation of parity (see section 2.6) to speed up the diagonalisation process.

3.5 NRG flows and fixed points

So far we have explained how the thermodynamic properties of a quantum impurity system can be calculated via the NRG. Beyond this practical use, the NRG also provides a framework for understanding these results, particularly the universality that can arise in these systems, in terms of renormalisation group (RG) flows and fixed points.

The recursion relation between $\hat{H}_N$ and $\hat{H}_{N+1}$, given by Eqn. (3.14), can be considered as an example of a RG transformation and can be written formally as

$$\hat{H}_{N+1} = \hat{T}[\hat{H}_N] \ , \tag{3.23}$$

where the operator $\hat{T}$ is thus defined. A RG transformation takes knowledge of a system on one scale and uses it to derive information on another scale. In certain cases, such as PMS, the transformation does not change the *form* of the Hamiltonian; it only changes the parameters that enter it. In such cases one can consider the Hamiltonian to be represented by a point in parameter space; a series of transformations of the Hamiltonian then corresponds to a trajectory through this space. Such a trajectory is known as a RG flow. Even though the NRG transformations do not preserve the form of the Hamiltonian, we may think of successive NRG transformations (*i.e.*, successive NRG iterations) as corresponding to a flow through an *effective* parameter space. As increasing the number of NRG iterations is equivalent to reducing the energy scale/temperature, the system flows through the effective parameter space as energy scale/temperature is reduced.

One important point arising from the existence of these flows is that certain points can arise in the effective parameter space at which applying the RG transformation leaves the Hamiltonian unchanged. These are the fixed points (FPs), as discussed in the context of PMS in section 2.4. At such a fixed point[5], with a Hamiltonian $\hat{H}^*$,

$$\hat{T}[\hat{H}^*] = \hat{H}^* \ . \tag{3.24}$$

Fixed points are classified according to how nearby RG flows behave. Stable fixed points are ones for which the effect of $\hat{T}$ on any Hamiltonian near to the fixed point in effective parameter space is to move it closer to the fixed point. Stable fixed points therefore "attract" nearby RG flows. Unstable fixed points, by contrast, repel nearby RG flows. Unstable FPs cannot therefore be reached from any other point in effective parameter space (although systems may pass arbitrarily close to an unstable FP before flowing onwards to a stable FP). These types of fixed point are illustrated in Fig. 3.5.

[5]NRG fixed points are usually defined via $\hat{H}^* = \hat{T}^2[\hat{H}^*]$, as even and odd chains exhibit different behaviour. This technical point is unimportant to the general discussion given here.

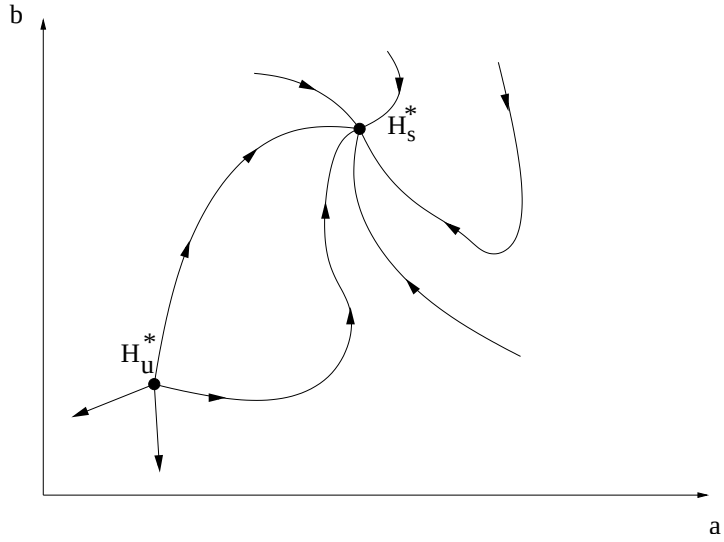


Figure 3.5: Diagram illustrating some RG flows and fixed points. a and b are the effective parameters of the Hamiltonian. H_s^* is a stable fixed point, and attracts surrounding flows. H_u^* is unstable and repels them.

In general it is non-trivial to determine the nature of a particular fixed point, but one method which can sometimes be used is as follows [11, 18]. Consider a Hamiltonian, $\hat{H}_N$, that is near to the fixed point, $\hat{H}^*$, in parameter space, such that $\hat{H}_N = \hat{H}^* + \delta\hat{H}$, where $\delta\hat{H}$ is small compared to $\hat{H}^*$. We can then write $\hat{H}_{N+1}$ as

$$\begin{aligned} \hat{H}_{N+1} = \hat{H}^* + \delta\hat{H}' &= \hat{T}[\hat{H}_N] \\ &= \hat{T}[\hat{H}^* + \delta\hat{H}] \\ &= \hat{H}^* + \hat{T}[\delta\hat{H}] \\ &= \hat{H}^* + \mathcal{M}\delta\hat{H} + \mathcal{O}(\delta\hat{H}^2) \\ \delta\hat{H}' &\approx \mathcal{M}\delta\hat{H}, \end{aligned} \tag{3.25}$$

where $\hat{T}[\delta\hat{H}]$ has been expanded as a Taylor series in $\delta\hat{H}$. $\mathcal{M}$ is a matrix which describes the transformation $\hat{T}$ to first order. Its eigenvectors are given by

$$\mathcal{M}O_l = \lambda_l O_l \ . \tag{3.26}$$

$\delta\hat{H}$ and $\delta\hat{H}'$ may be expanded in terms of these eigenvectors, giving

$$\delta\hat{H} = \sum_l a_l(N)O_l \ , \quad \delta\hat{H}' = \sum_l a_l(N+1)O_l \ , \tag{3.27}$$

such that

$$\begin{aligned}\delta\hat{H}' &= \mathcal{M}\sum_l a_l(N)O_l \\ &= \sum_l \lambda_l a_l(N)O_l \ ,\end{aligned} \tag{3.28}$$

so that

$$a_l(N+1) = \lambda_l a_l(N) \ , \tag{3.29}$$

which implies

$$a_l(N+1) = \lambda_l^N C_l \ , \tag{3.30}$$

where C_l is independent of N. We therefore arrive at

$$\delta\hat{H}' = \sum_l \lambda_l^N C_l O_l \ . \tag{3.31}$$

In order to classify a fixed point, we wish to know what happens to $\delta\hat{H}'$ as N increases. For each eigenvector, O_l, there are three possibilities:

If $\lambda_l > 1$ then the effective parameters of $\delta\hat{H}'$ increase as N increases, such that as successive RG transformations are applied, the system flows away from the FP. In this case the eigenvector O_l is said to be "relevant". On the other hand, if $\lambda_l < 1$ then the effective parameters of $\delta\hat{H}'$ decrease with N, such that as successive RG transformations are applied, the system flows towards from the FP. The eigenvector O_l is then said to be "irrelevant". When $\lambda_l = 1$, no RG flow occurs in the direction of O_l to first order, so that the eigenvector is said to be "marginal". In this case further analysis is required, as higher orders of $\delta\hat{H}$ may result in an eigenvector being relevant or irrelevant. In general there are many eigenvectors and a FP can only be stable if there are no relevant eigenvectors. As mentioned, this type of analysis of a FP is generally non-trivial. However, by carrying out the renormalisation explicitly, *e.g.*, by carrying out the NRG, one can establish the nature of the FPs without resorting to such analysis; however, it remains an important conceptual basis.

As the NRG procedure is carried out, the energy scale is reduced. Ultimately, as iteration number N goes to infinity, the system must end up at a stable FP. These stable FPs therefore correspond to the possible ground states of the system. Systems with very different initial parameters may ultimately flow with similar trajectories towards the same stable FP. This illustrates what is known as universality – two very different systems may behave similarly on low-energy scales despite behaving very differently at high energies. It may be thought from the above discussion that the unstable FPs are unimportant. This is however not necessarily the case. Although ultimately the system must flow to a stable FP, a RG flow may well pass close to an unstable FP, and the system may remain near to such a FP for very many RG

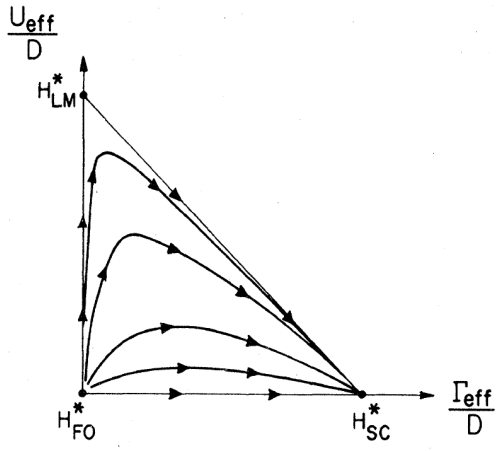


Figure 3.6: RG flows for the ph-symmetric Anderson model, showing that all Hamiltonians ultimately arrive at the SC fixed point, but the path to this point is dependent on the initial parameters. Systems with large initial $\frac{U}{\Gamma}$ will flow near to the LM fixed point. Reproduced from Ref. [11].

transformations/NRG iterations (and hence over an extended temperature/energy range). We will see cases where this occurs in the following chapters.

We now illustrate some of these ideas for the ph-symmetric 1AIM, Eqn. (3.2) with $\epsilon = -U/2$. For this model, there is just one stable FP, which is always reached after enough NRG iterations, *i.e.*, at sufficiently low temperature. This is the strong coupling (SC) fixed point, at which the impurity spin is screened by the lead electrons [11]. As discussed in section 2.4, the flow of a Hamiltonian to the SC fixed point represents the Kondo effect. There are two other FPs for the ph-symmetric 1AIM; the local moment (LM) FP and the free orbital (FO) FP, which are both unstable.

The schematic RG flow diagram, as established by NRG [11] is shown in Fig. 3.6. $\hat{H}^*_{LM}$ is the LM FP, $\hat{H}^*_{FO}$ is the FO FP and $\hat{H}^*_{SC}$ is the SC FP. The initial parameters U and Γ are generally small (relative to D, the half-bandwidth), so the initial Hamiltonian is near the FO fixed point. If $\frac{U}{\Gamma} \gg 1$, *i.e.*, if the system is strongly correlated, then the system will flow near to the LM fixed point en route to the SC fixed point. If $\frac{U}{\Gamma} \lesssim 1$ then the system will flow straight to the SC fixed point, not going near to the LM fixed point. But the fact that ultimately all ph-symmetric Anderson model systems flow to the SC fixed point, *regardless* of their initial parameters, shows that the low-energy behaviour of the ph-symmetric Anderson model is the same for all values of parameters.

One further point which deserves to be made explicit is that a system may have more than one stable FP, separated by a so-called critical FP, each of which having a "basin of attraction", see Fig. 3.7. If one varies the initial parameters, such that the separatrix between the two basins of attraction is crossed, then the ultimate stable FP changes discontinuously. This means that the ground state of the system changes

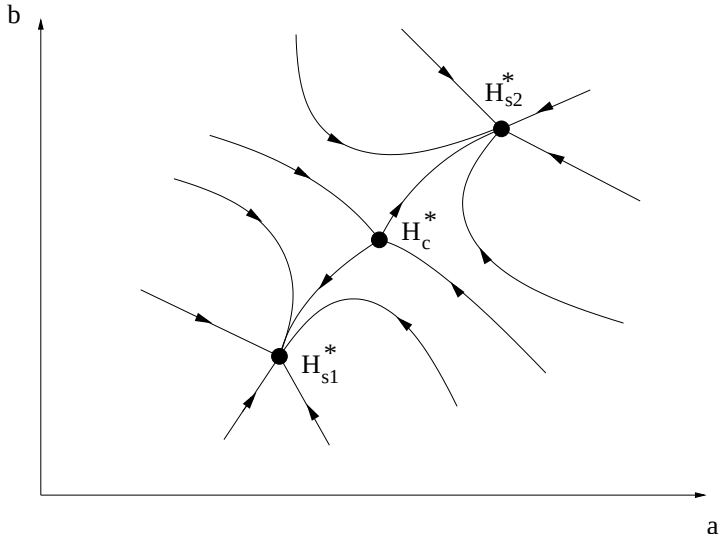


Figure 3.7: A schematic RG flow diagram for a system with two stable FPs, H^*_{s1} and H^*_{s2}, separated by a critical FP, H^*_c. Each stable FP has a basin of attraction, separated by a separatrix along which the system flows to the critical FP. a and b are the effective parameters of the model.

discontinuously as some parameter is changed – corresponding to a quantum phase transition (QPT). If the system is initially exactly on the separatrix between the two basins, the system will then flow to the critical FP. This situation, illustrated in Fig. 3.7, is exemplified by the 2IKM – the two stable FPs correspond to the local singlet and Kondo singlet ground states, whilst the critical FP is the two-channel Kondo FP, as discussed in section 2.8.

We now move on to discuss how dynamical information may be obtained from the NRG.

3.6 Calculating dynamical properties from the NRG

As discussed above, the NRG provides approximate eigenstates of a quantum impurity system on all energy scales; from these states we can calculate the thermodynamic properties of such a system. However, we can also calculate dynamical properties in terms of correlation functions such as the Green's functions of the system. [In this discussion we concentrate on the Green's functions, but other correlation functions can be calculated in much the same way.] The (retarded) Green's functions of a (time-translation invariant) system are defined as

$$G_{ij;\sigma}(t) = -i\theta(t)\langle\{d_{i\sigma}(t), d^\dagger_{j\sigma}(0)\}\rangle \ , \tag{3.32}$$

where $\theta(t)$ is the unit step function, the curly braces represent an anticommutator, and the angled brackets represent a thermal expectation value. It is generally more convenient to work with the Fourier-transformed Green's functions given by

$$G_{ij;\sigma}(\omega) = \int_{-\infty}^{\infty} d\omega \exp(-i(\omega + i\eta)t) G_{ij;\sigma}(t) = \langle\langle d_{i\sigma}; d_{j\sigma}^{\dagger}\rangle\rangle_{\omega} \ , \tag{3.33}$$

with η a positive infinitesimal (for retarded Green's functions), included to ensure convergence. The single-particle spectra (also somtimes known as the spectral densities, or simply the spectra) of a system, $D_{ij;\sigma}(\omega)$, are defined by[6]

$$D_{ij;\sigma}(\omega) = -\frac{1}{\pi}\text{Im } G_{ij;\sigma}(\omega) \ , \tag{3.34}$$

which can be written in the so-called Lehmann representation [3] as

$$D_{ij;\sigma}(\omega) = \sum_{a,b} \langle b|d_{i\sigma}|a\rangle\langle a|d_{j\sigma}^{\dagger}|b\rangle \frac{\exp(-\beta E_a)}{Z} \delta(\omega + E_a - E_b) \ , \tag{3.35}$$

where the set of states $\{|a\rangle\}$ is the set of eigenstates of the system, E_a are the eigenenergies, and $Z = \sum_a \exp(-\beta E_a)$ is the partition function. The single-particle spectra can therefore be seen to be a weighted sum of the transitions between states upon adding or removing a particle from the system; in other words, a weighted sum of the single-particle excitations of the system.

As discussed, the states calculated by the NRG at a particular iteration are those relevant for a particular energy scale. In order to calculate the spectra for all frequencies (even at $T = 0$), the states calculated at every iteration must therefore be used. The original method [130, 131] of calculating spectral functions from the NRG was simply to calculate the spectrum at each iteration N and then, bearing in mind that each iteration corresponds to a certain characteristic energy scale $\omega_N \sim T_N$, producing the full spectrum by taking the spectrum for each iteration at frequencies $\omega \sim \omega_N$ and piecing them together [130, 131]. This method however suffers from a number of problems. First, the spectra for the different iterations must be pieced together in a somewhat ad hoc fashion [130], which can lead to the total spectral weight (*i.e.*, the integral of the spectrum over all frequency) being inaccurately calculated. Second, excitations from states in *all* iterations are counted, which results in an overcounting of excitations. This is because excitations from a state which is retained at iteration N are not only counted in the spectrum for iteration N, but also, to some extent, in the spectra for later iterations, as the states for these later iterations are created from the kept states of iteration N.

Another problem is that excitations are calculated from the states of every iter-

[6]The real parts of the Green's functions can be obtained from the spectra via Hilbert transform, so we concentrate solely on calculating the spectra [120].

ation, even though these states are not necessarily good approximations to the true eigenstates of the system. Particularly, at zero temperature one should calculate excitations only from the ground state of the system. In the above approach however, the high frequency part of the spectrum is calculated from the early iterations – the lowest energy states of which are not good approximations to the true ground state. This is a particular problem in the case of systems with small symmetry breaking perturbations, such as a weak magnetic field. In these cases, the early iterations do not "know" about the perturbation. The high-frequency part of the spectrum will therefore not reflect the perturbation, even though it is known that a weak magnetic field, for instance, has a large effect on the spectrum at high frequencies [132], when the impurity becomes polarised.

3.6.1 The Anders-Schiller basis set

The solution to the above problems was indicated by Anders and Schiller, who pointed out that the set of all the discarded states of all the iterations (considering all the states of the final iteration to be discarded) forms a complete basis set [133, 134]. This can be understood as follows. For any early iteration, before any states have been discarded, the states form a complete set. It is only when states begin to be discarded that completeness is lost. However, for any particular iteration the discarded states are necessarily orthogonal to the kept states, and as the states (discarded and kept) of all subsequent iterations are formed from only the kept states, the discarded states of iteration N are orthogonal to *all* the states of iterations $M > N$. One can therefore see that the set of all the discarded states, from all iterations, forms a complete set. This is known as the Anders-Schiller (AS) basis set.

This set of states contains the best approximations to the actual eigenstates of the system on all energy scales – the best approximations to the lowest energy states are those of the last iteration, and the best approximations to the higher energy states are those which were discarded at earlier iterations. Instead of calculating excitations between states of the same iteration, and then piecing together the resulting spectra for all iterations, one can calculate the excitations between the states in the AS basis. No ad-hoc piecing together of spectra is required, overcounting of excitations is avoided as only discarded states are contained in the AS basis, and at zero-temperature only excitations from the best approximation to the ground state (the lowest energy state of the final iteration) are counted. This method is referred to as the full density matrix (FDM) method [29, 30]. Throughout this thesis we use the FDM method to calculate dynamical properties, and we now give a brief description of it.

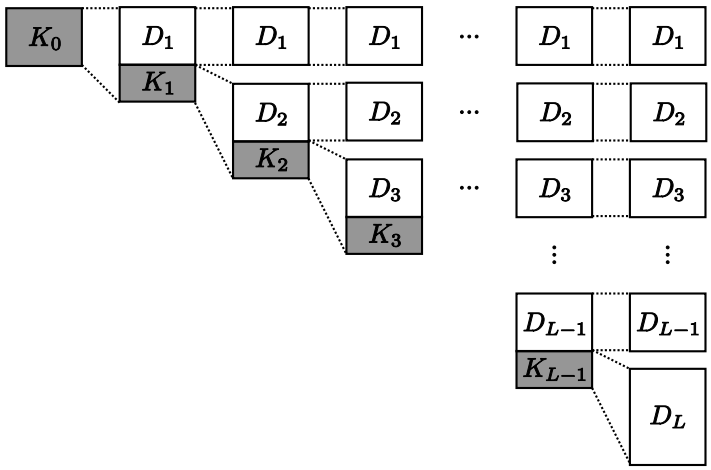


Figure 3.8: Illustration of the Anders-Schiller basis, reproduced from Ref. [100]. States of each iteration, N, are either discarded 'D_N' or kept 'K_N'. The Anders-Schiller basis is the set of all discarded states from all iterations, shown in the rightmost column. This is a complete set and contains the most accurate approximations to the true eigenstates on all energy scales.

3.6.2 The full density matrix method

The FDM method requires a novel conceptual view of the NRG process. Normally one considers an extra orbital being added to the Wilson chain at every iteration. In the FDM approach, one always considers the entire chain, comprising all the orbitals, but with the couplings to successive orbitals being switched on at successive iterations. At iteration N therefore, a state of the system of the impurity and the chain orbitals up to and including orbital f_N is labeled $|s\rangle$, for "system". The state of the rest of the (as yet uncoupled) chain is labeled $|e\rangle$, for "environment", so that the overall state is $|se\rangle = |s\rangle \bigotimes |e\rangle$. The unity operator in the AS basis is therefore written as [134]

$$\hat{1} = \sum_{N>N_0}^{L} \sum_{se} |se\rangle_N^D \, {}_N^D\langle se| \ , \tag{3.36}$$

where $|se\rangle_N^D$ is a discarded state of iteration N, L is the total number of iterations carried out, and N_0 is the last iteration for which all states are kept. The states of the iteration N_0 form a complete set, so we can write an arbitrary (local) operator in this basis as [30]

$$\hat{A} = \sum_{ss'e} |se\rangle_{N_0}^K [A_{KK}^{N_0}]_{ss'} \, {}_{N_0}^K\langle s'e| = \sum_{N>N_0}^{L} \sum_{XX'}^{\neq KK} \hat{A}_{XX'}^N \ , \tag{3.37}$$

with $XX' = KK, KD, DK, DD$, with K representing kept, D representing discarded. In the right hand equality the KK part of each iteration is expressed in

terms of the XX' terms of the next iteration using

$$\hat{A}^{N-1}_{KK} = \sum_{XX'} \hat{A}^{N}_{XX'} = \sum_{ss'e} \sum_{XX'} |se\rangle^{X}_{N} [A^{N}_{XX'}]_{ss'} {}^{X'}_{N}\langle s'e| \ . \tag{3.38}$$

In order to calculate correlation functions, we require the density matrix of the system, which in the AS basis is given by [30]:

$$\begin{aligned} \hat{\rho} &= \sum_{N>N_0}^{L} \sum_{se} |se\rangle^{D}_{N} \frac{e^{-\beta E^{N}_{s}}}{Z} {}^{D}_{N}\langle se| \\ &= \sum_{N>N_0}^{L} w_N \hat{\rho}^{N}_{DD} \ . \end{aligned} \tag{3.39}$$

In the second line we have split the density matrix into a sum of density matrices, one for the discarded states at each iteration. The weighting factor $w_N = 4^{(L-N)} Z^{D}_{N}/Z$ with $Z^{D}_{N} = \sum_{s}^{D} e^{-\beta E^{N}_{s}}$ contains a smooth peak spanning 5-10 iterations around the iteration with $T_N = 1/\beta$.[7] It therefore performs the task of selecting the appropriate iterations for a given temperature. By expressing the operators as in Eqn. (3.37), spectral functions can be written in terms of similar sums

$$\begin{aligned} \mathcal{F}_{ij;\sigma} &= -\frac{1}{\pi} \mathrm{Im} \langle\langle \hat{A}_{ij;\sigma}; \hat{B}_{ij;\sigma} \rangle\rangle_{\omega} \\ &= \sum_{N>N_0}^{L} w_N \mathcal{F}^{N}_{ij;\sigma} \ , \end{aligned} \tag{3.40}$$

with [30]

$$\mathcal{F}^{N}_{ij;\sigma} = \sum_{M>N_0}^{N} \sum_{ss'} \sum_{XX'}^{\neq KK} [B^{M}_{X'X} \rho^{[MN]}_{XX}]_{s's} [A^{M}_{XX'}]_{ss'} \delta(\omega - E_s + E_{s'}) \ , \tag{3.41}$$

where $[\rho^{[MN]}_{XX}]_{ss'} = \sum_{e} {}^{X}_{M}\langle se|\hat{\rho}^{N}_{DD}|s'e\rangle^{X}_{M}$. Eqn. (3.40) therefore gives

$$\begin{aligned} \mathcal{F}_{ij;\sigma} &= \sum_{N>N_0}^{L} w_N \sum_{M>N_0}^{N} \sum_{ss'} \sum_{XX'}^{\neq KK} [B^{M}_{X'X} \rho^{[MN]}_{XX}]_{s's} [A^{M}_{XX'}]_{ss'} \delta(\omega - E_s + E_{s'}) \ , \\ &= \sum_{M>N_0}^{L} \sum_{ss'} \sum_{XX'}^{\neq KK} [B^{M}_{X'X} \sum_{N=M}^{L} w_N \rho^{[MN]}_{XX}]_{s's} [A^{M}_{XX'}]_{ss'} \delta(\omega - E_s + E_{s'}) \ , \\ &= \sum_{M>N_0}^{N} \sum_{ss'} \sum_{XX'}^{\neq KK} [B^{M}_{X'X} \rho^{M,red}_{XX}]_{s's} [A^{M}_{XX'}]_{ss'} \delta(\omega - E_s + E_{s'}) \ , \end{aligned} \tag{3.42}$$

[7] The factor of 4^{L-N} is a degeneracy factor arising from summing over the environment orbitals. For a two-lead system, such as the 2AIM, this factor is 16^{L-N}.

where in the second line we have changed the summations, and the "reduced" density matrix for iteration M is defined by $\rho_{XX}^{M,red} = \sum_{N=M}^{L} w_N \rho_{XX}^{[MN]}$. These density matrices are labeled the reduced density matrices, as they relate to the system with the environment orbitals decoupled and their degrees of freedom traced over. These reduced density matrices must be calculated in order to evaluate correlation functions, and this is a non-trivial procedure. After one has performed all the NRG iterations, one must then iterate backwards from the final NRG iteration – this means that one must retain the unitary transformation matrices that take the system from one iteration to the next for all iterations. Doing so makes the calculation rather more computationally demanding. One starts with the (diagonal) reduced density matrix for the last iteration, $\rho_{DD}^{L,red}$. The unitary transformation matrix which takes one from iteration $L-1$ to iteration L is then used to transform this into $w_L \rho_{KK}^{[L-1,L]}$ in the basis of iteration $L-1$. To form the total $\rho^{L-1,red}$ we must add the DD part to this, which is given by $\rho_{DD}^{L-1,red} = w_{L-1}\rho_{DD}^{[L-1,L-1]}$. The reduced density matrix for any iteration M can be calculated in this manner and is then given by

$$\rho^{M,red} = w_M \rho_{DD}^{[MM]} + \sum_{N>M}^{L} w_N \rho_{KK}^{[MN]} \ . \tag{3.43}$$

Once these reduced density matrices are calculated we can put them into Eqn. (3.42) and calculate the desired correlation functions.

Having calculated the spectra, one further step is required. The spectra calculated from the NRG are discrete, *i.e.*, they consist of a set of δ-functions. This is due to the fact that the conduction band, which contains a continuum of states, was discretised at the beginning of the procedure. In order to obtain realistic spectral functions, the δ-functions which arise from the NRG must therefore be broadened in some way, in order to give continuous spectral functions. To this end we replace each δ-function with a logarithmic Gaussian [29, 135]:

$$\delta(\omega) \to \frac{e^{-b^2/4}}{b\omega_n\sqrt{\pi}} \exp\left[-\frac{(\ln\omega - \ln\omega_n)^2}{b^2}\right] \ , \tag{3.44}$$

where the parameter b controls the width of the Gaussian[8]. One must be careful not to pick b too high – as then spectral features will be washed out by the broadening, but also not too low – otherwise artifacts of the discretisation will appear in the spectral functions. To this end we take $b \simeq 0.7$ throughout this thesis.

The spectral functions calculated from the NRG in the way described contain logarithmic oscillations at low frequency [136]. This is because the poles tend to cluster around certain energies – a natural consequence of the logarithmic discreti-

[8]The particular choice of a logarithmic Gaussian, although somewhat arbitrary, is well suited for dealing with the logarithmic oscillations that tend to arise in NRG spectral functions [135].

sation of the conduction band. There are a number of methods for dealing with these oscillations. One method is to calculate the so-called self-energies of the system as well as the Green's functions [135]. One can then combine the two to give more accurate spectral functions, as we now discuss.

3.6.3 Self-energy method of calculating Green's functions

The self-energy matrix of a system, $\mathbf{\Sigma}_\sigma(\omega)$ (for σ-spin electrons, with $[\mathbf{\Sigma}_\sigma(\omega)]_{ij} = \Sigma_{ij;\sigma}(\omega)$, with i, j labelling the *interacting* sites), is defined by the Dyson equation,

$$\mathbf{G}_\sigma(\omega)^{-\mathbf{1}} = [\mathbf{G}^{\mathbf{0}}_\sigma(\omega)]^{-1} - \mathbf{\Sigma}_\sigma(\omega) \ , \tag{3.45}$$

where $\mathbf{G}^{\mathbf{0}}_\sigma(\omega)$ is the matrix of Green's functions for the non-interacting system, with $[\mathbf{G}^{\mathbf{0}}_\sigma(\omega)]_{ij} = G^0_{ij;\sigma}(\omega)$ the Green's function between sites i and j for the non-interacting system. $\mathbf{G}_\sigma(\omega)$ is the matrix of Green's functions for the full, interacting system, with $[\mathbf{G}_\sigma(\omega)]_{ij} = G_{ij;\sigma}(\omega)$. For the 2AIM, with two dot levels, $\{i, j\} = \{1, 2\}$, such that the matrices in Eqn. (3.45) are of dimension 2×2. From the Dyson equation, it can be seen that the self-energies contain the effects of the interactions on the Green's functions of the system.

Expressions for $G_{ij;\sigma}(\omega)$ are readily derived by an equation-of-motion method, which gives the following expression for the retarded correlator between operators $\hat{A}$ and $\hat{B}$ [3]

$$z\langle\langle \hat{A}; \hat{B}\rangle\rangle_\omega = \langle\{\hat{A}, \hat{B}\}\rangle + \langle\langle[\hat{A}, \hat{H}]; \hat{B}\rangle\rangle_\omega \ , \tag{3.46}$$

where $z = \omega + i\eta$, with η a positive infinitesimal, and $\langle\langle \hat{A}; \hat{B}\rangle\rangle_\omega$ denotes the Fourier transform of the retarded correlator, as in Eqn. (3.33). Defining $F_{ij;\sigma}(\omega)$ functions as

$$F_{ij;\sigma}(\omega) = \langle\langle[\hat{H}_U, d_{i\sigma}]; d^\dagger_{j\sigma}\rangle\rangle_\omega = U_i\langle\langle \hat{n}_{i\bar{\sigma}} d_{i\sigma}; d^\dagger_{j\sigma}\rangle\rangle_\omega \ , \tag{3.47}$$

with U_i the onsite repulsion for site i, and $\bar{\sigma}$ the opposite spin to σ, it is straightforward to show that (see Appendix B)

$$\mathbf{\Sigma}_\sigma = -\mathbf{F}_\sigma \mathbf{G}^{-1}_\sigma \ , \tag{3.48}$$

a result which turns out to be of great practical use. We can calculate both $F_{ij;\sigma}$ and $G_{ij;\sigma}$ functions via the NRG as explained above. Then we can use Eqn. (3.48) to find $\Sigma_{ij;\sigma}$, and together with easily-derived exact expressions for the non-interacting Green's functions, we can get improved dot Green's functions via Eqn. (3.45). This is known as the self-energy method [135]. This method allows more accurate access to spectral functions because i), the non-interacting Green's functions appear explicitly and are treated exactly, and ii), the oscillations in dynamical quantities cancel out to some extent via Eqn. (3.48), which itself makes use of more information from

the NRG than $\mathbf{G}_\sigma(\omega)$ alone. Throughout this thesis, wherever dynamical properties are calculated we use this self-energy method. The down side to using this method is that it comes at an increased computational cost, as one must calculate not only the Green's functions, but also the $F_{ij;\sigma}$ functions.

This concludes our discussion of the methods used to calculate dynamical properties of quantum impurity systems within the NRG. We now go on to look at how we can calculate the conductance of such systems, in particular, that of the 2AIM.

3.7 Calculating the conductance of the 2AIM

The quantity most commonly measured in quantum dot experiments, and a quantity in which the Kondo effect is clearly manifest, is the differential conductance of the quantum dot device, defined as the derivative of the current between the two leads, I, with respect to the bias voltage applied between the two leads, V (also known as the source-drain bias). $G_c(T,V)$ is used to denote the differential conductance as a function of temperature and bias. When a finite bias is applied across the quantum dot device, the system is no longer in equilibrium, making the problem very difficult to deal with theoretically. We therefore concentrate mainly on calculating the zero-bias conductance, $G_c(T,0) = \lim_{V\to 0} G_c(T,V)$. In section 3.7.4 we look at some approximations that can be made in order to calculate the finite-bias conductance from the NRG, including a novel approach which allows one to calculate the conductance to leading order in the interdot tunnel-coupling for *arbitrary* bias.

3.7.1 Meir-Wingreen approach

The standard method of calculating the zero-bias conductance through a region of interacting electrons, such as a quantum dot, is to use a result of Meir and Wingreen [123], relating the zero-bias conductance of a quantum impurity system to the single-particle spectra. For a single dot level coupled to two equivalent leads, the Meir-Wingreen (MW) equation reads [123]:

$$G_c(T,V=0) = \frac{e^2}{h} G_0 \sum_\sigma \int_\infty^\infty d\omega \left(-\frac{\partial f(\omega)}{\partial \omega}\right) \pi\Gamma D_\sigma(T,V=0,\omega) \ , \tag{3.49}$$

where $f(\omega) = \frac{1}{e^{\beta(\omega-\mu)}+1}$ is the equilibrium Fermi function of either lead, with μ the common zero-bias chemical potential of the leads. $D_\sigma(T,0,\omega)$ is the equilibrium spectrum for σ-spin electrons on the dot level, and $\Gamma = \Gamma_1 + \Gamma_2$ is the sum of the hybridisations to the two leads. G_0 is a factor which describes the asymmetry in the dot-lead couplings, *viz.*

$$G_0 = \frac{4\Gamma_1\Gamma_2}{(\Gamma_1+\Gamma_2)^2} \ , \tag{3.50}$$

such that for symmetric dot-lead couplings ($\Gamma_1 = \Gamma_2$), $G_0 = 1$, and in the asymmetric limit ($\Gamma_1/\Gamma_2 \to 0$ or ∞) $G_0 \to 0$. For multi-level quantum dot systems the MW approach is only valid for "proportional couplings", *i.e.*, when $\mathbf{\Gamma}^{(1)} = \alpha\mathbf{\Gamma}^{(2)}$, with α a constant, and the $\mathbf{\Gamma}^{(\nu)}$ matrices defined as

$$[\mathbf{\Gamma}^{(\nu)}]_{mn} = 2\pi\rho_T V_{m\nu} V_{n\nu} \ , \tag{3.51}$$

where $V_{m\nu}$ is the coupling between dot level m and lead ν, and ρ_T is the total density of states of either lead.

The relation $\mathbf{\Gamma}^{(1)} = \alpha\mathbf{\Gamma}^{(2)}$ does not however hold for the 2AIM, and in consequence the zero-bias conductance cannot in general be related to the single-particle spectra. At zero temperature however, we may use a simple, exact scattering approach, as we now describe.

3.7.2 Scattering approach

For a Fermi liquid at zero temperature, inelastic scattering vanishes at zero energy [137]. As the 2AIM is known to have a Fermi liquid ground state for all values of its parameters[9], an expression for the zero-temperature, zero-bias conductance can be obtained by considering only the coherent/elastic contribution to the current. The zero-temperature, zero-bias conductance is then related to the zero-frequency $\mathbf{T}$-matrix [123], via a Landauer-type formula [95, 138–142]:

$$G_c(T = 0, V = 0) = \frac{e^2}{h} \sum_\sigma |2\pi\rho_T T_{12;\sigma}(0)|^2 \ . \tag{3.52}$$

$T_{12;\sigma}(\omega)$, which gives the probability amplitude of an incoming electron scattering from one lead to the other (the transmission probability amplitude), is defined by[10]

$$G_{1k,2k';\sigma}(\omega) = \frac{1}{z - \epsilon_k} T_{12;\sigma}(\omega) \frac{1}{z - \epsilon_{k'}} \ , \tag{3.53}$$

with $G_{1k,2k';\sigma}(\omega)$ the zero-temperature propagator connecting the $k\sigma$ state in lead 1 with the $k'\sigma$ state in lead 2. From this definition it is easy to show that for the

[9] As illustrated, for example, by the vanishing of the imaginary parts of the self-energies as $\omega \to 0$, discussed further in section 4.1.

[10] Note that we have assumed that the $\mathbf{T}$-matrix element connecting the state with wavevector k in lead 1 and the state with wavevector k' in lead 2 is independent of k and k'. This is the case when the dot-lead tunnel-couplings are k, k' independent, as we consider throughout this work.

2AIM $|\pi\rho_T T_{12;\sigma}(\omega)|^2 = \Gamma_1\Gamma_2|G_{12;\sigma}(\omega)|^2$, and so

$$\begin{aligned} G_c(T=0,V=0) &= \frac{4e^2}{h}\Gamma_1\Gamma_2\sum_\sigma |G_{12;\sigma}(0)|^2 \\ &= \frac{e^2}{h}\Gamma_1\Gamma_2\sum_\sigma |G_{ee;\sigma}(0) - G_{oo;\sigma}(0)|^2 \ , \end{aligned} \tag{3.54}$$

where the second equality is readily shown to follow from the definition of the even and odd orbitals when the system is LR symmetric (see section 2.6).

From Eqn. (3.54), it is straightforward to show that [59, 95, 96, 143]

$$G_c(0,0) = \frac{e^2}{h}\sum_\sigma \sin^2(\delta_{e\sigma} - \delta_{o\sigma}) \ , \tag{3.55}$$

provided the system is LR-symmetric, where $\delta_{\alpha\sigma}$ is the α-channel phase shift for σ-spin electrons, which we define and discuss in section 4.1. Furthermore, at ph symmetry (see section 4.1, Eqn. (4.20)) it can be shown that $\delta_{e\sigma} = \pi - \delta_{o\sigma}$ [25, 96], and one therefore obtains the key result,

$$G_c(0,0) = \frac{e^2}{h}\sum_\sigma \sin^2(2\delta_{e\sigma}) \ . \tag{3.56}$$

This is very useful as we can determine the phase shifts from the NRG energy levels without having to calculate dynamical properties, as discussed in section 4.2.1.

As discussed, Eqn. (3.54) is exact for the 2AIM in the limits of zero temperature and zero bias. We may extend it to finite temperature approximately by neglecting inelastic scattering [123], to obtain

$$G_c(T,0) \simeq \frac{4e^2}{h}\Gamma_1\Gamma_2\sum_\sigma \int_{-\infty}^{\infty}\left[-\frac{\partial f}{\partial\omega}\right]|G_{12;\sigma}(\omega,T)|^2 d\omega \ . \tag{3.57}$$

with $G_{12;\sigma}(\omega,T)$ the finite-temperature propagator connecting dot levels 1 and 2. We stress that this extension to finite temperature is entirely heuristic; we do however expect it to give qualitatively correct results for sufficiently low temperatures, for which inelastic scattering is suppressed. The scattering approach therefore gives an exact expression for the zero-bias conductance of the 2AIM at zero temperature (Eqn. (3.54)) and an approximate expression at finite temperature (Eqn. (3.57)). We may however derive an *exact* expression for the zero-bias, finite-temperature conductance via linear-response theory, as we now discuss.

3.7.3 Linear-response approach

To calculate the zero-bias conductance at finite temperature exactly we use linear-response theory, as developed by Kubo [94, 144, 145]. This gives the conductance to leading order in some perturbing part of the Hamiltonian, $\hat{H}'$. Taking the perturbing part of the Hamiltonian to be the voltage bias (valid as $V \to 0$),

$$\hat{H}' = \sum_{\sigma} \left[\lambda eV \sum_{k} c^{\dagger}_{1k\sigma} c_{1k\sigma} - (1-\lambda) eV \sum_{k} c^{\dagger}_{2k\sigma} c_{2k\sigma} \right] , \tag{3.58}$$

where λ describes how the bias is partitioned between the leads; the chemical potentials of the two leads being $\mu_1 = \lambda eV$, $\mu_2 = -(1-\lambda)eV$, and $\lambda = 0.5$ corresponding to symmetric partitioning. The total voltage drop across the system is then seen to be $\lambda eV + (1-\lambda)eV = eV$.

The conductance can then be calculated to leading order in bias via perturbation theory in $\hat{H}'$, giving an exact result in the limit of zero bias. A lengthy derivation, given in Appendix C, leads to

$$G_c(T,0) = \frac{e^2}{h} [\lambda \bar{\sigma}_{11} + (1-\lambda)\bar{\sigma}_{22} - \bar{\sigma}_{12}] , \tag{3.59}$$

where

$$\bar{\sigma}_{\mu\nu} = \pi V_\mu V_\nu \lim_{\omega \to 0} \mathrm{Im} \frac{C_{\mu\nu}(\omega)}{\omega}, \tag{3.60}$$

with $C_{\mu\nu}(\omega)$ the current-current correlation functions[11]. These functions are defined as

$$C_{\mu\nu}(t) = -i\theta(t) \langle [\hat{j}_\mu(t), \hat{j}_\nu(0)] \rangle, \tag{3.61}$$

with Fourier transform

$$C_{\mu\nu}(\omega) = \int_{-\infty}^{\infty} C_{\mu\nu}(t) \exp\left(i(w + i\eta)t\right) dt, \tag{3.62}$$

and where $\mu, \nu = 1, 2$. $\hat{j}_\mu$ are current operators, here defined as

$$\hat{j}_\mu = \sum_{\sigma} \left(f^{\dagger}_{\mu\sigma} d_{\mu\sigma} - d^{\dagger}_{\mu\sigma} f_{\mu\sigma} \right) . \tag{3.63}$$

The current-current correlation functions can be calculated via the NRG, so we can calculate the zero-bias conductance at finite temperature from Eqn. (3.59)[12].

[11] This is a manifestation of the fluctuation-dissipation theorem, which states that the dissipation of some quantity can be expressed in terms of its fluctuations. In this case the dissipation of the current, the conductance, is expressed in terms of the current fluctuations, given by the current-current correlation functions.

[12] Eqn. (3.59) seems to suggest that the zero-bias conductance is dependent on λ, in contrast to Eqns. (3.54) and (3.57). This is not however the case, as in fact we find that $\bar{\sigma}_{11} = \bar{\sigma}_{22}$, even when the system is not LR symmetric.

Having looked at methods for calculating the zero-bias conductance at both zero and finite temperature, we now move on to look at how the finite-bias conductance may be calculated.

3.7.4 Finite-bias conductance

An exact expression for the conductance of the 2AIM at finite bias, when the system is not in equilibrium, is not currently available. As such, approximations are necessary. One way of proceeding is to make the common approximation of bias-independent self-energies [72, 73, 128]. By doing so within the scattering approach we obtain an approximate equation for the finite-bias, finite-temperature conductance [67, 146, 147],

$$G_c(T,V) = \frac{4e^2}{h}\sum_\sigma \Gamma_1\Gamma_2 \int_{-\infty}^{\infty}\left[-\lambda\frac{\partial f_1(\omega)}{\partial\omega} - (1-\lambda)\frac{\partial f_2(\omega)}{\partial\omega}\right]|G_{12;\sigma}(\omega,T)|^2 d\omega \ . \tag{3.64}$$

with $f_i(\omega) = \frac{1}{e^{\beta(\omega-\mu_i)}+1}$ the Fermi function for lead i. At zero temperature this reduces to

$$\begin{aligned} G_c(T=0,V) =& \frac{4e^2}{h}\sum_\sigma \Gamma_1\Gamma_2\Big[(1-\lambda)\big|G_{12;\sigma}(\omega=-(1-\lambda)eV))\big|^2 \\ &+ \lambda\big|G_{12;\sigma}(\omega=\lambda eV)\big|^2\Big] \ . \end{aligned} \tag{3.65}$$

In practice then, we find the zero-bias, zero-temperature conductance using the scattering approach (Eqn. (3.54)) and zero-bias, finite-temperature conductance using the linear-response approach (Eqn. (3.59)). We have checked that both approaches give the same results in the limit of low temperature (see for example Fig. 4.9). In order to make tangible contact with experiments carried out at finite bias (see chapter 7), we calculate the approximate finite-bias conductance via Eqn. (3.64).

The limit of weakly-coupled dots

Whilst the finite-bias conductance of the 2AIM cannot be calculated exactly in general, there is one limit in which we can derive asymptotically exact results for arbitrary voltage bias. Carrying out perturbation theory in the dot-dot coupling, taking $\hat{H}' = \hat{H}_t$ (see Eqn. (2.18)), yields the leading-order contribution to the current, regardless of the bias or temperature. In the limit of weak tunnel-coupling between the two dot levels, *i.e.*, the limit of small $t \to 0$ (see Eqn. (2.16)), this result is asymptotically exact. We refer to this as the "leading order in t" (LOT) approach. The algebra is rather lengthy (the derivation is given in appendix D) but

the key result is

$$J(T,V) = \frac{4et^2}{h\Gamma_1\Gamma_2} \sum_\sigma \int_{-\infty}^{\infty} \mathrm{d}\omega \ [f_1(\omega) - f_2(\omega)] \, [\pi\Gamma_1 D^{(2)}_{11;\sigma}(\omega)][\pi\Gamma_2 D^{(1)}_{22;\sigma}(\omega)] \ . \quad (3.66)$$

where $J(T,V)$ is the current as a function of temperature and voltage bias. $D^{(2)}_{11;\sigma}(\omega)$ is the spectrum for dot 1 in the absence of dot 2, or equivalently, the spectrum for dot 1 for the system with $t = 0$. These spectra are therefore simply 1AIM spectra, as the $t = 0$ 2AIM is simply a pair of decoupled 1AIMs. Whilst this approach is valid for arbitrary temperature, we concentrate on the limit of zero temperature in this work. In this case, with $\mu_1 = \lambda eV$, $\mu_2 = -(1-\lambda)eV$, the above expression reduces to

$$J(0,V) = \frac{4et^2}{h\Gamma_1\Gamma_2} \sum_\sigma \int_{-(1-\lambda)eV}^{\lambda eV} d\omega \ [\pi\Gamma_1 D^{(2)}_{11;\sigma}(\omega)] \ [\pi\Gamma_2 D^{(1)}_{22;\sigma}(\omega)] \ , \quad (3.67)$$

Using the fact that $D_\sigma(\omega,\epsilon,\mu) = D_\sigma(\omega-\mu,\epsilon-\mu,0)$, where $D_\sigma(\omega,\epsilon,\mu)$ is the (equilibrium) spectrum for σ-spin electrons of a 1AIM with dot level energy ϵ and a chemical potential of μ, it is straightforward to show that Eqn. (3.67) can be written as

$$J(0,V) = \frac{4et^2}{h\Gamma_1\Gamma_2} \sum_\sigma \int_{-eV}^{0} d\omega \, [\pi\Gamma_1 D_\sigma(\omega, \epsilon_1 - \lambda eV, 0)] \, [\pi\Gamma_2 D_\sigma(\omega + eV, \epsilon_2 + (1-\lambda)eV, 0)] \ . \quad (3.68)$$

We may calculate the 1AIM spectra in the above equation via the NRG, and thereby calculate the current; to get the conductance, it is easiest to simply differentiate the current numerically. Differentiating Eqn. (3.67) *explicitly* with respect to bias voltage (using Liebniz's rule) to get the conductance gives

$$\begin{aligned} G_c(0,V) = \frac{4e^2t^2}{h\Gamma_1\Gamma_2} \sum_\sigma \Big[& (1-\lambda)[\pi\Gamma_1 D^{(2)}_{11;\sigma}(\omega = -(1-\lambda)eV))][\pi\Gamma_2 D^{(1)}_{22;\sigma}(\omega = -(1-\lambda)eV))] \\ & + \lambda[\pi\Gamma_1 D^{(2)}_{11;\sigma}(\omega = \lambda eV)][\pi\Gamma_2 D^{(1)}_{22;\sigma}(\omega = \lambda eV)] \\ + \int_{-(1-\lambda)eV}^{\lambda eV} & d\omega \frac{\partial}{\partial V} [\pi\Gamma_1 D^{(2)}_{11;\sigma}(\omega)] \ [\pi\Gamma_2 D^{(1)}_{22;\sigma}(\omega)] \Big] \ . \end{aligned} \quad (3.69)$$

In the zero-bias limit, the above equation yields:

$$G_c(0,0) = \frac{4e^2t^2}{h\Gamma_1\Gamma_2} \sum_\sigma [\pi\Gamma_1 D^{(2)}_{11;\sigma}(0)][\pi\Gamma_2 D^{(1)}_{22;\sigma}(0)] \ . \quad (3.70)$$

To leading order in t then, $G_c(0,0)$ is proportional to the product of the zero-frequency values of the spectra for the individual dots when $t = 0$. [We note that the above expression can also be obtained by taking the $t \to 0$ limit in Eqn. (3.54),

using the explicit expressions for the Green's functions given in Eqns. (4.8) – (4.10), and noting that as $t \to 0$, $t^* \to t$ (see chapter 4 for discussion of the renormalised interdot coupling, t^*).]

Having discussed the NRG in some detail, both as a numerical tool for solving quantum impurity Hamiltonians and as a framework for understanding the physical properties of such systems, we now turn to applying it to study the behaviour of the 2AIM.

CHAPTER 4

Kondo physics in the 2AIM

In this chapter we study the low-temperature behaviour of the 2AIM quite generally, looking at a wide range of parameters, and concentrating particularly on the Kondo physics that arises. Later in this thesis we show that *two-channel* Kondo physics can arise in the 2AIM, but we delay discussion of this aspect of the 2AIM until chapter 5.

This chapter begins with a discussion of the self-energies and Green's functions of the 2AIM, and some important analytic results are derived within the framework of Fermi liquid theory. The system is then studied in detail at particle-hole (ph) symmetry, that is (see section 2.6), with $\epsilon_1 = \epsilon_2 = -U/2$. The 2AIM at ph symmetry (and indeed throughout the regime in which each dot is essentially singly occupied) exhibits rich physics, resulting from the competition between Kondo physics and the interdot tunnel-coupling. This competition leads to a continuous crossover between Kondo singlet (KS) and local singlet (LS) regimes as interdot tunnel-coupling strength is increased [94]. This crossover is manifest in the phase shifts and thermodynamics of the system, which are calculated via the NRG, and these additionally clearly indicate the fixed points of the system. As discussed in the previous chapter, dynamic properties may also be obtained via the NRG. We concentrate on the single-particle spectra and the zero-bias conductance of the 2AIM, finding in particular that the KS-LS crossover gives rise to a strong enhancement of the zero-bias conductance at low temperature, which reaches the unitary limit at zero temperature[1]. We also investigate the effect of an interdot repulsion (U') and unequal dot-lead couplings ($\Gamma_1 \neq \Gamma_2$) on the 2AIM, both of which would be expected to arise in TCDQD experiments [67].

The system is then studied away from ph symmetry, first with equal dot level energies, $\epsilon_1 = \epsilon_2$, and then more generally with both dot level energies allowed to vary freely. Moving away from ph symmetry, as may be achieved in TCDQD

[1]Some of these results have been previously obtained by Izumida et al. [94]. We will indicate where this is the case.

experiments by varying gate voltages, allows the number of electrons on the dots to vary. Whilst the existence of unpaired electrons on the dots gives the possibility of Kondo physics, mixed-valence regimes (in which charge fluctuations on the dots are significant) also arise. These regimes have enhanced zero-bias conductance at low temperature, giving rise to "Coulomb blockade" peaks in the conductance which reflect the atomic-limit phase diagram, discussed in section 2.10.

This chapter is concluded by looking at the finite-bias conductance of the 2AIM. In the limit of weak interdot coupling, we compare the asymptotically-exact perturbative approach to the approximation of bias-independent self-energies (both approaches are outlined in section 3.7.4). Whilst the two methods give reasonably good agreement for low bias voltage, the bias-independent self-energies approximation fails to capture adequately certain Coulomb blockade features at large bias.

4.1 Self-energies and Friedel Sum Rule

The Green's functions (or propagators) of the system can be expressed in terms of the non-interacting Green's functions and the self-energies of the system via the Dyson equation (cf. Eqn. (3.45)),

$$\mathbf{G}_\sigma(\omega)^{-\mathbf{1}} = [\mathbf{G}^{\mathbf{0}}_\sigma(\omega)]^{-1} - \mathbf{\Sigma}_\sigma(\omega) \ . \tag{4.1}$$

[Note that in the absence of a magnetic field, as considered in this chapter, all quantities are independent of spin, σ.] The non-interacting Green's functions, $[\mathbf{G}^{\mathbf{0}}_\sigma(\omega)]_{ij} = G^0_{ij;\sigma}(\omega)$ ($\{i,j\} = \{1,2\}$ label the dot levels), can in turn be calculated simply via equation-of-motion methods [3, 120, 122]. One begins with the retarded atomic-limit, $t = 0$ (t being the interdot tunnel-coupling) propagators for the non-interacting system, $g_{ij;\sigma}(\omega)$, given by

$$g_{ij;\sigma}(\omega) = \frac{\delta_{ij}}{z - \epsilon_i} \ , \tag{4.2}$$

where $g_{ii;\sigma}$ is the atomic-limit, $t = 0$ propagator for σ-spin electrons on dot level i, with $z = \omega + i\eta$, and η a positive infinitesimal. The equation-of-motion for the non-interacting system is then [3, 100, 120]

$$[g_{ii;\sigma}(\omega)]^{-1} G^0_{ij;\sigma}(\omega) = \delta_{ij} + \sum_{k'} V_{i,k'} G^0_{k'j;\sigma}(\omega) \ . \tag{4.3}$$

Here, $k' = \{1, 2, 1\mathbf{k}, 2\mathbf{k}\}$ with $1\mathbf{k}, 2\mathbf{k}$ labeling states with wavevector $\mathbf{k}$ in lead $1, 2$. $G^0_{1\mathbf{k}i;\sigma}(\omega)$ is then the propagator connecting dot level i with lead state $1\mathbf{k}$. $V_{i,k'}$ is the hopping matrix element connecting sites i and k', such that $V_{1,2} = V_{2,1} = t$,

$V_{i,j\mathbf{k}} = V_{j\mathbf{k},i} = \delta_{ij}V_i$. For the 2AIM, we obtain

$$\begin{aligned}[g_{11;\sigma}(\omega)]^{-1}G^0_{11;\sigma}(\omega) &= 1 + \Delta_1 G^0_{11;\sigma}(\omega) + t^2 g_{22;\sigma}(\omega)\left[\frac{1}{1-\Delta_2 g_{22;\sigma}(\omega)}\right] G^0_{11;\sigma}(\omega) \\ &= 1 + \Delta_1 G^0_{11;\sigma}(\omega) + \frac{t^2}{z-\epsilon_2-\Delta_2} G^0_{11;\sigma}(\omega)\ ,\end{aligned} \tag{4.4}$$

where $\Delta_i = \sum_{\mathbf{k}} \frac{|V_i|^2}{z-\epsilon_{\mathbf{k}}}$. For the infinitely-wide flat bands which we consider[2], $\Delta_i = -i\Gamma_i$ [3], and therefore

$$G^0_{11;\sigma}(\omega) = \left[(z-\epsilon_1+i\Gamma_1) - \frac{t^2}{z-\epsilon_2+i\Gamma_2}\right]^{-1}, \tag{4.5}$$

and likewise

$$G^0_{22;\sigma}(\omega) = \left[(z-\epsilon_2+i\Gamma_2) - \frac{t^2}{z-\epsilon_1+i\Gamma_1}\right]^{-1}. \tag{4.6}$$

The off-diagonal non-interacting Green's function, $G^0_{12;\sigma}(\omega)$, can also be calculated via Eqn. (4.3), giving

$$G^0_{12;\sigma}(\omega) = \frac{t}{(z-\epsilon_1+i\Gamma_1)(z-\epsilon_2+i\Gamma_2)-t^2}. \tag{4.7}$$

Having derived expressions for the non-interacting Green's functions, we can go on to find the full Green's functions, $G_{ij;\sigma}(\omega)$, in terms of the self-energies, $\Sigma_{ij;\sigma}(\omega)$ (or vice versa) using the Dyson equation (Eqn. (4.1)). This yields

$$G_{11;\sigma}(\omega) = \left[(z-\epsilon_1+i\Gamma_1-\Sigma_{11}(\omega)) - \frac{(t+\Sigma_{12}(\omega))^2}{z-\epsilon_2+i\Gamma_2-\Sigma_{22;\sigma}(\omega)}\right]^{-1}, \tag{4.8}$$

$$G_{22;\sigma}(\omega) = \left[(z-\epsilon_2+i\Gamma_2-\Sigma_{22}(\omega)) - \frac{(t+\Sigma_{12}(\omega))^2}{z-\epsilon_1+i\Gamma_1-\Sigma_{11;\sigma}}\right]^{-1}, \tag{4.9}$$

$$G_{12;\sigma}(\omega) = \frac{t+\Sigma_{12;\sigma}(\omega)}{(z-\epsilon_1+i\Gamma_1-\Sigma_{11;\sigma}(\omega))(z-\epsilon_2+i\Gamma_2-\Sigma_{22;\sigma}(\omega)) - (t+\Sigma_{12;\sigma}(\omega))^2}\ . \tag{4.10}$$

By comparison of Eqns. (4.8) – (4.10) and Eqns. (4.5) – (4.7), it is easy to see that the interacting Green's functions have precisely the same form as the non-interacting Green's functions, the only difference between the two being that $t \to t + \Sigma_{12;\sigma}(\omega)$ and $\epsilon_i \to \epsilon_i + \Sigma_{ii;\sigma}(\omega)$ when interactions are switched on. The bare parameters ϵ_i and t are said to be renormalised in the presence of interactions.

As discussed in section 3.7, the 2AIM is a Fermi liquid for all values of its

[2] In our NRG calculations we must, of course, use a finite bandwidth. We take the half-bandwidth to be $D = 100\Gamma_1$ throughout, this being large enough that the difference from the $D \to \infty$ limit is not significant.

parameters. A Fermi liquid is a system whose low-energy excitations are in one-to-one correspondence with those of its non-interacting counterpart, such that the low-energy properties of the system evolve continuously as the interactions are turned on [19, 20]. The general properties of such systems were studied by Luttinger and coworkers in the 1960s [148–151], and a number of important results were derived. A key result that we make use of is[3]

$$\Sigma^{I}_{ij;\sigma}(\omega) \overset{\omega \to 0}{\sim} \omega^2 \ , \tag{4.11}$$

with $\Sigma_{ij;\sigma}(\omega) = \Sigma^{R}_{ij;\sigma}(\omega) - i\ \Sigma^{I}_{ij;\sigma}(\omega)$, such that $-\Sigma^{I}_{ij;\sigma}(\omega)$ is the imaginary part of $\Sigma_{ij;\sigma}(\omega)$.[4] Combining the above result with Eqns. (4.8) – (4.10), it is straightforward to show that at ph symmetry, for which $\Sigma^{R}_{ii;\sigma}(0) = U/2$ and therefore $\epsilon^{*}_{i} = \epsilon_i + \Sigma_{ii;\sigma}(0) = 0\ \forall\ i$ [3, 94],

$$G^{I}_{12;\sigma}(0) = G^{R}_{11;\sigma}(0) = G^{R}_{22;\sigma}(0) = 0 \ , \tag{4.12}$$

with the Green's functions given by $G_{ij;\sigma}(\omega) = G^{R}_{ij;\sigma}(\omega) - iG^{I}_{ij;\sigma}(\omega)$.

Another important result which can be derived from Luttinger's results [148] is the so-called Friedel sum rule [3, 152]. This relates the number of electrons on the dot levels to parameters of the model in terms of the so-called phase shifts, and we now outline its derivation for the 2AIM. The total number of σ-spin electrons on the dot levels is given by [3, 120, 121]

$$\begin{aligned} \langle \hat{n}_{1\sigma} + \hat{n}_{2\sigma} \rangle &= -\frac{1}{\pi} \mathrm{Im} \sum_{\nu=1,2} \int_{-\infty}^{0} G_{\nu\nu;\sigma}(\omega) d\omega \ , \\ &= n_{\mathrm{imp};\sigma} \ . \end{aligned} \tag{4.13}$$

where the second equality follows in the wide, flat band limit, $D \to \infty$ [3, 97, 100], with $n_{\mathrm{imp};\sigma}$ the difference in the number of σ-spin electrons in the system with and without the impurities present. In one of his seminal papers [150], Luttinger proved that for a Fermi liquid,

$$I_{L,\sigma} = -\frac{1}{\pi} \mathrm{Im\ Tr} \int_{-\infty}^{0} d\omega \left[\left[\frac{\partial \mathbf{\Sigma}_{\sigma}(\omega)}{\partial \omega} \right] \mathbf{G}_{\sigma}(\omega) \right] = 0 \ , \tag{4.14}$$

where we refer to $I_{L,\sigma}$ as the Luttinger integral. Rearranging Eqns. (4.8) – (4.10) gives expressions for the self-energies in terms of the Green's functions. These expressions may then be differentiated and the results inserted into Eqn. (4.14). With

[3] Note that we set the zero-bias Fermi level of the leads to be the zero of energy throughout this thesis.

[4] This definition is conventional for retarded correlation functions [3].

some straightforward manipulation this yields

$$I_{L,\sigma} = -\frac{1}{\pi}\mathrm{Im}\int_{-\infty}^{0} d\omega \left[[G_{11;\sigma}(\omega) + G_{22;\sigma}(\omega)] - 2\mathrm{det}\ \mathbf{G}_\sigma(\omega) - \frac{1}{\mathrm{det}\ \mathbf{G}_\sigma}(\omega)\frac{\partial \mathrm{det}\mathbf{G}_\sigma(\omega)}{\partial\omega}\right] . \tag{4.15}$$

Noting that the first two terms in the integral (in small square brackets) give $n_{\mathrm{imp};\sigma}$, and using Eqn. (4.14) gives

$$n_{\mathrm{imp};\sigma} = \frac{1}{\pi}\mathrm{Im}\int_{-\infty}^{0} d\omega \frac{\partial\ (\ln \det\ \mathbf{G}_\sigma(\omega))}{\partial\omega} = \frac{1}{\pi}\delta_\sigma\ , \tag{4.16}$$

where the total phase shift for σ-spin electrons is given by

$$\begin{aligned} \delta_\sigma &= \mathrm{Im}\ \ln\ \det\ \mathbf{G}_\sigma(0) - \mathrm{Im}\ \ln\ \det\ \mathbf{G}_\sigma(-\infty) \\ &= \arg\ \det\ \mathbf{G}_\sigma(0) - \arg\ \det\ \mathbf{G}_\sigma(-\infty)\ . \end{aligned} \tag{4.17}$$

In the case of LR symmetry ($\epsilon_1 = \epsilon_2 = \epsilon$ and $V_1 = V_2 = V$, so that $\Gamma_1 = \Gamma_2 = \Gamma$) it is convenient to work in the parity basis discussed in section 2.6. From the definitions of the even and odd orbitals, Eqn. (2.23), and using the fact that $G_{12;\sigma}(\omega) = G_{21;\sigma}(\omega)$ (by time-reversal symmetry) and $G_{11;\sigma}(\omega) = G_{22;\sigma}(\omega)$ (by LR symmetry), it follows that

$$\begin{aligned} G_{eo;\sigma}(\omega) &= G_{oe;\sigma}(\omega) = G_{11;\sigma} - G_{22;\sigma} = 0\ , \\ G_{ee;\sigma}(\omega) &= G_{11;\sigma} + G_{12;\sigma} = \frac{1}{z - (\epsilon + t) + i\Gamma - \Sigma_{ee;\sigma}(\omega)}\ , \\ G_{oo;\sigma}(\omega) &= G_{11;\sigma} - G_{12;\sigma} = \frac{1}{z - (\epsilon - t) + i\Gamma - \Sigma_{oo;\sigma}(\omega)}\ , \end{aligned} \tag{4.18}$$

where $\Sigma_{\alpha\alpha;\sigma}(\omega) = \Sigma_{11;\sigma}(\omega) \pm \Sigma_{12;\sigma}(\omega)$, with $\alpha = e(o)$ corresponding to the $+(-)$ sign. The total phase shift can then be written

$$\begin{aligned} \delta_\sigma &= \arg\ G_{ee;\sigma}(0) + \arg\ G_{oo;\sigma}(0) + 2\pi \\ &= \delta_{e\sigma} + \delta_{o\sigma}\ , \end{aligned} \tag{4.19}$$

as $-\arg\ \det\ \mathbf{G}(-\infty) = -\arg\ G_{ee;\sigma}(-\infty) - \arg\ G_{oo;\sigma}(-\infty) = 2\pi$ (which can be shown from Eqn. (4.18)), and where we define the even and odd-channel phase shifts for σ-spin electrons as $\delta_{\alpha\sigma} = \pi + \arg\ G_{\alpha\alpha;\sigma}(0)$, such that $\delta_{\alpha\sigma} \in [0, \pi]$ and

$$n_{\mathrm{imp};\sigma} = \frac{1}{\pi}(\delta_{e\sigma} + \delta_{o\sigma})\ . \tag{4.20}$$

At ph symmetry $n_{\mathrm{imp};\sigma} = 1$ precisely, and therefore $\delta_{e\sigma} + \delta_{o\sigma} = \pi$.[5] Taking the

[5] Phase shifts are defined modulo π [25, 152] so one could also define the odd-channel phase shift $\delta_{o\sigma}$ to be between $-\pi$ and 0, as in Refs. [25, 96], for instance. If this is done, then at ph symmetry $\delta_{e\sigma} = -\delta_{o\sigma}$.

arguments of the even and odd Green's functions, Eqn. (4.18), at zero frequency, it is straightforward to show that for the LR-symmetric 2AIM

$$\delta_{\alpha\sigma} = \tan^{-1}\left[\frac{\Gamma}{\epsilon \pm t + \Sigma^R_{11;\sigma}(0) \pm \Sigma^R_{12;\sigma}(0)}\right] , \tag{4.21}$$

with the $+(-)$ sign for $\alpha = e(o)$, and $\tan^{-1} x$ taken to be between 0 and π.

With this expression for the phase shifts, one can also relate the zero-frequency value of the single-particle spectra to the phase shifts at LR symmetry, using Eqn. (4.21) and taking the imaginary parts of Eqns. (4.8) – (4.10). This yields

$$\begin{aligned} &\pi\Gamma D_{11;\sigma}(0) = \pi\Gamma D_{22;\sigma}(0) = \sin^2\delta_{e\sigma} , \\ &\pi\Gamma D_{12;\sigma}(0) = 0 . \end{aligned} \tag{4.22}$$

4.2 Particle-hole symmetry

We now begin our study of the 2AIM at ph symmetry. As discussed in section 2.6, with $\epsilon_1 = \epsilon_2 = -\frac{U}{2}$ the 2AIM is ph symmetric, and $n_{\mathrm{imp};\sigma} = \langle \hat{n}_{1\sigma}\rangle + \langle \hat{n}_{2\sigma}\rangle = 1$ by symmetry [94]. We initially consider the case of equal dot-lead couplings, $\Gamma_1 = \Gamma_2 = \Gamma$, and delay consideration of the effect of unequal dot-lead couplings until section 4.2.6. Hitherto, the 2AIM has been studied almost exclusively at ph symmetry [91–95], at the centre of the regime in which the system has two electrons on the dots. We begin with a general overview of the physics of the ph-symmetric 2AIM, and we recap some known results [91, 93–95].

As discussed in section 2.10, the ground state of the atomic-limit 2AIM at ph symmetry is a singlet state for all $t \neq 0$, and the lowest excited state is a degenerate spin-triplet. We label the splitting between the singlet and the triplet $\delta E = -\frac{U}{2} + \frac{U}{2}\sqrt{1+\frac{16t^2}{U^2}}$. For $\frac{t}{U} \ll 1$, $\delta E \simeq 4t^2/U$, equal to the effective antiferromagnetic exchange coupling (J) that arises between the impurities in the low-energy effective 2IKM (see section 2.7). The ground state is of dominant (1,1) character and is known as the local singlet (LS) state. For $\frac{t}{U} \gg 1$, $\delta E \simeq 2t - \frac{U}{2}$, and the singlet ground state has two electrons in the bonding MO, which has equal 1-orbital and 2-orbital character. This is known as the bonding singlet (BS) state [94]. The triplet excited states have one electron in the bonding orbital and one in the antibonding orbital. As $\frac{t}{U}$ is increased, the singlet ground state of the atomic-limit, ph-symmetric 2AIM evolves smoothly, gaining more (2,0)/(0,2) character. Likewise, the triplet excited states evolve smoothly, and there is no quantum phase transition (QPT) between the LS and BS regimes. This discussion is illustrated in Fig. 4.1, upper panel. We now wish to consider the full system, with the dots coupled to the leads.

We start by considering the full system with $\frac{t}{U} \ll 1$. In this case, we consider

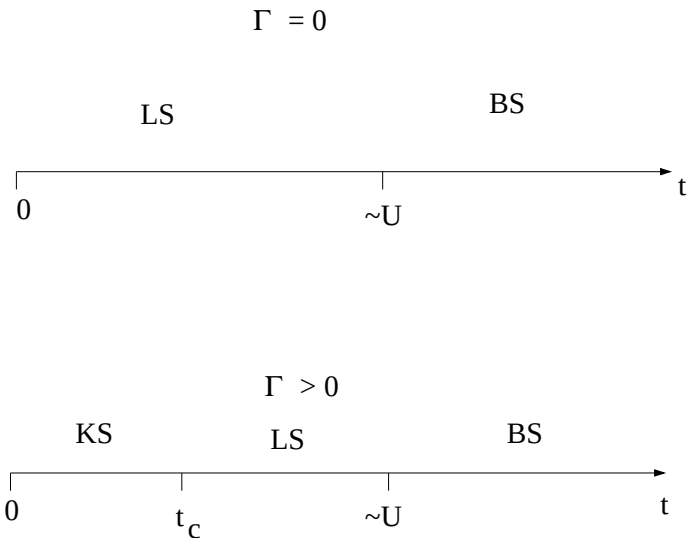


Figure 4.1: The ground state of the 2AIM at ph symmetry as a function of interdot coupling. In the atomic limit ($\Gamma = 0$, discussed in section 2.10) the ground state evolves continuously from the LS state to the BS state, the crossover between the two occurring for $t \sim U$. In the lead-coupled system ($\Gamma \neq 0$), the low-t ground state is the KS state, with a continuous crossover to the LS state when $t \simeq t_c$, with t_c the value of t for which $T_{\rm K} \sim J = \frac{4t^2}{U}$ [94] (or equivalently $\delta_{e\sigma} = \pi/4$, see section 4.2.1). As t is increased further there is a continuous crossover between LS and BS states, as in the atomic limit [94].

initially a second-order SW transformation of the 2AIM, yielding the 2IKM, with $J = \frac{4t^2}{U}$ (see section 2.8). The low-energy behaviour of the 2IKM is rather well understood [25, 44–49]. As there are only two low-energy scales present in the 2IKM ($T_{\rm K}$ and J), we expect two different regimes to arise for the 2AIM: $J \gg T_{\rm K}$ and $J \ll T_{\rm K}$[6]. If $J \gg T_{\rm K}$, *i.e.*, at relatively large t (but still with $\frac{t}{U} \ll 1$), then the two spins lock up into a LS state at low temperature, and no Kondo effects occur. If $J \ll T_{\rm K}$, *i.e.*, at small t, then each dot spin undergoes a Kondo effect with its lead at low temperature, giving a Kondo singlet (KS) ground state. As mentioned in section 2.8, the 2IKM has a QPT between the KS and LS phases. It is well-known, however, that the interlead charge transfer present in the 2AIM destroys this pristine QPT, and smears it out into a continuous crossover [25, 59, 91–93, 117, 119, 153][7].

For $\frac{t}{U} \gg 1$ by contrast, the SW transformation is not appropriate and the atomic-limit ground state is the BS state. Upon coupling to the leads, no Kondo effects occur as there are no degrees of freedom which can be quenched. As in the atomic limit, upon increasing t there is no QPT between the LS and the BS regimes [94]. The above discussion is illustrated in Fig. 4.1.

[6] We use $T_{\rm K}$ to denote the Kondo scale for each dot in the 2AIM when $t = 0$. If $\Gamma_1 \neq \Gamma_2$, then the $t = 0$ Kondo scales for the two dots are not equal, and we denote them $T_{\rm K}^{(1)}$ and $T_{\rm K}^{(2)}$.

[7] Note that when the interdot tunnel-coupling present in the 2AIM is replaced by an explicit interdot antiferromagnetic exchange coupling, there is no interlead charge transfer, and a QPT exists [154, 155].

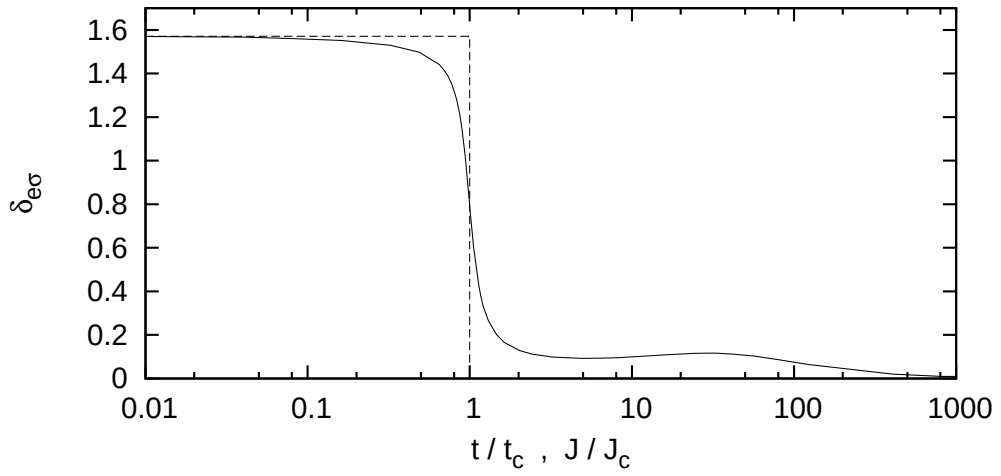


Figure 4.2: Even-channel phase shift, $\delta_{e\sigma}$, against interdot coupling; J/J_c for the 2IKM (dashed line) and t/t_c for the LR and ph-symmetric 2AIM (solid line), with J_c the critical value of J for the 2IKM, and t_c defined by $\delta_{e\sigma}(t = t_c) = \pi/4$. For the 2AIM, $\tilde{U} = U/\Gamma = 20$ and for the 2IKM $\rho J_1 = \rho J_2 = 0.093$, chosen so that $T_{\rm K}$ for the two systems are the same. For these parameters, $J_c \simeq 3.3 \times 10^{-5}\ D$, and $t_c \simeq 0.123\ \Gamma$. Our results for the 2AIM agree well with Ref. [94].

We therefore have a simple physical picture of the system for all values of $\frac{t}{U}$. This will prove invaluable in understanding the properties of the 2AIM at ph symmetry.

4.2.1 Phase shifts

We now look at the phase shifts of the LR and ph-symmetric 2AIM, previously calculated by Izumida et al. [94], as these are indicative of the KS-LS crossover in the model, and determine the conductance behaviour (see below). As discussed, the even and odd-channel phase shifts sum to π at ph symmetry (see section 4.1), so we need only consider the even-channel phase shift, $\delta_{e\sigma}$. We can calculate the phase shifts via the NRG by calculating the self-energies and then using Eqn. (4.21). However, we may also obtain the phase shifts from the NRG energy levels, without having to calculate any dynamical quantities, thereby saving a great deal of computer time[8]. To do so, we note that the Fermi liquid FP to which the 2AIM ultimately flows corresponds to a system of two free leads with potential scattering on their zero orbitals [94]. We therefore calculate the energy levels of such a system, tuning the magnitude of the potential scattering until the energy levels match up with those calculated via the NRG for the 2AIM. We can then calculate the phase shifts using

[8]Note that we effectively make comparison between the two methods of calculating the phase shifts when we compare different methods of calculating the zero-temperature, zero-bias conductance in Fig. 4.9.

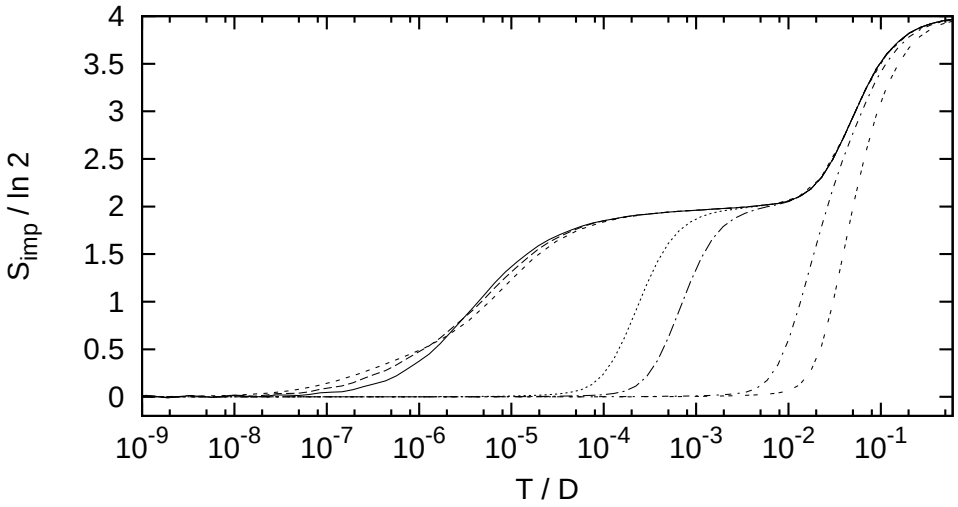


Figure 4.3: Impurity contribution to the entropy, $S_{\rm imp}$, against temperature for the LR and ph-symmetric 2AIM with $\tilde{U} = U/\Gamma = 20$ and $\tilde{t} = t/\Gamma = 0$ (solid line), 0.1 (long-dashed line), 0.123 (short-dashed line), 0.6 (dotted line), 1 (dot-long-dashed line), 5 (dot-short-dashed line), 10 (double short-dashed line).

[12]

$$\delta_{e\sigma} = \tan^{-1}\left(\frac{\pi\bar{K}}{2}\right) \ , \tag{4.23}$$

where $\bar{K} = \frac{K}{D}$ is the magnitude of the potential scattering in units of the half-bandwidth.

As discussed in section 2.8, for the 2IKM $\delta_{e\sigma} = 0$ in the LS phase ($J > J_c$) and $\frac{\pi}{2}$ in the KS phase ($J < J_c$), changing discontinuously between the two as J is increased and the QPT is crossed [44–47]. This is illustrated in Fig. 4.2. For the 2IKM then, there are two stable strong coupling (SC) FPs: the LS FP, which corresponds to two free leads with zero potential scattering, and the KS FP, corresponding to two free leads with infinite potential scattering on their zero orbitals.

For the 2AIM, in which, as discussed, interlead charge-transfer processes (given by Eqn. (2.28)) destroy the pristine QPT, the even-channel phase shift goes continuously from $\frac{\pi}{2}$ in the limit of $t \to 0$, to zero in the limit $t \to \infty$, as shown in Fig. 4.2. We label by t_c the value of t for which $\delta_{e\sigma} = \frac{\pi}{4}$. Unlike for the 2IKM however, there is a continuous *line* of stable SC FPs connecting the KS and LS FPs, with the potential scattering increasing continuously along the line as one goes from LS to KS FPs [94].

4.2.2 Thermodynamics

We now go on to look at the thermodynamics of the system, beginning with the dot contribution to the entropy of the system, $S_{\rm imp}$, as calculated via the NRG and

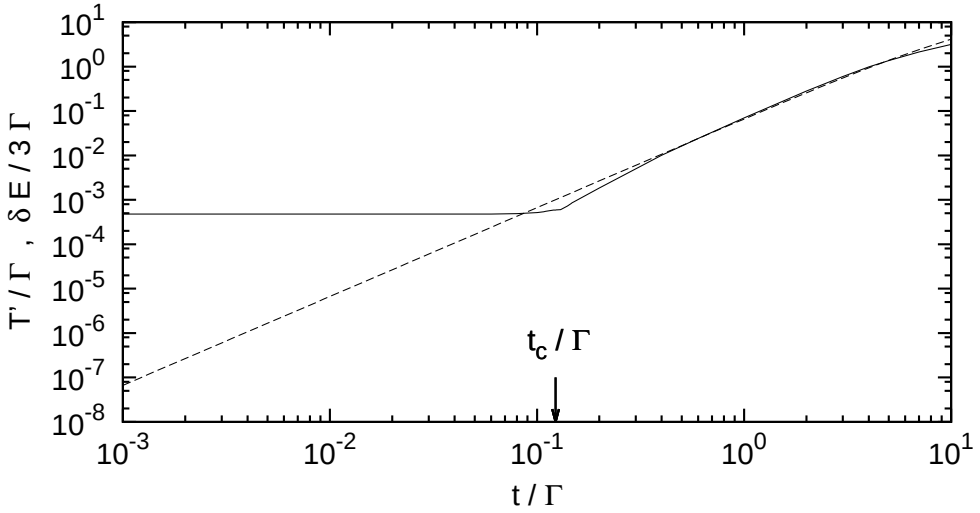


Figure 4.4: T' (solid line), defined as the scale on which the entropy goes to zero (specifically $S_{\rm imp}(T') = \ln 2$) against t for the LR and ph-symmetric 2AIM with $\tilde{U} = 20$. $T_{\rm K} \simeq 5 \times 10^{-4}\ \Gamma$ in this case, with $T_{\rm K}$ defined via $S_{\rm imp}(T_{\rm K}) = \ln 2$ for the $t = 0$ system. Also plotted is $c\delta E/\Gamma$ with $c \simeq 3$ (dashed line, δE being the atomic-limit splitting between the singlet ground state and the first triplet excited state), which agrees closely with T' for $t \gg t_c \simeq 0.123\ \Gamma$ in this case. For $t \ll t_c$, $T' \simeq T_{\rm K}$.

shown in Fig. 4.3.[9] In the high-temperature limit, $S_{\rm imp} = \ln 16 = 4 \ln 2$ for the 2AIM regardless of the parameters, as all 16 atomic-limit dot states are thermally accessible. In this case the system is near the free orbital (FO) FP, corresponding to a system of two free leads with zero potential scattering, and two decoupled orbitals. All states of the decoupled orbitals are therefore equally probable, and the entropy associated with this FP is therefore $\ln 16$. All the 2AIM systems are near this FP at sufficiently high temperature, but it is unstable, and the systems flow away from it on the scale of $\sim \max(t, U)$, below which scale the doubly-occupied and unoccupied isolated dot states become thermally inaccessible. For $\frac{t}{U} \gg 1$ the entropy drops to zero at this point as only the BS ground state is accessible, and the system flows directly from the FO FP to a SC FP. For $\frac{t}{U} \ll 1$ the entropy drops to $\ln 4$ at this point, as only the four (1,1) states remain accessible, and the system flows near to the local moment (LM) FP at intermediate temperatures. This corresponds to a system of two free leads with zero potential scattering, and two decoupled spin-$\frac{1}{2}$'s. The LM FP is unstable, and the system flows from here on to a stable SC FP.

In all cases the entropy goes to zero in the low-temperature limit. Fig. 4.4 shows the scale on which the entropy goes to zero as a function of $\tilde{t} = t/\Gamma$. For $\frac{t}{U} \ll 1$, we consider the low-energy effective 2IKM, for which the low-temperature ($T \ll U$)

[9] We will generally refer to this simply as the entropy, but it must be remembered that we are really talking about the difference between the entropy of the system with and without the impurities present, as discussed in section 3.3. Recall that we take $k_B = 1$ throughout this work.

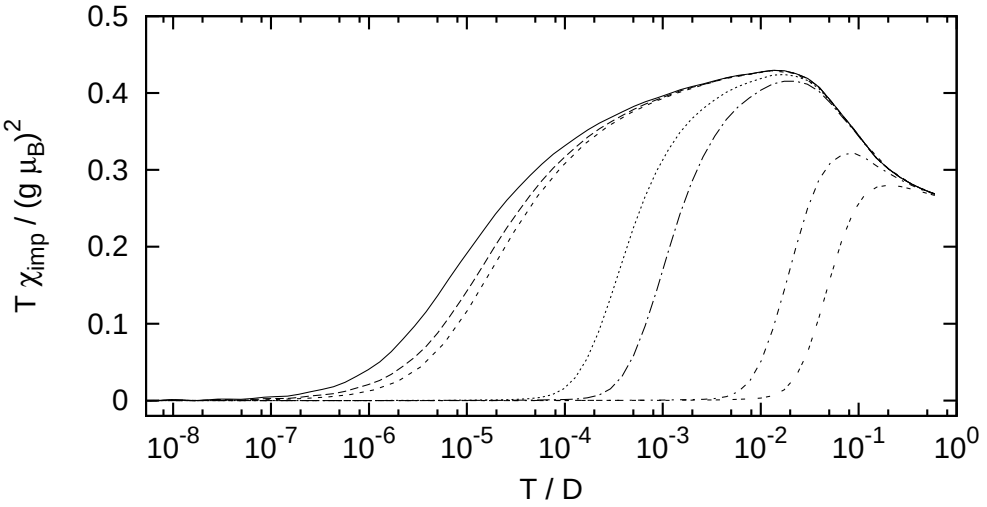


Figure 4.5: Impurity contribution to the magnetic susceptibility, $\chi_{\rm imp}$, as a function of temperature for the LR and ph-symmetric 2AIM with $\tilde{U} = U/\Gamma = 20$ and $\tilde{t} = t/\Gamma = 0$ (solid line), 0.1 (long-dashed line), 0.123 (short-dashed line), 0.6 (dotted line), 1 (dot-long-dashed line), 5 (dot-short-dashed line), 10 (double-short-dashed line). $t_c \simeq 0.123\ \Gamma$ and as $\tilde{t}$ increases, the temperature at which $\chi_{\rm imp}$ goes to zero increases.

entropy behaviour is dependent on the comparative values of J and $T_{\rm K}$. Deep in the KS regime ($J/T_{\rm K} \ll 1$, or equivalently $t \ll t_c$), the entropy goes to zero on the scale of $T_{\rm K}$, as this is the scale on which the dot degrees of freedom are Kondo quenched by the leads. On the other hand, deep in the LS regime ($J/T_{\rm K} \gg 1$, $t \gg t_c$) the entropy goes to zero on the scale of $J = \frac{4t^2}{U} \simeq \delta E$, as below this energy, only the LS state is thermally accessible. For very large values of t, $\frac{t}{U} \gtrsim 1$, no Kondo physics occurs and the entropy goes to zero on the scale of δE, the atomic-limit splitting between singlet ground state and the first triplet excited states. This behaviour is seen clearly in Fig. 4.4 which shows the scale on which the entropy goes to zero, T', against $\tilde{t}$ for the ph-symmetric 2AIM. T' is seen to be $\sim \mathcal{O}(\delta E)$ for $t \gg t_c$, whereas for $t \ll t_c$, $T' \sim T_{\rm K}$.

We can also observe the fixed points of the model in the magnetic susceptibility (defined in Eqn. (3.22)), plotted against temperature in Fig. 4.5. In the limit of high temperature, $T\chi_{\rm imp}/(g\mu_B)^2 \simeq 0.25$, regardless of the value of t, as expected for the FO FP, which corresponds to a pair of free orbitals, decoupled from the leads [11]. In the limit of low temperature, $T\chi_{\rm imp}/(g\mu_B)^2 = 0$ regardless of t, indicative of the SC FP. For sufficiently low values of t, the susceptibility goes up to $T\chi_{\rm imp}/(g\mu_B)^2 \lesssim 0.5$ at intermediate temperatures, the value expected for a pair of free spin-$\frac{1}{2}$'s. The increase in $T\chi_{\rm imp}/(g\mu_B)^2$ as temperature is decreased from the high-temperature limit is then indicative of flow to the LM FP. $T\chi_{\rm imp}/(g\mu_B)^2$ does not reach 0.5 for any value of t, as the system never flows all the way to the LM FP, it being unstable;

the system may however flow *near* to it for some range of temperatures. For high values of $\frac{t}{U}$, the system flows directly from the FO FP to the SC FP, with no flow near to the LM FP. We note also that the scale on which $T\chi_{\rm imp}/(g\mu_B)^2$ vanishes is essentially the same as that on which the entropy vanishes (to within a constant of order unity); this being unsurprising since the vanishing of both the entropy and $T\chi_{\rm imp}/(g\mu_B)^2$ occurs when the system flows to the SC FP[10].

4.2.3 Spectra

We now move on to look at the dynamics of the 2AIM at ph symmetry, beginning with the single-particle spectrum, $D_{11;\sigma}(\omega) = -\frac{1}{\pi}\mathrm{Im}\, G_{11;\sigma}(\omega)$, at zero temperature. Spectra for the system are shown in Fig. 4.6, concentrating on the case of $\frac{t}{U} \ll 1$. Note that we are considering the LR-symmetric case at zero field, so that $D_{\nu\nu;\sigma}(\omega)$ is independent of dot index $\nu = \{1, 2\}$ or the spin-index σ – we therefore show only $D_{11;\sigma}(\omega)$. Also, due to the ph symmetry of the system, $D_{11;\sigma}(\omega) = D_{11;\sigma}(-\omega)$, so we only show results for $\omega > 0$.

At high frequency all the spectra have peaks at $\omega \simeq \pm\frac{U}{2}$. These are Hubbard satellite peaks, and correspond to simple one-electron processes in which an electron is added to or removed from the dots – the energy required to carry out such processes being $\simeq U/2$. These peaks have a width $\sim \mathcal{O}(\Gamma)$, due to the lifetime broadening of the dot levels caused by coupling the dots to the leads [3].

The low-frequency part of the spectrum is more interesting. For $t = 0$, the 2AIM consists of two entirely separate 1AIMs. The spectrum is therefore the same as that for the 1AIM, showing a low-frequency peak of width $\sim T_{\rm K}$ going up to a maximum value of $\pi\Gamma D_{11;\sigma}(\omega) = 1$ as $\omega \to 0$ [3]. This is the Kondo resonance and represents the low-energy spin-flip excitations that occur in the Kondo effect. Furthermore, $\pi\Gamma D_{11;\sigma}(\omega) \sim 1 - \omega^2$ as $\omega \to 0$, characteristic of Fermi liquid behaviour [3]. As $\tilde{t}$ is increased from zero, the zero-frequency value of the spectrum decreases, until for $t = t_c \simeq 0.123\Gamma$, $\pi\Gamma D_{11;\sigma}(0) = 0.5$ (discussed further later). As $\tilde{t}$ is increased further the Kondo resonance splits, giving rise to two maxima, one at positive frequency and one at negative frequency. These maxima correspond to excitations connecting the singlet ground state to the triplet excited states, and therefore occur at $\omega \simeq \pm\delta E$.

One can approximately estimate the condition for the existence of the Kondo peak splitting by consideration of a low-frequency expansion of the spectrum [3]. Taking the imaginary part of Eqn. (4.8) gives an expression for the spectrum in terms of the self-energies. As the 2AIM is a Fermi liquid, the self-energy can be

[10]There is one further fixed point which we have not yet discussed; the (critical) two-channel Kondo (2CK) FP [59, 119, 153], near which the ph-symmetric 2AIM can flow, provided $\tilde{U}$ is sufficiently large. We discuss the circumstances in which this FP can be observed in chapter 5.

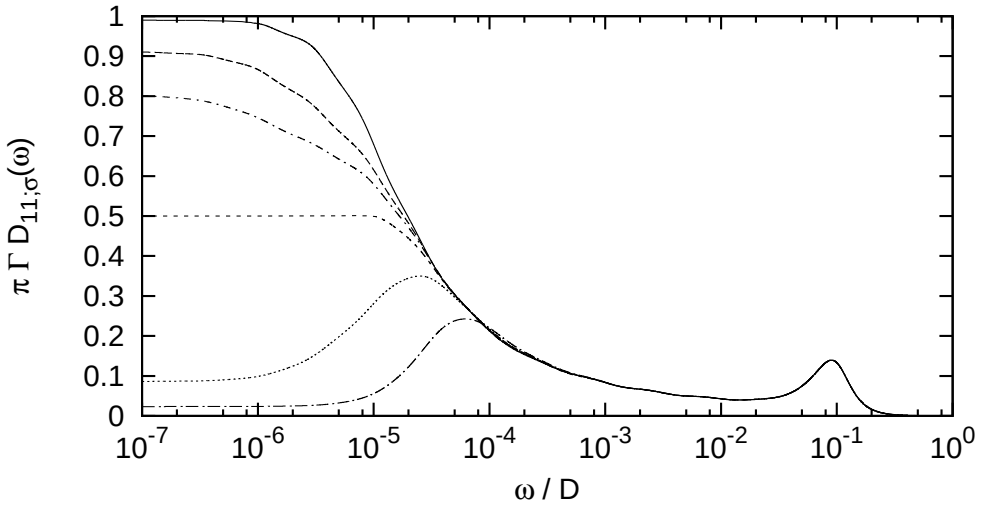


Figure 4.6: Zero-temperature single-particle spectra for the LR and ph-symmetric 2AIM with $\tilde{t} = t/\Gamma = 0$ (solid line), 0.1 (long-dashed line), 0.11 (dot-short-dashed line), 0.123 (short-dashed line), 0.15 (dotted line), 0.2 (dot-long-dashed line), and $\tilde{U} = U/\Gamma = 20$. In this case $t_c \simeq 0.123\ \Gamma$. The zero-frequency value of the spectrum decreases as $\tilde{t}$ increases.

expanded as a Taylor series in frequency as follows:

$$\Sigma_{ij;\sigma}(\omega) \simeq \Sigma^R_{ij;\sigma}(0) + \omega \left[\Sigma^R_{ij;\sigma}\right]'(0) \ , \tag{4.24}$$

where we have ignored the imaginary part of the self-energy (which goes as $\sim \omega^2$ as $\omega \to 0$, see Eqn. (4.11)), and we have taken the real part of the self-energy to first order. In the above equation, $\left[\Sigma^R_{ij;\sigma}\right]'(0) = \left[\frac{\partial \Sigma^R_{ij;\sigma}(\omega)}{\partial \omega}\right]_{\omega=0}$. Using this result, and with some straightforward manipulation we obtain

$$\pi\Gamma D_{11;\sigma}(\omega) \overset{\omega\to 0}{\sim} \tfrac{1}{2}\left[\frac{1}{(\omega' - t')^2 + 1} + \frac{1}{(\omega' + t')^2 + 1}\right] \ , \tag{4.25}$$

with

$$t' = \frac{t + \Sigma_{12;\sigma}(0)}{\sqrt{\Gamma_1\Gamma_2}} = \frac{t^*}{\sqrt{\Gamma_1\Gamma_2}} \ , \tag{4.26}$$

and $\omega' = \omega/(Z\Gamma)$, with $Z = \left[1 - [\Sigma^R_{11;\sigma}]'(0)\right]^{-1}$ the so-called quasiparticle weight. From this expression it is simple to show that $\omega = 0$ is a maximum in $\pi\Gamma D_{11;\sigma}(\omega)$ for $t' < \frac{1}{\sqrt{3}}$ and a minimum for $t' > \frac{1}{\sqrt{3}}$.

From Eqn. (4.21) one can show that at ph symmetry, $t' = 1$ gives $\delta_{e\sigma} = \frac{\pi}{4}$, as the renormalised dot level energy ($\epsilon^* = \epsilon + \Sigma_{11;\sigma}(0)$) is zero at ph symmetry. The conditions $t' = 1$ and $\delta_{e\sigma} = \frac{\pi}{4}$ are therefore equivalent for the LR and ph-symmetric 2AIM. Furthermore, as t_c is defined by $\delta_{e\sigma}(t = t_c) = \frac{\pi}{4}$, $t = t_c$ is also equivalent to $t' = 1$. As the Kondo resonance in the spectrum is expected to split for $t' < 1$,

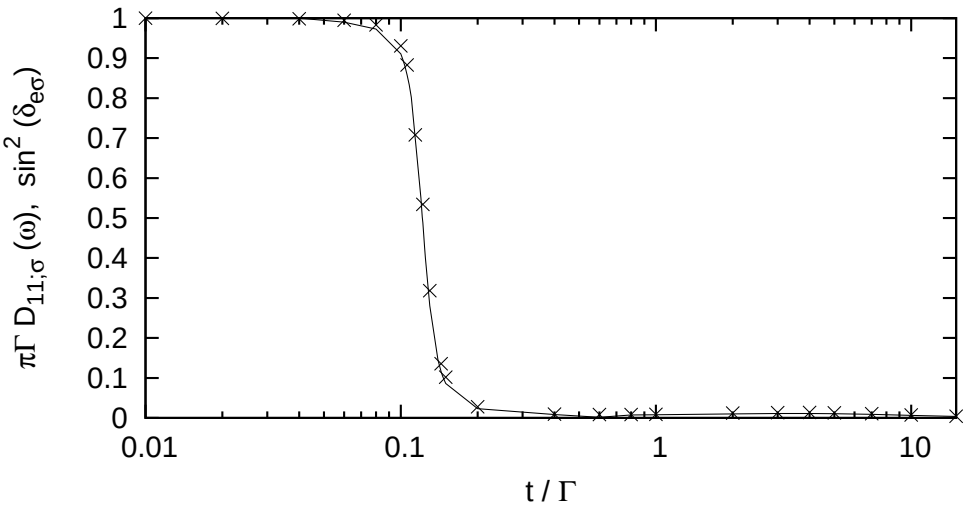


Figure 4.7: Zero-frequency value of the single-particle spectra ($\pi\Gamma D_{11;\sigma}(0)$, solid line) for the LR and ph-symmetric 2AIM with $\tilde{U} = U/\Gamma = 20$, and $T = 0$. $t_c \simeq 0.123\ \Gamma$. Also shown is $\sin^2(\delta_{e\sigma})$ (crosses). Agreement between the two is seen to be good.

the splitting is therefore expected to occur at some value of $t < t_c$. This is not apparent in the NRG results shown in Fig. 4.6, for which the splitting is only visible for $t \gtrsim t_c$. This is not entirely surprising, as it known to be extremely difficult to capture small splittings in spectral functions with the NRG, in part due to the splittings being washed out by the broadening procedure inherent in the NRG [129]. We have tried reducing the broadening parameter used (see section 3.6.2) is order to more accurately capture the splitting, but logarithmic oscillations arise in the data obscuring the splitting.

The zero-frequency value of the spectrum can be related to the even-channel phase shift, as given by Eqn. (4.22)[11]. This result is confirmed in Fig. 4.7. For $t = 0$, the even-channel phase shift is $\frac{\pi}{2}$, and $\pi\Gamma D_{11;\sigma}(0) = 1$; in the limit of $t \to \infty$, the even-channel phase shift goes to zero, as does $\pi\Gamma D_{11;\sigma}(0)$. At the middle of the crossover between the KS and LS regimes, $t = t_c$, the even-channel phase shift is $\frac{\pi}{4}$ and $\pi\Gamma D_{11;\sigma}(0) = 0.5$. As the phase shifts are calculated without recourse to the FDM method of calculating the spectral functions, the excellent agreement in Fig. 4.7 shows that the FDM method is capable of accurately capturing the zero-frequency behaviour of the system.

4.2.4 Conductance

The zero-bias conductance at zero temperature, $G_c(0,0)$, can be calculated exactly using the scattering approach [95], Eqn. (3.54), via the off-diagonal Green's function,

[11] It may also be expressed in terms of t' as $\pi\Gamma D_{11;\sigma}(0) = \frac{1}{1+t'^2}$.

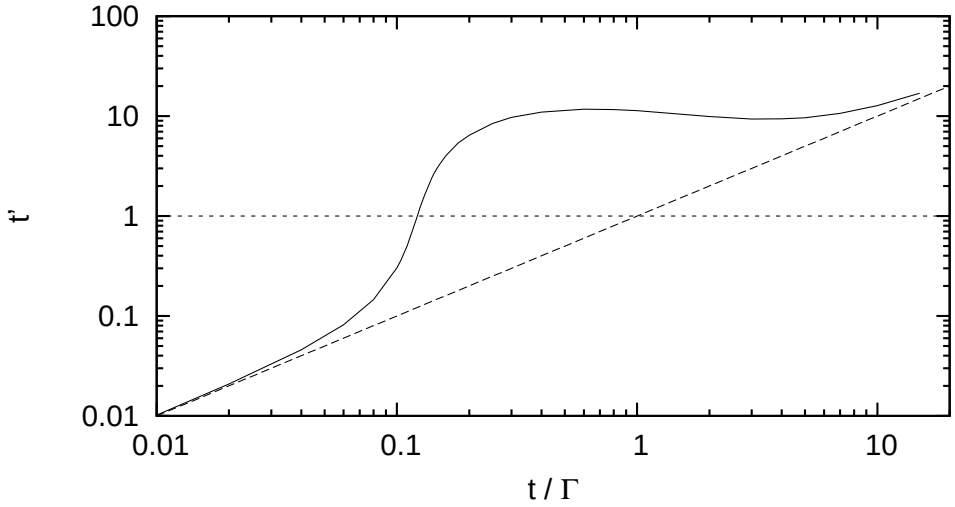


Figure 4.8: $t' = t^*/\sqrt{\Gamma_1\Gamma_2} = [t + \Sigma_{12;\sigma}(0)]/\sqrt{\Gamma_1\Gamma_2}$ for the LR ($\Gamma_1 = \Gamma_2 = \Gamma$) and ph-symmetric 2AIM as a function of $\tilde{t} = t/\Gamma$ with $\tilde{U} = 20$ (solid line). Also shown are the lines $t' = \tilde{t}$ (long-dashed line) and $t' = 1$ (short-dashed line). $G_c(0,0) = 2e^2/h$ arises for $t' = 1$, and $t = t_c \simeq 0.123\ \Gamma$.

$G_{12;\sigma}(\omega)$. As $G^I_{12;\sigma}(0) = 0$ at ph symmetry (see section 4.1), $G_c(0,0)$ is controlled entirely by $G^R_{12}(0)$. Furthermore, at ph symmetry Eqn. (4.10) becomes

$$G_{12;\sigma}(0) = \frac{t^*}{(t^*)^2 - \Gamma_1\Gamma_2}\ , \tag{4.27}$$

and using Eqn. (3.54) one can show that at ph symmetry $G_c(0,0)$ can be written purely as a function of t' [94][12]

$$G_c(0,0) = \frac{8e^2}{h}\frac{t'^2}{(t'^2+1)^2}\ . \tag{4.28}$$

$G_c(0,0)$ is thus maximal, and equal to the unitary limit of $G_c(0,0) = 2e^2/h$, when $t' = 1$, or equivalently when $\delta_{e\sigma} = \frac{\pi}{4}$, $t = t_c$ (recall that these conditions are all equivalent). From Eqn. (4.28), in the limit $t' \gg 1$, $G_c(0,0) \sim 1/t'^2$, whereas for $t' \ll 1$, $G_c(0,0) \sim t'^2$. t' can be calculated from the NRG and is shown in Fig. 4.8 as a function of $\tilde{t} = t/\Gamma$ (as previously calculated in Ref. [94]). The off-diagonal self energy, $\Sigma_{12;\sigma}(0)$ goes to zero in the limits $t \to 0, \infty$, such that $t' \simeq \tilde{t}$ in these limits.

$G_c(0,0)$ may then be calculated via the even-channel phase shift (Eqn. (3.56)), the off-diagonal Green's function (Eqn. (3.54), or equivalently via t', Eqn. (4.28)), or via the linear-response approach (Eqns. (3.59) – (3.63)). In Fig. 4.9 we show

[12]We note that Eqn. (4.28) reduces to Eqn. (2.36) in the non-interacting limit. We note also that the result derived via slave-boson mean field theory in Ref. [95] for $G_c(0,0)$ in the interacting case, is in fact only correct in the non-interacting limit.

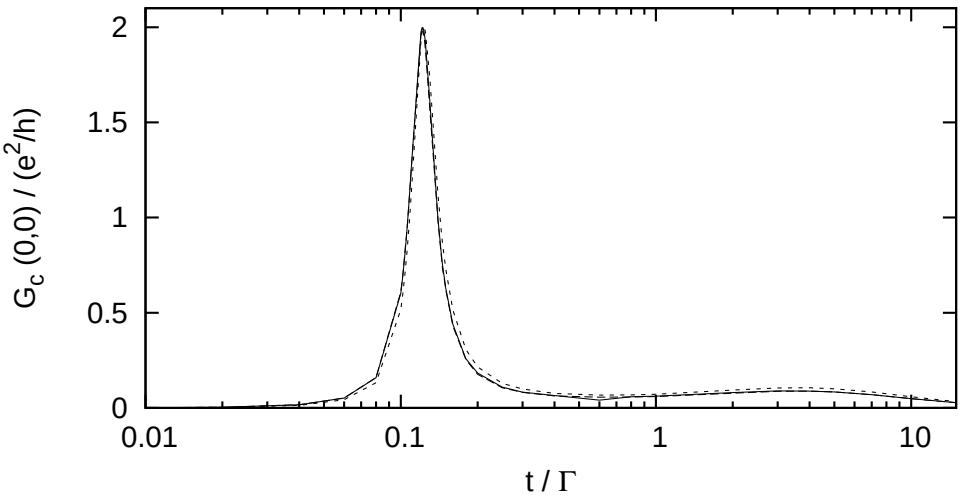


Figure 4.9: Zero-bias, zero-temperature conductance ($G_c(0,0)$) in units of e^2/h as a function of $\tilde{t} = t/\Gamma$ for the ph and LR-symmetric 2AIM with $\tilde{U} = 20$, calculated from the even-channel phase shift (Eqn. (3.56), solid line), from the Green's functions (Eqn. (3.54), dotted line), and from the linear-response formula (Eqns. (3.59) – (3.63), dashed line). We find excellent agreement between the three methods. Unitary $G_c(0,0) = 2e^2/h$ arises for $t = t_c \simeq 0.123\ \Gamma$.

$G_c(0,0)$ as a function of the interdot coupling (as previously calculated in Ref. [94]), calculated by these three methods. It is immediately obvious that these approaches agree very well.

The main feature in Fig. 4.9 is the large peak (going up to the unitary limit, $G_c = 2e^2/h$) which occurs at $t = t_c \simeq 0.123\Gamma$ (for which $\delta_{e\sigma} = \frac{\pi}{4}$, $t' = 1$ and $J = \frac{4t^2}{U} \sim T_{\rm K}$). By plotting $G_c(0,0)$ against $J = \frac{4t^2}{U}$ (this is shown in chapter 5, Fig. 5.8), we find that for the value of $\tilde{U} = 20$ considered here, the width of the peak is $\delta J \sim \mathcal{O}(T_{\rm K})$, this being the only low-energy scale in the problem[13] [96]. It is well-known, for instance from Poor Man's Scaling (see section 2.4), that $T_{\rm K}$ decreases exponentially as $\tilde{U}$ is increased [3, 17]. As the unitary conductance peak occurs for $J = \frac{4t^2}{U} \sim T_{\rm K}$, it moves to lower $\tilde{t}$ as $\tilde{U}$ is increased and t_c decreases [94]. The width of the peak also decreases as $\tilde{U}$ is increased and $T_{\rm K}$ decreases [94].

Either side of the unitary conductance peak, $G_c(0,0)$ is low. For $t \gg t_c$, the singlet that forms at low temperatures is effectively decoupled from the leads, so that, whilst electron tunneling between the dots is strong, tunneling between the dots and the leads is weak. As electrons are required to hop both between the dots and the leads, *and* between the two dots themselves in order for current to flow, the zero-bias conductance is low. For $t \ll t_c$, the two Kondo singlets that form are effectively decoupled, so the converse is true: electron tunneling between dots

[13] For very high values of $\tilde{U}$ ($\gtrsim 40$) this is not the case. We discuss this in the context of 2CK physics in chapter 5.

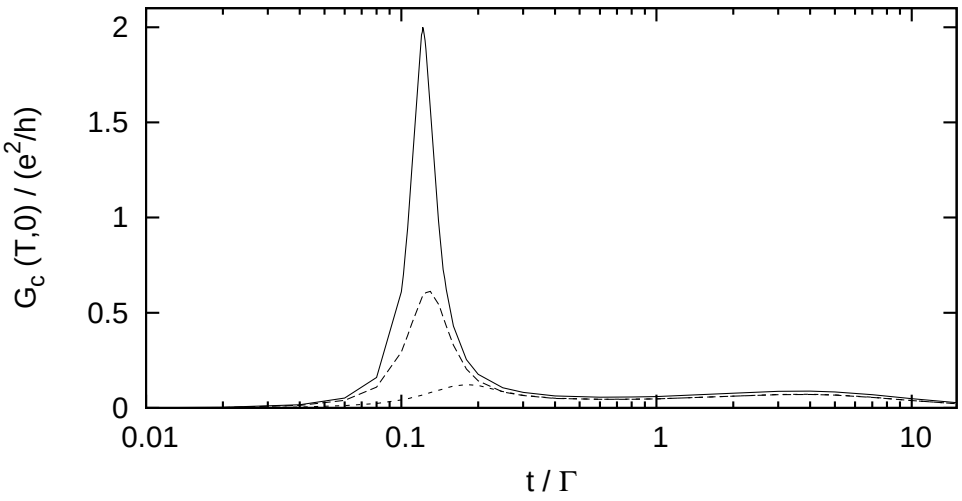


Figure 4.10: Zero-bias, finite-temperature conductance ($G_c(T,0)$) of the LR and ph-symmetric 2AIM as a function of $\tilde{t}$, calculated via the linear-response approach for $\tilde{T} = T/\Gamma = 0$ (solid line), 0.0001 (long-dashed line), 0.001 (short-dashed line) and $\tilde{U} = U/\Gamma = 20$. $T_{\rm K} \simeq 5 \times 10^{-4}\ \Gamma$ for these parameters.

and leads is strong, due to the Kondo effect, but tunneling between the two dots is weak. This again results in low zero-bias conductance. The unitary conductance peak in Fig. 4.9 can then be understood physically, as being the result of an optimal balance between the Kondo effect, which allows facile electron transfer between dots and leads, and the pairing up of the dot spins into a local singlet, which allows facile electron transfer between the dots. Another way of understanding the existence of this unitary conductance peak is to note that as t is increased, the system crosses over continuously from the KS regime, with $\delta_{e\sigma} \simeq \frac{\pi}{2}$, to the LS regime with $\delta_{e\sigma} \simeq 0$. The even-channel phase shift therefore passes through $\frac{\pi}{4}$ at the crossover, which gives rise to unitary conductance, as can be seen from Eqn. (3.56).

A second, smaller peak in the zero-bias conductance occurs for $t \simeq U/4$ [94], see Fig. 4.9 (the peak occurs at $\tilde{t} \simeq 5$). This peak in the conductance corresponds to the small maximum in $\delta_{e\sigma}$ seen in Fig. 4.2, and occurs when the mixing of the (2,0) and (0,2) states into the atomic-limit ground state becomes significant. It is therefore indicative of the crossover between LS and BS regimes [94].

At finite temperature, the zero-bias conductance can be calculated using the exact linear-response approach described in section 3.7.3. Results are shown in Fig. 4.10, and we note that similar calculations were carried out in Ref. [94]. Increasing temperature destroys the unitary conductance peak when $T \sim \mathcal{O}(T_{\rm K})$. For $t \leq t_c$ increasing temperature decreases $G_c(T,0)$ monotonically, as the Kondo effects occurring at zero temperature are destroyed on the scale of $T \sim T_{\rm K}$. For $t > t_c$, increasing the temperature from zero increases $G_c(T,0)$, with a maximum at $T \sim \delta E$,

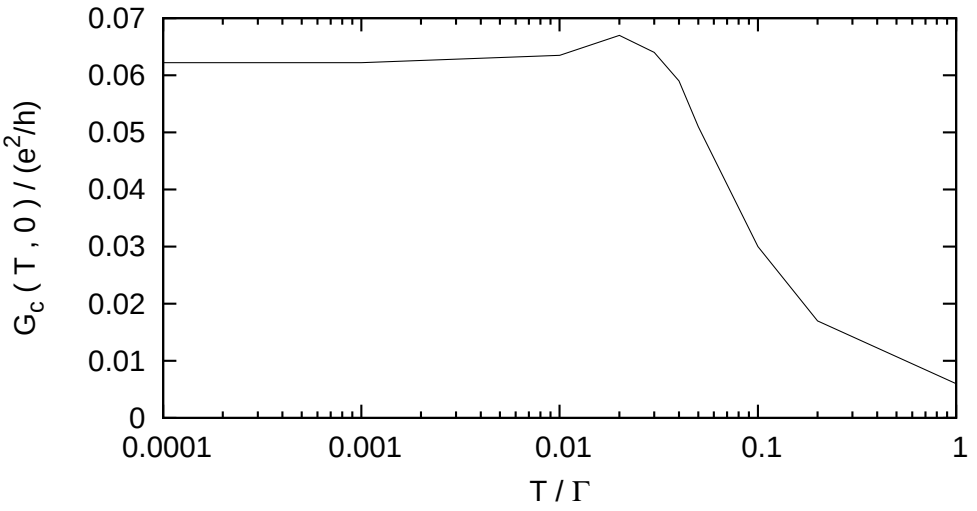


Figure 4.11: Zero-bias conductance, $G_c(T,0)$, as a function of temperature for $\tilde{t} = t/\Gamma = 0.6 > \tilde{t}_c$ and all other parameters the same as Fig. 4.10. There is a (slight) maximum at $T \sim \delta E \simeq 4t^2/U \simeq 0.07\ \Gamma$.

as shown in Fig. 4.11. As the temperature is increased further, $G_c(T,0)$ dies away. The increase in $G_c(T,0)$ can be understood physically as being caused by excitations between the atomic-limit singlet ground state and the triplet excited states, which become thermally accessible when the temperature becomes comparable to the splitting between these states, δE.

4.2.5 Effect of interdot repulsion

We now briefly consider the effect of introducing an interdot repulsion term, parameterised by U' (see Eqn. (2.21)), to the LR and ph-symmetric 2AIM (we note that previous work on this system was carried out in Ref. [156])[14]. Physically one would expect such a repulsion to be weaker than the onsite repulsion ($U' \ll U$) in an experimental TCDQD system. To maintain ph symmetry, we take $\epsilon_1 = \epsilon_2 = -U/2 - U'$.

We may investigate the effect of an interdot repulsion by carrying out a second-order SW transformation of the LR and ph-symmetric 2AIM with an interdot repulsion term, in the same way as described for the standard ($U' = 0$) 2AIM in section 2.7. Considering $U' \ll U$, one can derive a low-energy effective model which has the form of the 2IKM; the only difference from the $U' = 0$ case is that the interdot

[14]We also note that work has been carried out on introducing an interdot repulsion to a related model, in which the two dots are coupling by an antiferromagnetic exchange coupling, rather than a tunnel-coupling [154, 155]. The behaviour of this model is somewhat different to that of the 2AIM: as there is no interlead charge transfer, a QPT arises. Also, as the interdot antiferromagnetic exchange coupling is a bare parameter of the model, varying U' has no effect upon it.

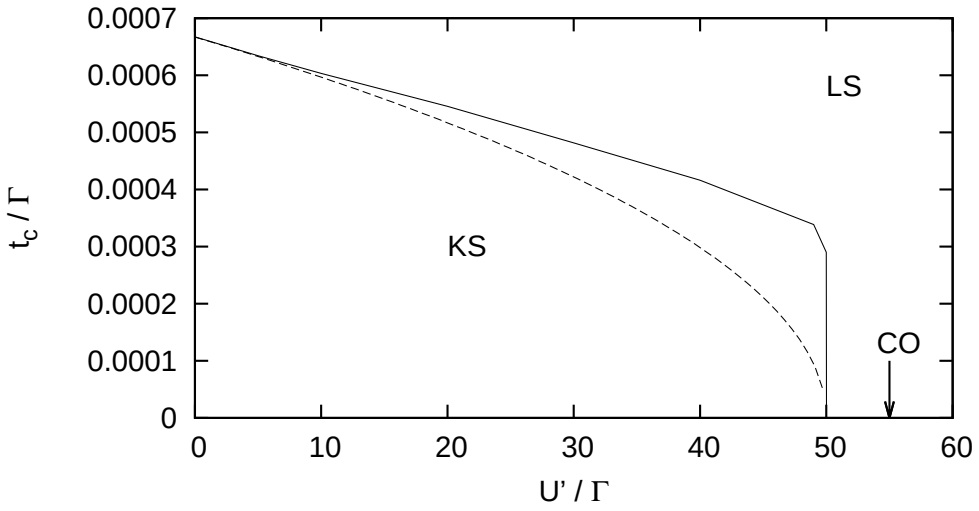


Figure 4.12: t_c (solid line), defined by $\delta_{e\sigma}(t = t_c) = \frac{\pi}{4}$, against U'/Γ for the LR and ph-symmetric 2AIM with $\tilde{U} = U/\Gamma = 50$. Increasing U' causes t_c to decrease, as discussed in the text. Also, plotted (dashed line) is Eqn. (4.30), taking $\alpha \simeq 8$ and defining $T_{\rm K}$ via the condition $S_{\rm imp}(T = T_{\rm K}) = \ln 2$ for the $t = 0$, $U' = 0$ system. The CO phase exists only for $t = 0$, $U' \gtrsim U$.

antiferromagnetic exchange coupling, J, is dependent on U', with

$$J \simeq \frac{4t^2}{U - U'} \ . \tag{4.29}$$

The dot-lead couplings, J_1, J_2, by contrast, can be shown to be independent of U'. This means that for a given t, increasing U' will increase the J arising in the effective low-energy model. Therefore the t required to fulfill the condition $J = J_c \sim T_{\rm K}$, namely t_c, will decrease as U' increases. From the above equation, and using the fact that for the 2IKM $J_c = \alpha T_{\rm K}$ with α a constant of order unity [45, 46, 48], one obtains

$$t_c \simeq \sqrt{\frac{\alpha T_{\rm K}(U - U')}{4}} \ . \tag{4.30}$$

NRG results for t_c (with t_c defined by $\delta_{e\sigma}(t = t_c) = \frac{\pi}{4}$) against U' are given in Fig. 4.12, and compared with Eqn. (4.30). We see that the agreement is good for $U' \ll U$, confirming the basic picture given by the SW transformation. For $t = 0$, the model becomes the capacitively-coupled DQD model, which for $U' \simeq U$ exhibits a QPT between KS and charge-ordered (CO) phases [125–127, 156]. The system is a non-Fermi liquid in the CO phase at low energies, and has a residual entropy of $\ln 2$. For $U' \ll U$, increasing t from zero causes the KS ground state to evolve continuously, crossing over to the LS ground state when $t \simeq t_c$. This is illustrated by $\delta_{e\sigma}$, which decreases continuously from $\frac{\pi}{2}$ to zero as t is increased for $U' \ll U$. For $U' \gg U$, on the other hand, where the $t = 0$ ground state is a CO state, the

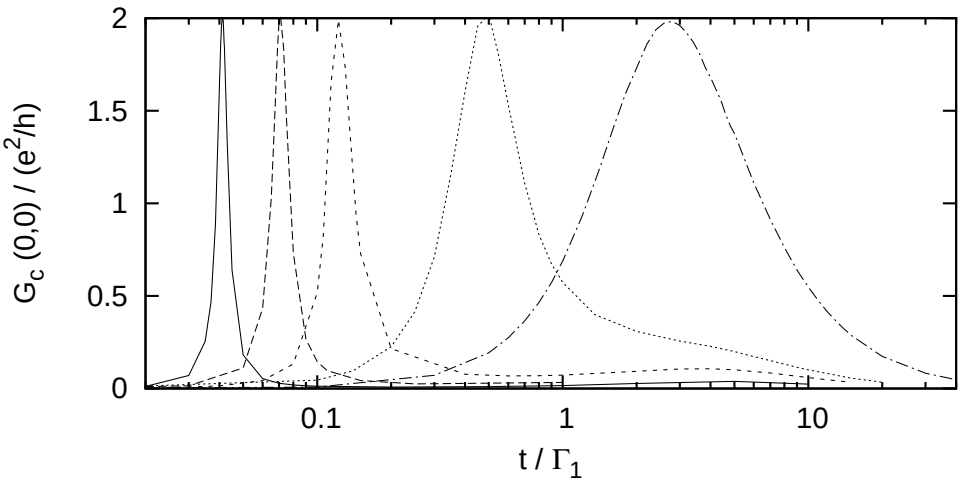


Figure 4.13: Zero-bias, zero-temperature conductance ($G_c(0,0)$) of the ph-symmetric 2AIM with $\tilde{U} = U/\Gamma_1 = 20$, as a function of $\tilde{t} = t/\Gamma_1$ for $\tilde{\Gamma}_2 = \Gamma_2/\Gamma_1 = 0.5$ (solid line), 0.75 (long-dashed line), 1 (short-dashed line), 5 (dotted line), 10 (dot-dashed line). Increasing $\tilde{\Gamma}_2$ causes the unitary conductance peak to move to higher $\tilde{t}$.

introduction of even an infinitesimal interdot tunnel-coupling destabilises the CO FP, making the ground state of the system a local singlet. This is illustrated by the vanishing of the CO phase residual entropy upon application of any interdot tunnel-coupling. As U' increases t_c goes to zero for $U' \simeq U$, and the crossover between LS and KS regimes becomes a QPT between KS and CO phases.

4.2.6 Unequal dot-lead couplings

We now look at the effect of taking the dot-lead couplings to be unequal, $\Gamma_1 \neq \Gamma_2$, taking $\Gamma_1 \geq \Gamma_2$. We set $\epsilon_1 = \epsilon_2 = -U/2$ such that the system remains at ph symmetry, and consider the effect of varying Γ_2 at fixed Γ_1: clearly this means that the 2AIM is no longer LR symmetric. In this case, we define t_c via the zero-bias, zero-temperature conductance, with $G_c(0,0) = 2e^2/h$ when $t = t_c$. In the LR-asymmetric case the conductance is still given in terms of $t' = t^*/\sqrt{\Gamma_1\Gamma_2}$, by Eqn. (4.28), such that $t' = 1$ gives unitary conductance, and therefore corresponds to $t = t_c$.

For the 2IKM, one can establish how J_c varies with the dot-lead couplings in the limit of $J_1 \gg J_2$ via scaling arguments [112, 117], as discussed in section 2.8. The result is (cf. Eqn. (2.27))

$$J_c \sim \left(\frac{1}{\rho J_2} - \frac{1}{\rho J_1}\right)^{-1} T_{\mathrm{K}}^{(1)} \ , \tag{4.31}$$

with the key point being that as J_2 is reduced, with J_1 fixed, J_c decreases. For the

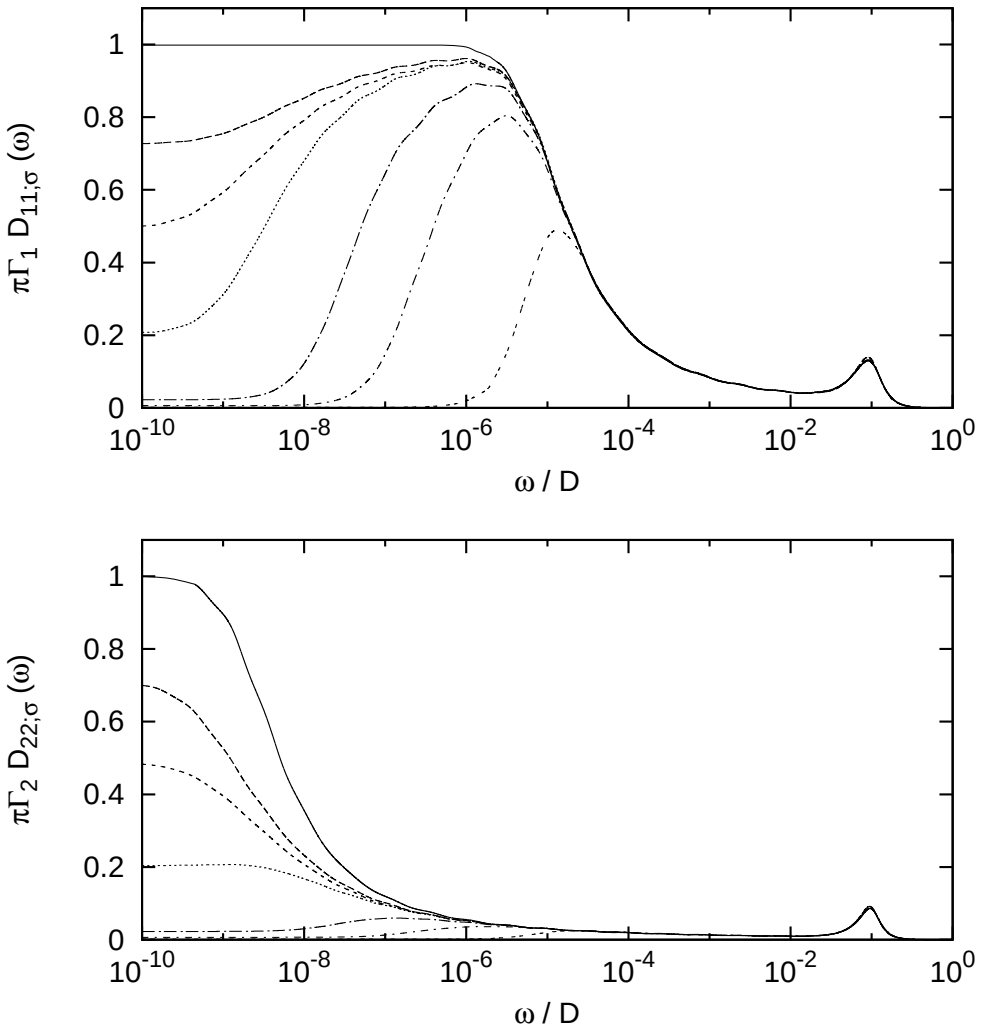


Figure 4.14: Single-particle spectra for dot 1 ($\pi\Gamma_1 D_{11;\sigma}(\omega)$, top panel) and dot 2 ($\pi\Gamma_2 D_{22;\sigma}(\omega)$, bottom panel) for the ph-symmetric 2AIM with $\tilde{U} = 20$ and $\Gamma_2/\Gamma_1 = 0.5$ for $\tilde{t} = t/\Gamma_1 = 0$, 0.04, 0.0412, 0.043, 0.05, 0.06, 0.1. As t is increased the Kondo resonances at zero frequency in both spectra are eroded. $t_c \simeq 0.0412\ \Gamma_1$ for these parameters. For $t \gg t_c$, the low-frequency maxima occurring in both spectra are at $\omega \sim J$, although those in the dot 2 spectra are difficult to discern.

2AIM then, for which $t_c = \sqrt{UJ_c/4}$ (provided $\frac{t}{U} \ll 1$), we expect to see a reduction in t_c as Γ_2 is reduced at fixed Γ_1 (analogous to reducing J_2 at fixed J_1 in the 2IKM, see section 2.7). Fig. 4.13, showing $G_c(0,0)$ for the 2AIM against $\tilde{t} = t/\Gamma_1$ for various values of Γ_2/Γ_1, illustrates this, with unitary conductance arising for $t = t_c$. As Γ_2/Γ_1 is decreased, the unitary conductance peak moves to lower values of t as t_c decreases[15].

[15]We can use Eqn. (2.27) and the expression $t_c = \sqrt{UJ_c/4}$ to derive an expression for how t_c depends on Γ_2 in the limit of $\Gamma_1 \gg \Gamma_2$ (provided $U \gg \Gamma_1, \Gamma_2$, such that the SW transformation is valid). This limit is, however, rather difficult to access in NRG calculations, as it requires a very

We also look at the spectra of the system with $\Gamma_1 \neq \Gamma_2$, shown in Fig. 4.14. Deep in the KS regime, when $t \ll t_c$, $\pi\Gamma_1 D_{11;\sigma}(0) \approx 1$ due to the Kondo resonance with width $\sim T_{\rm K}^{(1)}$, and likewise $\pi\Gamma_2 D_{22;\sigma}(0) \approx 1$, where the width of the Kondo resonance in the spectrum for dot 2 is $\sim T_{\rm K}^{(2)}$ (recall that $T_{\rm K}^{(1)}, T_{\rm K}^{(2)}$ are the Kondo scales for dots 1 and 2 respectively when $t = 0$). This is readily understood, as dot 1(2) is Kondo quenched by lead 1(2) on the scale of $T_{\rm K}^{(1)}(T_{\rm K}^{(2)})$. Deep in the LS regime, by contrast, no Kondo effects occur, and the zero-frequency values of the spectra are low. From Eqns. (4.8) and (4.9) it is straightforward to show that at ph symmetry $\pi\Gamma_\nu D_{\nu\nu;\sigma}(0) = \frac{1}{1+t'^2}\ \forall\nu$, even if the system is not LR symmetric, such that the zero-frequency values of the dot 1 and dot 2 spectra, as plotted in Fig. 4.14, are the same. The zero-frequency value of both spectra decrease continuously as t is increased, and for $t = t_c \simeq 0.0412\ \Gamma_1$ (equivalent to $t' = 1$), $\pi\Gamma_1 D_{11;\sigma}(0) = \pi\Gamma_2 D_{22;\sigma}(0) = 0.5$, as in the LR-symmetric case (see Fig. 4.6).

Looking at the spectra at finite frequencies, and considering the spectrum for dot 1 first, we see that for $t \neq 0$ the spectrum has a maximum, with deviations from the $t = 0$ spectrum occurring for $\omega \lesssim J$, this being the scale on which the pristine $t = 0$ Kondo physics is disrupted [112]. For dot 2 also, deviations from the $t = 0$ spectrum are apparent for frequencies, $\omega \lesssim J$. As t is increased the Kondo resonances in both spectra are eroded, and deep in the LS regime ($t \gg t_c$), the only low-energy features in both spectra are peaks at $\omega \sim \pm J = \pm\frac{4t^2}{U}$, corresponding to excitations between singlet and triplet atomic-limit states (these peaks are difficult to discern in the dot 2 spectra because of their low intensity).

4.3 Results for equal dot level energies ($\epsilon_1 = \epsilon_2$)

Having looked at the 2AIM at ph symmetry in some detail in the previous sections, we now consider the more general case in which the dot energy levels are allowed to vary. In this section we consider the 2AIM with equal dot level energies ($\epsilon_1 = \epsilon_2 = \epsilon$), before looking at the model with arbitrary dot level energies in the next section. For convenience, we consider the case of LR symmetry ($\Gamma_1 = \Gamma_2 = \Gamma$), except where we specifically state otherwise. Due to the ph symmetry of the Hamiltonian for $\epsilon = -\frac{U}{2}$ (see section 2.6), we need only consider $\epsilon \geq -\frac{U}{2}$ (for $U' = 0$ which we take throughout this section), as the properties for the system with $\epsilon < -\frac{U}{2}$ can be obtained via a simple ph transformation[16].

We begin with a brief recap of the atomic-limit behaviour of the system, discussed in section 2.10. In the atomic limit, with $t = 0$, the ground state has a (1,1)

large ratio of U/Γ_2 meaning that $T_{\rm K}^{(2)}$ is very small. To capture the low-energy physics very many NRG iterations must be performed, which is both time consuming and allows numerical errors to accumulate. We have therefore not been able to access genuinely the limit $\Gamma_1 \gg \Gamma_2$.

[16] For instance, defining $x = \epsilon + \frac{U}{2}$, $[G_c(0,0)](x) = [G_c(0,0)](-x)$ and $n_{\rm imp}(x) = 4 - n_{\rm imp}(-x)$.

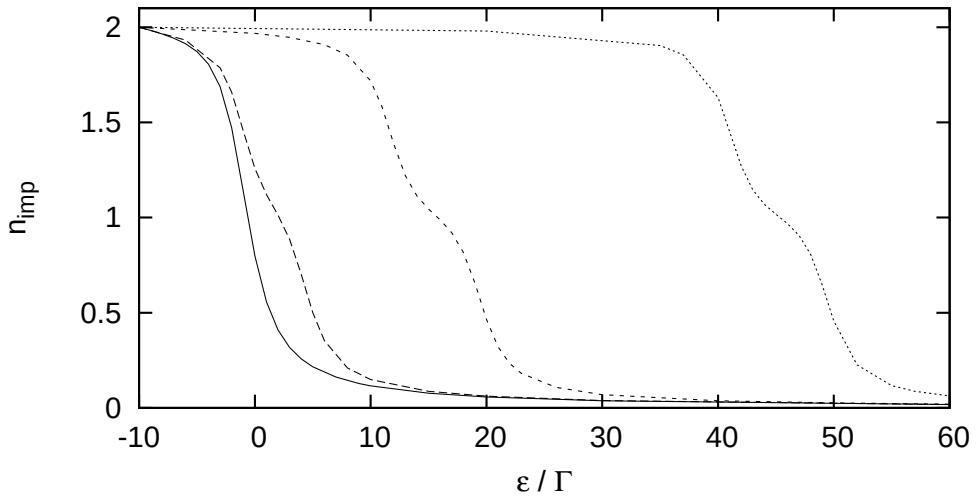


Figure 4.15: $n_{\rm imp}$ for the LR-symmetric 2AIM as a function of $\tilde{\epsilon} = \epsilon/\Gamma$ with $\tilde{U} = U/\Gamma = 20$ and $\tilde{t} = t/\Gamma = 0$ (solid line), 5 (long-dashed line), 20 (short-dashed line), 50 (dotted line). $\tilde{\epsilon} = -10$ is the ph-symmetric point.

configuration for $-U < \epsilon < 0$ and a (0,0) configuration for $\epsilon > 0$. Whereas for $t = 0$ the total number of electrons on the dots goes straight from zero to two as ϵ is decreased, for $t \neq 0$ there is an intervening one-electron regime, in which the single electron resides equally on the two dot levels. If $\frac{t}{U} \ll 1$, then the one-electron regime exists for $-t \lesssim \epsilon < t$, whereas for $\frac{t}{U} \gg 1$, it exists for $t - \frac{U}{2} \lesssim \epsilon < t$. The width of the one-electron regime therefore increases from $\simeq 2t$ in the low $\frac{t}{U}$ limit, to $\simeq \frac{U}{2}$ in the high $\frac{t}{U}$ limit. At high $\frac{t}{U}$ we can of course picture the dots as forming bonding and antibonding orbitals, with on-site repulsion $\frac{U}{2}$. Upon coupling to the leads, the discrete changes in dot charge become continuous crossovers, with width $\sim \Gamma$.

To illustrate the variation of dot occupancy upon varying the dot level energies, we now study how $n_{\rm imp} = \sum_\sigma n_{{\rm imp};\sigma}$ varies with ϵ, as shown in Fig. 4.15. At ph symmetry, $n_{\rm imp}$ is exactly two by symmetry. As ϵ is increased from its ph-symmetric value, $n_{\rm imp}$ decreases, and in the limit $\epsilon \to \infty$, $n_{\rm imp}$ goes to zero. In the limit of weak interdot coupling (low t), the system behaves essentially as two separate 1AIMs. Therefore $n_{\rm imp}$ decreases from two to zero over a range of $\sim \Gamma$ as ϵ increases past zero, as would be the case for a system of two entirely separate 1AIMs. This is illustrated by the solid ($t = 0$) line in Fig. 4.15. As t is increased, this behaviour changes little until $t \gtrsim \Gamma$, when a nascent $n_{\rm imp} \simeq 1$ regime appears as a shoulder in the data in Fig. 4.15 (see long-dashed ($\tilde{t} = 5$) line), the width of this regime being $\sim 2t$. As t increases further, the one-electron regime gets wider until, when $\frac{t}{U} \gg 1$, it has a width of $\sim \frac{U}{2}$ (see dotted ($\tilde{t} = 50$) line in Fig. 4.15). For any value of t there is a two-electron regime (provided $\tilde{U} \gg 1$), but there is only

a well-defined one-electron regime, in which $n_{\rm imp} \simeq 1$ and charge fluctuations are suppressed, if $t \gg \Gamma$.

The charge susceptibility, given by the derivative of $n_{\rm imp}$ with respect to ϵ,[17] gives a measure of the charge fluctuations on the DQD. Plateaus in Fig. 4.15 therefore correspond to regimes with suppressed charge fluctuations. We can see that for $t = 0$ charge fluctuations are suppressed in the two and zero-electron regimes, but not for $n_{\rm imp} \simeq 1$, *i.e.*, there is no regime in which there is essentially one electron on the DQD. As t is increased charge fluctuations begin to be suppressed for $n_{\rm imp} \simeq 1$, indicating the creation of a genuine one-electron regime[18].

Provided the system is deep in the two-electron regime ($-U \ll \epsilon \ll 0$) with $\frac{t}{U} \ll 1$ then each dot level contains essentially one electron. A SW transformation can then be carried out to second order to give a low-energy effective model of 2IKM form, the parameters of which are dependent on ϵ.[19] The parameters of this effective 2IKM are

$$\begin{aligned} J_\nu &= 2V_\nu^2 \left[\frac{1}{\epsilon_\nu + U} - \frac{1}{\epsilon_\nu} \right] , \\ J &= \frac{4t^2}{U} , \end{aligned} \tag{4.32}$$

with $\nu = 1, 2$, such that the dot-lead couplings, J_ν, are at a minimum at ph symmetry, and increase as one moves away from this point. This increase means that as one moves away from ph symmetry, $T_{\rm K}$ increases, as can be seen from Poor Man's Scaling (Eqn. (2.12)). J is clearly independent of ϵ. The condition for the crossover from KS to LS regimes in the 2AIM is $J = J_c \sim T_{\rm K}$. Therefore, as ϵ increases away from ph symmetry, J_c and $t_c = \sqrt{UJ_c/4}$ increase. This can be seen in Fig. 4.16, in which we plot $J_c = 4t_c^2/U$ (with t_c defined as the value of t for which unitary $G_c(0,0)$, indicative of the KS-LS crossover, arises[20]) against ϵ. We can see that the relation $J_c \sim T_{\rm K}$ (specifically we find $J_c \simeq 8T_{\rm K}$, with $T_{\rm K}$ defined by $S_{\rm imp}(T_{\rm K}) = \ln 2$ for the $t = 0$ system) holds throughout the two-electron regime, even well away from ph symmetry. The SW transformation for the $\frac{t}{U} \ll 1$ system discussed above becomes invalid when ϵ approaches the Fermi level (*i.e.*, for $\epsilon \gtrsim 0$), as charge fluctuations on the dots become significant. The system then moves to a mixed valence (MV) regime, in which charge states with two, one and zero electrons on the DQD are significant. Increasing ϵ further leads to the number of electrons on the DQD

[17] The charge susceptibility is given specifically by $\chi_c = \frac{-1}{k_B T} \left[\langle (\sum_\nu \hat{n}_\nu)^2 \rangle - \langle \sum_\nu \hat{n}_\nu \rangle^2 \right] = \frac{\partial n_{\rm imp}}{\partial \epsilon}$.

[18] For the relatively low value of $\tilde{U}$ in Fig. 4.15, the one-electron regime appears for large t as more of a shoulder in the data, rather than a clear plateau.

[19] This is a generalisation of the SW transformation at ph symmetry, discussed in section 2.7. We consider the result of carrying out this this generalised SW transformation to *third* order in section 5.4.

[20] This definition of t_c is equivalent to defining it via the phase shifts as $[\delta_{o\sigma} - \delta_{e\sigma}](t = t_c) = \frac{\pi}{2}$, which reduces to $\delta_{e\sigma}(t = t_c) = \frac{\pi}{4}$ at ph symmetry.

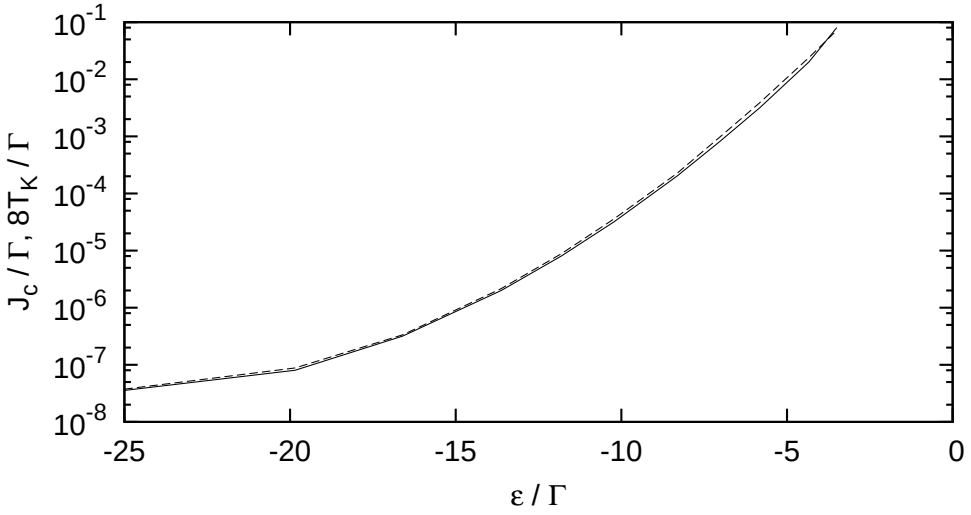


Figure 4.16: J_c, defined by $J_c = 4t_c^2/U$, as a function of ϵ for the LR-symmetric 2AIM with $\tilde{U} = 50$ (solid line). Also plotted is $8T_{\rm K}(\epsilon)$ (dashed line). The agreement between the two curves is very good, in fact, the lines are difficult to distinguish. $\tilde{\epsilon} = -25$ is the ph-symmetric point.

going to zero, and as such no Kondo physics can arise.

Considering now the case of $\frac{t}{U} \gg 1$ we may use the MO picture of the 2AIM. In the zero and two-electron regimes no Kondo physics can occur, as the bonding MO is either unoccupied or doubly occupied. In the one-electron regime (which occurs for $t - \frac{U}{2} \ll \epsilon \ll t$) however, the ground state has essentially one electron in the bonding orbital, with an onsite correlation of $\frac{U}{2}$, as discussed in section 2.6. This correlation suppresses charge fluctuations on the bonding orbital. In this case, the antibonding orbital is very high in energy, and can therefore be safely ignored, leaving an effective single-level model. The bonding orbital is coupled to both leads (1 and 2) with hybridisation strength $\frac{\Gamma}{2}$ (see Eqn. (2.25)), but as there is only a single active dot level in the problem, the two leads can be combined into a single effective lead (see section 2.1), to which the bonding orbital couples with hybridisation strength Γ. As such, virtual spin-flip processes can occur, and we therefore expect the possibility of a Kondo effect, in which the spin of the single bonding orbital electron is screened by the lead electrons. We refer to this as a "bonding" Kondo effect.

As mentioned, the onsite repulsion for the bonding orbital is $\frac{U}{2}$, and the hybridisation to the single effective lead is Γ. The bonding Kondo scale, denoted T_K^B, is $\sim \exp(-\pi U/16\Gamma)$ [99], and therefore much greater than $T_{\rm K}$ for the ph-symmetric 2AIM (for which the relevant onsite repulsion is U and the hybridisation is Γ, such that $T_{\rm K} \sim \exp(-\pi U/8\Gamma)$). We thus expect $T_{\rm K}^B$ for the 2AIM with $\frac{t}{U} \gg 1$ to be similar to $T_{\rm K}$ for the ph-symmetric 2AIM with a Coulomb repulsion of $U/2$. For the 2AIM with $\tilde{U} = 20$ and $\tilde{t} = 50$, we find that the bonding Kondo scale (defined by

$S_{\rm imp}(T = T_{\rm K}^B) = \frac{1}{2}\ln 2$ in the middle of the one-electron regime) is $T_K^B \simeq 0.01\ \Gamma$, similar to $T_{\rm K}$ for the ph-symmetric 2AIM with $\tilde{U} = 10$, which is found to be $\simeq 0.017\ \Gamma$, and much greater than $T_{\rm K}$ for the ph-symmetric 2AIM with $\tilde{U} = 20$, which is $\simeq 5 \times 10^{-4}\ \Gamma$.

Evidence of the bonding Kondo effect is seen in the impurity contribution to the entropy of the system (not shown), in which a $\ln 2$ plateau occurs for intermediate temperatures – indicative of a LM FP with a single free spin-$\frac{1}{2}$ corresponding to the bonding electron – before the entropy goes to zero at low temperatures – indicative of the screening of the bonding electron spin. Further evidence of the bonding Kondo effect occurs in the zero-bias conductance of the system, as we now discuss.

4.3.1 Conductance

Having determined the essential physics of the LR-symmetric 2AIM away from ph symmetry, we now move on to look at how this is reflected in the zero-bias conductance. At zero temperature, we may use Eqn. (3.54) and the expressions derived for the dot Green's functions (Eqn. (4.10)) to obtain an exact equation for the zero-bias conductance in terms of the renormalised parameters. This yields

$$G_c(0,0) = \frac{8e^2}{h}\frac{t'^2}{[(\epsilon'^2 - t'^2 - 1)^2 + 4\epsilon'^2]}\ , \tag{4.33}$$

where $\epsilon' = \epsilon^*/\Gamma = (\epsilon + \Sigma_{11;\sigma}(0))/\Gamma$. It is trivially seen that at ph symmetry, for which $\epsilon' = 0$, this result reduces to Eqn. (4.28). It is also easy to show that for any value of ϵ', $G_c(0,0)$ is maximal and equal to the unitary limit of $2e^2/h$ when $t' = \sqrt{1+\epsilon'^2}$, such that at ph symmetry unitary conductance arises for $t' = 1$.

Fig. 4.17 (bottom panel) shows the zero-bias conductance at zero temperature of the LR-symmetric 2AIM, as a function of $\tilde{\epsilon}$ for various values of $\tilde{t}$. We find that for low t ($t \leq t_c^{ph}$, with t_c^{ph} the value of t_c at ph symmetry) the conductance has a maximum at ph symmetry ($\tilde{\epsilon} = -10$ in Fig. 4.17). This can be understood in terms of Eqn. (4.33), which for $t'^2 \ll \epsilon'^2 + 1$ (*i.e.*, in the limit of low t) becomes

$$G_c(0,0) \simeq \frac{8e^2}{h}\frac{t'^2}{(1+\epsilon'^2)^2}\ . \tag{4.34}$$

which is clearly maximal for $\epsilon' = 0$, *i.e.*, at ph symmetry. Physically for low t, one expects the conductance to be limited by the hopping of electrons between the dots, and this is reflected in the t'^2 factor in the above expression. As t is small, dot-lead electron transfer is expected to be similar to the $t = 0$ case, so that as ϵ is varied for the LR-symmetric 2AIM we expect to see behaviour that is qualitatively similar to the 1AIM: relatively high conductance at ph symmetry, which dies away as ϵ is increased away from ph symmetry. This is of course what is seen in Fig. 4.17

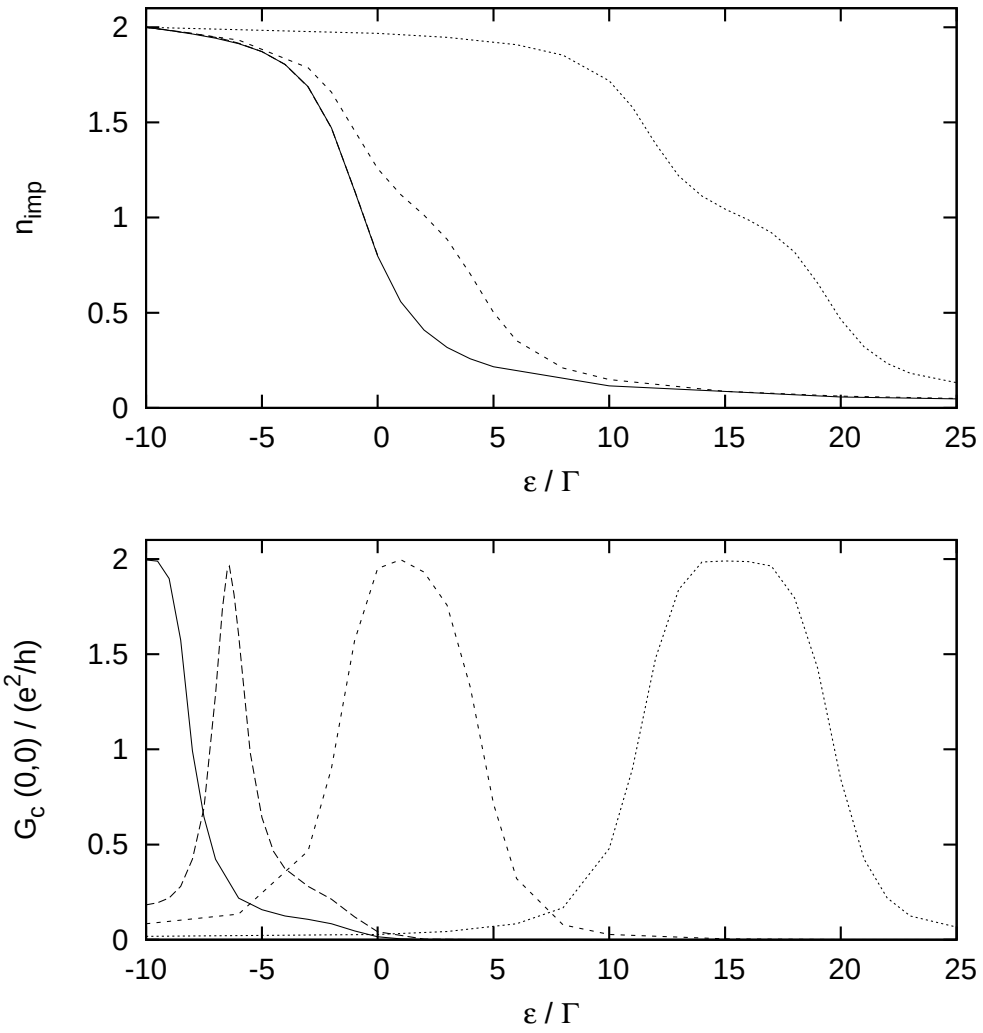


Figure 4.17: Top panel: $n_{\rm imp}$ for the LR-symmetric 2AIM as a function of $\tilde{\epsilon} = \epsilon/\Gamma$ with $\tilde{U} = U/\Gamma = 20$ and $\tilde{t} = t/\Gamma = 0.123$ (solid line), 0.2 (long-dashed line), 5 (short-dashed line), 20 (dotted line). Plots for $\tilde{t} = 0.123$ and 0.2 are indistinguishable. $\tilde{\epsilon} = -10$ is the ph-symmetric point. Bottom panel: Zero-bias, zero-temperature conductance, $G_c(0,0)$ for the same parameters. The conductance maximum moves to higher values of $\tilde{\epsilon}$ as $\tilde{t}$ increases. $t_c^{ph} \simeq 0.123\ \Gamma$ for these parameters.

bottom panel for $t \leq t_c^{ph}$ (solid line).

As t is increased past t_c^{ph} we see the conductance peak splitting into two (only one component of which is shown in Fig. 4.17 bottom panel, the other being at $\epsilon < -U/2$, $G_c(0,0)$ being symmetric about the ph symmetric point), such that there exists a minimum in the conductance at ph symmetry. If $t \ll \Gamma$ (long-dashed line in Fig. 4.17), then unitary $G_c(0,0)$ occurs in the two-electron regime (as can be seen by comparison of the two panels in Fig. 4.17), at the ϵ for which $J = 4t^2/U \sim T_{\rm K}(\epsilon)$. As t is increased such that $t \gtrsim \Gamma$ (short-dashed line), the conductance peak moves

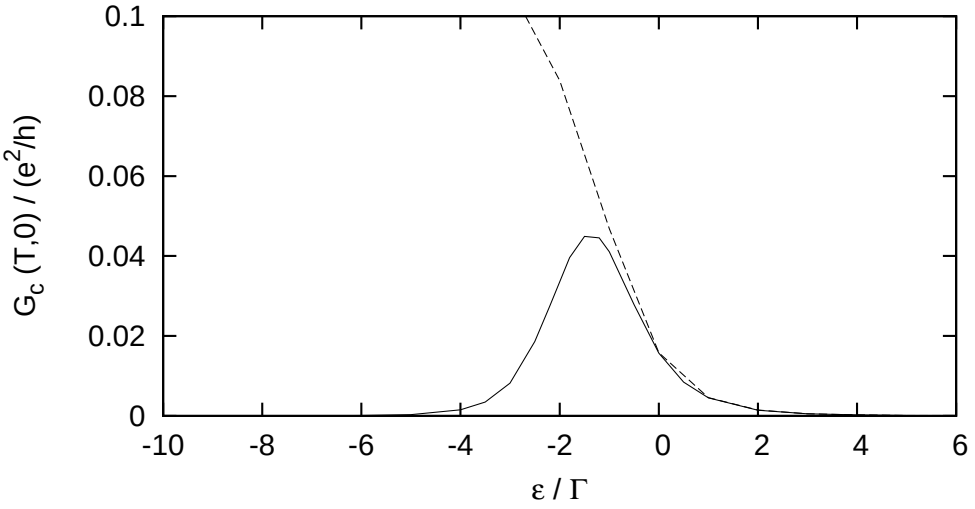


Figure 4.18: Zero-bias, finite-temperature conductance, $G_c(T,0)$ for the LR-symmetric 2AIM as a function of $\tilde{\epsilon} = \epsilon/\Gamma$ for $t = t_c^{ph} = 0.123\ \Gamma$ with $\tilde{U} = U/\Gamma = 20$ and $T = 0.1\ \Gamma$ (solid line) and $T = 0$ (dashed line). Note that the scale on the y-axis only goes up to $0.1e^2/h$ – the conductance at zero temperature goes up to $2e^2/h$ at ph symmetry ($\tilde{\epsilon} = -10$). For the parameters used here, $T_K \simeq 5 \times 10^{-4}\ \Gamma$ at ph symmetry – the solid line is for a much greater temperature than this.

to the nascent one-electron regime. In the limit of high $\frac{t}{U}$ we switch to the MO picture. In this case, we expect high conductance in the one-electron regime due to a bonding Kondo effect. This occurs when the bonding MO is just below the Fermi level, so that it is singly occupied. We therefore see a unitary conductance peak of width $\sim U/2$ (the width of the one-electron regime) centred at $\epsilon \sim t - U/4$ (the centre of the one-electron regime) in Fig. 4.17 (dotted line).

Finite-temperature conductance

We now have a brief but representative look at the zero-bias conductance at finite temperature, as calculated via the linear-response approach (see section 3.7.3). Looking first at the case of $t = t_c^{ph}$,[21] we find that the strong conductance peak in the vicinity of ph symmetry (see Fig. 4.18, dashed line) is killed off when the temperature becomes greater than $\sim T_K$. The conductance in the vicinity of $\epsilon = 0$, the MV regime, on the other hand dies away only when the temperature becomes comparable to Γ, just as for the MV regime of the 1AIM. At temperatures higher than T_K but lower than Γ then, we observe a peak in the zero-bias conductance in the vicinity of $\epsilon = 0$, as shown in Fig. 4.18. This behaviour is similar to that for the 1AIM, for which this type of Coulomb blockade structure is also observed for $T_K \ll T \ll \Gamma$, with enhanced zero-bias conductance in the vicinity of values of ϵ for

[21] Qualitatively similar behaviour is found for $t < t_c^{ph}$.

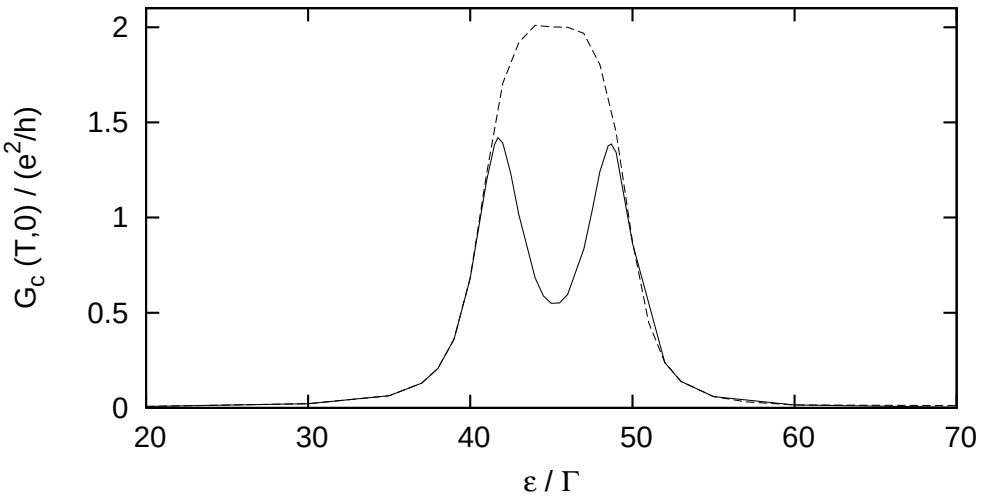


Figure 4.19: Zero-bias, finite-temperature conductance, $G_c(T,0)$, for the LR-symmetric 2AIM as a function of $\tilde{\epsilon} = \epsilon/\Gamma$ for $\tilde{t} = t/\Gamma = 50$ with $\tilde{U} = U/\Gamma = 20$ and $T = 0.1\ \Gamma$ (solid line) and $T = 0$ (dashed line). The bonding Kondo scale at the centre of the one-electron regime ($\tilde{\epsilon} \simeq 45$) is $T_{\rm K}^B \simeq 0.01\ \Gamma$ – the solid line is for a greater temperature than this.

which atomic-limit charge degeneracy arises.

Considering the high $\frac{t}{U}$ case, we use the MO picture. In this case, $G_c(0,0)$ is unitary in the centre of the one-electron regime as a result of the bonding Kondo effect which occurs at low temperature, as discussed above. This effect is thermally destroyed when the temperature becomes comparable to $T_{\rm K}^B$, which as discussed is much greater than $T_{\rm K}$ at ph symmetry. At the edges of the one-electron regime are MV regimes, for which the zero-temperature conductance dies away on the scale of $T \sim \Gamma$. Therefore, similar to the case of low values of $\frac{t}{U}$, shown in Fig. 4.18, Coulomb blockade structure is visible for the 2AIM with $t \gg U$ for temperatures $T_{\rm K}^B \ll T \ll \Gamma$. This is shown in Fig. 4.19. At temperatures above $T_{\rm K}^B$, we observe zero-bias conductance peaks in the vicinity of values of ϵ for which atomic-limit charge degeneracy arises.

4.3.2 Unequal dot-lead couplings

Thus far in this section we have considered the 2AIM away from ph symmetry but still with LR symmetry. We now briefly consider the 2AIM with $\epsilon_1 = \epsilon_2 = \epsilon$ but $\Gamma_1 \neq \Gamma_2$, such that the system is not LR symmetric. The zero-bias, zero-temperature conductance ($G_c(0,0)$) as a function of ϵ for various values of t is shown in Fig. 4.20. We have taken $\Gamma_2/\Gamma_1 = 0.5$. We see that for low values of t ($t \leq t_c^{ph} \simeq 0.25\ \Gamma_1$) the conductance is maximal at ph symmetry, as in the LR-symmetric case. As t is increased, the conductance peak splits so that maximal $G_c(0,0)$ occurs away from

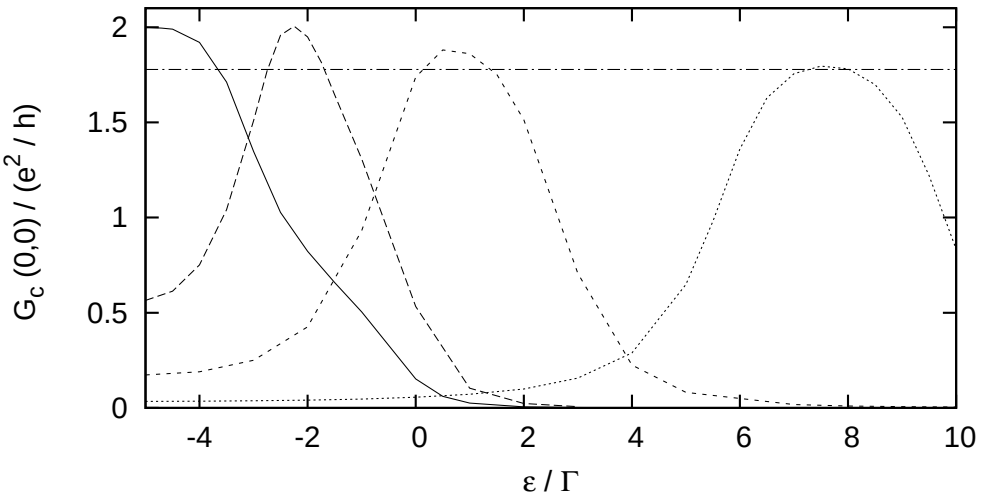


Figure 4.20: $G_c(0,0)$ (in units of e^2/h) as a function of $\tilde{\epsilon}$ for the 2AIM with $\tilde{U} = U/\Gamma_1 = 10$ and $\Gamma_2/\Gamma_1 = 0.5$ for $\tilde{t} = t/\Gamma_1 = 0.25$ (solid line), 0.5 (long-dashed line), 3 (short-dashed line), 10 (dotted line). As $\tilde{t}$ increases the conductance maximum moves to higher ϵ. Also marked on is $G_c(0,0) = G_0 \frac{2e^2}{h} \simeq 1.77 \frac{e^2}{h}$ (dot-dashed line), the peak conductance in the limit of high $\frac{t}{U}$. $t_c^{ph} \simeq 0.25\ \Gamma_1$, and $\tilde{\epsilon} = -5$ is the ph-symmetric point.

ph symmetry. In contrast to the LR-symmetric case however, the conductance away from ph symmetry never reaches the unitary limit, $G_c(0,0) = 2e^2/h$. In the limit of high $\frac{t}{U}$ a one-electron regime exists, and high zero-bias conductance is observed in this regime due to a bonding Kondo effect, as in the LR-symmetric case. As the bonding MO is now coupled asymmetrically to the leads, there is an asymmetry factor in the conductance (see Eqn. (3.49)), meaning that $G_c(0,0)$ does not reach the unitary limit, rather it goes up to $\frac{2e^2}{h} G_0$, with G_0 given by (cf. Eqn. (3.50))

$$G_0 = \frac{4\Gamma_1\Gamma_2}{(\Gamma_1 + \Gamma_2)^2} \ . \tag{4.35}$$

For the parameters in Fig. 4.20, this gives $G_c(0,0) = \frac{2e^2}{h} G_0 \simeq 1.77 e^2/h$ in the one-electron regime for $\frac{t}{U} \gg 1$. In Fig. 4.20 we can see that the maximal $G_c(0,0)$ goes to this value as $\tilde{t} \to \infty$, essentially reaching this limiting value for $\tilde{t} = 10$ (dotted line).

4.4 Results for unequal dot level energies ($\epsilon_1 \neq \epsilon_2$)

Having looked at the system with equal dot level energies, we now move on to consider the 2AIM more generally, with $\epsilon_1 \neq \epsilon_2$, relevant to TCDQD experiments, in which dot level energies may be tuned independently via adjustment of gate voltages (we look at the 2AIM with $\epsilon_1 \neq \epsilon_2$ in relation to experimental data in

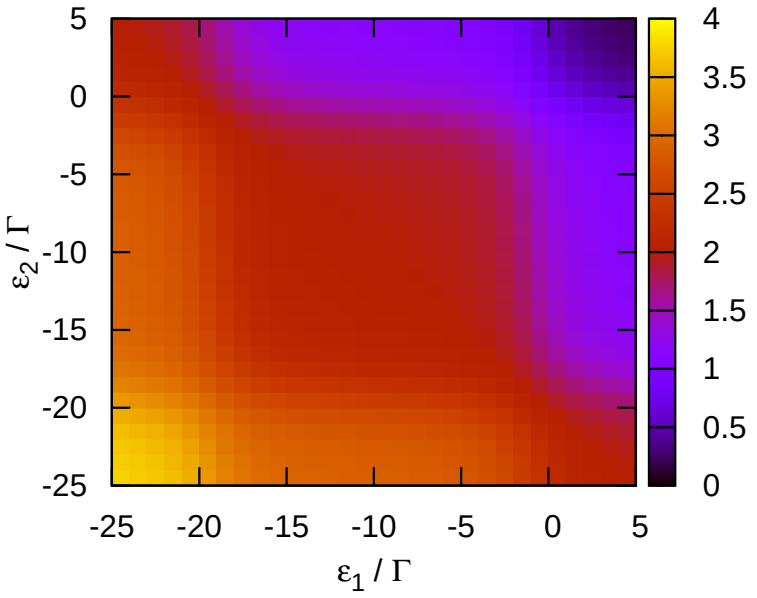


Figure 4.21: $n_{\rm imp}$ for the 2AIM as a function of ϵ_1 and ϵ_2, with $\tilde{U} = U/\Gamma = 20$ and $\tilde{t} = t/\Gamma = 1$ at zero temperature.

chapter 7). Here, we give a brief introduction to the physics of the system with unequal dot level energies, hoping that the results presented here give an insight into the rich physics accessible in the 2AIM. We concentrate in this section on the case of equal dot-lead couplings ($\Gamma_1 = \Gamma_2 = \Gamma$) for simplicity.

Altering the dot level energies leads to variations in the dot occupancy, $n_{\rm imp}$, which is calculated as a function of the two dot energy levels, ϵ_1 and ϵ_2, shown in Fig. 4.21 for $\tilde{t} = t/\Gamma = 1$ and $\tilde{U} = U/\Gamma = 20$. In the atomic limit, $n_{\rm imp}$ is trivially calculated, as discussed in section 2.11, and can be read off from the atomic-limit phase diagrams given in Fig. 2.7. Upon coupling to the leads, $n_{\rm imp}$ closely resembles the atomic-limit behaviour (cf. Figs. 2.7 (b) and 4.21), except that the discrete changes which arise in the atomic limit are broadened into continuous changes over an energy range of $\sim \Gamma$. Although we only show data for $\tilde{t} = 1$, this remains true for all values of t.

We move on to look at the zero-temperature, zero-bias conductance of the 2AIM, given generally by

$$G_c(0,0) = \frac{8e^2}{h} \frac{t'^2}{[(\epsilon_1'\epsilon_2' - t'^2 - 1)^2 + (\epsilon_1' + \epsilon_2')^2]} \ , \tag{4.36}$$

with $\epsilon_1' = \epsilon_1^*/\Gamma_1 = [\epsilon_1 + \Sigma_{11;\sigma}(0)]/\Gamma_1$ and $\epsilon_2' = \epsilon_2^*/\Gamma_2 = [\epsilon_2 + \Sigma_{22;\sigma}(0)]/\Gamma_2$. This result is straightforwardly derived via Eqns. (3.54), (4.8) – (4.10) and is easily seen to reduce to Eqn. (4.33) in the case of LR symmetry, and to Eqn. (4.28) in the case of both LR and ph symmetry. From Eqn. (4.36), it is a matter of straightforward algebra to show that unitary $G_c(0,0)$ can only arise if $\epsilon_1' = \epsilon_2'$ *and* $t'^2 = \epsilon_1'\epsilon_2' + 1$. If $\Gamma_1 \neq \Gamma_2$ but $\epsilon_1 = \epsilon_2$ (as in section 4.3.2), then unitary $G_c(0,0)$ only arises at ph symmetry, where $\epsilon_1' = \epsilon_2' = 0$, whereas away from ph symmetry $\epsilon_1' \neq \epsilon_2'$. In the case of $\Gamma_1 = \Gamma_2$, $\epsilon_1^* = \epsilon_2^*$ is required for unitary $G_c(0,0)$, and we expect this to occur only along the line $\epsilon_1 = \epsilon_2$.

We show NRG results for $G_c(0,0)$ in Fig. 4.22 for two cases; $\tilde{t} = 0.123$ and $\tilde{t} = 1$, both with $\tilde{U} = 20$. For $\tilde{t} = 0.123$, $t = t_c^{ph}$ (the value of t_c at ph symmetry) so that unitary conductance arises at ph symmetry ($\epsilon_1/\Gamma = \epsilon_2/\Gamma = -\tilde{U}/2 = -10$), and dies away as one departs from ph symmetry, see Fig. 4.22 top panel. For $\tilde{t} = 1$, the system is deep in the LS regime at ph symmetry, so the conductance is low here. Comparing Fig. 4.22 lower panel to Fig. 4.21 shows that for this value of $\tilde{t}$, high conductance occurs in the MV regimes. These are regimes in which charge fluctuations on the dot are significant, and therefore strong sequential, one-electron tunneling occurs. Note that in Fig. 4.22 lower panel, whilst the conductance for certain values of $\epsilon_1 \neq \epsilon_2$ is near unitary, it only truly reaches the unitary limit for $\epsilon_1 = \epsilon_2$.

We have not calculated the conductance for the system with $\frac{t}{U} \gg 1$ but we can predict the behaviour rather simply in terms of the MO picture. We expect it to be somewhat similar to that for the non-interacting limit, discussed in section 2.11. High conductance arises when: a) one of the MOs is at, or just below, the Fermi level, such that it contains one electron, the spin of which is Kondo quenched by the leads, and b) when the singly-occupied MO is roughly equally coupled to the leads, such that the G_0 asymmetry factor that arises in the expression for the conductance is large (see Eqn. (3.49)).

So far we have discussed the zero-bias conductance at zero temperature. It is interesting, and relevant to experimental data (see chapter 7), to consider the conductance maps shown in Fig. 4.22 at *finite* temperature as shown in Fig. 4.23 (for $\tilde{T} = 0.01$). Comparing the lower panels of Fig. 4.22 and 4.23 ($\tilde{t} = 1$) shows little difference. The high conductance here occurs in MV regimes, such conductance being due to sequential one-electron tunneling processes. Such processes die away only when the temperature is $\sim \mathcal{O}(\Gamma)$, and the temperature used in the calculation of Fig. 4.23 is less than this. Comparing the top panels of Figs. 4.22 and 4.23 ($\tilde{t} = 0.123$) by contrast, shows that the temperature has a very significant effect in this case. The high zero-temperature conductance that arises in the vicinity of ph symmetry dies away when the temperature becomes greater than $\sim T_K$, as discussed in section 4.2.4. At temperatures higher than T_K what remains is Coulomb blockade

structure, with relatively high conductance in the MV regimes (note the scale in Fig. 4.23 upper panel – the maximum conductance is $\sim 0.1\ e^2/h$).

Conductance plots (such as those shown in Fig. 4.23) for experimental systems are often used to estimate the parameters of the system (as we discuss further in chapter 7). When Coulomb blockade structure is visible, enhanced conductance occurs for parameters at which there is atomic-limit charge degeneracy. From the conductance data then, one can identify lines of atomic-limit charge degeneracy, and therefore one can identify the atomic-limit phase diagram. Once the atomic-limit phase diagram is known, the parameters of the system can be readily estimated; one may simply calculate the atomic-limit phase diagram for the system with arbitrary parameters, and then tune these parameters until the calculated phase diagram matches the experimentally-determined one. It is important to note, however, that the Coulomb blockade structure is only clearly evident for $T \gtrsim T_{\rm K}$. One must therefore be a little cautious in carrying out this procedure, as the conductance plots at low temperature (*e.g.*, Fig. 4.22 upper panel) do not *necessarily* reflect the atomic-limit phase diagram.

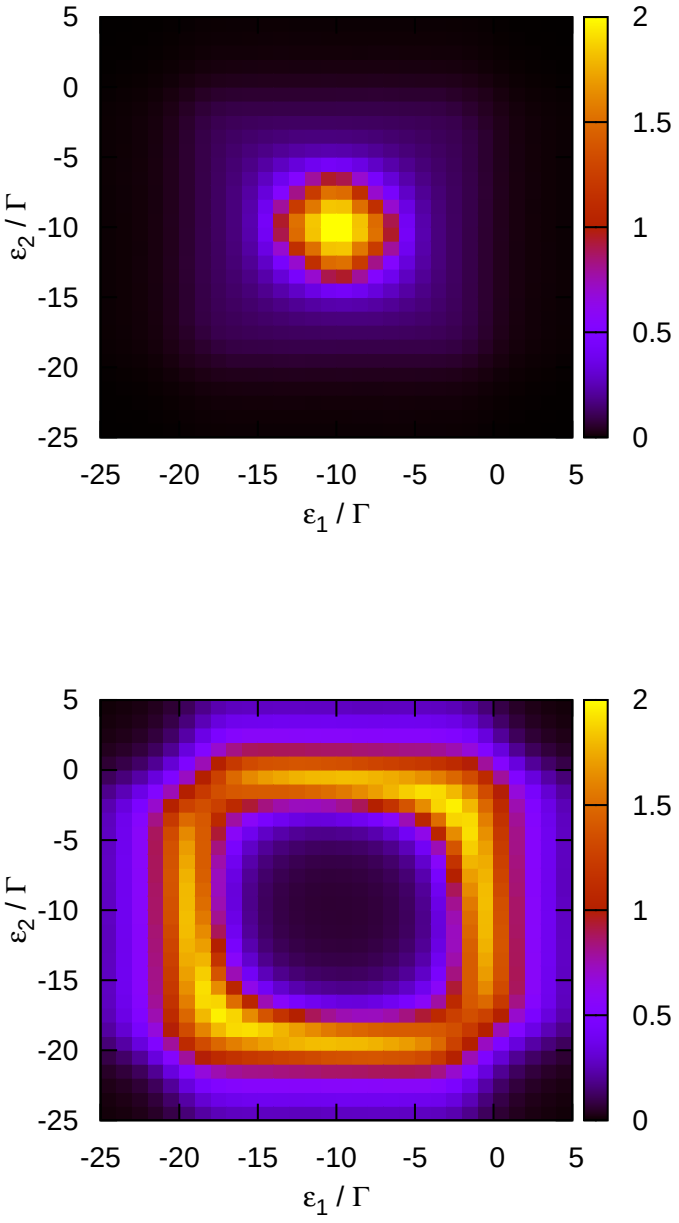


Figure 4.22: Zero-bias, zero-temperature conductance, $G_c(0,0)$ (in units of e^2/h), of the 2AIM as a function of $\tilde{\epsilon}_1 = \epsilon_1/\Gamma$ and $\tilde{\epsilon}_2 = \epsilon_2/\Gamma$, with $\tilde{U} = U/\Gamma = 20$, $\Gamma_1 = \Gamma_2 = \Gamma$, and $\tilde{t} = t/\Gamma = 0.123$ (upper panel), 1 (lower panel). Ph symmetry occurs at $\epsilon_1/\Gamma = \epsilon_2/\Gamma = -10$, at the centre of the plots.

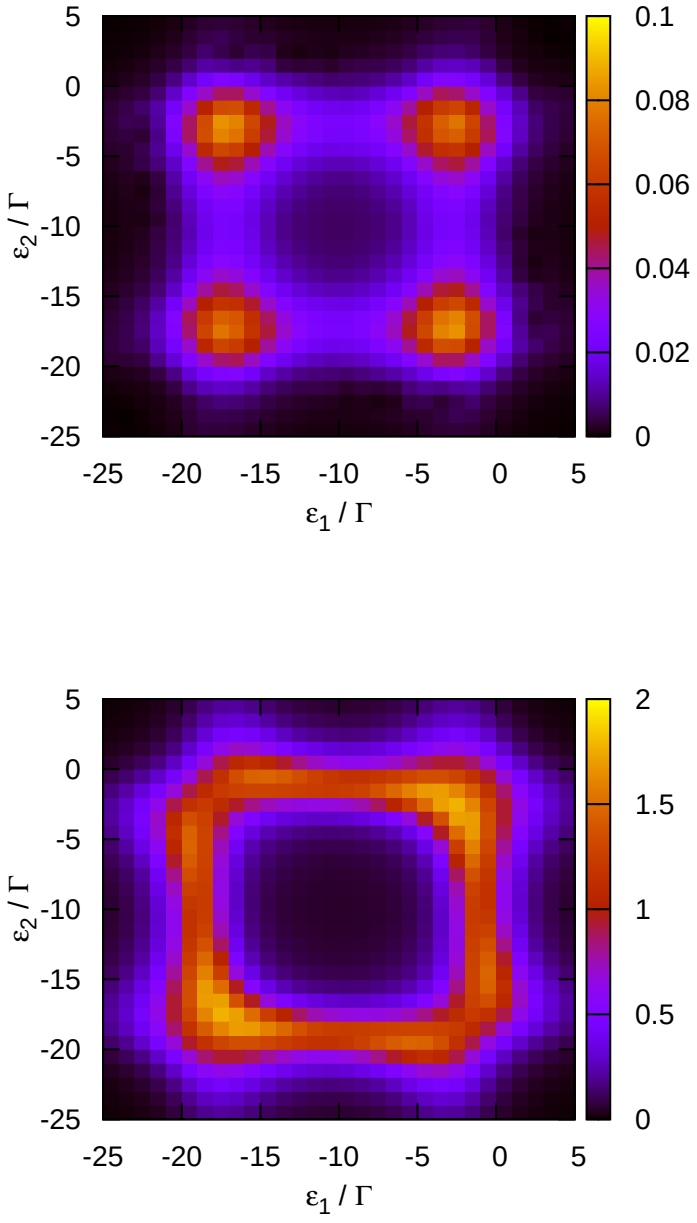


Figure 4.23: Zero-bias conductance, $G_c(T,0)$ (in units of e^2/h), of the 2AIM as a function of $\tilde{\epsilon}_1 = \epsilon_1/\Gamma$ and $\tilde{\epsilon}_2 = \epsilon_2/\Gamma$, with $\tilde{U} = U/\Gamma = 20$, $\Gamma_1 = \Gamma_2 = \Gamma$, $\tilde{T} = T/\Gamma = 0.01$, and $\tilde{t} = t/\Gamma = 0.123$ (upper panel), 1 (lower panel). Note the scale on the upper panel is different from that used for the other conductance plots. Ph symmetry occurs at $\epsilon_1/\Gamma = \epsilon_2/\Gamma = -10$, at the centre of the plots.

4.5 Finite-bias conductance of the 2AIM

In the final section of this chapter, we investigate the finite-bias conductance of the 2AIM, concentrating on zero temperature ($G_c(0,V)$) for simplicity. As discussed in section 3.7.4, it is notoriously difficult to calculate the finite-bias conductance of quantum impurity systems, and in practice approximations have to be made. A common approximation is to assume that the self-energies of the system are independent of bias, which yields Eqn. (3.65), and it is this at which we look first.

4.5.1 Bias-independent self-energy approximation

Concentrating on the LR and ph-symmetric 2AIM, we show $G_c(0,V)$ as calculated via the bias-independent self-energies approximation (BISEA, Eqn. (3.65)) in Fig. 4.24. We have taken the partitioning of the voltage bias between the leads to be symmetric for simplicity ($\lambda = 0.5$, see section 3.7.4). We see that as t is increased from zero, a zero-bias conductance peak rises up, until at $t = t_c$ it reaches the unitary limit, $G_c(0,0) = 2e^2/h$ (recall that at ph symmetry t_c is defined as the t for which unitary conductance arises). This conductance peak has a width $\delta(eV) \sim \mathcal{O}(T_\mathrm{K})$ (for the parameters used in Fig. 4.24, $T_\mathrm{K} \simeq 5 \times 10^{-6} D$). As t is increased further, so that $t > t_c$, the zero-bias peak lowers and splits for some value of $t > t_c$, giving two maxima whose positions go to $V \sim \pm\delta E$ as $t \to \infty$, with δE the atomic-limit singlet-triplet splitting[22]. As for the spectrum, see section 4.2.3, one can perform an approximate low-frequency expansion of $|G_{12;\sigma}(\omega)|^2$, and putting this into Eqn. (3.65) gives

$$G_c(0,V) \overset{V\to 0}{\sim} \frac{2e^2}{h} \frac{4t'^2}{(1+t'^2-(eV')^2)^2 + 4(eV')^2} \,, \tag{4.37}$$

where $V' = \frac{V}{Z\Gamma}$, with Z the quasiparticle weight (see section 4.2.3). From this result, it is easy to show that $V = 0$ is a maximum for $t' < 1$ and a minimum for $t' > 1$. The splitting in $G_c(0,V)$ should then occur for $t' \gtrsim 1$, equivalent to $t \gtrsim t_c$. In the NRG data, Fig. 4.24, we cannot discern a splitting until quite a high value of t is reached ($\tilde{t} \simeq 0.4$, whereas $\tilde{t}_c \simeq 0.123$), presumably for the same reasons that the splitting in the spectrum as a function of frequency ($\pi\Gamma D_{11;\sigma}(\omega)$) is not apparent until it reaches a sufficient magnitude, as discussed in section 4.2.3.

4.5.2 Conductance in the limit of weakly-coupled dots

As discussed in section 3.7.4, we may calculate the conductance for arbitrary voltage bias to leading order in the interdot coupling, t, via Eqn. (3.69). This result becomes exact in the limit of weak interdot coupling, *i.e.*, as $t \to 0$. In the rest of this section we investigate this "leading order in t" (LOT) approach.

[22] Clearly in Fig. 4.24 we only see one of these maxima – the other is at negative bias.

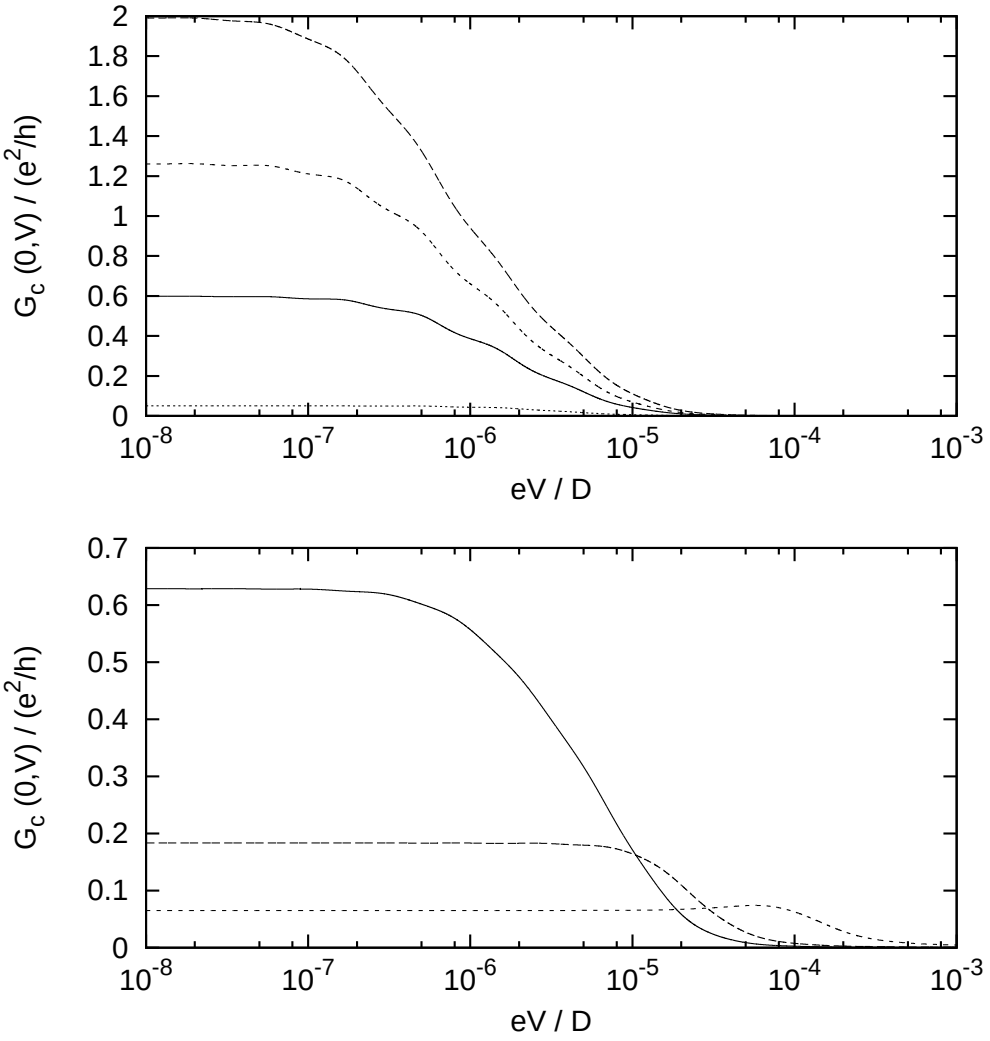


Figure 4.24: Finite-bias, zero-temperature conductance, $G_c(0,V)$, for the LR and ph-symmetric 2AIM with $\tilde{U} = 20$ and $t \leq t_c$ (top panel) and $t > t_c$ (lower panel). For the top panel $\tilde{t} = t/\Gamma = 0.06$ (dotted line), 0.1 (solid line), 0.11 (short-dashed line) and 0.123 (long-dashed line). For the lower panel $\tilde{t} = 0.15$ (solid line), 0.2 (long-dashed line) and 0.4 (short-dashed line). All results were calculated via Eqn. (3.65). Note that $t_c \simeq 0.123\ \Gamma$ and we have taken the voltage partitioning parameter to be $\lambda = 0.5$. The splitting in the finite-bias conductance is just about visible for $\tilde{t} = 0.4$ (lower panel), with a slight maximum at $eV/D \simeq 10^{-4}$.

Zero-bias conductance

At zero bias we can calculate $G_c(0,0)$ exactly via Eqn. (3.54) so we begin by looking at results from the LOT approach in the zero-bias limit, comparing these results to the exact results, shown in Fig. 4.25. This allows us to see for what values of interdot coupling (t) the LOT approach is valid, at least at zero bias. In Fig. 4.25, we see that the LOT results are accurate for $t \lesssim 0.05\Gamma < t_c = 0.123\Gamma$.

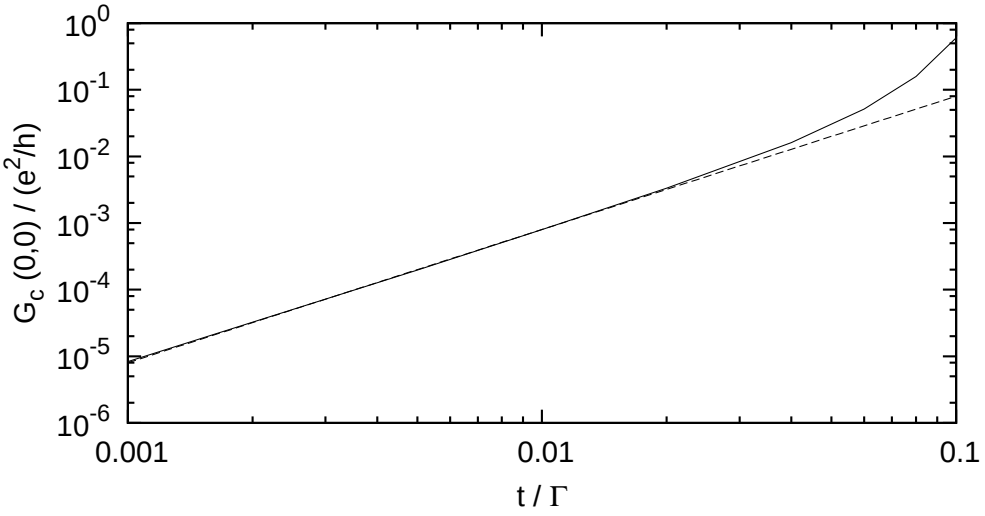


Figure 4.25: Zero-bias, zero-temperature conductance ($G_c(0,0)$) of the ph and LR-symmetric 2AIM for low values of $\tilde{t}$ with $\tilde{U} = 20$, calculated via the LOT approach (Eqn. (3.69), dashed line), and exactly via Eqn. (3.54) (solid line). Agreement is seen to be good for sufficiently low values of $\tilde{t} \lesssim 0.05$. For the parameters used here, $t_c \simeq 0.123\ \Gamma$.

Finite-bias conductance

Having looked at the zero-bias conductance, and established that the LOT is accurate for sufficiently weak interdot coupling (low t), we now move on to look at finite-bias conductance. We take $\tilde{t} = 0.02$ and consider the LR and ph-symmetric 2AIM, such that we expect that the LOT results to be accurate.

Results for the finite-bias conductance calculated via the LOT and the BISEA are shown in Fig. 4.26. Note that the results for $\lambda = x$ are the same as for $\lambda = 1-x$, so we only show $\lambda \geq 0.5$. We find that at low bias ($eV \ll U$), the two give similar results, as can be seen by comparing the two plots in Fig. 4.26. Both approaches capture the Kondo resonance, which has width $\sim \mathcal{O}(T_{\rm K})$. It can be seen that the BISEA gives a slightly inaccurate peak width, although it does correctly capture the decrease in Kondo peak width as λ increases from 0.5. Whilst the BISEA is exact in the limits of $U \to 0$ and $V \to 0$ separately, it is gratifying to see that even in a strongly-correlated system, it captures the conductance well for relatively high bias (up to $eV \sim \Gamma \ll U$ in Fig. 4.26). At very high bias, however, we find that the BISEA fails adequately to capture the Coulomb blockade peaks (at $eV \sim U/2 = 10\Gamma$) in the conductance, as seen by comparing the two plots in Fig. 4.26.

Whilst we haven't investigated the LOT approach comprehensively, the results we have presented show that this method can be used to calculate the finite-bias conductance of the 2AIM and that it is an improvement on the common BISEA at

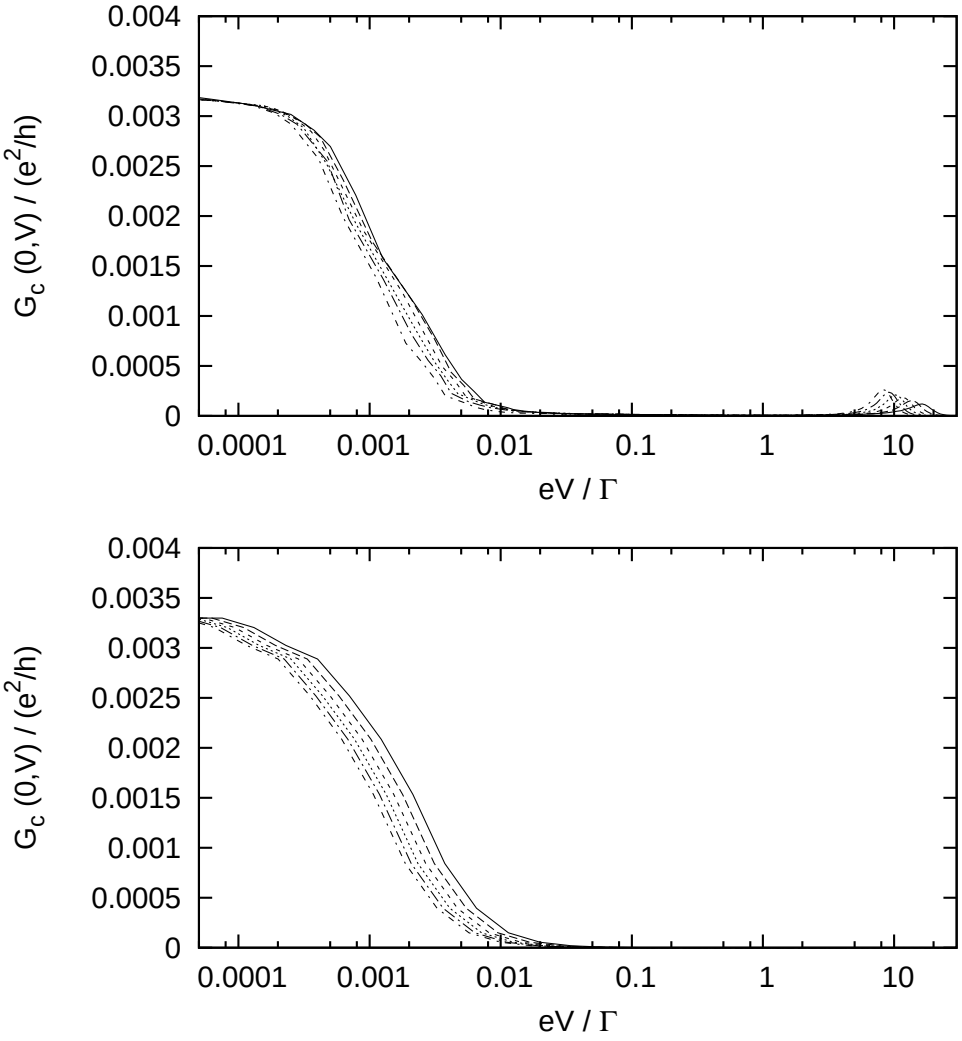


Figure 4.26: Zero-temperature conductance of the 2AIM at LR and ph symmetry as a function of source-drain bias, calculated via the LOT approach with $\lambda = 0.5$ (solid line), 0.6, 0.7, 0.8, 0.9, 1. $\tilde{U} = U/\Gamma = 20$, $\tilde{t} = t/\Gamma = 0.02$ (top panel). The same calculated with the BISEA (bottom panel) – we see that this approximation fails to capture the high-bias ($eV \sim 10\Gamma \sim U$) features adequately. In both cases increasing λ from $0.5 \rightarrow 1$ leads to a decrease in the width of the zero-bias (Kondo) peak.

high bias.

CHAPTER 5

Two-channel Kondo physics in the 2AIM

In the previous chapter we studied the low-temperature behaviour of the 2AIM over a wide range of parameters, showing that the system exhibits a rich range of Kondo physics. One aspect of the 2AIM that we did not look at was the possibility of observing two-channel Kondo (2CK) physics, and it is to this that we now turn our attention.

2CK physics is known to arise in the 2IKM [25, 44–51]. At the critical point ($J = J_c$), which separates the LS and KS phases, the system ultimately flows to neither the local singlet (LS) or Kondo singlet (KS) fixed points (FPs), rather it flows to the 2CK FP on the lowest energy scales [50, 51, 114]. All the FPs discussed in chapter 4 are Fermi liquid FPs, the effective Hamiltonians for which may be written simply in terms of a pair of free leads (with possible potential scattering) and free impurity spins/levels. The impurity contribution to the entropy of the system near any of these FPs is $\ln N$, with N an integer describing the ground state degeneracy of the impurities in the effective Hamiltonian. On the other hand, when a system is near the non-Fermi liquid 2CK FP the impurity contribution to the entropy is $\frac{1}{2}\ln 2$, as discussed in chapter 1.

As discussed in section 2.7, the 2AIM (in the regime in which there is essentially one electron on each dot) is related to the 2IKM by a second-order Schrieffer-Wolff (SW) transformation. Given that this is case, the question naturally arises, can 2CK physics be observed in the 2AIM, or equivalently, are there any circumstances in which the 2AIM flows near to the 2CK FP? To answer this question, the terms arising from the *third-order* SW transformation of the 2AIM (see section 2.9) must be accounted for, as these involve interlead charge transfer, which is known to destabilise the 2CK FP for the 2IKM [49, 59, 60, 115], such that the FP is unstable for all values of interdot exchange coupling, J. Due to this interlead charge transfer, the 2CK FP is always unstable for the 2AIM [59, 60, 91–94, 96], and as such the system ultimately flows to a SC FP as $T \to 0$. Provided the terms which destabilise

the 2CK FP are small, however, the system may still flow near to the 2CK FP over an appreciable temperature range [59]. In cases where the system does flow near to the 2CK FP, we label the scale on which it does so, $T_{\rm K}^{2CK}$. The scale on which the system then flows on to a SC FP is labeled T^*. Provided there is a clear scale separation, $T^* \ll T_{\rm K}^{2CK}$, the 2AIM is near to the 2CK FP in the temperature range, $T^* \ll T \ll T_{\rm K}^{2CK}$.

We begin this chapter then by briefly summarising the well-known behaviour of the 2IKM, and then go on to look at the effect of interlead charge transfer, as included in the 2AIM. Comparing the 2AIM to its effective low-energy model derived via third-order SW transformation; the H_3 model (see section 2.9), the low-temperature properties of these two models are found to agree closely, as one would expect. We also compare these two models to the H_3' model, studied in Ref. [59], comprised of the 2IKM with an additional *direct* interlead charge-transfer term (see section 2.9). The behaviour of this model is noticeably different from the 2AIM and H_3 models, showing that the *cotunneling* interlead charge transfer present in the 2AIM/H_3 model has a more significant effect on destabilising the 2CK FP than the direct interlead charge-transfer term present in the H_3' model.

Charge transfer is suppressed for the LR and ph-symmetric 2AIM as $\tilde{U} = U/\Gamma$ is increased. For sufficiently large values of $\tilde{U}$, the scale separation $T^* \ll T_{\rm K}^{2CK}$ is achieved, such that 2CK physics arises for temperatures $T^* \ll T \ll T_{\rm K}^{2CK}$. This is indicated by a plateau in the impurity contribution to the entropy of $S_{\rm imp} = \frac{1}{2}\ln 2$, corresponding to flow near to the 2CK FP. However, for the large values of $\tilde{U}$ required to achieve the scale separation, the $T_{\rm K}^{2CK}$ scale is very small, such that 2CK physics cannot be observed in the LR and ph-symmetric 2AIM at experimentally realisable temperatures.

We go on to look at the effect of an interdot repulsion on the 2CK physics in the LR and ph-symmetric 2AIM, particularly to see whether this increases the temperature scale on which 2CK physics can be observed. Provided $U' \ll U$, the interdot repulsion is found to have little effect on the temperature range in which 2CK physics occurs. We also study the 2AIM away from ph symmetry, concentrating on the LR-symmetric case for simplicity, to see if ph asymmetry is helpful in increasing the scale on which 2CK physics occurs. This is however not the case. We therefore conclude that observation of genuine 2CK physics in an experimental tunnel-coupled DQD system, as modelled by the 2AIM, is unlikely at the current time.

As it is the interlead charge transfer present in the 2AIM that prevents observation of 2CK physics at experimental temperatures, one may ask whether systems with three or four (or even more) quantum dots in series between two leads might provide a better pathway for observing 2CK physics; interlead charge transfer being reduced as more dots are placed between the leads [117]. We address this ques-

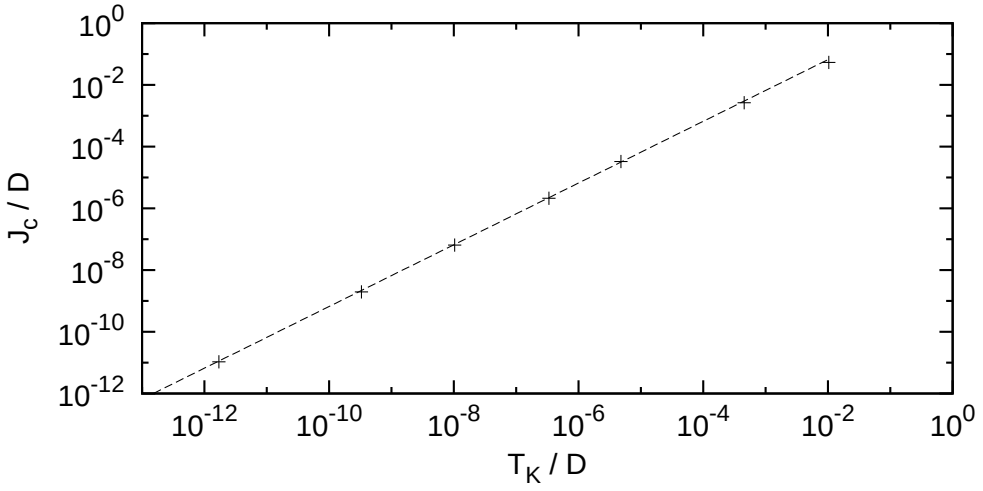


Figure 5.1: The critical interimpurity exchange coupling, J_c, plotted against the Kondo scale, T_K, for the LR-symmetric 2IKM with various values of $J_1 = J_2$ (crosses). Also plotted is $J_c = \alpha T_\mathrm{K}$ with $\alpha \simeq 8$ (dashed line), which is seen to agree closely with the data. T_K is defined via $S_\mathrm{imp}(T = T_\mathrm{K}) = \ln 2$ for the $J = 0$ system.

tion in the final section of this chapter, and conclude that whilst these systems are more likely to exhibit 2CK physics at experimentally realisable temperatures, their manufacture is likely to be difficult.

5.1 Two-impurity Kondo model

We begin with a brief overview of the 2CK physics exhibited by the 2IKM (see section 2.8 for details of the model). It is well known that the LR-symmetric 2IKM ($J_1 = J_2$) exhibits a quantum phase transition (QPT), separating KS and LS phases, at a critical value of the interimpurity exchange coupling J; with $J_c \sim \mathcal{O}(T_\mathrm{K})$, and T_K the Kondo scale of the system when the spins are decoupled, $J = 0$ [25, 45–47, 49]. The FP for the transition is distinct from those of the LS or KS phases, and corresponds to the 2CK FP, as known, *e.g.*, from conformal field theory [25, 49–51, 116] and NRG [25] (strictly, the critical FPs for the 2IKM and the 2CK model lie on a marginal manifold parameterised by potential scattering [116], such that the finite size spectra for the two FPs differ [25, 116]). On decreasing the temperature/energy scale at $J = J_c$, the system flows from a LM FP – where the dot spins are effectively decoupled from each other and from the leads, with a corresponding entropy $S_\mathrm{imp} = \ln 4$ – to the critical 2CK FP characterised by $S_\mathrm{imp} = \frac{1}{2}\ln 2$, on the scale $T \sim T_\mathrm{K}$ (so that T_K is also in effect the two-channel Kondo scale, *i.e.*, $T_\mathrm{K}^{2CK} \sim T_\mathrm{K}$). As one approaches the QPT ($|J - J_c| \to 0$), the T^* scale vanishes in power law fashion, with $T^* \sim |J - J_c|^2/T_\mathrm{K}$ [49, 59, 112, 116, 118, 153], and as the 2CK FP is stable

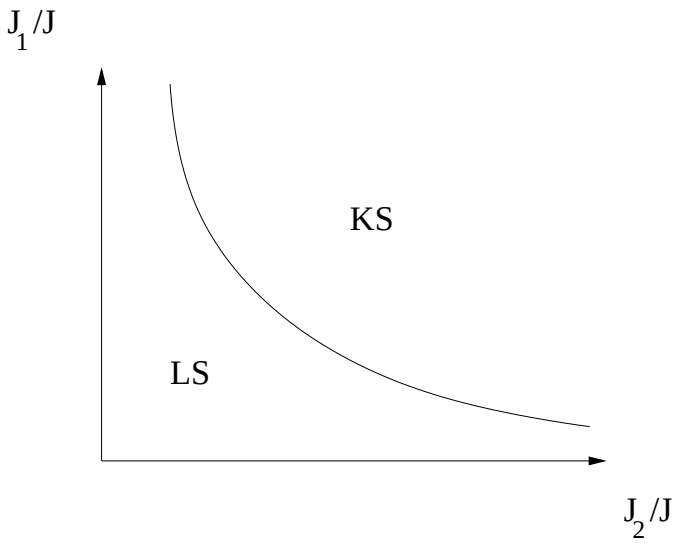


Figure 5.2: Schematic phase diagram for the 2IKM in the J_1-J_2 plane, for a fixed J. Along the phase boundary the 2CK FP is the stable FP for the system, and as such $T^* = 0$ along this line.

precisely at the QPT, the T^* scale is zero here.

We comment in passing on the relation [45–48, 95] $J_c = \alpha T_K$ with α a constant, which we find from NRG calculations indeed holds for sufficiently small $\rho J_1 \ll 1$. The precise value of α naturally depends on how T_K (pertaining to $J = 0$) is defined; and in this there is freedom of choice. In practice we choose T_K to be the temperature for which $S_{imp}(T_K) = \ln 2$, halfway between $S_{imp} = \ln 4$ characteristic of the LM FP and the zero-temperature entropy $S_{imp} = 0$ for the stable strong coupling FP in the KS phase. With this, the constant $\alpha \simeq 8$, as shown in Fig. 5.1, in which we plot J_c against T_K and find straight line behaviour. If instead we had chosen to define T_K as 8/2.2 times the temperature for which $S_{imp} = \ln 2$, then $\alpha \simeq 2.2$; as often quoted in the literature [45–48, 95]. There is however no fundamental distinction between these different practical definitions of T_K.

While the comments above refer to the LR-symmetric case, the QPT is also known [112, 116, 117] to remain robust to LR asymmetry, $J_1 \neq J_2$, with a line of 2CK critical FPs in the (J_1, J_2) plane separating LS and KS phases (illustrated in Fig. 5.2); and a critical J_c dependent on both $T_K^{(1)}$ and $T_K^{(2)}$, the two distinct $J = 0$ Kondo scales now arising. In the strongly LR-asymmetric case (taking $J_1 \gg J_2$), one can understand physically the existence of a critical J_c (for which the system flows to the 2CK FP) as follows [112, 117]. As the temperature is lowered, spin 1 forms a Kondo singlet with lead 1 on the scale of $T_K^{(1)}$ ($\gg T_K^{(2)}$). On energy scales below $T_K^{(1)}$ the effective model which remains is comprised of spin 2, coupled to lead 2 with a *renormalised* coupling, $\tilde{J}_2$, and also coupled to lead 1 via virtual polarisation of the Kondo singlet, with antiferromagnetic coupling, $J_1^{\rm eff}$. The effective model is

therefore of 2CK form, with the couplings to the two leads given by [112, 117, 157]:

$$\begin{aligned} \rho\tilde{J}_2 &\sim \left[\frac{1}{\rho J_2} - \frac{1}{\rho J_1}\right]^{-1} , \\ \rho J_1^{\text{eff}} &\sim \frac{J}{T_{\text{K}}^{(1)}} . \end{aligned} \tag{5.1}$$

Since only J_1^{eff} is dependent on J, one can tune J to give $J_1^{\text{eff}} = \tilde{J}_2$, in which case the spin is symmetrically coupled to the two leads and the system therefore flows to the 2CK FP, as the two leads overscreen the spin (see section 2.5). The J which achieves this is $J = J_c$ with [112, 117, 157]

$$J_c \sim \left[\frac{1}{\rho J_2} - \frac{1}{\rho J_1}\right]^{-1} T_{\text{K}}^{(1)} \tag{5.2}$$

in the limit of extreme asymmetry ($\frac{J_1}{J_2} \to \infty$). In the LR-asymmetric case it is found that $T_{\text{K}}^{2CK} \sim \min(T_{\text{K}}^{(1)}, T_{\text{K}}^{(2)})$ [112] (recall that in the LR-symmetric case, $T_{\text{K}}^{2CK} \sim T_{\text{K}}$).

5.2 Effect of charge transfer

Having discussed the 2CK physics that arises in the 2IKM (regardless of LR asymmetry) at the critical point ($J = J_c$), we now look at the effect of adding interlead charge transfer processes to the 2IKM, focussing on the LR-symmetric case. These destroy the QPT occurring in the 2IKM, and with it the stability of the 2CK quantum critical point; the pristine transition being replaced by a continuous crossover between KS and LS ground states, characterised by a stable SC FP with $S_{\text{imp}}(T = 0) = 0$. This is well known for the 2AIM [91, 92, 94] and H_3' [59, 60, 115] models; and our NRG calculations indicate the same for the H_3 model (unsurprisingly, it being the effective low-energy model for the 2AIM).

Although the 2CK FP is rendered unstable by charge transfer, with decreasing T the system may first flow close to it on a scale $T \sim T_{\text{K}}$ (as for the 2IKM) – evident, *e.g.*, in a characteristic $\frac{1}{2}\ln 2$ entropy plateau – before flowing to the stable SC FP on a low-energy Fermi liquid scale T^* (which we calculate in practice from $S_{\text{imp}}(T^*) = \frac{1}{4}\ln 2$, halfway between the characteristic values for the 2CK FP and stable SC FP). *If* this situation arises, then the 2CK FP is effectively 'visible' at finite temperature, occurring over an appreciable T-window provided

$$T^* \ll T \ll T_{\text{K}} . \tag{5.3}$$

The obvious questions then are [59]: under what conditions does this behaviour

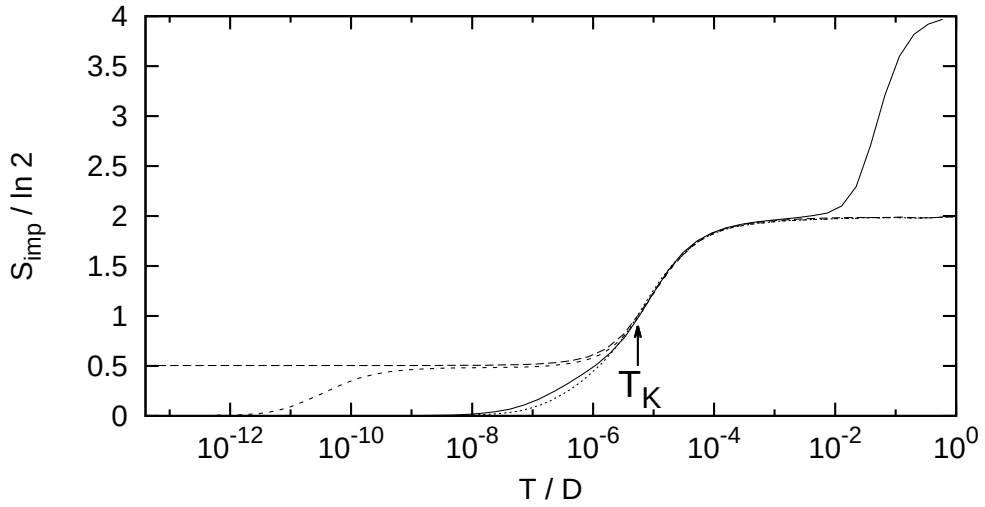


Figure 5.3: $S_{\rm imp}(T)$ for: the LR and ph-symmetric 2AIM with $t = t_c$ and $\tilde{U} = U/\Gamma = 20$ (solid line), and the 2IKM (long-dashed), the H_3 model (dotted line) and the H_3' model (short-dashed line) with $\rho J_1 = \rho J_2 = 0.093$, $J = J_c$. The H_3 and H_3' models have charge-transfer coefficients appropriate for comparison to the 2AIM model. The common Kondo scale, $T_{\rm K}$, is indicated by an arrow.

arise? And for the 2AIM in particular (as the canonical model for TCDQDs), does it occur for experimentally realistic temperatures?

To answer these questions we consider explicitly the temperature dependence of the entropy, $S_{\rm imp}(T)$. As for the 2IKM, $T_{\rm K}$ is the Kondo scale when the spins/dots are decoupled, viz. $J = 0$ for the spin-models H_3 and H_3', and $t = 0$ for the 2AIM; with $T_{\rm K}$ defined via $S_{\rm imp}(T_{\rm K}) = \ln 2$, as above (although in practice the resultant $T_{\rm K}$ differs insignificantly from that which can be read off, *e.g.*, Fig. 5.3 from $S_{\rm imp}(T_{\rm K}) = \ln 2$ for the systems with their critical interdot coupling, $J = J_c$ for the spin models and $t = t_c$ for the 2AIM). To optimise the possibility of observing the 2CK FP at finite temperature we follow Ref. [59] and consider $J = J_c$ ($\sim T_{\rm K}$) for all spin models and $t = t_c$ for the 2AIM – where the models flow closest to the 2CK FP – chosen [59] in either case so that the even-channel phase shift $\delta_{e\sigma} = \frac{\pi}{4}$.

Fig. 5.3 shows NRG results for $S_{\rm imp}(T)$ for the LR and ph-symmetric 2AIM with $U/\Gamma = \tilde{U} = 20$ (solid line), with $T_{\rm K}$ as indicated. We wish to compare this to spin-models (H_3, H_3' and 2IKM) with the same $T_{\rm K}$, to which end we consider $\rho J_1 = \rho J_2 = 0.093$ (which value differs somewhat from that given by the SW transformation, reflecting simply the fact that for $\tilde{U} = 20$ the SW asymptotics for ρJ_1 have not quite been reached). And for the spin models with charge transfer, we take $V_{LR} = \sqrt{J_c J_1^2/U}$, as in section 2.9 (just after Eqn. (2.28)).

On decreasing temperature for the 2IKM with $J = J_c$ (long-dashed line in Fig. 5.3), the system naturally flows to the 2CK FP ($S_{\rm imp} = \frac{1}{2}\ln 2$) for $T \sim T_{\rm K}$, and

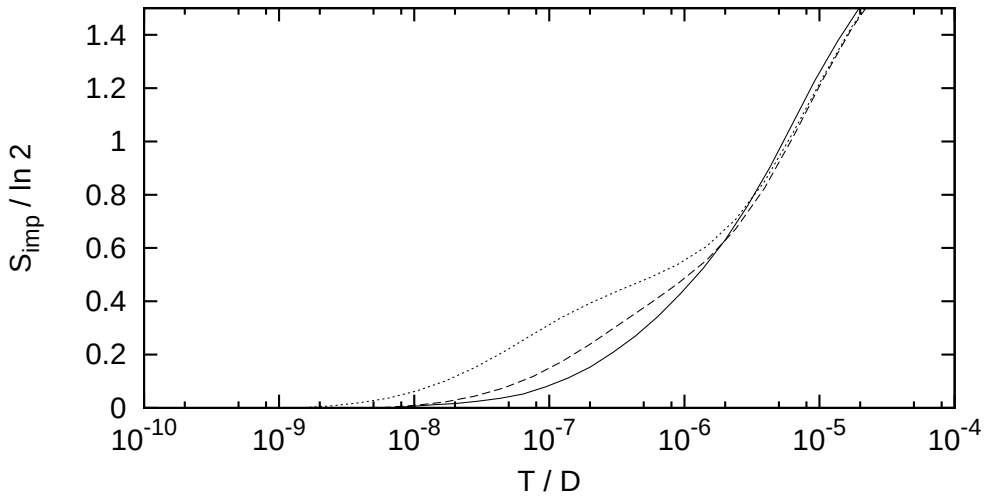


Figure 5.4: $S_{\rm imp}(T)$ for the full H_3 model (solid line), as well as the H_3 model without the second ($\hat{\mathbf{S}}_1 \times \hat{\mathbf{S}}_2$) term in Eqn. (5.4) (dotted line), and the H_3 model without the first ($\hat{\mathbf{S}}_1 \cdot \hat{\mathbf{S}}_2$) term in Eqn. (5.4) (dashed line). A $\frac{1}{2}\ln 2$ plateau is slightly more prominent for the "reduced" H_3 models, with the second term in Eqn. (5.4) having a slightly greater effect on $S_{\rm imp}(T)$. The parameters used are the same as those in Fig. 5.3.

remains there. For the H_3' model (short-dashed line), with direct interlead tunneling, there is a clear $\frac{1}{2}\ln 2$ entropy plateau before flow to the stable SC FP ($S_{\rm imp} = 0$) on the scale $T \sim T^*$; with $T^* \ll T_{\rm K}$ in this case, so that 2CK physics arises over an appreciable temperature window. The behaviour of the LR and ph-symmetric 2AIM with $\tilde{U} = 20$ (solid line) is quite different. After descent on the scale $T \sim U$ from its trivial high-temperature limit $S_{\rm imp} = \ln 16$ to the LM FP with $S_{\rm imp} = \ln 4$, the system flows *directly* to the SC FP on the scale $T \sim T_{\rm K}$; with no hint of flow in the vicinity of the 2CK FP. The H_3 model (dotted line) is also seen to exhibit the same low-energy behavior.

Concentrating on the H_3 model for a moment, it is interesting to consider which of the interlead charge-transfer terms has the greatest effect in destabilising the 2CK FP. To reiterate, the charge-transfer terms in the H_3 model are given by (cf. Eqn. (2.28))

$$\hat{H}_3 = V_{LR}\left[\sum_\sigma (f^\dagger_{1\sigma} f_{2\sigma} + f^\dagger_{2\sigma} f_{1\sigma})\hat{\mathbf{S}}_1 \cdot \hat{\mathbf{S}}_2 + 2\hat{\mathbf{A}} \cdot (\hat{\mathbf{S}}_1 \times \hat{\mathbf{S}}_2)\right] . \qquad (5.4)$$

To investigate which of the two charge-transfer terms (the $\hat{\mathbf{S}}_1 \cdot \hat{\mathbf{S}}_2$ term and the $\hat{\mathbf{S}}_1 \times \hat{\mathbf{S}}_2$ term) is more significant, *i.e.*, which gives a greater contribution to the T^* scale, we have studied the H_3 model excluding each of the charge-transfer terms in turn. Taking $\rho J_1 = \rho J_2 = 0.093$, $J = J_c$ and $V_{LR} = \sqrt{J_c J_1^2/U}$, $S_{\rm imp}(T)$ for each of these "reduced" H_3 models is shown in Fig. 5.4, and compared to the full H_3 model. We see that the two charge-transfer terms have a not dissimilar effect on destabilising

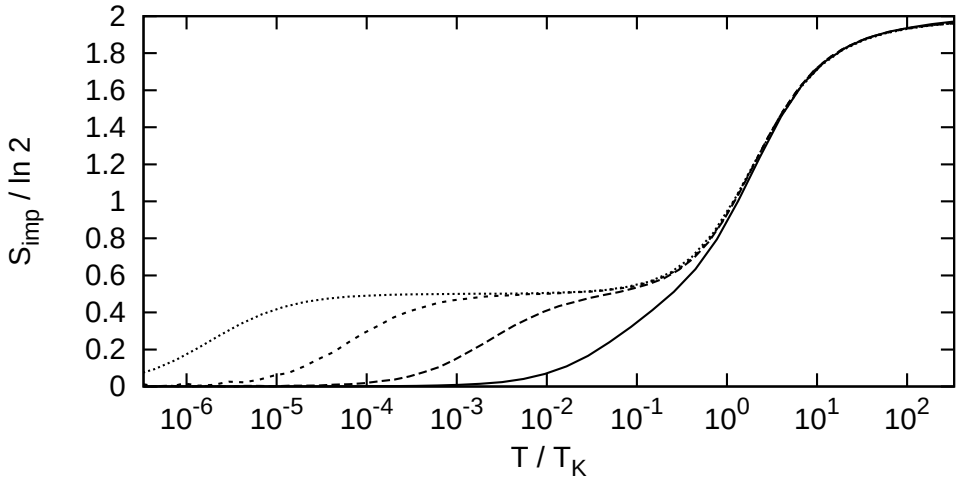


Figure 5.5: $S_{\rm imp}(T)$ for the 2AIM with $t = t_c$ and $\tilde{U} = U/\Gamma = 20$ (solid line), 30 (long-dashed line), 40 (short-dashed line), 50 (dotted line). A plateau at $S_{\rm imp} = \frac{1}{2}\ln 2$ appears as $\tilde{U}$ is increased. The data have been scaled by the Kondo temperature of the system.

the 2CK FP, as illustrated by the fact that the two "reduced" H_3 models have roughly similar T^* scales (the scale on which $S_{\rm imp} \to 0$ in Fig. 5.4), although the second term ($\hat{\mathbf{S}}_1 \times \hat{\mathbf{S}}_2$) seems to be slightly more significant. The key point is that Fig. 5.4 shows that both of the two charge-transfer terms are important and neither should be neglected in an effective, low-energy description of the 2AIM. In Ref. [59] the $\hat{\mathbf{S}}_1 \times \hat{\mathbf{S}}_2$ term was neglected (and $\hat{\mathbf{S}}_1 \cdot \hat{\mathbf{S}}_2$ replaced by its expectation value at the critical point [60]); unsurprisingly in light of the above data, the resulting model does not reproduce the low-temperature physics of the 2AIM.

Returning to the LR and ph-symmetric 2AIM, the 2CK FP, as manifest in a $\frac{1}{2}\ln 2$ entropy plateau, does not then occur for $\tilde{U} = U/\Gamma = 20$ (or in its effective low-energy model, H_3, see Fig. 5.3). To observe it in the 2AIM necessitates a larger $\tilde{U}$ in order to suppress interlead cotunneling charge transfer (*i.e.*, to reduce V_{LR} in the effective low-energy model), although this also reduces $T_{\rm K}$ itself (since [3] $T_{\rm K} \propto \exp[-\pi\tilde{U}/8]$). To illustrate this, Fig. 5.5 shows $S_{\rm imp}(T)$ *vs* $T/T_{\rm K}$ for the LR and ph-symmetric 2AIM, for increasing values of $\tilde{U}$, with $t = t_c$. On increasing the interaction strength, a $\frac{1}{2}\ln 2$ entropy plateau appears, indicating the opening of a temperature window in which the system flows in the vicinity of the 2CK FP, with a clear scale separation $T^* \ll T_{\rm K}$ for sufficiently large $\tilde{U}$, in practice $U/\Gamma \gtrsim 40$. In this regime, we find that

$$T^* = b\left(\frac{U}{\Gamma}\right)^2 \frac{T_{\rm K}^2}{U}\ , \quad \text{2AIM} \tag{5.5}$$

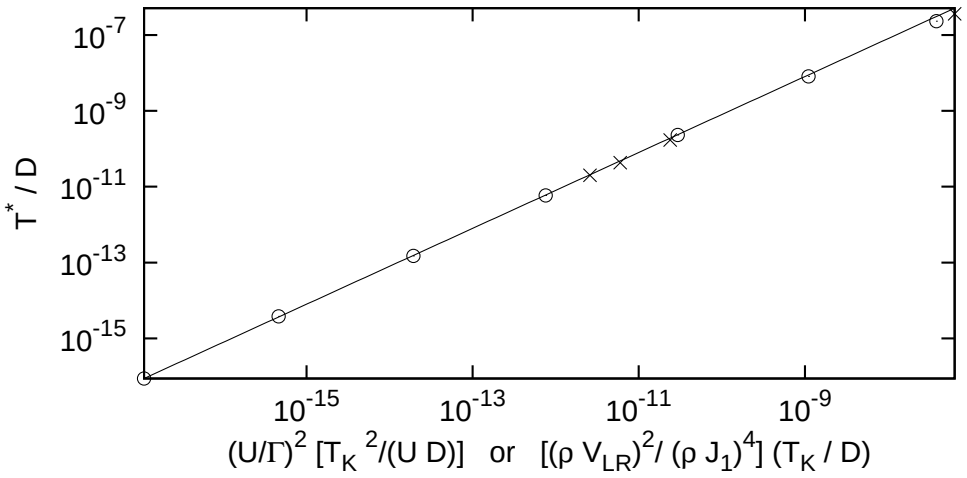


Figure 5.6: T^*/D against $\tilde{U}^2 T_{\rm K}^2/(UD)$ for the LR and ph-symmetric 2AIM with $t = t_c$ (circles), and against $[(\rho V_{LR})^2/(\rho J_1)^4](T_{\rm K}/D)$ for the H_3 model with $J = J_c$ and $V_{LR} = \sqrt{J_1^2 J_c/U}$ (crosses). Also plotted is the line $y \simeq 8x$. Data for both models fall onto this line when plotted in this way, verifying Eqns. (5.5) and (5.6).

with $b \simeq 8$ a constant. Using the SW expressions for the coefficients in the H_3 model (see sections 2.7 and 2.9, Eqns. (2.26) and (2.28)) to convert the above equation into an equation for T^* for the H_3 model gives

$$T^* = a \frac{1}{(\rho J_1)^4} (\rho V_{LR})^2 T_{\rm K} \ , \qquad H_3 \text{ model} \tag{5.6}$$

with $a \simeq b$ (from the NRG we find that $a \simeq b \simeq 8$). This equation, and the above equation for the 2AIM, is verified in Fig. 5.6. The behaviour $T^* \propto T_{\rm K}^2$ not only arises in the 2AIM, but also [59] in the H_3' model. Here it is found [59] that

$$T^* = b' (\rho V'_{LR})^2 T_{\rm K} \ , \qquad H_3' \text{ model} \tag{5.7}$$

with $b' \sim 10^2$ approximately constant, $V'_{LR} = \frac{1}{4} V_{LR}$ and (as above) $(\rho V_{LR})^2 = J_c (\rho J_1)^2/U$. Since $J_c \sim T_{\rm K}$ itself, Eqn. (5.7) gives $T^* \propto T_{\rm K}^2$, as does Eqn. (5.6). The key difference between the expression for T^* for the H_3 and H_3' models is then the $(\rho J_1)^{-4}$ factor, which means that T^* is always (for strong correlations, $\rho J_1 \ll 1$) greater for the 2AIM/H_3 model than for the H_3' model, so it will be much more difficult to satisfy Eqn. (5.3), and thereby observe 2CK physics, in the 2AIM/H_3 model than in the H_3' model. We conclude that cotunneling interlead charge transfer, as present in the 2AIM/H_3 model, is more disruptive to 2CK physics in the 2IKM than direct interlead charge transfer, as present in the H_3' model.

As mentioned above, increasing $\tilde{U}$ in the 2AIM in order to access a reasonable

temperature window for 2CK physics, naturally has the effect of reducing $T_{\rm K}$, temperatures lower than which are needed to access the 2CK regime. From Fig. 5.5, $\tilde{U} \gtrsim 40$ is in practice required for a reasonable window to arise. But for $\tilde{U} = 40$, our NRG results give $T_{\rm K}/U \sim 4 \times 10^{-9}$. Taking $U = 2$ meV, as is experimentally typical [68, 81, 85, 158], this corresponds to $T_{\rm K} \sim 10^{-7}$ K – far lower than can be reached in experiment (a minimum of around 10 mK). Even reducing $\tilde{U}$ to 30, where a $\frac{1}{2}\ln 2$ 'plateau' is just about visible in Fig. 5.5, yields $T_{\rm K} \sim 10^{-5}$ K, some three orders of magnitude lower than what is experimentally feasible. In contrast to previous estimates (based on study of the H_3' model [59]), our conclusion is that it is highly unlikely 2CK physics could realistically be observed in TCDQDs.

A notable feature of all the above models, and indeed of the 2CK model, is that, provided the systems flow near to the 2CK FP for some range of temperatures, *i.e.*, provided $T^* \ll T_{\rm K}^{2CK}$, the RG flow from the 2CK FP on to a SC FP is universal [114, 115]; the physics of these systems on energy scales $\ll T_{\rm K}^{2CK}$ is a universal function of T^*. This is manifest in the entropy graphs shown in Fig. 5.5, for which the entropy curves for $T \ll T_{\rm K}^{2CK} \sim T_{\rm K}$ can be rescaled onto a single universal curve (for values of $\tilde{U}$ for which there is a separation of energy scale, $T^* \ll T_{\rm K}^{2CK} \sim T_{\rm K}$). This universality is discussed in detail in Ref. [114], and the analytic crossover function for the entropy (valid for $T \ll T_{\rm K}$ provided $T^* \ll T_{\rm K}$) is [58, 114]

$$S_{\rm imp}(T) = \tfrac{1}{2}\ln 2 + \tilde{S}\left(\frac{T}{\tilde{T}^*}\right) \ , \tag{5.8}$$

where the universal function $\tilde{S}(t)$ is given by

$$\tilde{S}(t) = \frac{1}{t}\left[\psi\left(\tfrac{1}{2}+\frac{1}{t}\right) - 1\right] - \ln\left[\frac{1}{\sqrt{\pi}}\Gamma\left(\tfrac{1}{2}+\frac{1}{t}\right)\right] \ , \tag{5.9}$$

with $\psi(z)$ the digamma function, $\Gamma(z)$ is the gamma function, and $\tilde{T}^*$ is a particular definition of the crossover scale on which the system flows from the 2CK FP to a SC FP, found to be proportional to our definition such that $\tilde{T}^* \simeq 1.8 \times T^*$. In Fig. 5.7 we show $S_{\rm imp}(T)$ for a number of quite different systems, all of which flow near to the 2CK FP before flowing on to a SC FP, with the temperature rescaled in terms of T^*. We see that all the entropy curves collapse on to the universal entropy curve (Eqn. (5.8)), as discussed in Ref. [114].

While we have focussed above on LR-symmetric two-impurity systems, the physics of the models considered remains qualitatively the same when LR symmetry is broken: interlead charge transfer, whether of cotunneling or direct form, destroys the QPT exhibited by the 2IKM. If we consider breaking LR symmetry by decreasing just one of the dot-lead couplings, then interlead charge transfer is suppressed, leading to a decrease in the T^* scale. This raises the question whether 2CK physics

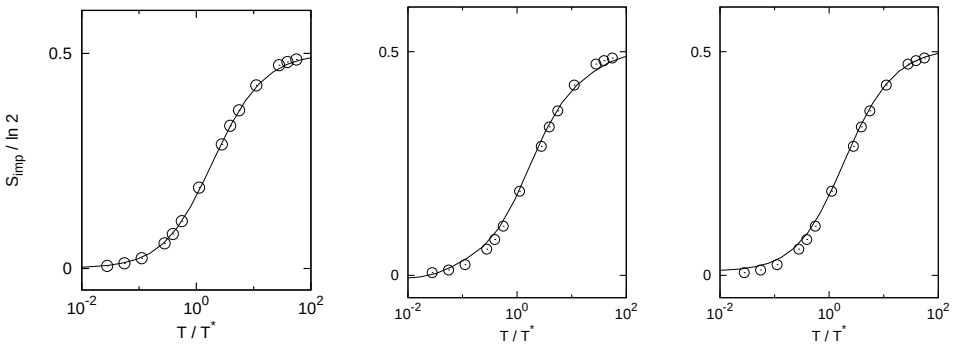


Figure 5.7: $S_{\rm imp}(T)$ for a number of different models all with $T^* \ll T_{\rm K}$ showing that, upon rescaling the temperature in terms of T^*, the entropy curve for the crossover from the 2CK FP ($S_{\rm imp} = \frac{1}{2}\ln 2$) to the SC FP ($S_{\rm imp} = 0$) is universal. The models shown here are: the LR and ph-symmetric 2AIM with $\tilde{U} = 50$ and $t = t_c$ (left panel), the H_3' model with $\rho J_1 = \rho J_2 = 0.093$, $J = J_c$, $\rho V_{LR} = 5 \times 10^{-5}$ (middle panel), and the 2CK model with $\rho J_1 = 0.093$ and $\rho J_2 = 0.0925$ (right panel). These models all flow near to the 2CK FP before flowing on to a SC FP when $T \sim T^*$ due to cotunneling interlead charge transfer (for the 2AIM), direct interlead charge transfer (for the H_3' model), and LR asymmetry (for the 2CK model). The circles give the analytic universal crossover function described in the text (Eqn. (5.8)), which is seen to agree well with all three sets of data.

might more readily be observed in a strongly asymmetric TCDQD device. That is not however the case. As for the LR-asymmetric 2IKM, the (experimentally relevant) 2AIM, if it flows at all in the vicinity of the 2CK FP, does so on the scale of $\min(T_{\rm K}^{(1)}, T_{\rm K}^{(2)})$. Decreasing, *e.g.*, Γ_2 at fixed Γ_1 will thus not only reduce the T^* scale, but also the scale $T_{\rm K}^{(2)}$ on which the system flows to the 2CK FP. Introducing LR-asymmetry in this way therefore decreases the temperature at which 2CK physics might be observed.

Dynamics

Having looked at the thermodynamic properties of the 2AIM with very strong correlations, we now move on to look at the dynamic properties of the system, beginning with the zero-bias, zero-temperature conductance, $G_c(0,0)$. Fig. 5.8 shows $G_c(0,0)$ against $J = 4t^2/U$ for the LR and ph-symmetric 2AIM with $\tilde{U} = 20$, and for the H_3 and H_3' models with $\rho J_1 = \rho J_2 = 0.093$ and $V_{LR} = \sqrt{J_1^2 J/U}$, the same parameters used in Fig. 5.3. The curves for the 2AIM and H_3 models are similar, as expected, given that the H_3 model is the low-energy effective model of the 2AIM (the difference reflects the fact that the SW transformation is only exact in the limit of strong correlations, $\tilde{U} \to \infty$). Most notable though is that the width of the conductance peak is much narrower for the H_3' model than for the other two models. In Ref. [59], it was shown that the width of the conductance peak for the H_3' model as a function of J is $\delta J \sim \sqrt{T_K T^*}$ (with T^* measured at the centre of the conductance

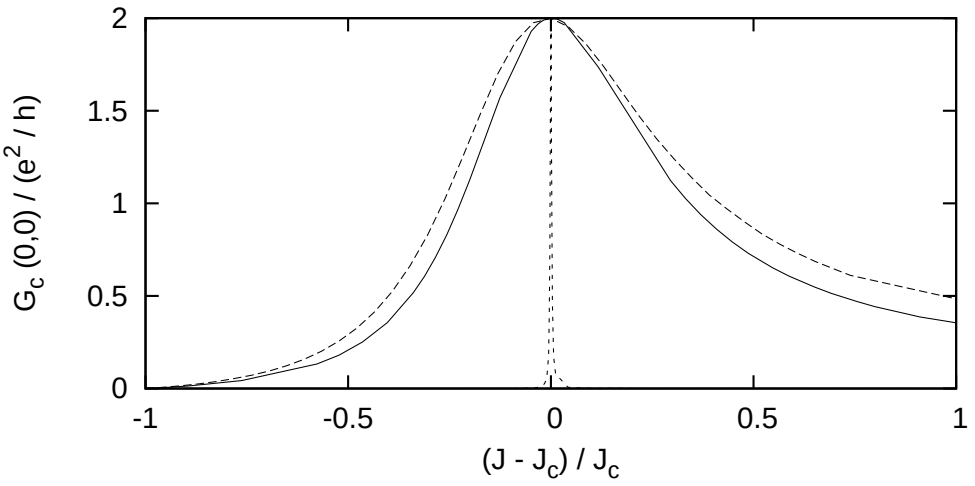


Figure 5.8: Zero-temperature, zero-bias conductance ($G_c(0,0)$) of the 2AIM (with $J = 4t^2/U$, solid line), the H_3 model (long-dashed line) and the H_3' model (short-dashed line). The parameters used are the same as those in Fig. 5.3.

peak, *i.e.*, for $J = J_c$), and the fact that its width in Fig. 5.8 is $\ll T_K \sim J_c$ indicates the clear scale separation $T^* \ll T_K$. For the 2AIM we have investigated the peak width as well, and this is shown in Fig. 5.9. We find that just as for the H_3' model, $\delta J \sim \sqrt{T_K T^*}$ for the 2AIM (with T^* again measured at the centre of the conductance peak, *i.e.*, with $t = t_c$). The much wider peak for the 2AIM than for the H_3' model in Fig. 5.8 indicates the much greater T^* scale. We stress that our conductance results are in full agreement with both previous work on the 2AIM [94], and recent work on the H_3' model [59, 60]: that the 2AIM and the H_3' model give different results is a natural consequence of the fact that they are not simply related by SW transformation.

In addition to the zero-bias conductance, one may also calculate the finite-bias conductance. We calculate this quantity (at zero temperature, $G_c(0,V)$) via the bias-independent self-energies approximation (Eqn. (3.65)), as illustrated in Fig. 5.10 (solid line) for the LR and ph-symmetric 2AIM with $t = t_c$ and $\tilde{U} = 50$, with clear scale separation, $T^* \ll T_{\rm K}$. There is a unitary zero-bias peak in $G_c(0,V)$ with width $\delta(eV) \sim \mathcal{O}(T^*)$.[1] This is consonant with recent work by Sela et al. [119], in which the finite-bias conductance of the H_3' model with $J = J_c$ was studied, and a zero-bias peak width of order T^* was found. Also plotted in Fig. 5.10 is the dot spectrum (dashed line) for the LR and ph-symmetric 2AIM with $\tilde{U} = 50$ and $t = t_c$. This has a zero-frequency value of $\pi\Gamma D_{11;\sigma}(0) = 0.5$, as discussed in section 4.2.3. In contrast to the finite-bias conductance, the T^* scale does not show up in the

[1] With T^* defined via the entropy ($S_{\rm imp}(T^*) = \frac{1}{4}\ln 2$), the peak half-width half-maximum is $\simeq 10T^*$.

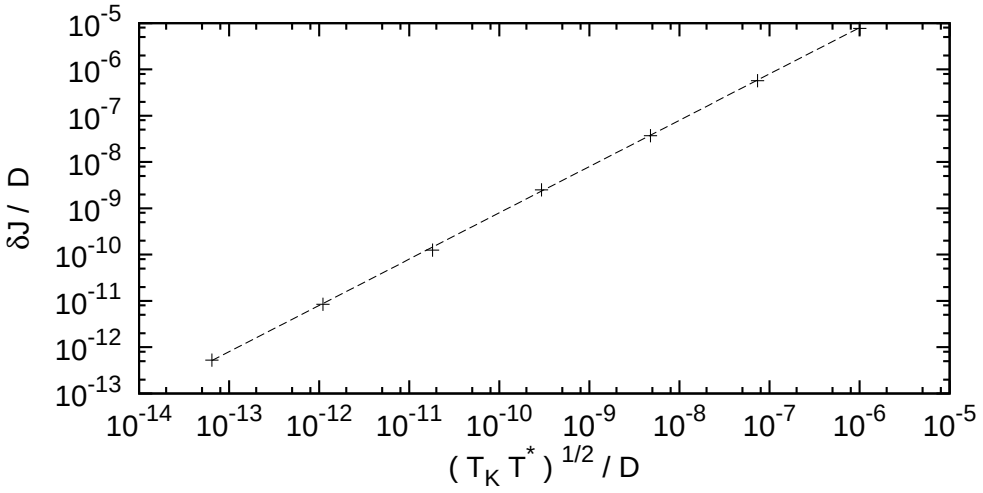


Figure 5.9: Half-width half-maximum (δJ) of the unitary conductance peak in the zero-bias, zero-temperature conductance of the LR and ph-symmetric 2AIM (crosses), plotted against $\sqrt{T_K T^*}$. We find that $\delta J \simeq 8\sqrt{T_K T^*}$, given by the dashed line. T_K and T^* are defined via $S_\mathrm{imp}(T^*) = \frac{1}{4}\ln 2$ with $t = t_c$, and $S_\mathrm{imp}(T_\mathrm{K}) = \ln 2$ for the $t = 0$ system.

spectrum, and the zero-frequency peak has a width $\sim \mathcal{O}(T_K)$.[2] This is in line with recent work on the H_3' model [115, 116], in which the spectrum was calculated for $J = J_c$ (see bottom-middle panel of Fig. 1 in Ref. [115] and LR-symmetric line in Fig. 2 of Ref. [116]). In Ref. [116] it is shown that for the LR-symmetric H_3' model with $J = J_c$, the zero-temperature spectrum goes as $\sim 0.5 + \alpha\omega$ in the limit of low frequency (with $\alpha > 0$ a constant). As the flow from the 2CK FP to the SC FP is universal, we would expect the same behaviour for the 2AIM (provided $T^* \ll T_\mathrm{K}$), which would yield a maximum in the spectrum at finite frequency. The maximum observed for the LR-symmetric H_3' model in Ref. [116] (Fig. 2) is however very slight. That we do not observe a maximum in our NRG results (Fig. 5.10, dashed line) is therefore perhaps unsurprising, given the broadening issues discussed previously in section 4.2.3.

5.3 Interdot repulsion

In any experimental tunnel-coupled double quantum dot (TCDQD) system, some degree of interdot electronic repulsion will arise, although physically one would expect $U' \ll U$. It is therefore interesting, and experimentally relevant, to ask what effect a small ($U' \ll U$) interdot repulsion term has on the possibility of observing 2CK physics in the 2AIM. As discussed in section 4.2.5, considering a second-order

[2] With T_K defined via the entropy ($S_\mathrm{imp}(T_K) = \ln 2$ for the $t = 0$ system), the peak half-width half-maximum is $\simeq 10T_K$.

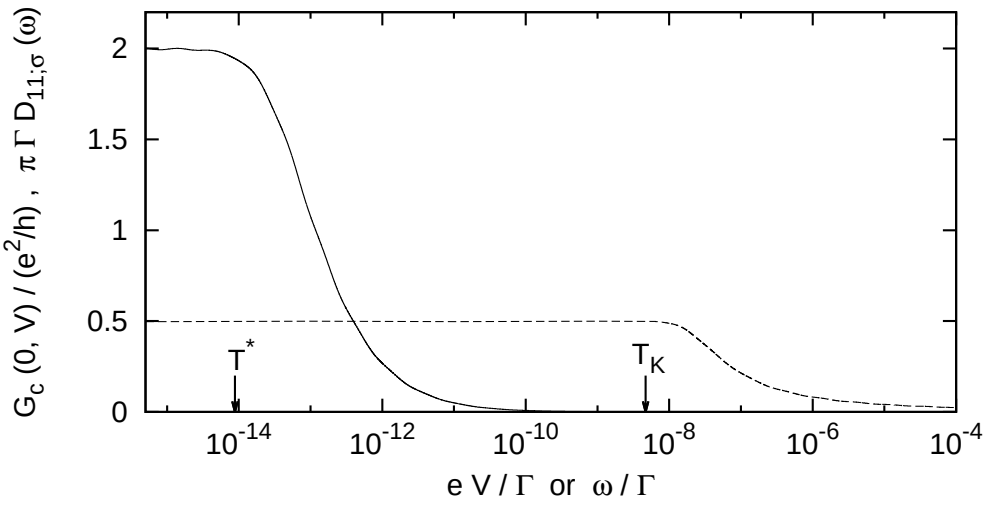


Figure 5.10: NRG-calcultate single-particle spectrum, $\pi\Gamma D_{11;\sigma}(\omega)$ (dashed line) and finite-bias, zero-temperature conductance, $G_c(0,V)$ (solid line) for the LR and ph-symmetric 2AIM with $\tilde{U} = U/\Gamma = 50$, $t = t_c$.

SW transformation of the LR-symmetric 2AIM at ph symmetry shows that t_c (recall that $\delta_{e\sigma}(t = t_c) = \pi/4$) depends on U' as follows (cf. Eqn. (4.30))

$$t_c = \sqrt{\frac{\alpha T_{\rm K}(U - U')}{4}} \ . \tag{5.10}$$

In order to investigate 2CK physics in the 2AIM with an interdot repulsion we must also consider the third-order terms arising from the SW transformation.[3] With finite U', and to leading order in U'/U, the third-order charge-transfer terms arising in the SW transformation become

$$\begin{aligned}\hat{H}_3(U') = {} & 2V_{LR}\left(1 + \frac{U'}{2U}\right)\hat{\mathbf{A}}\cdot\hat{\mathbf{S}}_1 \times \hat{\mathbf{S}}_2 \\ & + \left[V_{LR}\left(1 + \frac{U'}{2U}\right)\left(\hat{\mathbf{S}}_1\cdot\hat{\mathbf{S}}_2\right) - \frac{V_{LR}}{8}\left(\frac{U'}{U}\right)\right]\sum_\sigma\left(f^\dagger_{1\sigma}f_{2\sigma} + f^\dagger_{2\sigma}f_{1\sigma}\right) \ .\end{aligned} \tag{5.11}$$

Expanding Eqn. (5.10) in powers of U'/U, it is straightforward to show that to leading order in U'/U, $t_c = t_c^0(1 - \frac{U'}{2U})$, with t_c^0 the value of t_c for $U' = 0$. Putting this into Eqn. (5.11) and setting $t = t_c$ gives

$$\hat{H}_3(U', t = t_c) = \hat{H}_3(0, t = t_c^0) - \frac{V_{LR}^0}{8}\left(\frac{U'}{U}\right)\sum_\sigma\left(f^\dagger_{1\sigma}f_{2\sigma} + f^\dagger_{2\sigma}f_{1\sigma}\right) \ . \tag{5.12}$$

[3]It is relatively easy to generalise the third-order SW transformation outlined in Appendix A to finite U', as introducing a finite U' does not change the third-order terms which arise in the SW transformation, it only changes the energy denominators.

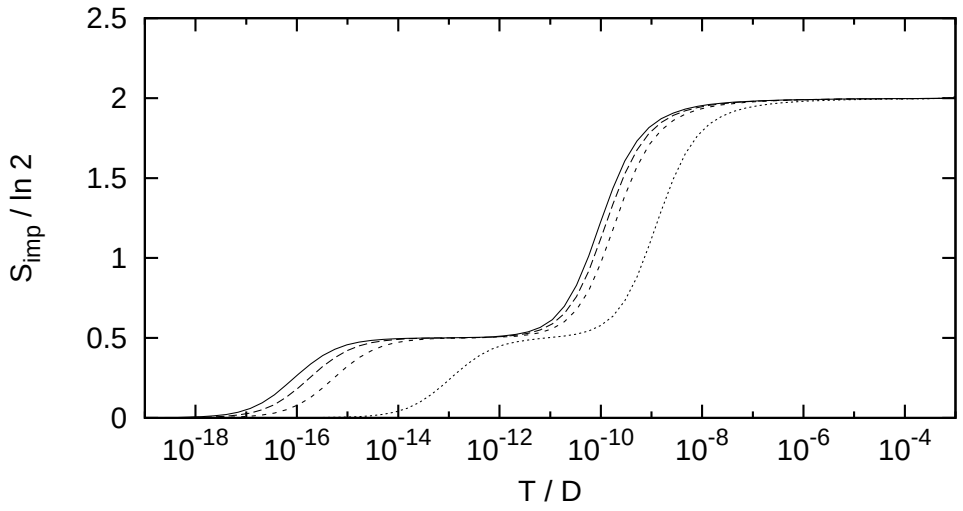


Figure 5.11: $S_{\rm imp}(T)$ for the LR and ph-symmetric 2AIM with $\tilde{U} = U/\Gamma = 50$, $t = t_c$ and $\tilde{U}' = U'/\Gamma = 0$ (solid line), 30 (long-dashed line), 40 (short-dashed line), 49 (dotted line). Even a relatively large $\tilde{U}' = 30$ has little effect on the $T_{\rm K}$ and T^* scales, as discussed in the text. Only when U' becomes comparable to U do the scales change significantly.

where V^0_{LR} is V_{LR} with $t = t^0_c$. So we find that, to leading order in U'/U, the only difference in the interlead charge-transfer terms created by a finite U', provided we retune $t^0_c \to t_c$, is an additional direct interlead hopping term with a relatively small coefficient (equal to $\frac{V^0_{LR}}{8}\left(\frac{U'}{U}\right)$). We have seen that such a term, present in the H'_3 model, gives a smaller contribution to T^* than the other terms present in Eqn. (5.12) [59, 60, 96], given by $\hat{H}_3(0, t = t^0_c)$. We therefore expect a small $U' \ll U$ to have little effect on the T^* scale. As discussed in section 4.2.5, a finite U' is not expected to affect $T_{\rm K}$ either (as it does not affect the effective dot-lead exchange couplings), and we therefore expect a small but finite U' to have little effect on the possibility of observing 2CK physics.

The energy scales T^* and $T_{\rm K}$ are clearly manifest in $S_{\rm imp}$, which is shown in Fig. 5.11 for the LR and ph-symmetric 2AIM with $\tilde{U} = 50$ (giving a clear separation of scales for $U' = 0$), and various values of U'. The entropy drops from $\ln 4$ on the scale of $T_{\rm K}$,[4] and T^* is the scale on which the entropy goes to zero; when the system is close to the 2CK FP $S_{\rm imp} \simeq \frac{1}{2}\ln 2$ [52, 53]. We can see that even a relatively large $\tilde{U}' = 30$ has little effect on the temperature range in which 2CK physics can be observed ($T^* \ll T \ll T_{\rm K}$), changing neither the $T_{\rm K}$ or T^* scales significantly, as discussed above. Increasing U' further, such that it is comparable with U and the above arguments become invalid, erodes the separation of energy scales, as can be seen in the $U'/\Gamma = 49$ data (dotted line), in Fig. 5.11. Increasing U' to this extent is therefore detrimental to the observation of 2CK physics[5].

[4] Recall that $T_{\rm K}$ is the Kondo scale for the $t = 0$ system, defined via $S_{\rm imp}(T_{\rm K}) = \ln 2$.

[5] The effect of increasing U' to such an extent is qualitatively similar to the effect of decreasing

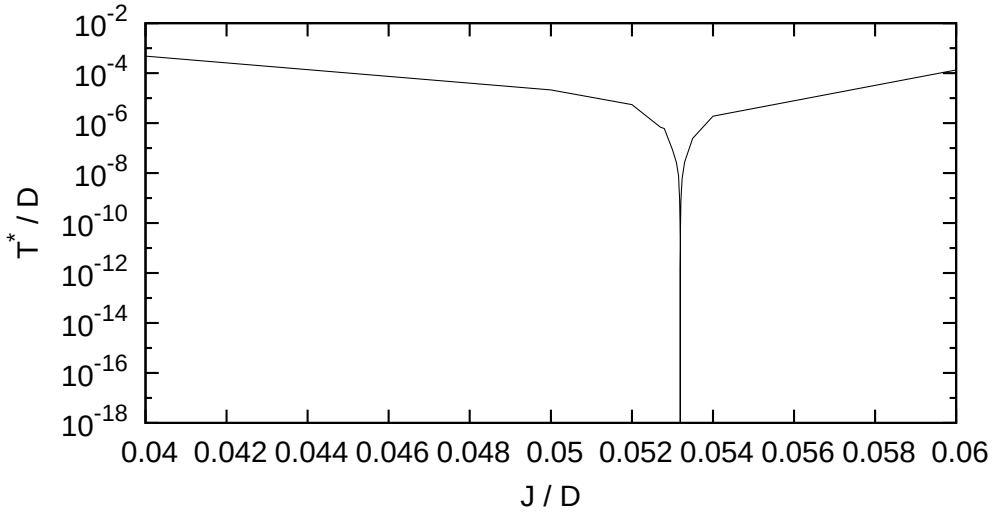


Figure 5.12: T^* against J for the LR-symmetric 2IKM with $\rho J_1 = \rho J_2 = 0.25$, and with an additional c term (given in Eqns. (5.13) and (5.20)) with $c = 0.001D$. The T^* scale vanishes at the point $J = J_c \simeq 0.053D$.

5.4 The 2AIM away from ph symmetry

Having established that 2CK physics is not likely to be observed in a TCDQD at ph symmetry, even one with an interdot repulsion, we now move on to investigate whether moving away from ph symmetry is helpful in increasing the temperature scale on which 2CK physics can be observed in a TCDQD. To investigate this, we carry out a SW transformation on the 2AIM away from ph symmetry, concentrating on the case of $\epsilon_1 = \epsilon_2 = \epsilon$ for simplicity. Provided the 2AIM is deep in the two-electron regime ($-U \ll \epsilon \ll 0$; $U/t, \tilde{U} \gg 1$), such that there essentially one electron on each dot, we may generalise the SW transformation carried out at ph symmetry (see Appendix A and Eqns. (2.26) – (2.29)) to arbitrary ϵ. Following the procedure described in Appendix A, after somewhat lengthy algebra, we find that the resulting low-energy effective model is given by

$$\begin{aligned}\hat{H}_{\text{eff}} &= \hat{H}_{\text{2IKM}} \\ &+ \sum_{\nu} K_\nu(\hat{n}_{0\nu} - 1) + \sum_{\sigma}(f^\dagger_{2\sigma} f_{1\sigma} + f^\dagger_{1\sigma} f_{2\sigma})(a + b\ \hat{\mathbf{S}}_1 \cdot \hat{\mathbf{S}}_2) \\ &+ 2b\hat{\mathbf{A}} \cdot (\hat{\mathbf{S}}_1 \times \hat{\mathbf{S}}_2) + c\hat{\mathbf{B}} \cdot (\hat{\mathbf{S}}_1 + \hat{\mathbf{S}}_2)\end{aligned} \tag{5.13}$$

U in the $U' = 0$ case – in either case both T^* and T_{K} increase, but T^* increases faster, so that the separation of scales is destroyed.

with $\hat{n}_{0\nu} = \sum_\sigma f^\dagger_{\nu\sigma} f_{\nu\sigma}$, $\nu = 1, 2$, and coefficients given by

$$J_\nu = -2NV_\nu^2 \left[\frac{1}{\epsilon} - \frac{1}{\epsilon + U}\right] , \tag{5.14}$$

$$J = 4t^2/U , \tag{5.15}$$

$$K_\nu = -\frac{NV_\nu^2}{2} \left[\frac{1}{\epsilon} + \frac{1}{\epsilon + U}\right] , \tag{5.16}$$

$$a = \frac{NV_1V_2t}{4} \left[\frac{1}{\epsilon^2} + \frac{1}{(\epsilon + U)^2} + \frac{2}{U}\left(\frac{1}{\epsilon} - \frac{1}{\epsilon + U}\right)\right] , \tag{5.17}$$

$$b = NV_1V_2t \left[\frac{1}{\epsilon^2} + \frac{1}{(\epsilon + U)^2} - \frac{2}{U}\left(\frac{1}{\epsilon} - \frac{1}{\epsilon + U}\right)\right] , \tag{5.18}$$

$$c = NV_1V_2t \left[\frac{1}{\epsilon^2} - \frac{1}{(\epsilon + U)^2}\right] . \tag{5.19}$$

$\hat{\mathbf{A}}$ is given in Eqn. (2.29), and the vector operator $\hat{\mathbf{B}}$, appearing in the final term in Eqn. (5.13) (which we denote the c term), is given by

$$\hat{\mathbf{B}} = \sum_{\sigma,\sigma'} \left(f^\dagger_{1\sigma} \boldsymbol{\sigma}_{\sigma\sigma'} f_{2\sigma'} + f^\dagger_{2\sigma} \boldsymbol{\sigma}_{\sigma\sigma'} f_{1\sigma'} \right) . \tag{5.20}$$

We note that $\hat{\mathbf{B}}$ obeys the same commutation relations as $\hat{\mathbf{A}}$ and it is therefore *not* a spin operator [96]. At ph symmetry the coefficients have the following values: $K_\nu = a = c = 0$, $J_\nu = 8NV_\nu^2/U$, $b = V_{LR}$, such that Eqn. (5.13) reduces to Eqns. (2.26) and (2.28). As one moves away from ph symmetry, the dot-lead couplings (J_ν) increase leading to an increase in T_K as discussed in section 4.3 (whereas J is independent of ϵ). The coefficients K_ν, a, b, c also increase as one moves away from ph symmetry.

We would like to know whether introducing ph asymmetry is helpful for increasing the temperature scale on which 2CK physics can be observed in the 2AIM. We should therefore consider what effect the terms in Eqn. (5.13) will have on the T^* scale. The K_ν terms describe potential scattering in the leads, which is known not to destabilise the 2CK FP in the 2IKM [48], even if the magnitude of potential scattering is different in the two leads [117], so we would not expect these terms to have an effect on the T^* scale. The a term (see Eqn. (5.13)) is a direct interlead charge transfer term, which gives a contribution to T^* [59, 60], but this contribution is small in comparison to that arising from the b terms ($\hat{\mathbf{S}}_1 \cdot \hat{\mathbf{S}}_2$ and $\hat{\mathbf{S}}_1 \times \hat{\mathbf{S}}_2$ terms) - recall that direct interlead transfer gives rise to a smaller T^* scale than cotunneling charge transfer. The c term (the $\hat{\mathbf{S}}_1 + \hat{\mathbf{S}}_2$ term) is rather complicated, but it clearly involves interlead cotunneling charge-transfer processes, which one would expect to destabilise the 2CK FP for the 2IKM. By studying the 2IKM with an additional c

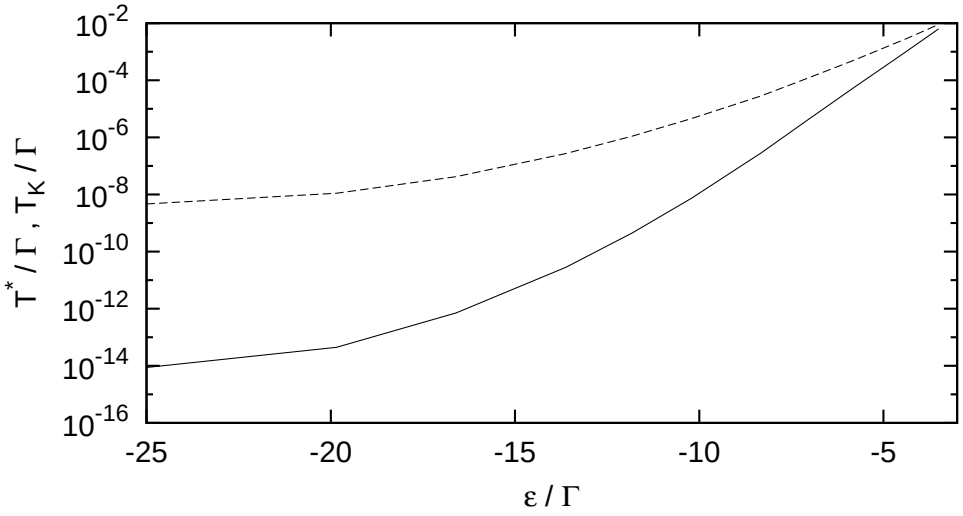


Figure 5.13: T^* (for $t = t_c$, solid line) and $T_{\rm K}$ (dashed line) against $\tilde{\epsilon} = \epsilon/\Gamma$ for the LR-symmetric 2AIM with $\tilde{U} = U/\Gamma = 50$. $\tilde{\epsilon} = -25$ is the ph-symmetric point.

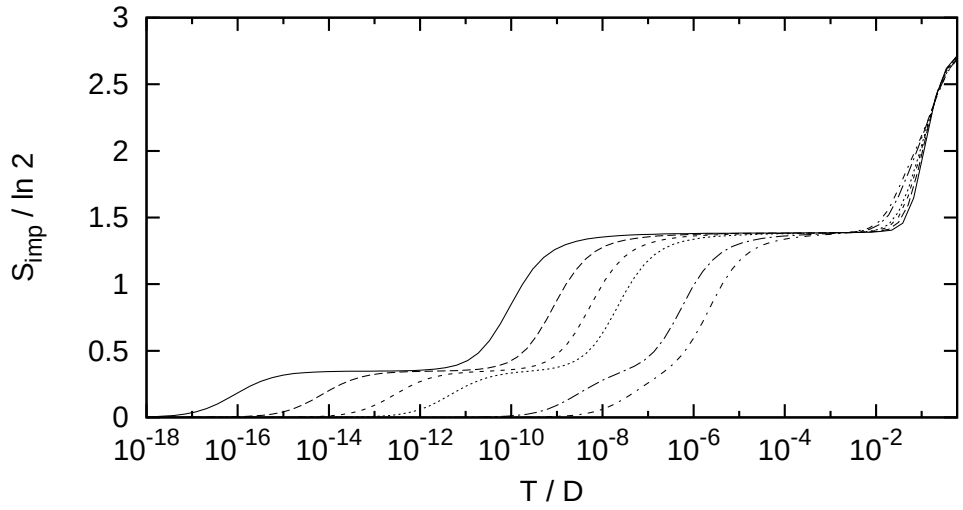


Figure 5.14: $S_{\rm imp}(T)$ for the LR-symmetric 2AIM with $\tilde{U} = 50$ and $t = t_c$ for $\epsilon/\Gamma = \tilde{\epsilon} = -25, -19.9, -16.6, -13.6, -11.8, -8.4, -7.1$. As ϵ (and therefore t_c) is increased, both the T^* and $T_{\rm K}$ scales increase, and the $\frac{1}{2}\ln 2$ entropy plateau is eroded, until for $\tilde{\epsilon} \simeq -7$ there is no evidence of it.

term, we have however found no evidence that this term destabilises the 2CK FP. This is illustrated in Fig. 5.12, in which the T^* scale is plotted as a function of J for the 2IKM with an additional c term. The T^* scale is seen to vanish at the critical point $J = J_c$, indicating that at this point the 2CK FP is stable, even though interlead cotunneling charge transfer is present.[6] Why this should be the case is not

[6]It is possible that T^* does not vanish at this point but is merely very small. However we have

obvious to us at this point, and it does indeed seem somewhat surprising. Regardless of this, the T^* is always finite (due to the a, b terms), and as we move away from ph symmetry we expect the T^* scale to increase, as the magnitude of interlead charge transfer (given by the coefficients a, b) increases. This increase will tend to make observing 2CK physics more difficult as ph asymmetry increases.

In Fig. 5.13 we show the $T_{\rm K}$ and T^* (for $t = t_c$) scales for the LR-symmetric 2AIM with $\tilde{U} = 50$, as a function of $\tilde{\epsilon}$. We see that, as expected, both the T^* and $T_{\rm K}$ scales increase as one moves away from ph symmetry by increasing ϵ. As the difference between the scales decreases with increasing ph asymmetry, moving away from ph symmetry is not helpful for observing 2CK physics[7]. Looking at $S_{\rm imp}$ as a function of temperature for the LR-symmetric 2AIM with $\tilde{U} = 50$, $t = t_c$, and various values of ϵ, as shown in Fig. 5.14, we see that the highest ϵ for which a $\frac{1}{2}\ln 2$ plateau is still visible is roughly $\tilde{\epsilon} \simeq -8$, and taking $U = 2$meV, $T_{\rm K}$ here is roughly $10^{-6}K$, much lower than can be reached experimentally. It seems therefore unlikely that 2CK physics could be accessed in a TCDQD simply by moving away from ph symmetry.

5.5 Two-channel Kondo physics in longer quantum dot chains

We have shown in this chapter that observing 2CK physics in a standard TCDQD, as modelled by the 2AIM, is unlikely at the present time, as an extremely low temperature is required. We conclude this chapter with a brief discussion of the possibility of observing 2CK physics in longer dot chains.

We consider first a system comprised of three quantum dots in series between two metallic leads, which may be modelled in the first instance by three spins coupled antiferromagnetically in series between two metallic leads, with the terminal spins coupled antiferromagnetically to the leads. We label this model the three-impurity Kondo model (3IKM), an obvious extension of the 2IKM, and note that it has been previously studied in Refs. [112, 157]. The system has no interlead charge transfer and flows to the stable 2CK FP on the lowest energy scales for *any* value of interdot coupling, J, provided the system is LR symmetric (as for any odd-numbered spin chain [112, 157]). The two-channel Kondo scale, $T_{\rm K}^{2CK}$, is found to depend on J, with a maximum when $J \sim T_{\rm K}$, for which $T_{\rm K}^{2CK} \sim T_{\rm K}$ [112, 157].

Considering a more realistic model of a triple quantum dot chain, consisting of three dot *levels* tunnel-coupled in series between two leads with the terminal dot levels tunnel-coupled to the leads (a model we label the three-impurity Anderson

purposefully chosen a large c coefficient in our NRG calculations (as well as a large $T_{\rm K}$), such that any finite minimum in $T^*(J)$ should be easily found. It therefore seems unlikely that T^* is small but non-zero at $J = J_c$.

[7] The effect of moving away from ph symmetry is again qualitatively similar to that of decreasing $\tilde{U}$ at ph symmetry; both $T_{\rm K}$ and T^* increase, but T^* increases more rapidly.

model, 3AIM), then interlead charge transfer naturally arises. We can imagine carrying out a (fourth-order) SW transformation on such a model, which would give rise to the 3IKM with additional interlead charge-transfer terms[8]. When charge transfer is added to the 3IKM a finite T^* scale will arise. For a system of N dot levels in series, the coefficient of the interlead charge transfer terms arising under a SW transformation is $V_{LR} \sim (\frac{t}{U})^{N-1} \frac{V_1 V_2}{U}$, with V_1, V_2 the two dot-lead tunnel-couplings, and t the interdot tunnel-coupling, taken to be equal between each adjacent pair of dots. For a triple dot system then, provided it is strongly correlated ($U/t, \tilde{U} \gg 1$) V_{LR} is much less than for an analogous double dot system, and one therefore expects the T^* scales which arise to be much lower. Provided the system is LR symmetric, and with $J = 4t^2/U$ tuned to $J \simeq T_{\rm K}$, a triple dot system therefore has a much lower T^* scale and a similar $T_{\rm K}^{2CK}$ scale to an analogous double dot system, making a three dot system a reasonable candidate for the observation of 2CK physics. Such a three dot system may however be rather difficult to manufacture, particularly with the LR symmetry required to observe 2CK physics[9].

Having considered a three dot chain, we turn to consider one with four dots in series between two metallic leads. We consider first a model with four spins coupled antiferromagnetically in series between two metallic leads, which we label the four-impurity Kondo model (4IKM). For such a system, as for any even-numbered spin chain, the exchange coupling J between the spins (all of which are taken to be equal) can be tuned to a critical value, J_c, for which the system flows to the 2CK FP [112]. This is independent of whether the system is LR symmetric. For the LR-symmetric 4IKM, $J_c \sim T_{\rm K}$ and $T_{\rm K}^{2CK} \sim T_{\rm K}$ [112], just as for the 2IKM (we have checked this with the NRG). In the LR-asymmetric case the 2CK FP can still be reached, but now $T_{\rm K}^{2CK} \ll T_{\rm K}^{(1)}, T_{\rm K}^{(2)}$ [112]. Considering a LR-symmetric system, going from two to four dots will decrease the interlead charge transfer, and therefore should decrease T^*, with little change to the $T_{\rm K}^{2CK}$ scale. 2CK physics should therefore be observable at higher temperatures in a four dot system than an analogous TCDQD.

In principle then, a three or four dot chain should provide a more realistic prospect of observing 2CK physics at experimentally realisable temperatures. In order to test this, one should carry out NRG calculations for the 3AIM and 4AIM, and see for what temperatures a $\frac{1}{2}\ln 2$ plateau in the entropy is visible (just as we did for the 2AIM). The only practical difference between studying these models with the NRG and studying the 2AIM, is that the initial Hamiltonian, $\hat{H}_0$, is different. For the 2AIM, $\hat{H}_0$ has 16 eigenstates, for the 3AIM it has 64, and for the 4AIM it

[8] There would be no third-order terms, as all third-order hopping processes result in a change in dot occupancy.

[9] LR asymmetry in the 3IKM introduces a finite T^* scale on which the system flows away from the 2CK FP – provided this scale is much smaller than $T_{\rm K}$ then 2CK physics can still be observed in principle. For this to be the case we require $|J_1 - J_2| \ll T_{\rm K}$, with J_1, J_2 the dot-lead exchange couplings [157].

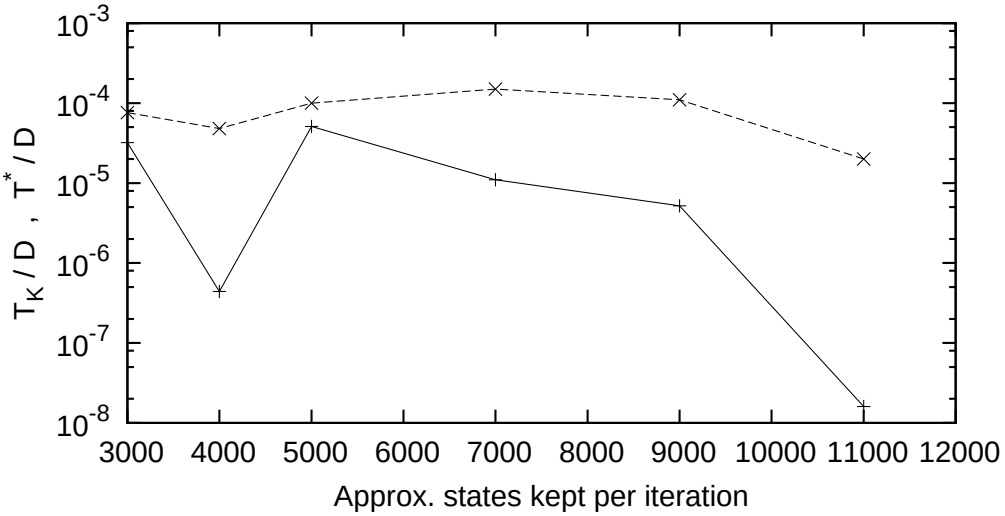


Figure 5.15: $T_{\rm K}$ and T^* (for $t = t_c$) scales for the LR and ph-symmetric 4AIM with $\tilde{U} = U/\Gamma = 10$, calculated from the NRG-calculated $S_{\rm imp}$, as a function of the number of states kept at each iteration. The results vary strongly with number of states kept, even for very high numbers of states, and as such we cannot rely on these results.

has 256 eigenstates. In practice this means that one must retain many more states at each NRG iteration for the 4AIM and 3AIM than the 2AIM, particularly at the early iterations. We find that one must retain a very large number of states to get accurate results. We have carried out preliminary investigations of the 3AIM and 4AIM using the NRG, keeping increasing numbers of states. Even keeping the maximum number of states feasible (~ 10000 at each iteration) we have failed to obtain convergence of results. This is illustrated for the 4AIM in Fig. 5.15, in which we show the $T_{\rm K}$ and T^* (for $t = t_c$) scales, calculated via the NRG, with varying numbers of states kept at each iteration. We see that as the number of states kept is increased the scales change dramatically (by orders of magnitude), and even keeping the maximum number of states feasible (~ 10000) convergence of results is not reached.

From the arguments given above it seems likely that a three or four dot system would provide a better possibility of observing 2CK than a two dot system, although these systems would be more difficult to manufacture. LR asymmetry in these systems would also be hard to avoid, and if present it would have a detrimental effect on the prospect of observing 2CK physics (as, for the 3IKM it destabilises the 2CK FP, and for the 4IKM it reduces $T_{\rm K}^{2CK}$ significantly [112]). More work, in particular, accurate NRG calculations, are however required in order to confirm this.

CHAPTER 6

Magnetic field effects in even-impurity models

In this chapter, we look at the effect of applying a magnetic field to a number of models containing an even number of impurities, including the 2IKM and the 2AIM, investigating the Kondo physics, in particular the 2CK physics, that arises. Considering first the LR-symmetric 2IKM, it is shown that in addition to the well-known zero-field QPT, a finite-field QPT also arises between local singlet (LS) and Kondo singlet (KS) phases for $J > J_c$, and this QPT is also characterised by the 2CK FP. The LS and KS phases are therefore cleanly separated by a phase boundary in the h-J plane, along which the 2CK FP is stable. We derive a low-energy effective model for the 2IKM in the presence of a finite field near to the phase boundary, and thereby show that the scale on which the system flows to the 2CK FP at the finite-field QPT is lower than at zero field. In the presence of a uniform magnetic field the pristine QPT is destroyed by introducing LR asymmetry to the 2IKM. However, we also look at the effect of applying a *staggered* magnetic field on the spins, in addition to the uniform field. Although we have not carried out a comprehensive study of LR-asymmetric 2IKM, consideration of a low-energy effective model suggests that the 2CK FP can be rendered stable by tuning both staggered and uniform fields, for $J > J_c$, when the system is in the LS phase at zero field, and we confirm this picture via explicit NRG calculations.

A system of four spins coupled in series between two leads (the 4IKM, as discussed briefly in section 5.5) is known to behave in a qualitatively similar fashion to the 2IKM at zero field [112, 117], with a QPT separating KS and LS phases at $J = J_c$. We therefore go on to look at the 4IKM, investigating the similarities at finite field (concentrating on the LR-symmetric case in a purely uniform field). In fact, the 4IKM is found to undergo two distinct QPTs as field strength is increased, provided $J \gg J_c$, with each QPT characterised by the 2CK FP. We also find that

as field strength is increased with $J < J_c$, there is a single QPT. As there is known to be only one QPT upon varying J at zero field [112], at $J = J_c$, we conjecture that the phase diagram for the 4IKM contains two phase boundaries, one of which terminates at $h = 0, J = J_c$, and the other terminating at $h = 0, J = 0$. Whilst some physical arguments are put forward to support this, further work is needed to properly establish this form of the phase diagram. The scales on which the system flows to the 2CK FP at each of the finite-field QPTs (for $J \gg J_c$) are estimated via consideration of low-energy effective models, and both are shown to be smaller than that for the QPTs arising in the 2IKM at either zero or finite field. Having looked at two and four spin chains (the 2IKM and the 4IKM), we postulate that a chain of $2N$ spins coupled symmetrically in series between two leads will undergo N QPTs as field strength is increased, provided one starts in the LS phase ($J > J_c$) at zero field. This is shown to be the case for the six-spin chain model – the 6IKM – with $J \gg J_c$ via NRG calculations, although more work is needed in order to fully elucidate the behaviour of a general even-numbered spin chain in a field.

We then go on to look at the 2AIM in the presence of a finite uniform field, beginning with the system at LR and ph symmetry. As at zero field, the existence of charge transfer smears the pristine QPT present in the LR-symmetric 2IKM into a continuous crossover in the 2AIM, such that there is a line of crossovers between LS and KS regimes in the h-J plane. Observing 2CK physics at finite field is found to be unfeasible in experimental TCDQD systems, as extremely low temperatures are required, even lower than at zero field. We go on to look at the effect of unequal dot-lead couplings ($\Gamma_1 \neq \Gamma_2$) in the 2AIM at finite field. As mentioned, breaking LR symmetry in the system destroys the finite-field QPT even in the absence of charge transfer, and we find that the relative magnitude of the charge transfer and the LR asymmetry dictates the low-temperature, zero-bias conductance in the vicinity of the finite-field crossover. We finish the chapter by looking at the effect of applying a magnetic field to the 2AIM away from ph symmetry, concentrating on the LR symmetric system, finding a rich range of behaviour, including the existence of spin-polarised currents.

6.1 Two-impurity Kondo model

At zero field, the trivial atomic limit of the 2IKM (*i.e.*, Eqn. (2.26) with $J_1 = J_2 = 0$) has a singlet ground state, $|S\rangle = \frac{1}{\sqrt{2}}(|\uparrow\downarrow\rangle - |\downarrow\uparrow\rangle)$ (the arrows representing the two dot spins), with a degenerate triplet at energy J above the ground state. Application of a (uniform) magnetic field to the dot spins (Eqn. (2.20)) lowers the energy of one triplet component, $|T_1\rangle = |\uparrow\uparrow\rangle$ (for $h > 0$), with a triplet-singlet energy difference $E_{T_1} - E_S = (J - h)$. As the field is tuned there is a level crossing, and at a 'critical' field $h = J$ the ground state is doubly degenerate, constituting as such a pseudospin-

$\frac{1}{2}$ comprised of $|S\rangle$ and $|T_1\rangle$.

The energies of the remaining $|T_0\rangle$ and $|T_{-1}\rangle$ triplet components lie at least J above the ground state. On coupling the dot spins to the leads, only the pseudospin-$\frac{1}{2}$ need therefore be retained in the low-energy manifold of dot states, provided $J \gg T_{\rm K} \sim J_c$ (or $J \gg \min(T_{\rm K}^{(1)}, T_{\rm K}^{(2)})$ for $J_1 \neq J_2$); since $T_{\rm K}$ (defined as usual for $J = 0$) is the sole low-energy scale in the problem when $J = 0$. In other words, the $|T_0\rangle$ and $|T_{-1}\rangle$ triplet components may be neglected provided $J \gg J_c$, and only the pseudospin-$\frac{1}{2}$ need be retained. Since this pseudospin can be flipped by the Kondo exchange on coupling to the leads, and since it is coupled to two leads, we thus expect [159] that 2CK physics should arise in the 2IKM with $J \gg J_c$, at a critical field $h = h_c \sim J$.

The preceding physical argument may be put on firmer footing by deriving an effective low-energy model for the 2IKM with $J \gg J_c$ and $h \simeq h_c$, retaining only the states which form the two components of the pseudospin (with local unity operator $\hat{1}' = |S\rangle\langle S| + |T_1\rangle\langle T_1|$); *i.e.*, from $\hat{H}_{\rm eff} = \hat{1}'\hat{H}_{\rm 2IKM}\hat{1}'$ to leading order, with $\hat{H}_{\rm 2IKM}$ in Eqn. 2.26. This procedure is outlined in Appendix E, and yields the following effective low-energy model $\hat{H}_{\rm eff} = \hat{H}'_{\rm eff} + \hat{O}$:

$$\begin{aligned}\hat{H}_{\rm eff} = &\tfrac{1}{2}J_1\left[\hat{S}^z_{01}\hat{\tau}^z + \sqrt{2}\frac{(\hat{S}^+_{01}\hat{\tau}^- + \hat{S}^-_{01}\hat{\tau}^+)}{2}\right] \\ &+ \tfrac{1}{2}J_2\left[\hat{S}^z_{02}\hat{\tau}^z + \sqrt{2}\frac{(\hat{S}^+_{02}\hat{\tau}^- + \hat{S}^-_{02}\hat{\tau}^+)}{2}\right] \\ &+ \hat{O}\ ,\end{aligned} \tag{6.1}$$

(in addition to $\hat{H}_{\rm leads}$, taken as read). Here $\hat{\boldsymbol{\tau}}$ denotes the pseudospin-$\frac{1}{2}$, with components $\hat{\tau}^z = \frac{1}{2}(|T_1\rangle\langle T_1| - |S\rangle\langle S|)$, $\hat{\tau}^+ = |T_1\rangle\langle S|$ and $\hat{\tau}^- = (\hat{\tau}^+)^\dagger$. Recall that (cf. Eqn. (2.14))

$$\hat{\mathbf{S}}_{\mathbf{0}\nu} = \sum_{\sigma,\sigma'} f^\dagger_{\nu\sigma}\boldsymbol{\sigma}_{\sigma\sigma'}f_{\nu\sigma'}\ . \tag{6.2}$$

$\hat{O}$ is given by $\hat{O} = \hat{O}_1 + \hat{O}_2$ with

$$\begin{aligned}\hat{O}_1 =&\tfrac{1}{4}J_1\hat{S}^z_{01} + \tfrac{1}{4}J_2\hat{S}^z_{02}\ , \\ \hat{O}_2 =&(J-h)\hat{\tau}^z\ .\end{aligned} \tag{6.3}$$

The first two lines of $\hat{H}_{\rm eff}$, denoted $\hat{H}'_{\rm eff}$, comprise a 2CK model (see section 2.5) with both channel anisotropy (for $J_1 \neq J_2$), which is well known to be a relevant perturbation to the 2CK FP [49, 57, 115]; and with spin anisotropy, known to be irrelevant to the 2CK FP [57, 160].

Since any channel anisotropy destroys the stability of the 2CK FP, we consider first the LR-symmetric case $J_1 = J_2$. Now we must consider the effect of $\hat{O} =$

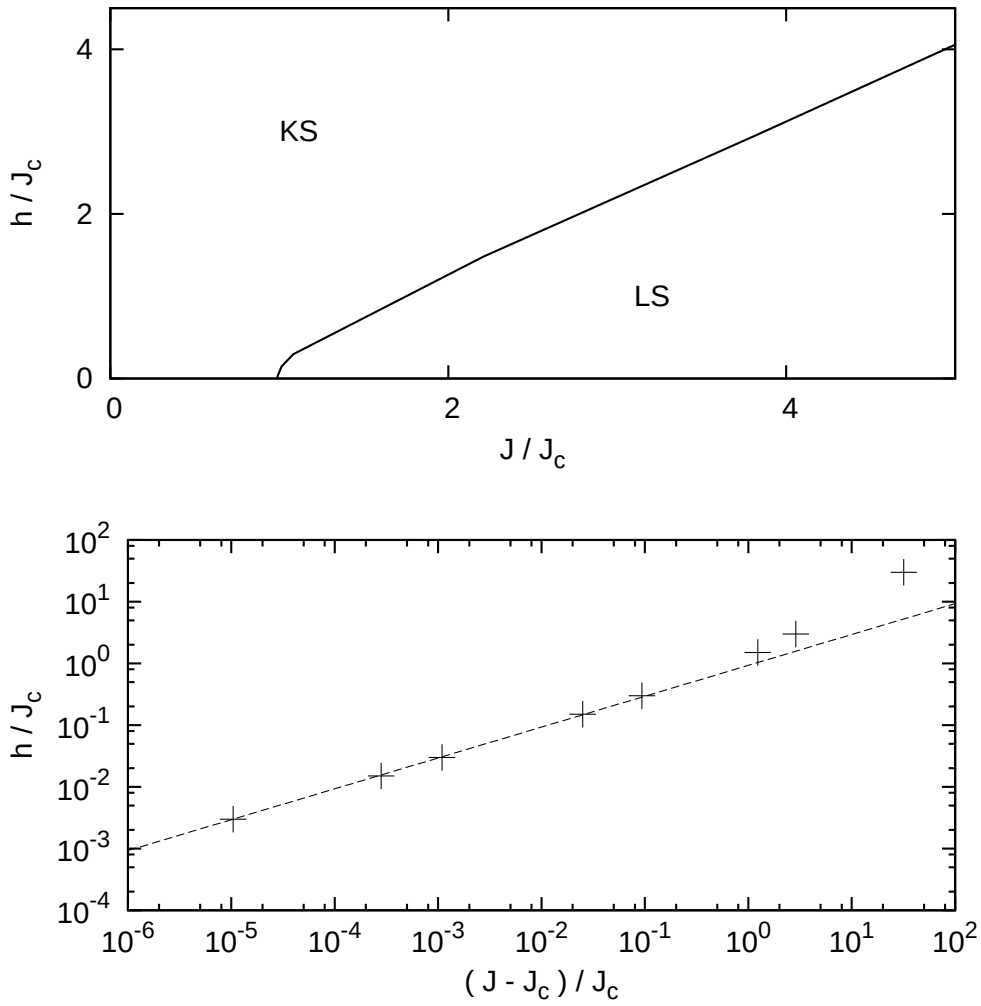


Figure 6.1: Phase diagram for the LR-symmetric 2IKM with $\rho J_1 = \rho J_2 = 0.093$ as function of h/J_c and J/J_c (top panel), and as function of h/J_c and $(J - J_c)/J_c$, on a log-log scale (bottom panel, crosses). Also plotted in the bottom panel is the line $h/J_c \simeq 0.9\sqrt{(J - J_c)/J_c}$ (dashed line). J_c is the critical value of J at zero field.

$\hat{O}_1 + \hat{O}_2$, each term of which is a relevant perturbation [160], separately rendering the 2CK FP unstable (as we have also confirmed directly via NRG on Eqn. (6.1)), breaking as they do the up-down spin symmetry of the problem. However for any given J, $J_1 = J_2$, the magnetic field h is a free parameter; which can then be tuned to ensure a vanishing *coefficient* of the relevant primary field associated with $\hat{O}$. The physical reason for this is that $\hat{O}_1$ and $\hat{O}_2$ break the same (spin) symmetry at the 2CK FP. Their combined effect can be cancelled by tuning h. Thus there is a critical field $h = h_c$, where $\hat{O}$ is rendered ineffective, and the 2CK FP is in consequence stable. This is the critical field, $h = h_c$. From the physical arguments above we expect $h_c \sim J$, so that the $|S\rangle$ and $|T_1\rangle$ states are near-degenerate (although not

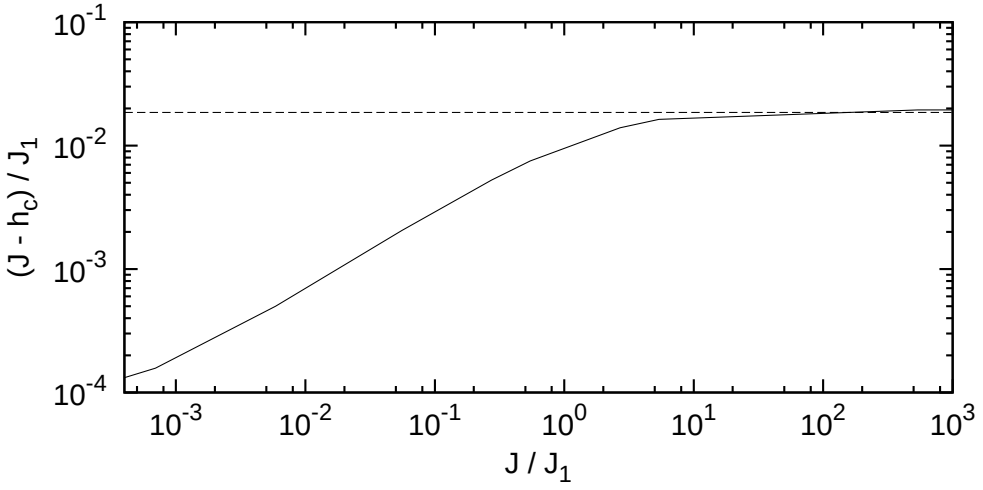


Figure 6.2: $a(J)/J_1 = (J - h_c)/J_1$ for the LR-symmetric 2IKM with $\rho J_1 = \rho J_2 = 0.093$ (solid line): $J/J_1 \gtrsim 1$ is required before $a(J)$ reaches its $J/J_1 \to \infty$ limiting value. Also shown (dashed line) is the value of value of $(J - h_c)/J_1$ for the low-energy effective model, Eqns. (6.1) and (6.3). Agreement between the two is seen to be good in the limit $J/J_1 \gg 1$.

identically J, as this would make the coefficient of $\hat{O}_2$ zero in Eqn. (6.3), leaving only the relevant $\hat{O}_1$ term, which would then make the 2CK FP unstable).

The above arguments imply that for the LR-symmetric 2IKM ($J_1 = J_2$) with $J \gg J_c$, there should be a QPT at a critical h_c, with a 2CK critical FP; and hence a line of 2CK critical FPs in the (h, J)-plane. We have confirmed this with NRG calculations on the 2IKM. Fig. 6.1 (top panel) shows an illustrative phase diagram for fixed $J_1 = J_2$ as a function of $(h/J_c, J/J_c)$ (recall that J_c is the critical J for zero-field, with $J_c \sim T_{\rm K}$); the critical line $h_c(J/J_c)$ separating an $h > h_c$ phase which is continuously connected to the zero-field KS state, from that connected to the zero-field LS phase. Although the arguments given above apply strictly to $J \gg J_c$, the transition is seen to extend continuously down to $J = J_c$ (as a simple appeal to continuity would suggest).

As discussed above, we expect $h_c \sim J$ to arise for sufficiently large J. Moreover, as $J - h_c$ is the coefficient of $\hat{O}_2$ required to "cancel out" the effect of the relevant perturbation $\hat{O}_1$, which itself has no dependence on J, we expect $J - h_c$ to go to a constant in this limit. We therefore expect the phase boundary in Fig. 6.1 (upper panel) to take the form $h_c = -a(J)+J$, with $a(J)$ going to a constant for $J/J_1 \gg 1$.[1] Looking specifically at $a(J)$ (defined from the above equation as $a(J) = J - h_c$), see Fig. 6.2, we find that it does in fact go to a constant for $J/J_1 \gg 1$, as expected. For

[1]For first-order perturbation theory to give a low-energy effective model which agrees *quantitatively* with the bare model, we require $J_1/J \ll 1$, so that second-order contributions (of order $\sim \mathcal{O}\left(\frac{J_1^2}{J}\right)$) are negligible compared to the first-order terms (which have coefficients $\sim \mathcal{O}(J_1)$).

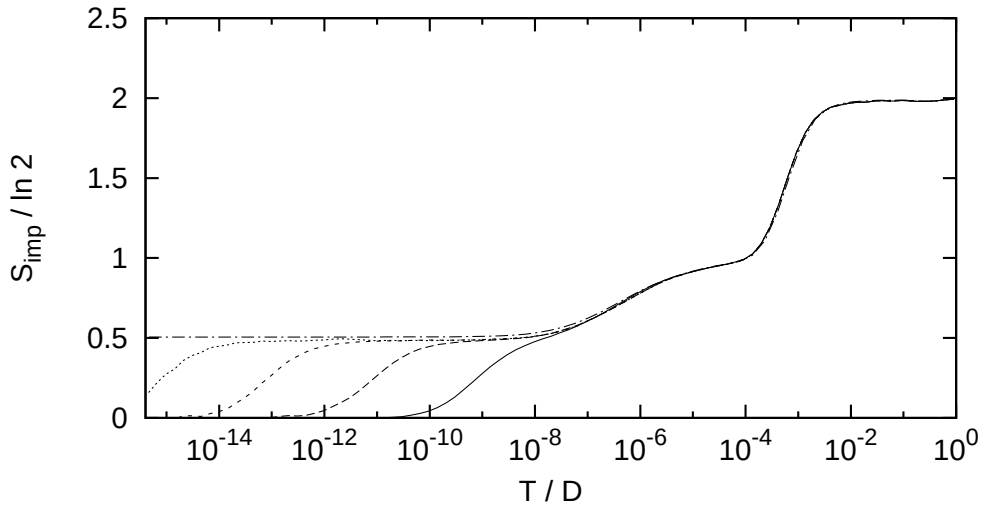


Figure 6.3: $S_{\rm imp}(T)$ for the 2IKM with $h = h_c$ and $(J_1 - J_2)/D = 0, 10^{-6}, 10^{-5}, 10^{-4}, 10^{-3}$, with $\rho J_1 = 0.093$ and $J = 0.001D$ ($\gg J_c$ in all cases). A plateau at $S_{\rm imp} = \frac{1}{2}\ln 2$ appears as J_2 is increased.

lower values of J/J_1, $a(J)$ has some dependence on J. This dependence is however weak enough that it does not significantly affect the gradient (given by $1 - \frac{da(J)}{dJ}$) of the phase boundary in Fig. 6.1 (upper panel) for $J/J_c \gtrsim 2$, such that the gradient is found to be $\simeq 1$ for $J/J_c \gtrsim 2$. In the limit of large J/J_1 the value of $a(J)$ also agrees well with that obtained from an NRG calculation directly on the low-energy effective model (Eqns. (6.1) and (6.3)) itself (the result of which is given by the dashed line in Fig. 6.2).

Whilst the above perturbative arguments for the form of the line $h_c(J)$ are valid for $J/J_c \gg 1$, for small $J - J_c$ they are not applicable. In the limit $J \to J_c$, we find from our numerical calculations, that $h_c/J_c \simeq c\sqrt{J/J_c - 1}$, as illustrated in Fig. 6.1 (lower panel), with $c \simeq 0.9$ a constant of order unity. Although we only probe this limit numerically, we have looked at rather small values of $(J - J_c)/J_c$ (down to $\sim 10^{-6}$), and it therefore seems reasonable to assume that the aymptotic form of the phase boundary is $h_c/J_c \simeq c\sqrt{J/J_c - 1}$ as $J \to J_c$.

For $J_1 \neq J_2$, $\hat{H}_{\rm eff}$ (Eqn. (6.1)) is channel anisotropic. The 2CK FP is consequently unstable [49, 57, 115], as likewise follows from the arguments above for the 2IKM at $h = h_c$ (at least for $J \gg J_c$). The system instead flows to a stable SC FP with $S_{\rm imp}(T = 0) = 0$; albeit that for sufficiently small $|J_1 - J_2|$, flow arises *from* the 2CK critical FP ($S_{\rm imp} = \frac{1}{2}\ln 2$) to the stable SC FP, on a scale T^* known from the 2CK model [57] to vanish as $T^* \sim |J_1 - J_2|^2$. The validity of this picture has been confirmed by NRG and is illustrated in Fig. 6.3, showing the temperature-dependence of $S_{\rm imp}(T)$ for the 2IKM at the critical $h = h_c$ for fixed J and J_1, upon decreasing J_2 from $J_2 = J_1$ where the 2CK critical FP is stable. The low-energy

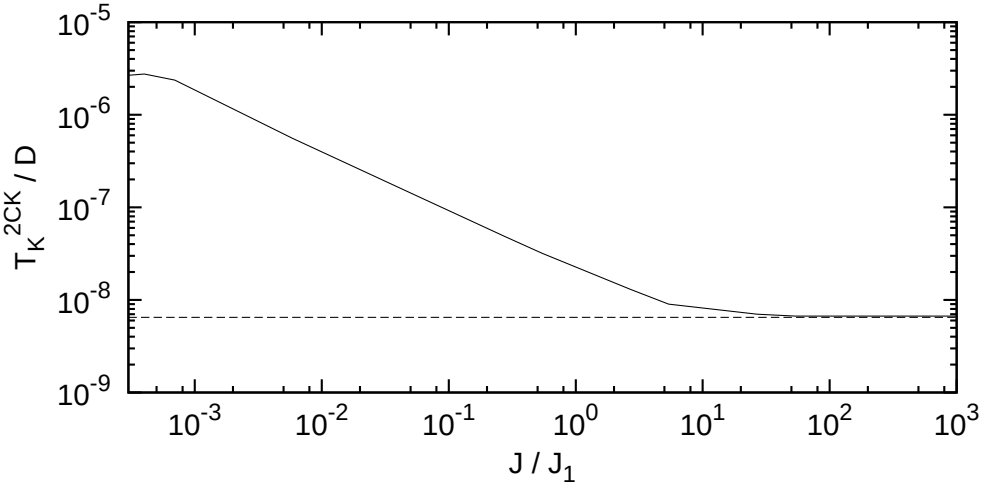


Figure 6.4: $T_{\rm K}^{2CK}$ (defined by $S_{\rm imp}(T_{\rm K}^{2CK}) = \frac{3}{4}\ln 2$, between the values of $S_{\rm imp}$ for the LM and 2CK FPs) along the LS-KS phase boundary ($h = h_c$) for the LR-symmetric 2IKM with $\rho J_1 = \rho J_2 = 0.093$ (solid line). As J is increased, $T_{\rm K}^{2CK}$ decreases from the zero field ($J = J_c \simeq 5\times 10^{-4} J_1$) value and converges for $J/J_1 \gg 1$ (specifically, convergence is reached for $J/J_1 \gtrsim 10$) . Also shown is the value of $T_{\rm K}^{2CK}$ for the low-energy effective model, Eqns. (6.1) and (6.3). Agreement between the two models is seen to be good in the limit $J/J_1 \gg 1$.

scale T^* – which in practice may be identified from $S_{\rm imp}(T^*) = \frac{1}{4}\ln 2$ – is immediately evident on increasing $J_1 - J_2$ from zero; and analysis of the numerics indeed confirms it to vanish as $T^* \sim |J_1 - J_2|^2$.

We also note that the two-channel Kondo scale (call it $T'_{\rm K}$) on which the $\frac{1}{2}\ln 2$ entropy plateau in Fig. 6.3 is reached, is visibly lower than its counterpart shown in Fig. 5.3 for the 2IKM at zero field (with the same ρJ_1), which is $T_{\rm K} \sim \exp(-1/\rho J_1)$ [3, 17]. This can be understood from the low-energy model $\hat{H}'_{\rm eff}$ (as appropriate to Fig. 6.3), it being sufficient to consider the channel-symmetric case $J_1 = J_2$. This is a spin-anisotropic 2CK model, of form $\hat{H}'_{\rm eff} = \sum_{\nu=1,2}[J_z \hat{S}^z_{0\nu}\hat{\tau}^z + \frac{1}{2}J_\perp(\hat{S}^+_{0\nu}\hat{\tau}^- + \hat{S}^-_{0\nu}\hat{\tau}^+)]$ with (see Eqn. 6.1) exchange couplings $J_z = J_1/2$ and $J_\perp = J_1/\sqrt{2}$ (each less than J_1). And the characteristic low-energy scale for the model, $T'_{\rm K}$, on which temperature scale the $\frac{1}{2}\ln 2$ entropy is approached, is readily shown from perturbative scaling [3, 17] to be

$$T'_{\rm K} \propto \exp\left(-\tfrac{\pi}{2\rho\sqrt{c}} + \tfrac{1}{\rho\sqrt{c}}\tan^{-1}\left[\frac{|J_z|}{\sqrt{c}}\right]\right) \ , \qquad (6.4)$$

with $c = |J_z^2 - J_\perp^2|$, which for Eqn. (6.1) gives $T'_{\rm K} \propto \exp(-\frac{\pi}{2}\frac{1}{\rho J_1})$, whence $T'_{\rm K} \ll T_{\rm K}$. This means, in other words, that much lower temperatures are needed to observe 2CK physics at the critical point of the 2IKM at finite field than at zero field.

We look at the scale on which the system flows to the 2CK FP (and the $\frac{1}{2}\ln 2$ entropy plateau is reached) for the 2IKM along the phase boundary (*i.e.*, as a function of J and with $h = h_c$) in Fig. 6.4 (solid line). Here we label this scale $T_{\rm K}^{2CK}$. This

is compared to the same quantity for the low-energy effective model, Eqn. (6.1), given by the dashed line. For large J ($J/J_1 \gg 1$), $T_{\rm K}^{2CK}$ is expected to be $\sim T_{\rm K}'$, as discussed above. $T_{\rm K}^{2CK}$ should therefore be independent of J in this limit, and this is indeed found to be the case, with the limiting value of $T_{\rm K}^{2CK}$ agreeing well with the low-energy effective model. $T_{\rm K}^{2CK}$ is also seen to be much smaller at finite field than at zero field ($J/J_c = 1$, for which $J/J_1 \simeq 5 \times 10^{-4}$), for which $T_{\rm K}^{2CK} \sim T_{\rm K}$, as discussed in chapter 5.

6.1.1 Staggered field

We have seen above that if $J_1 \neq J_2$ then the 2CK FP is not stable for the 2IKM for any finite uniform field strength, h. However, we may also consider the effect of applying *unequal* magnetic fields to the two dot spins. We may parameterise these two fields in terms of a uniform field (as discussed above) and a staggered field, given by

$$\hat{H}_{B,stag} = -h_s(\hat{S}_1^z - \hat{S}_2^z) \ . \tag{6.5}$$

In this section we discuss the possibility of reaching the 2CK FP for the LR-asymmetric 2IKM in the presence of simultaneous uniform and staggered fields. In order to understand the effect of the fields, we first look at the atomic limit.

We consider first the effect of a purely staggered field on the atomic-limit 2IKM. A staggered field has no effect on the $|T_1\rangle$ and $|T_{-1}\rangle = |\downarrow\downarrow\rangle$ eigenstates, which have an energy of $J/4$. In the presence of a staggered field, however, $|S\rangle$ and $|T_0\rangle = \frac{1}{\sqrt{2}}[|\uparrow\downarrow\rangle + |\downarrow\uparrow\rangle]$ mix, such that the eigenstates are now $|S'\rangle$ and $|T_0'\rangle$, given by

$$\begin{aligned} |S'\rangle &= \frac{1}{\sqrt{1+b^2}}\left(|S\rangle + b|T_0\rangle\right) \ , \\ |T_0'\rangle &= \frac{1}{\sqrt{1+b^2}}\left(-b|S\rangle + |T_0\rangle\right) \ , \end{aligned} \tag{6.6}$$

with b, a function of h_s/J, given by

$$b = F\left(\frac{h_s}{J}\right) = \frac{J}{2h_s}\left(\sqrt{1+\frac{4h_s^2}{J^2}} - 1\right) \ . \tag{6.7}$$

Note that in the limit $h_s/J \to 0$, $b \to h_s/J$, whereas in the limit $h_s/J \to \infty$, $b \to 1$. The exact atomic-limit energies of $|S'\rangle$ and $|T_0'\rangle$ are

$$E_{S',T_0'} = -\frac{J}{4} \pm \sqrt{\frac{J^2}{4} + h_s^2} \ , \tag{6.8}$$

with $E_{S'}$ corresponding to the minus sign, such that $|S'\rangle$ is the ground state.

Having considered the effect of applying a purely staggered field, we now consider

the effect of additionally applying a uniform field. The *sole* effect of such a field in the atomic limit is to decrease the energy of the $|T_1\rangle$ state, and increase the energy of the $|T_{-1}\rangle = |\downarrow\downarrow\rangle$ state, by an energy h. The energy difference between the $|S'\rangle$ and $|T_1\rangle$ states is given by $\delta E(h, h_s) = -h + \frac{J}{2} + \frac{J}{2}\sqrt{1 + \frac{4h_s^2}{J^2}}$, such that the uniform field h may be tuned to bring the $|S'\rangle$ and $|T_1\rangle$ into degeneracy. At this field, the ground state is then doubly degenerate, and thereby constitutes a pseudospin-$\frac{1}{2}$ comprised of $|S'\rangle$ and $|T_1\rangle$.

As the other triplet atomic-limit states, $|T_{-1}\rangle$ and $|T_0'\rangle$, lie $\sim \mathcal{O}(J)$ above the ground state, we may then carry out first-order perturbation theory in J_1, J_2, retaining just the $|S'\rangle$ and $|T_1\rangle$ states, in the presence of a staggered field, as well as a uniform field, $h \simeq \frac{J}{2} + \frac{J}{2}\sqrt{1 + \frac{4h_s^2}{J^2}}$. The low-energy effective model is then valid provided the atomic-limit states projected out are sufficiently higher in energy than those retained, which in practice means $J \gg J_c$, with J_c the zero-field critical value of J. The resulting model is (see Appendix E for details)

$$\begin{aligned}\hat{H}_{\text{eff}} &= \frac{J_1}{2}\left[\hat{S}^z_{01}\hat{\tau}^z + \frac{(1-b)}{\sqrt{1+b^2}}\sqrt{2}\frac{(\hat{S}^+_{01}\hat{\tau}^- + \hat{S}^-_{01}\hat{\tau}^+)}{2}\right] \\ &+ \frac{J_2}{2}\left[\hat{S}^z_{02}\hat{\tau}^z + \frac{(1+b)}{\sqrt{1+b^2}}\sqrt{2}\frac{(\hat{S}^+_{02}\hat{\tau}^- + \hat{S}^-_{02}\hat{\tau}^+)}{2}\right] \\ &+ \hat{O} \\ &= \hat{H}'_{\text{eff}} + \hat{O}\ ,\end{aligned} \tag{6.9}$$

and $\hat{O} = \hat{O}_1 + \hat{O}_2$ with

$$\begin{aligned}\hat{O}_1 &= \frac{J_1}{4}\hat{S}^z_{01} + \frac{J_2}{4}\hat{S}^z_{02}\ , \\ \hat{O}_2 &= \left[\delta E(h, h_s)\right]\hat{\tau}^z\ ,\end{aligned} \tag{6.10}$$

and the pseudospin $\hat{\tau}$ is now comprised of the $|S'\rangle$ and $|T_1\rangle$ states (in the usual fashion). Comparison of the above low-energy effective model to that for the case of a purely uniform field (Eqns. (6.1) and (6.3)) shows that the effect of the staggered field is twofold. First, it affects the perpendicular parts of the dot-lead couplings (via the coefficient b, see Eqn. (6.7)), and secondly, it affects the field on the pseudospin, $\delta E(h, h_s)$. Note that in the limit $h_s \to 0$, the coefficient $b \to 0$, and Eqns. (6.9) and (6.10) reduce to Eqns. (6.1) and (6.3), as they should.

In order to understand the physics of the low-energy effective model, we write $J_1 = \frac{J_1+J_2}{2} + \frac{J_1-J_2}{2}$, and $J_2 = \frac{J_1+J_2}{2} - \frac{J_1-J_2}{2}$, such that $\hat{H}'_{\text{eff}}$ becomes:

$$\begin{aligned}\hat{H}'_{\text{eff}} =& \hat{H}''_{\text{eff}} + \hat{O}'_1 + \hat{O}'_2 \\ =& \hat{H}''_{\text{eff}} + \hat{O}'\ ,\end{aligned} \tag{6.11}$$

with

$$\begin{aligned}\hat{H}''_{\text{eff}} =& \frac{J_1+J_2}{4}\left[(\hat{S}^z_{01}+\hat{S}^z_{02})\hat{\tau}^z\right] \\ &+ \frac{\sqrt{2}}{4\sqrt{1+b^2}}[(J_1+J_2)-b(J_1-J_2)]\left[\frac{((\hat{S}^+_{01}+\hat{S}^+_{02})\hat{\tau}^- + (\hat{S}^-_{01}+\hat{S}^-_{02})\hat{\tau}^+)}{2}\right]\end{aligned} \tag{6.12}$$

and

$$\begin{aligned}\hat{O}'_1 &= \frac{J_1-J_2}{4}\left[(\hat{S}^z_{01}-\hat{S}^z_{02})\hat{\tau}^z\right] \ , \\ \hat{O}'_2 &= \frac{\sqrt{2}}{4\sqrt{1+b^2}}\left[(J_1-J_2)-b(J_1+J_2)\right]\left[\frac{\hat{\tau}^+(\hat{S}^-_{01}-\hat{S}^-_{02})+\hat{\tau}^-(\hat{S}^+_{01}-\hat{S}^+_{02})}{2}\right] \ ,\end{aligned} \tag{6.13}$$

The $\hat{O}$ terms (Eqn. (6.10)) become

$$\begin{aligned}\hat{O}_1 &= \frac{J_1+J_2}{8}(\hat{S}^z_{01}+\hat{S}^z_{02}) + \frac{J_1-J_2}{8}(\hat{S}^z_{01}-\hat{S}^z_{02}) = \hat{O}_{1A}+\hat{O}_{1B} \ , \\ \hat{O}_2 &= [\delta E(h,h_s)]\,\hat{\tau}^z \ ,\end{aligned} \tag{6.14}$$

such that overall,

$$\hat{H}_{\text{eff}} = \hat{H}''_{\text{eff}} + \hat{O}'_1 + \hat{O}'_2 + \hat{O}_{1A} + \hat{O}_{1B} + \hat{O}_2 \ . \tag{6.15}$$

Considering the terms in the above equation separately, we first note that $\hat{H}''_{\text{eff}}$ is a channel-isotropic, spin-anisotropic 2CK model, for which the 2CK FP is stable [57, 160]. Moving on to the other terms, NRG calculations show that $\hat{O}_{1B}$ is an irrelevant perturbation to the 2CK FP, whereas all the other terms in the above equation are found to be relevant[2]. However, these relevant terms $(\hat{O}'_1, \hat{O}'_2, \hat{O}_{1A}, \hat{O}_2)$ fall into two symmetry categories: those terms that break channel isotropy ($\hat{O}'_1$ and $\hat{O}'_2$) and those that only break up-down spin symmetry ($\hat{O}_{1A}$ and $\hat{O}_2$). We would expect each of these groups of terms to give rise to a particular relevant primary field when the system is near the 2CK FP. Now, for a given (J_1, J_2, J), there are *two* free parameters in the system (h and h_s). We therefore expect that these should be able to be tuned so as to ensure vanishing coefficients of *both* relevant primary fields, rendering them ineffective and hence the 2CK FP is stable at these critical fields.

The above arguments show that for the LR-asymmetric 2IKM, with $J \gg J_c$, whilst one cannot render the 2CK FP stable by tuning a uniform field alone (as seen in Fig. 6.3), one should be able to tune h *and* h_s to reach the 2CK FP. To test

[2]We simply add each of these perturbations to a channel-isotropic 2CK model in turn, and see which destabilise the 2CK FP, *i.e.*, which give zero residual entropy.

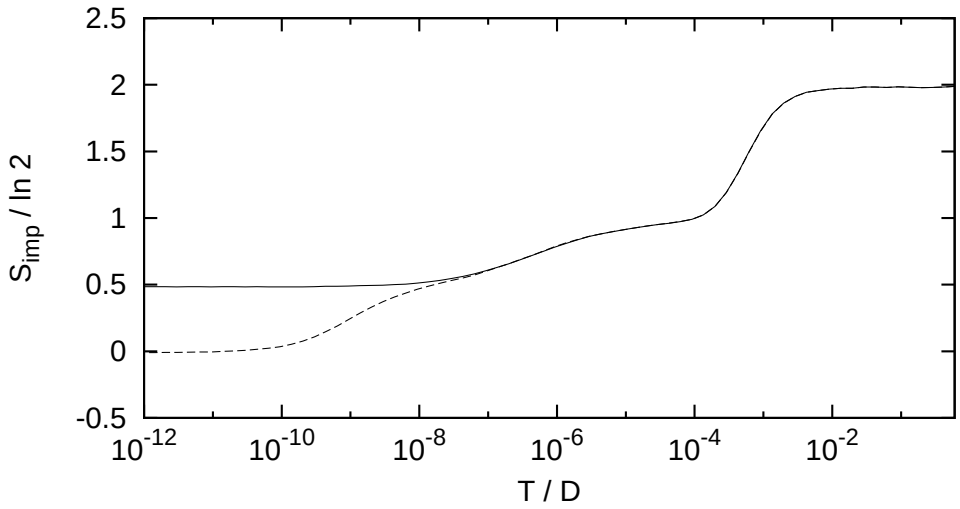


Figure 6.5: $S_{\rm imp}(T)$ for the LR-asymmetric 2IKM in the presence of a purely uniform magnetic field, with $h = 9.1319\times10^{-4}D$ (dashed line), and upon application of a small staggered field, $h_s = 5.38\times10^{-6}D$ (with slight retuning of the uniform field, $h = 9.131855\times10^{-4}D$, solid line). We see that the 2CK FP is unstable in the presence of a purely uniform field, but is rendered stable by application of an additional staggered field. The other parameters used are $\rho J_1 = 0.093$, $\rho J_2 = 0.0925$, and $J = 0.001D \gg J_c$.

this numerically, we have carried out NRG calculations. Fig. 6.5 shows $S_{\rm imp}$ against temperature for the LR-asymmetric 2IKM with $J \gg J_c$, first in the presence of a purely uniform magnetic field, where h has been tuned to minimise T^*, the scale on which the entropy goes to zero (dashed line). We find that there is no value of h which renders the 2CK FP stable, and as a result there is no residual entropy. Also shown is $S_{\rm imp}$ for the system in the presence of both uniform and staggered magnetic fields (solid line), with both fields tuned so as to render the 2CK FP stable, resulting in a residual $\frac{1}{2}\ln 2$ entropy. These results show that it is indeed possible to render the 2CK FP stable for a LR-asymmetric 2IKM in the presence of unequal magnetic fields on the two spins.

We have also carried out a series of NRG calculations for the LR-asymmetric 2IKM with the same (J_1, J_2) as Fig. 6.5, but $J \gtrsim J_c$. We find that in this case as well, one may tune both h and h_s in order to render the 2CK FP stable[3]. These calculations are rather time-consuming, as *two* fields must be tuned in order to find the critical point, and we have therefore only found two critical points at finite field for the LR-asymmetric 2IKM so far. However, it is well known that the LR-asymmetric 2IKM also has a critical point at zero field [112, 115–117], for $J = J_c$. From this fact, taken together with the fact that critical points exist for both $J \gg J_c$ and $J \gtrsim J_c$, it is natural to assume that a line of critical points exists in (J, h, h_s)-

[3]Taking $\rho J_1 = 0.093$, $\rho J_2 = 0.0925$, and $J = 5\times10^{-5}D \gtrsim J_c \simeq 3.3\times10^{-5}D$, we find that the 2CK FP is stable for $h \simeq 2.7\times10^{-5}D$ and $h_s \simeq 3.4\times10^{-7}D$.

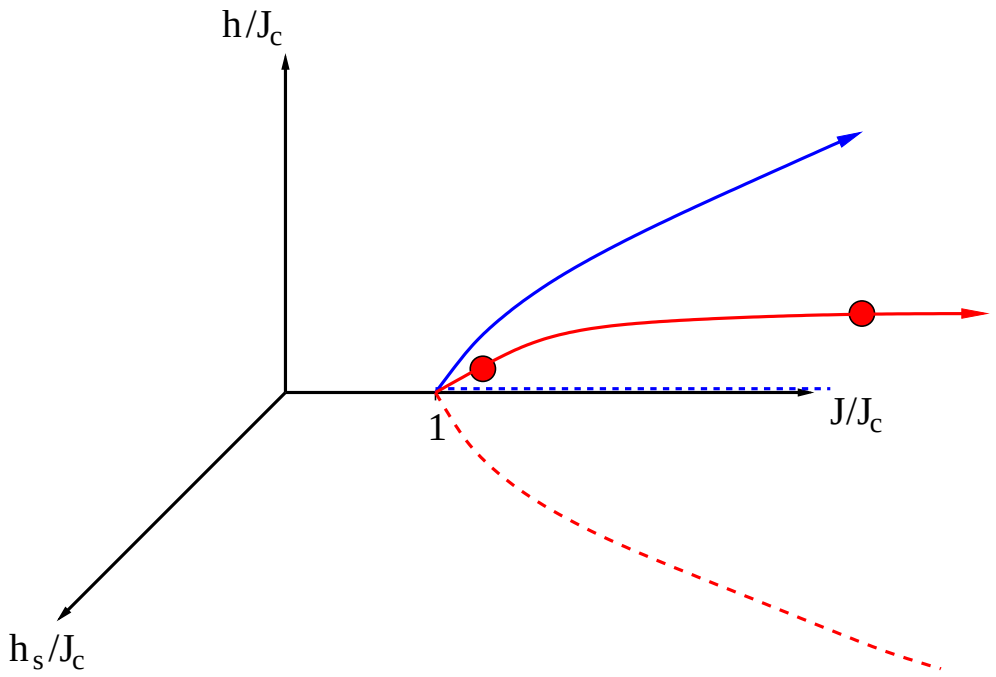


Figure 6.6: Schematic illustration of the critical lines of the LR-symmetric ($J_1 = J_2$, blue solid line) and LR-asymmetric 2IKM ($J_1 \neq J_2$, red solid line) in (J, h, h_s)-space. Each line is for fixed J_1, J_2. The dashed lines are the projections of the critical lines onto the $h = 0$ plane. Both cases have critical points at zero field ($h = 0, h_s = 0, J/J_c = 1$), J_c denoting the zero-field critical value of J. For the LR-symmetric case with any $J > J_c$, h can be tuned to reach the critical point, and a line of critical points therefore exists in the $h_s = 0$ plane (as discussed in section 6.1). The projection of this line onto the $h = 0$ plane (blue dashed line) is therefore along the J/J_c axis. In the LR-asymmetric case, for $J > J_c$ we believe that in general both h and h_s can be tuned in order to reach the critical point, and therefore we expect that there is a line of critical points in (J, h, h_s)-space. Whilst we have not established this definitively via numerical calculations, we have established that two critical points (denoted by red circles) exist at finite h and h_s for a particular LR-asymmetric 2IKM (with $\rho J_1 = 0.093$ and $\rho J_2 = 0.0925$). One of these points is for $J \gg J_c$, and one for $J \gtrsim J_c$. Taken along with the well-known zero-field critical point [112, 115–117], we believe it safe to assume that a continuous line of critical points exists for the LR-asymmetric 2IKM.

space for the 2IKM with *any* values of (J_1, J_2). For the LR-symmetric case, this line lies in the $h_s = 0$ plane (shown in Fig. 6.1), whereas for the general LR-asymmetric system, this is not the case. This picture is illustrated schematically, and explained further, in Fig. 6.6.

In the general LR-asymmetric case, we may ask what form the critical line takes. In order to determine this, we take a point on the critical line, with parameters denoted (J^0, h^0, h_s^0), and consider increasing J by some amount, $J^0 \to J^0 + \delta J$. In order to stay on the critical line we must retune $(h^0, h_s^0) \to (h^0 + \delta h, h_s^0 + \delta h_s)$. Looking at the low-energy effective model (Eqns. (6.11) - (6.15)), valid for $J \gg J_c$, and considering $\hat{O}'$ first, we note that it has no dependence on h, and with given (J_1, J_2), it depends solely on h_s/J (as the coefficient b is a function of h_s/J).

To maintain the vanishing coefficient of the primary field associated with $\hat{O}'$ (and therefore the stability of the 2CK FP), we then require that h_s/J is unchanged upon $(J^0, h^0, h_s^0) \to (J^0 + \delta J, h^0 + \delta h, h_s^0 + \delta h_s)$, *i.e.*, that

$$\frac{h_s^0}{J^0} = \frac{h_s^0 + \delta h_s}{J^0 + \delta J} = \alpha \ , \tag{6.16}$$

where α is a constant. Next considering the $\hat{O}$ terms, $\hat{O}_1$ has no dependence on the fields or J, so we expect that the coefficient of $\hat{O}_2$ (which is $\delta E(h, h_s, J) = -h + \frac{J}{2} + \frac{J}{2}\sqrt{1 + \frac{4h_s^2}{J^2}}$) is constant along the critical line, so that in order to stay on the critical line we require, $\delta E(h^0, h_s^0, J^0) = \delta E(h^0 + \delta h, h_s^0 + \delta h_s, J^0 + \delta J)$, which (after some simple algebra) yields

$$\delta h = \left(\frac{1 + \sqrt{1 + \alpha^2}}{2} \right) \delta J \ , \tag{6.17}$$

where we have used Eqn. (6.16). Taking the limit $\delta J \to 0$ gives differential equations for h and h_s, solution of which gives

$$\begin{aligned} h_s &= \alpha J \ , \\ h &= \left(\frac{1 + \sqrt{1 + \alpha^2}}{2} \right) J + d \ , \end{aligned} \tag{6.18}$$

this only being valid in the limit of large J/J_c, with d a constant. These equations then describe the line of critical points through (J, h, h_s)-space. Further numerical calculations are however required to confirm the form of this line. Note that in the LR-symmetric case, $h_s^0 = 0$, so that $\alpha = 0$, and we recover the high-J result, $h = J + d$, discussed in section 6.1.

6.2 Four-impurity Kondo model

Having looked at the 2IKM in a magnetic field, we now move on to consider an analogous system of four spins in series. At zero field it is known that the QPT that occurs in the 2IKM also occurs in any system with an even number of spins coupled in series, separating KS and LS phases [112], with the KS ground state consisting of the terminal spins locked up into singlets with the leads, and the remaining spins forming a singlet themselves, essentially decoupled from the terminal spins [112]. It is therefore interesting to consider whether the *finite-field* QPT arising in the 2IKM also arises in other even spin chains[4]. Work on this is ongoing, and in this section

[4]Odd-spin chains are known to flow to the 2CK FP at zero field for any value of interdot coupling [112, 157], provided they are LR symmetric. The low-energy effective model for these systems is of 2CK model form [112, 157], and applying a magnetic field to the bare model corresponds to a field

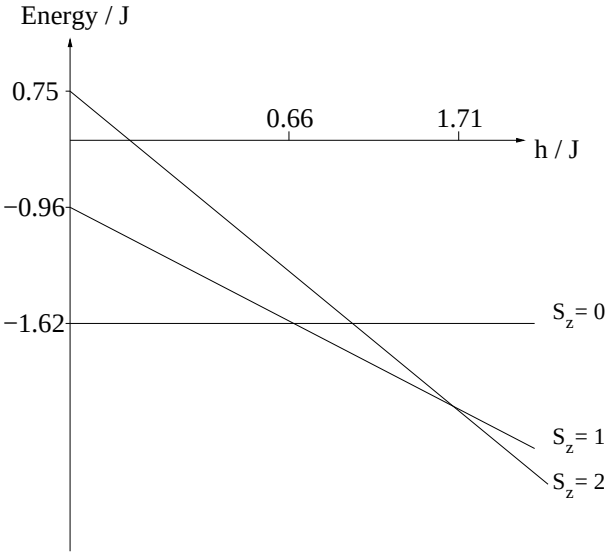


Figure 6.7: Atomic-limit energy levels for the 4IKM as a function of uniform magnetic field strength, h. Only the three ground states for $h \geq 0$ are shown. There are two successive changes in ground state as h is increased, occurring at $h/J \simeq 0.66, 1.71$.

we present our findings so far.

We concentrate primarily on the four-impurity Kondo model (4IKM), the Hamiltonian for which is

$$\hat{H}_{\rm 4IKM} = J_1 \hat{\mathbf{S}}_{01} \cdot \hat{\mathbf{S}}_1 + J_2 \hat{\mathbf{S}}_{02} \cdot \hat{\mathbf{S}}_4 + J(\hat{\mathbf{S}}_1 \cdot \hat{\mathbf{S}}_2 + \hat{\mathbf{S}}_2 \cdot \hat{\mathbf{S}}_3 + \hat{\mathbf{S}}_3 \cdot \hat{\mathbf{S}}_4) + \hat{H}_{\rm leads} \ , \quad (6.19)$$

such that the antiferromagnetic couplings between the spins (J) have been taken to be equal. $\hat{\mathbf{S}}_i$ ($i = \{1, 2, 3, 4\}$) represent the spin-$\frac{1}{2}$ impurities. We concentrate on the case of LR symmetry ($J_1 = J_2$) and a purely uniform magnetic field ($\hat{H}_B = -h(\hat{S}_1^z + \hat{S}_2^z + \hat{S}_3^z + \hat{S}_4^z) = -h\hat{S}_z$) for simplicity.

In the atomic limit, the ground state of the 4IKM with $0 \leq h \lesssim 0.66J$ is a non-degenerate state with $\langle \hat{S}^z \rangle = S_z = 0$ (see Fig. 6.7). Application of a magnetic field lowers the energies of states with $S_z > 0$ such that for $0.66J \lesssim h \lesssim 1.71J$ the ground state is an $S_z = 1$ state, whereas for $h \gtrsim 1.71J$ the ground is the $S_z = 2$ state with the simple form $|\uparrow\uparrow\uparrow\uparrow\rangle$, with the arrows representing the impurity spins (the other states discussed are not eigenstates of $\hat{S}_i^z$, $i = 1, 2, 3, 4$). When $h \simeq 0.66J$ the ground state is doubly degenerate between $S_z = 1$ and $S_z = 0$ states, and when $h \simeq 1.71J$ the ground state is doubly degenerate between $S_z = 2$ and $S_z = 1$ states. We therefore expect Kondo physics to arise near to the two critical fields: $h_{c1} \simeq 0.66J$, and $h_{c2} \simeq 1.71J$.

on the pseudospin in the effective 2CK model. As this is known to be a relevant perturbation to the 2CK model [115, 161], a uniform field will merely destroy the 2CK effect in these systems. We therefore do not consider odd spin chains here.

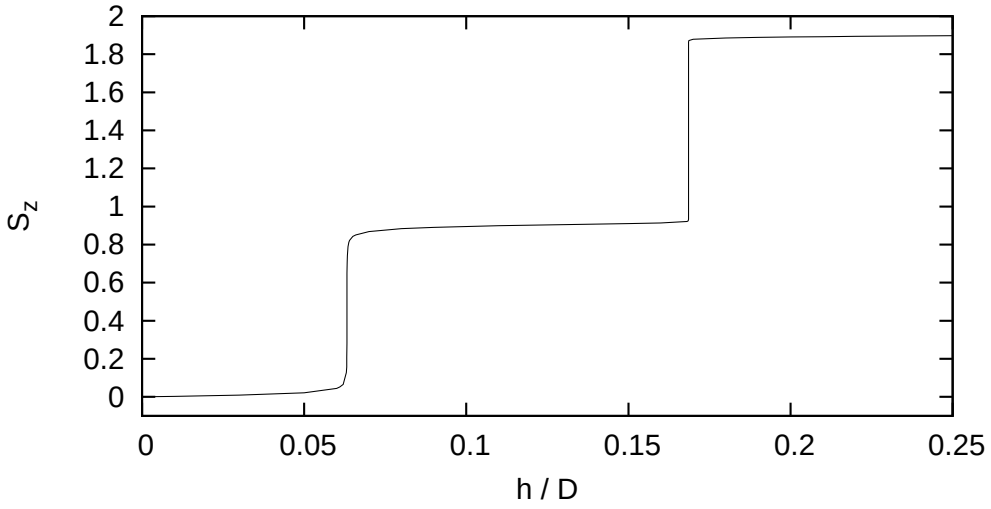


Figure 6.8: $S_z = \langle \hat{S}_z \rangle$ vs h for the LR-symmetric 4IKM with $\rho J_1 = \rho J_2 = 0.15$ and $J = 0.1D \gg J_c$. The rapid (but continuous) changes in S_z occur at $h \simeq h_{c1}, h_{c2}$.

As for the 2IKM, one may carry out first-order perturbation theory in the spin-lead couplings (the procedure is outlined in Appendix E) near the two atomic-limit degeneracy points, *i.e.*, with $J \gg J_c$ (J_c being the zero-field critical value), and $h \simeq h_{c1}$ or $h \simeq h_{c2}$. For $h \simeq h_{c1}$ the retained low-energy states are the lowest $S_z = 1$ state and the lowest $S_z = 0$ state, whereas for $h \simeq h_{c2}$ the lowest $S_z = 1$ and the $S_z = 2$ state are retained. In both cases, states which are not retained are $\sim \mathcal{O}(J)$ above the ground state, and the two retained states form a pseudospin-$\frac{1}{2}$, denoted $\hat{\boldsymbol{\tau}}$, which couples to the two leads. The effective models derived in both cases are of the form

$$\begin{aligned} \hat{H}_{\text{eff}} = & \frac{J_1}{2}\left[a\hat{S}^z_{01}\hat{\tau}^z + b(\hat{S}^+_{01}\hat{\tau}^- + \hat{S}^-_{01}\hat{\tau}^+)\right] \\ & + \frac{J_2}{2}\left[a\hat{S}^z_{02}\hat{\tau}^z + b(\hat{S}^+_{02}\hat{\tau}^- + \hat{S}^-_{02}\hat{\tau}^+)\right] \\ & + \hat{O} + \hat{H}_{\text{leads}} \ , \end{aligned} \tag{6.20}$$

with $\hat{O} = \hat{O}_1 + \hat{O}_2$ and

$$\begin{aligned} \hat{O}_1 &= c(J_1\hat{S}^z_{01} + J_2\hat{S}^z_{02}) \ , \\ \hat{O}_2 &= (\delta E' - h)\hat{\tau}^z \ , \end{aligned} \tag{6.21}$$

where $\delta E'$ is the zero-field energy difference between the two states retained; for $h = h_{c1}$, $\delta E' \simeq 0.66J$ and for $h = h_{c2}$, $\delta E' \simeq 1.71J$. The coefficients for $h = h_{c1}$ are $a \simeq 0.86$, $b \simeq 1.14$, $c \simeq 0.21$, whereas for the $h = h_{c2}$ effective model they are $a \simeq 0.14$, $b \simeq 0.54$, $c \simeq 0.46$. Recall that we solely consider the case of LR-symmetry,

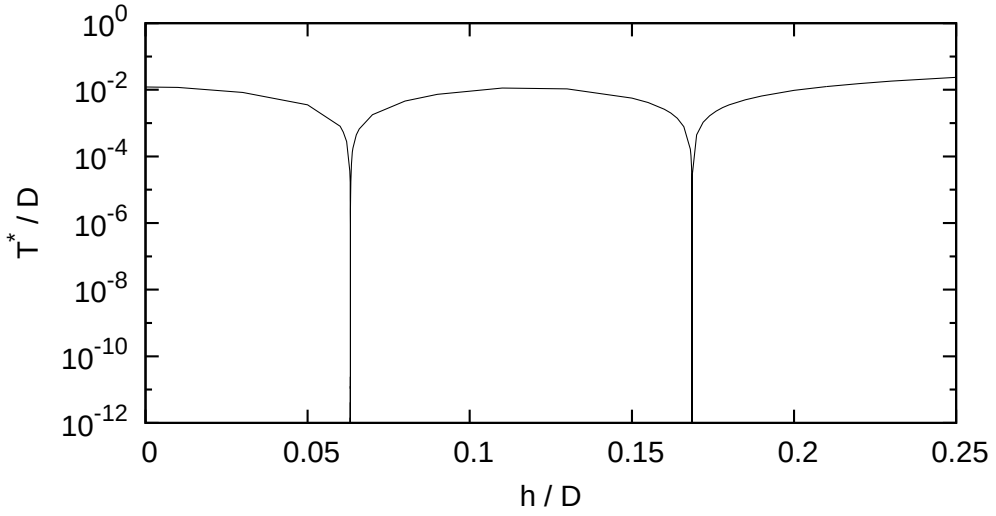


Figure 6.9: T^*, defined by $S_{\rm imp}(T^*) = \frac{1}{4}\ln 2$, as a function of field strength, h, for the LR-symmetric 4IKM with $\rho J_1 = \rho J_2 = 0.15$ and $J = 0.1D \gg J_c \simeq 0.003D$. The T^* scale is seen to vanish at the two critical points, $h = h_{c1}, h_{c2} \simeq 0.066D, 0.17D$.

i.e., $J_1 = J_2$.

Clearly these models are of the same form as the analogous effective model for the 2IKM (Eqn. (6.1)). We therefore expect the 2CK FP to be stable for $h = h_{c1}, h_{c2}$ for the 4IKM. From perturbative scaling arguments (see Eqn. (6.4)), one can estimate the scale on which the system flows to the 2CK FP, denoted $T_{\rm K}^{2CK}$, from the coefficients in Eqn. (6.20), finding that for $h = h_{c1}$, $T_{\rm K}^{2CK} \sim \exp(\frac{-1}{[\rho J_1/1.91]})$, whereas for $h = h_{c2}$, $T_{\rm K}^{2CK} \sim \exp(\frac{-1}{[\rho J_1/4.97]})$. In both cases then, $T_{\rm K}^{2CK}$ is much lower than at zero field, for which $T_{\rm K}^{2CK} \sim T_{\rm K} \sim \exp(\frac{-1}{\rho J_1})$ [112], and also much lower than the $T_{\rm K}^{2CK}$ which arises for the 2IKM at large fields (for which, $T_{\rm K}^{2CK} \propto \exp(\frac{-\pi}{2\rho J_1})$, as discussed previously). Because these scales are so small, it is unlikely that 2CK physics could be observed at finite field in an experiment on a four quantum dot system at finite field.

To confirm the picture of the LR-symmetric 4IKM discussed above, we have carried out NRG calculations. Taking $J \gg J_c$ such that at zero field the system is deep in the LS phase, we have considered the effect of applying a uniform magnetic field. The results for this are shown in Figs. 6.8 and 6.9. Beginning with Fig. 6.8, showing the expectation value of $\hat{S}_z$ ($\langle \hat{S}_z \rangle = S_z$) as a function of h, we see there are plateaus of $S_z \simeq 0, 1, 2$ with rapid (but continuous) changes between them occurring at $h \simeq h_{c1}, h_{c2}$. The ground states of the system far from the critical points are then essentially just the atomic-limit $S_z = 0, 1, 2$ ground states discussed above. Fig. 6.9 shows the scale on which the entropy goes to zero, defined by $S_{\rm imp}(T^*) = \frac{1}{4}\ln 2$, also as a function of h. T^* is seen to vanish at the two critical points, $h = h_{c1}, h_{c2}$, at which there is a residual $\frac{1}{2}\ln 2$ entropy indicating flow to the stable 2CK FP [52, 53].

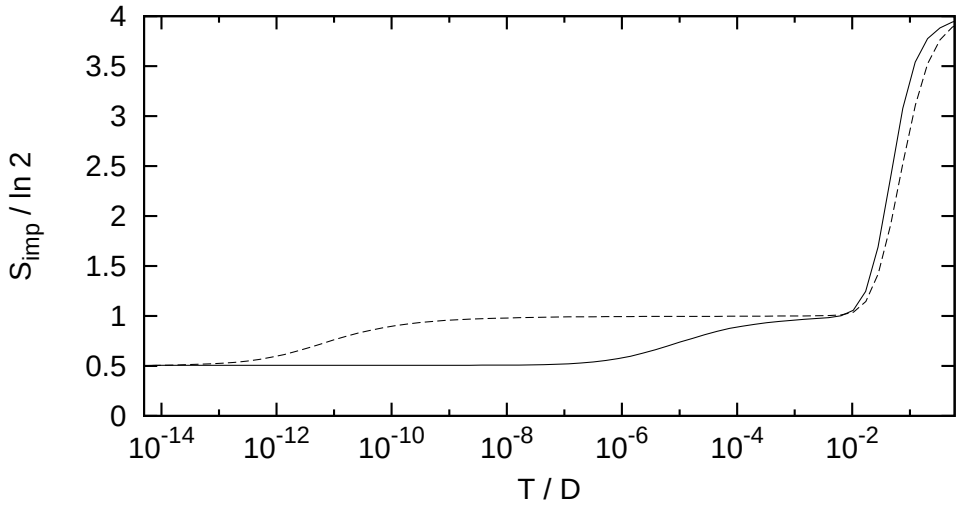


Figure 6.10: $S_{\rm imp}$ at the critical fields ($h = h_{c1}$ (solid line), h_{c2} (dashed line)) for the LR-symmetric 4IKM with $\rho J_1 = \rho J_2 = 0.15$ and $J = 0.1D \gg J_c \simeq 0.003D$. In both cases, the entropy goes to $\frac{1}{2}\ln 2$ when $T \sim T_{\rm K}^{2CK}$, indicative of flow to the 2CK FP. $T_{\rm K}^{2CK}$ is seen to be much lower at $h = h_{c2}$ than at $h = h_{c1}$.

$S_{\rm imp}(T)$ at the two critical points, shown in Fig. 6.10, confirms that $S_{\rm imp}(0)$ at both critical points is indeed $\frac{1}{2}\ln 2$. The data also shows that $T_{\rm K}^{2CK}$ is much smaller at the second critical point ($h = h_{c2}$), as discussed above. As in section 6.1.1, we have also carried out NRG calculations for the system with $J \gtrsim J_c$. Here we also find two critical points as h is increased[5].

Turning now to the 4IKM with $J < J_c$, we begin by considering the $J = 0$ case. For $J = 0$ and $h = 0$, the ground state of the 4IKM consists simply of the terminal spins forming Kondo singlets with their leads, and the central impurity spins remaining as free local moments. Upon application of an infinitesimal field the central impurity spins will be fully polarised, and as field is increased further, the Kondo singlets will be continuously polarised (on the scale of $h \sim T_{\rm K}$). We see therefore that there is a discontinuity upon increasing field strength at $h = 0$ for the $J = 0$ case. In the case of small but finite J ($J \ll J_c$), the $h = 0$ ground state contains two Kondo singlets (formed by the terminal spins) with the central spins now forming a singlet themselves, which is essentially decoupled from the Kondo singlets. As field is increased however, the Kondo singlets will be continuously polarised (again on the scale of $h \sim T_{\rm K}$), whereas we expect the decoupled central singlet to be polarised discontinuously when $h \simeq J \ll J_c \sim T_{\rm K}$, and for fields greater than this the ground state of the central pair of spins (essentially decoupled from the terminal spins) will have a $|\uparrow\uparrow\rangle$ configuration. This suggests that for $J < J_c$,

[5]Specifically we find that the 2CK FP is stable for $\rho J_1 = \rho J_2 = 0.15D$, $J = 0.004D \gtrsim J_c \simeq 0.003D$ and $h \simeq 0.0015D, 0.0062D$.

a *single* QPT should exist at $h \simeq J$. From NRG calculations on the 4IKM with $J \ll J_c$, we indeed find that as field strength increased, a single critical point is observed, at which the T^* scale vanishes and the 2CK FP is stable (indicated by a residual $S_{\rm imp}(T=0) = \frac{1}{2}\ln 2$), occurring at $h \simeq J$. [6]

It is interesting to consider what these findings imply for the phase diagram of the LR-symmetric 4IKM as a function of h and J, analogous to that for the LR-symmetric 2IKM (see Fig. 6.1). Varying J at zero field,there is known to be a single QPT, at $J = J_c \sim T_{\rm K}$ [112], and for both $J \gg J_c$ and $J \gtrsim J_c$, there are two QPTs as field strength is increased at fixed J, as discussed above. By contrast for $J < J_c$, there is a single QPT as field is increased, and for $J = 0$ this transition occurs at $h = 0$ (from the physical arguments above). At all of these transitions the 2CK FP is stable (except for the particular point $J = 0$, $h = 0$, where the ground state has the terminal impurity spins in Kondo singlets and the two central impurity spins free, with a residual $S_{\rm imp}(T=0) = \ln 4$). Furthermore, the $J = 0$, $h = 0^+$ ground state[7], consisting of two Kondo singlets and the central impurity spins in a $|\uparrow\uparrow\rangle$ configuration, is expected to be continuously connected to the $S_z = 2$ state (the ground state in the limit of high field) upon increasing field strength, as the Kondo singlets are continuously polarised by the field. We therefore conjecture that the phase diagram for the 4IKM is as illustrated in Fig. 6.11, with two lines of critical points, one terminating at $h = 0, J = 0$, and the other terminating at $J = J_c, h = 0$. This is the only phase diagram we can construct which is consistent with our NRG results. More work is however required to confirm this form of the phase diagram, particularly at low fields.

We now briefly consider longer even-numbered spin chains, connected in series between two leads, and coupled to the leads with antiferromagnetic exchange couplings, J_1 and J_2. We begin with the case $J \gg J_c$ (J_c, as ever, is the zero field critical point), and consider only the LR-symmetric ($J_1 = J_2$) case with equal interimpurity antiferromagnetic exchange couplings, J. For the 4IKM with $J \gg J_c$, recall that QPTs arise for fields at which atomic-limit ground state degeneracy occurs. Now, all even spin chains have a non-degenerate singlet ($S_z = 0$) ground state in the atomic limit, as well as excited states with $S_z = 0, 1, 2, ..., N$, where $2N$ is the number of spins in the chain. As field strength increases, successive atomic-limit ground state crossovers occur, with the S_z value of the ground state increasing from 1 to N in integer steps. With this in mind, we conjecture that *all* LR-symmetric $2N$ spin chains have N QPTs as uniform field strength is increased with $J > J_c$, occurring at fields for which atomic-limit degeneracy arises. At these points the doubly-degenerate atomic-limit ground state forms a pseudospin-$\frac{1}{2}$, which then couples to the leads to

[6] Specifically we find that the 2CK FP is stable for $\rho J_1 = \rho J_2 = 0.15$, $J = 0.001D < J_c \simeq 0.003D$ and $h \simeq 0.0012D$.

[7] 0^+ is a positive infinitesimal.

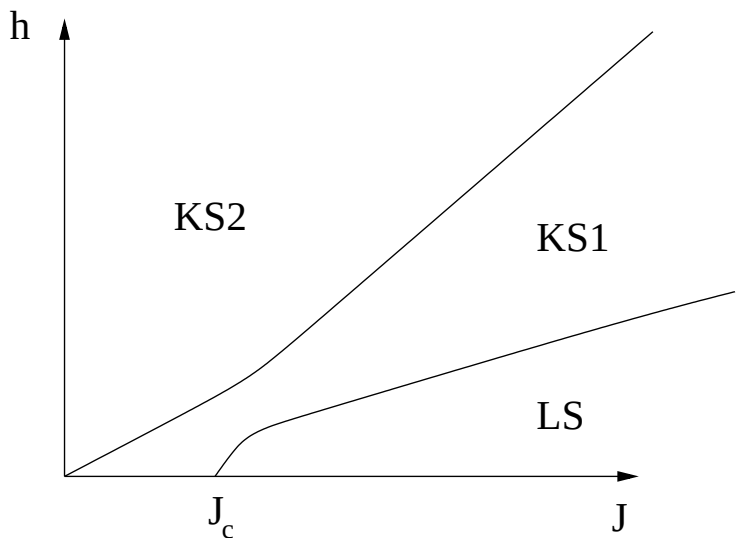


Figure 6.11: Schematic illustration of the proposed phase diagram for the 4IKM as a function of h and J. The KS2 ground state consists of the central spins in a $|\uparrow\uparrow\rangle$ configuration, with the two terminal spins in polarised Kondo singlets. The KS1 ground state consists of the central spins in a singlet state, with the two terminal spins in Kondo singlets, which are polarised at finite field. The LS ground state is simply the $S_z = 0$ atomic-limit ground state, essentially decoupled from the leads. For $J > J_c$, there are two successive QPTs as h is increased, whereas for $J < J_c$ there is only one, as found from our NGR calculations. At zero field there is a single QPT at finite J. We note that the point $J = h = 0$ is unique, in that the ground state here consists of the two terminal spins being locked up in Kondo singlets, and the central spins being free local moments.

give an effective 2CK model. Therefore the QPTs should each be characterised by the 2CK FP.

Looking at the LR-symmetric six spin chain (the six-impurity Kondo model, 6IKM, an obvious extension of the 4IKM) with $J \gg J_c$, and considering the effect of a uniform field, just as we did for the 4IKM, shows that in this case there are three critical fields at which the T^* scale vanishes, see Fig. 6.13, along with coincident sharp increases in S_z between plateaus of $S_z = 0, 1, 2, 3$, see Fig. 6.12. These occur close to the values of field strength for which the atomic-limit ground state is degenerate (we have verified this by diagonalising the atomic-limit system numerically). This behaviour is exactly analogous to that seen for the 4IKM in Figs. 6.8 and 6.9. This suggests that for all LR-symmetric even-numbered spin chains with $2N$ spins, provided $J \gg J_c$ at least, there exist N QPTs, which occur successively as field strength is increased. We have not looked at the 6IKM for lower values of J ($\lesssim J_c$), but the physical arguments made for the 4IKM should also apply here, and we therefore expect the phase diagram of the 6IKM to contain *three* critical lines, one of which terminates at $h = 0$, $J = J_c$, and the other two terminating at $h = 0, J = 0$. More generally, we believe it is likely that for a $2N$-spin chain, there are N lines of critical points in the h–J plane, with one terminating at $h = 0, J = J_c$,

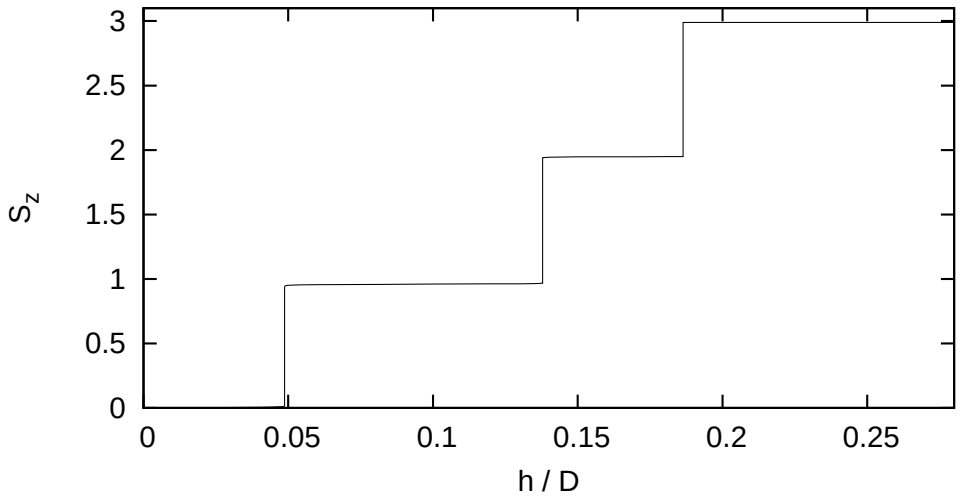


Figure 6.12: S_z vs h for the LR-symmetric 6IKM with $\rho J_1 = \rho J_2 = 0.093$ and $J = 0.1D \gg J_c$. Sharp but continuous increases in S_z occur near values of field strength for which atomic-limit degeneracy exists.

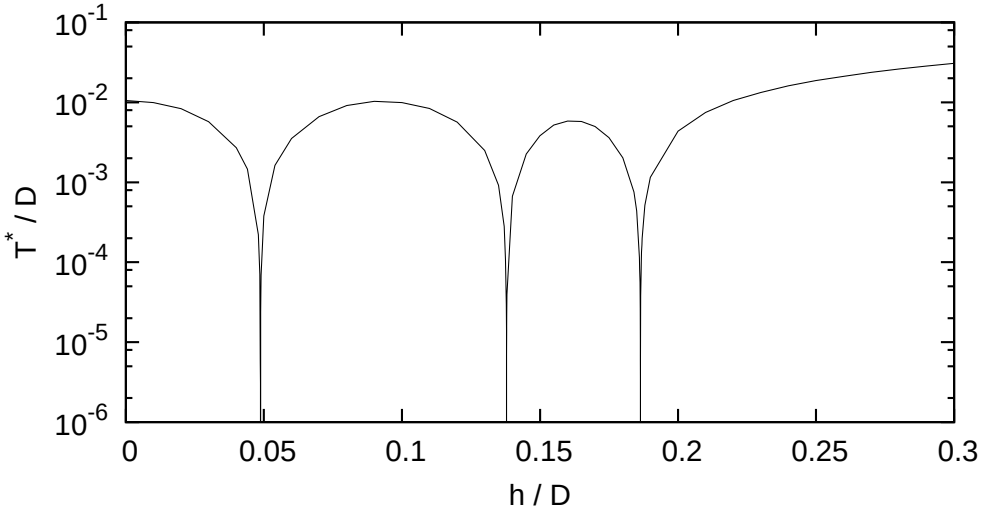


Figure 6.13: T^* as a function of field strength, h, for the LR-symmetric 6IKM with $\rho J_1 = \rho J_2 = 0.093$ and $J = 0.1D \gg J_c$. The T^* scale is seen to vanish at the three critical points, $h \simeq 0.05D, 0.14D, 0.18D$.

and $N - 1$ terminating at $h = 0, J = 0$. Further work is nevertheless required to establish satisfactorily the physics of these systems in the presence of the magnetic field.

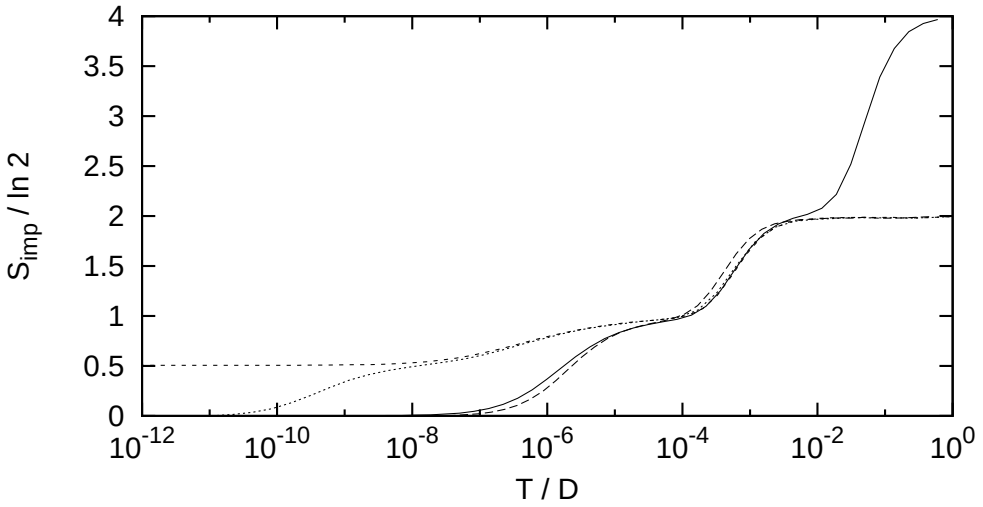


Figure 6.14: $S_{\rm imp}(T)$ for different models with $h \simeq h_c$. Shown for the 2IKM (short dashed line), H_3' model (dotted line), and H_3 model (long dash); in all cases, $\rho J_1 = \rho J_2 = 0.093$, $\rho J = 5 \times 10^{-4}$ ($\gg \rho J_c$), and $V_{LR} = \sqrt{J J_1 J_2 / U}$. For the 2AIM (solid line), we consider $U/\Gamma = 20$ and $t/\Gamma = 0.71$ (corresponding to $\rho J = \rho[4t^2/U] = 5 \times 10^{-4}$).

6.3 Two-impurity Anderson model

Having looked at the effect of a magnetic field on the Kondo physics exhibited by the spin models discussed above, we now go on to investigate the effect of a (uniform) field on the 2AIM. We begin by looking at the system at LR and ph symmetry. As discussed in section 6.1, 2CK physics arises in the 2IKM in the presence of a finite field, so we begin by considering the possibility of observing 2CK physics in the related 2AIM at finite field. We then go on to look at the conductance behaviour of the 2AIM in the presence of a magnetic field, before ending the chapter by investigating the effect of breaking LR and ph symmetry separately in sections 6.3.1 and 6.3.2.

Two-channel Kondo physics

Considering the ph-symmetric 2AIM at finite field, if $t \gg t_c$ (*i.e.*, $J = 4t^2/U \gg J_c$, but provided $t \ll U$, such that the SW transformation is valid. t_c is the zero-field crossover point between KS and LS regimes.), we expect similar behaviour to the 2IKM: a sufficiently large magnetic field $\sim h_c \sim J$ renders the singlet and lowest triplet atomic-limit states degenerate, suggesting the possibility of 2CK physics at low temperature. As was the case at zero field (section 5.2) however, whether 2CK physics can actually be observed in the 2AIM at finite field depends on the effect of charge transfer inherent to the model, since this destabilises the 2CK FP.

Following the approach of section 5.2, we compare the behaviour of the (LR-

symmetric) 2AIM with two effective low-energy models: the H_3' model (see Eqn. (2.30)) in a magnetic field $h \sim h_c$, and the result of a third-order Schrieffer-Wolff transformation of the 2AIM. The latter is found to be equivalent to the H_3 model (see Eqn. (2.28)) at $h \sim h_c$ upon retaining only the $|S\rangle$ and $|T_1\rangle$ dot states (*viz* $\hat{H}''_{\rm eff} = \hat{1}'(\hat{H}_{\rm 2IKM} + \hat{H}_3)\hat{1}'$), and is given explicitly by

$$\begin{aligned}\hat{H}''_{\rm eff} = \hat{H}_{\rm eff} - V_{LR}\Big[\sum_\sigma \sigma(f^\dagger_{1\sigma}f_{2\sigma} + f^\dagger_{2\sigma}f_{1\sigma})(\hat{\tau}_z - \tfrac{1}{4}) \\ + \tfrac{1}{\sqrt{2}}(f^\dagger_{1\uparrow}f_{2\downarrow} + f^\dagger_{2\uparrow}f_{1\downarrow})\hat{\tau}^- + \tfrac{1}{\sqrt{2}}(f^\dagger_{2\downarrow}f_{1\uparrow} + f^\dagger_{1\downarrow}f_{2\uparrow})\hat{\tau}^+\Big]\end{aligned} \tag{6.22}$$

where $\sigma = +/- \iff \uparrow / \downarrow$, and $\hat{H}_{\rm eff}$ is given by Eqn. 6.1.

Fig. 6.14 shows results for $S_{\rm imp}(T)$, in which the parameters are chosen to correspond to the 2AIM with $\tilde{U} = 20$, as considered earlier at zero field (Fig. 5.3). First, for comparison, the short-dashed line reproduces the 2IKM result from Fig. 6.3 for $J_1 = J_2$, where the 2CK critical FP is stable and hence $S_{\rm imp}(T = 0) = \frac{1}{2}\ln 2$. Next, the dotted line in Fig. 6.14 shows the behaviour of the corresponding H_3' model (containing direct interlead charge transfer, see Eqn. (2.30)) with $V_{LR} = \sqrt{JJ_1J_2/U}$. Since $\hat{H}_3'$ destabilises the 2CK FP there is ultimately a crossover to the SC FP with vanishing residual entropy, but the crossover scale here is sufficiently small compared to $T_{\rm K}^{2CK}$ that a $\frac{1}{2}\ln 2$ entropy plateau remains visible. The temperature window over which the plateau exists can be optimised by tuning h very slightly away from the critical h_c of the corresponding 2IKM; this has already been performed for the dotted line in Fig. 6.14 (where $(h - h_c)/h_c \simeq 2 \times 10^{-4}$).

Turning now to the 2AIM and H_3 models, we have repeated the process of searching for the widest $\frac{1}{2}\ln 2$ entropy plateau by varying h around h_c. However our calculations show no such plateau for the parameters considered ($\tilde{U} = 20$): the entropy always crosses directly from $\ln 2$ to zero, as illustrated by the solid and dashed lines in Fig. 6.14 (2AIM and H_3 models, respectively). This is not surprising, since it mirrors the $h = 0$ behaviour shown in Fig. 5.3: while the H_3' model for $\tilde{U} = 20$ shows a distinct 2CK entropy plateau, the 2AIM and H_3 models do not.

In section 5.2 we explained that the 2CK FP can indeed be observed at $h = 0$ in the 2AIM, if one considers the model at a larger $\tilde{U} \gtrsim 40$. It is thus natural to ask if the same is true for 2CK at finite field. We have undertaken preliminary calculations for $\tilde{U}$ up to 50 (in practice the largest for which the calculations are feasible) in an effort to answer this question. In each case we have examined the entropy around $h \simeq h_c \sim J$ for signs of a $\frac{1}{2}\ln 2$ plateau but, as illustrated in Fig. 6.15, do not find any sign of 2CK behaviour. Observation of 2CK physics relies of course on the separation of scales $T^* \ll T_{\rm K}^{2CK}$. Whereas at zero field, $T_{\rm K}^{2CK} \sim T_{\rm K}$, in the finite field case $T_{\rm K}^{2CK} \sim T'_{\rm K} \ll T_{\rm K}$ as is apparent from the low-energy effective

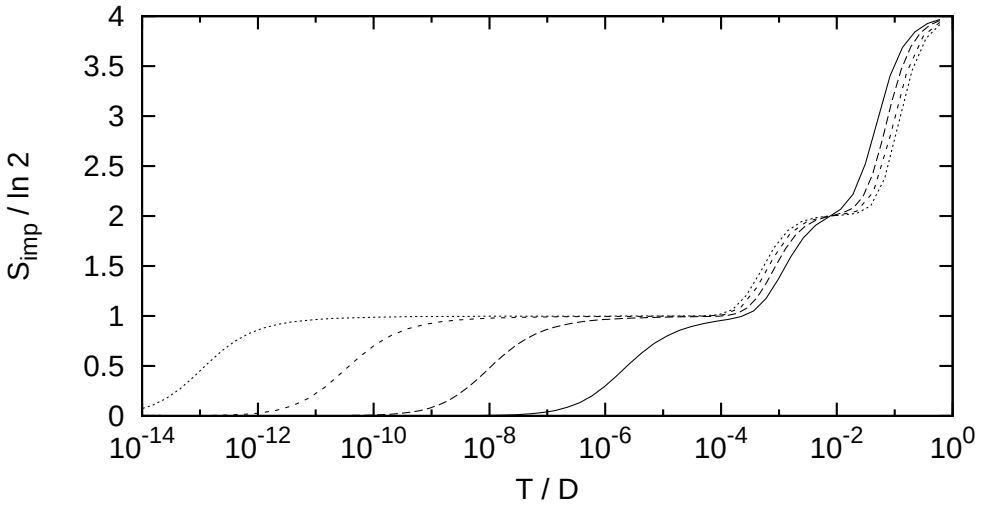


Figure 6.15: $S_{\rm imp}(T)$ for the 2AIM with $h \simeq h_c$, $t/\Gamma = 1 \gg t_c/\Gamma$, and $U/\Gamma = 20$ (solid line), 30 (long-dashed line), 40 (short-dashed line) and 50 (dotted line). As U/Γ increases, the $\ln 2$ entropy plateau extends to lower T, but for the values of U/Γ considered no $\frac{1}{2}\ln 2$ plateau is found. In each case h is tuned so as to minimise the scale on which the entropy goes to zero.

model, Eqn. (6.1). A much smaller T^*, arising from a larger $\tilde{U}$, is therefore required at finite field in order for 2CK physics to be observed. This suggests that if 2CK is to be found in the 2AIM at finite field, it will arise only for $\tilde{U}$ in excess of 50, for which the corresponding $T_{\rm K}^{2CK}$ will surely be out of range of experimental grasp.

Conductance

Having discussed the possibility of observing 2CK physics at finite field in the 2AIM, and shown it to be remote, we now move on to look at the zero-bias, zero-temperature conductance ($G_c(0,0)$) of the system. As 2CK physics cannot be observed even for the strongest correlations we have looked at ($\tilde{U} = 50$), we concentrate on the 2AIM with more moderate correlations (generally $\tilde{U} = 20$) in the rest of this chapter. We note that at LR and ph symmetry, but in the presence of a magnetic field, we can straightforwardly generalise the arguments in section 4.1 for the phase shifts to give the relation $\delta_{e\sigma} = \pi - \delta_{o\bar{\sigma}}$, with $\bar{\sigma}$ the opposite spin to σ. Using this result alongside Eqn. (3.55) shows that the contribution to $G_c(0,0)$ from the up-spin channel is equal to that from the down-spin channel at LR and ph symmetry, even in the presence of a field. Unitary conductance ($G_c(0,0) = 2e^2/h$) can only occur when the conductance in *each* spin channel is unitary (equal to e^2/h), and this occurs when $\delta_{o\uparrow} - \delta_{e\uparrow} = \delta_{o\downarrow} - \delta_{e\downarrow} = \frac{\pi}{2}$.

We may consider the effect of applying a field to the ph-symmetric 2AIM for three different regimes of interdot tunnel-coupling separately – the KS regime ($t \ll t_c$, with

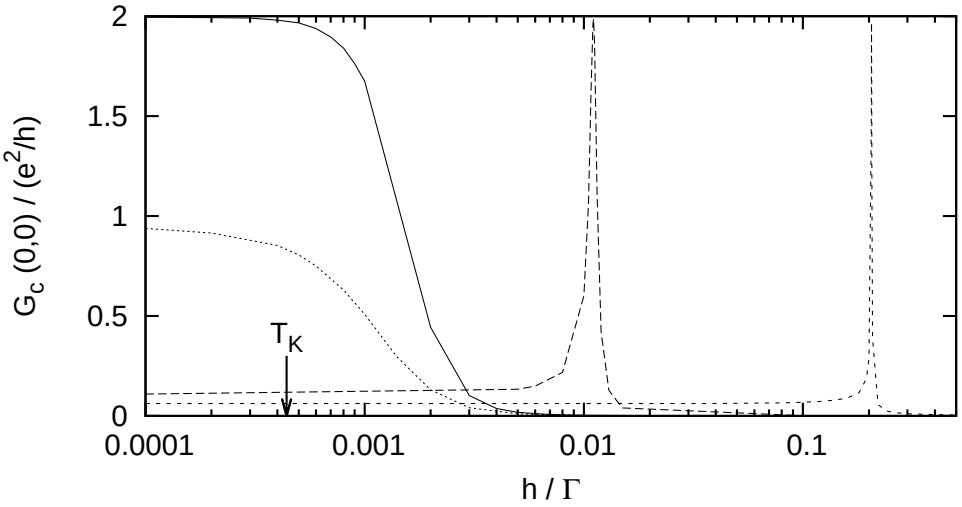


Figure 6.16: $G_c(0,0)$ for the LR and ph-symmetric 2AIM, in units of e^2/h, as a function of magnetic field strength, $h/\Gamma = \tilde{h}$, for $\tilde{t} = 0.106$ (dotted line), 0.123 (solid line), 0.25 (long-dashed line), 1 (short-dashed line) with $\tilde{U} = 20$. For these parameters, $\tilde{t}_c \simeq 0.123$. T_K is as marked, and for $t \leq t_c$ a field strength of this order (in practice a field strength of $\simeq 5T_K$) is required to destroy the enhanced zero-field conductance.

t_c the zero-field crossover point), the LS regime ($t_c \ll t \ll U$) and the BS regime ($t \gg U$) (see chapter 4 for discussion of these regimes at zero field). First, deep in the KS regime, applying a field merely destroys the zero-field Kondo effects when the field strength becomes $\sim \mathcal{O}(T_K)$. The zero-bias, zero-temperature conductance therefore decreases monotonically with field. This remains the case for $t \leq t_c$, as seen in Fig. 6.16 (solid and dotted lines correspond to $t \leq t_c$).

In the LS regime, the 2IKM exhibits a QPT as field is increased, at $h \simeq J$, separating the LS and the KS phases (see Fig. 6.1). In the 2AIM this is smeared into a continuous crossover by the charge transfer present. In the LS regime then ($t_c \ll t \ll U$), very different behaviour is observed from that in the KS regime (see long-dashed and short-dashed lines in Fig. 6.16). As h is increased from zero we see an increase in conductance with a maximum at $h \simeq h_c(t) \simeq J$, *i.e.*, at the crossover between LS and KS regimes, at which point the atomic-limit ground state is near degenerate. As field is increased further the zero-bias conductance dies off rapidly as one moves into the KS regime. At zero temperature, the peak in the zero-bias conductance as a function of h goes up to $G_c(0,0) = 2e^2/h$. In the LS regime then, a peak in $G_c(0,0)$ as a function of field is indicative of the LS-KS crossover.

Considering now the BS regime ($t \gg U$), the low-energy effective model given above (Eqn. (6.22)) is not valid, and the dots are treated as forming two MOs, each of which is coupled to both leads (see section 2.11). The effect of applying a magnetic field to such a two-level system was considered in Ref. [162]. In the

atomic limit, application of a magnetic field, $h \simeq h_c(t) \simeq \delta E$ (with δE the zero-field singlet-triplet splitting), causes the (2,0) singlet state (the zero-field ground state with two electrons in the bonding orbital and none in the antibonding orbital) and one component of the (1,1) triplet to become near degenerate, and as such form the components of a pseudospin-$\frac{1}{2}$, which we label $\hat{\tau}$. This pseudospin-$\frac{1}{2}$ is Kondo quenched by the leads at low temperature, leading to an enhanced zero-bias, zero-temperature conductance of $G_c(0,0) = \frac{2e^2}{h} G_0 = \frac{2e^2}{h} \frac{4\Gamma_1\Gamma_2}{(\Gamma_1+\Gamma_2)^2}$ [162], such that $G_c(0,0) = \frac{2e^2}{h}$ in the LR-symmetric case.

In the BS regime ($t \gg U$) a low-energy effective model can be derived for the 2AIM with $h \simeq h_c \simeq \delta E$, and it is given by[8] [162]

$$\begin{aligned}\hat{H}_{\text{eff}} = &\frac{8V_1^2}{U}\left[\hat{S}^z_{01}\hat{\tau}^z + \frac{\hat{S}^+_{01}\hat{\tau}^- + \hat{S}^-_{01}\hat{\tau}^+}{2}\right] + \frac{8V_2^2}{U}\left[\hat{S}^z_{02}\hat{\tau}^z + \frac{\hat{S}^+_{02}\hat{\tau}^- + \hat{S}^-_{02}\hat{\tau}^+}{2}\right] \\ &+ \frac{4V_1V_2}{U}\left[\sum_{\sigma,\nu} f^\dagger_{\nu\sigma} f_{\bar{\nu}\sigma}\hat{\tau}^z + (f^\dagger_{1\downarrow} f_{2\uparrow} + f^\dagger_{2\downarrow} f_{1\uparrow})\hat{\tau}^+ + (f^\dagger_{2\uparrow} f_{1\downarrow} + f^\dagger_{1\uparrow} f_{2\downarrow}\hat{\tau}^-)\right] \\ &+ \frac{V_1^2}{2t}\hat{S}^z_{01} + \frac{V_2^2}{2t}\hat{S}^z_{02} + \frac{V_1V_2}{4t}\sum_\nu\left[f^\dagger_{\nu\uparrow} f_{\bar{\nu}\uparrow} + f^\dagger_{\nu\downarrow} f_{\bar{\nu}\downarrow}\right] + (\delta E - h)\hat{\tau}^z \ ,\end{aligned} \tag{6.23}$$

with $\hat{H}_{\text{leads}}$ taken as read and $\bar{\nu} = 1(2)$ if $\nu = 2(1)$. Whilst this model appears rather complex, by making a simple canonical transformation it can be put into single-channel form [162]. Taking $a_\uparrow = \frac{1}{1+\lambda^2}[f_{1\uparrow} + \lambda f_{2\uparrow}]$, $a_\downarrow = \frac{1}{1+\lambda^2}[f_{1\downarrow} - \lambda f_{2\downarrow}]$, $c_\uparrow = \frac{1}{1+\lambda^2}[\lambda f_{1\uparrow} - f_{2\uparrow}]$, $c_\downarrow = \frac{1}{1+\lambda^2}[\lambda f_{1\downarrow} + f_{2\downarrow}]$, with $\lambda = \frac{V_1}{V_2}$, gives [162]

$$\hat{H}_{\text{eff}} = \frac{V_1^2 + V_2^2}{2t}\hat{S}^z_a + \frac{8(V_1^2+V_2^2)}{U}\left[\hat{S}^z_a\hat{\tau}^z + \frac{\hat{S}^+_a\hat{\tau}^- + \hat{S}^-_a\hat{\tau}^+}{2}\right] + (\delta E - h)\hat{\tau}^z \ , \tag{6.24}$$

with $\hat{\mathbf{S}}_a = \sum_{\sigma,\sigma'} a^\dagger_\sigma \boldsymbol{\sigma}_{\sigma\sigma'} a_{\sigma'}$, such that the pseudospin decouples entirely from the c lead. As the pseudospin is coupled only to a single effective channel in this model, 2CK physics cannot be observed in the BS regime ($t \gg U$) of the 2AIM at finite field, regardless of the correlation strength, $\tilde{U}$. However, in the BS regime, as in the LS regime, a finite-field conductance peak is indicative of the crossover to the KS regime, and in the LR-symmetric case, unitary zero-bias, zero-temperature conductance arises along the finite-field crossover (as in the LS regime, see above).

Fig. 6.17 illustrates the above findings. For the ph-symmetric 2AIM there exists a line of crossovers, $h_c(t)$, between the KS and LS regimes in the (h,t)-plane, such that $h_c(t = t_c) = 0$. Along the line we find enhanced $G_c(0,0)$ with unitary $G_c(0,0) = \frac{2e^2}{h}$ arising all the way along the crossover line in the case of LR symmetry. For the

[8] We write $\hat{H}_{\text{2AIM}}$ in the parity basis (see section 2.6) with $h \simeq \delta E$, take $\hat{H}_1$ to be the dot-lead couplings, and carry out a second-order SW transformation (see Appendix A), retaining only the states that make up the pseudospin-$\frac{1}{2}$. Terms of order $\sim \frac{1}{U}\left(\frac{U}{t}\right)^n, n \geq 2$ are neglected.

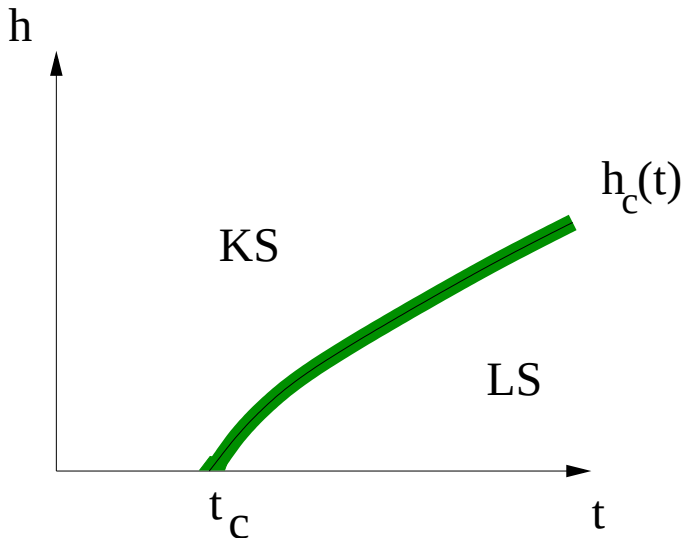


Figure 6.17: Illustration of the line of crossovers between KS and LS regimes for the ph-symmetric 2AIM in the (h,t)-plane. At zero field the crossover occurs at $t = t_c$, whereas for $t > t_c$, the crossover occurs at a finite field, given by $h = h_c(t)$, such that $h_c(t = t_c) = 0$. In the LR-symmetric case, unitary zero-bias, zero-temperature conductance ($G_c(0,0)$) arises all the way along the crossover line. In the LR-asymmetric case, unitary $G_c(0,0)$ occurs only for $t = t_c$, $h = 0$.

LR-asymmetric case, to which we now turn our attention, the line of crossovers still exists, and enhanced $G_c(0,0)$ arises along this line. *Unitary* $G_c(0,0)$ does not however arise at finite field in the LR-asymmetric case, as we now discuss.

6.3.1 Unequal dot-lead couplings

Having looked at the 2AIM at finite field with ph and LR symmetry, we now consider the effect of breaking these symmetries in turn – beginning with introducing LR asymmetry via the dot-lead couplings, *i.e.*, taking $\Gamma_1 \neq \Gamma_2$.

Regarding the prospect of observing 2CK physics in the 2AIM at finite field, we note that if $\Gamma_1 \neq \Gamma_2$, then we expect an additional term to arise in the expression for T^* of similar form to that for the LR-asymmetric 2IKM at finite field (see section 6.1), making it even more difficult to observe 2CK physics. Given that we were unable to observe 2CK physics in the LR-symmetric 2AIM at finite field, even for very high correlation strengths ($\tilde{U} = 50$), the possibility of observing it in a LR-asymmetric 2AIM at finite field seems very remote.

As we did for the LR-symmetric case, we now consider the zero-temperature, zero-bias conductance ($G_c(0,0)$) in the three different regimes of interdot coupling strength. In the KS regime ($t \ll t_c$), applying a magnetic field again merely destroys the Kondo effects occurring and therefore decreases $G_c(0,0)$ monotonically, with $G_c(0,0)$ dying away when $h \sim \mathcal{O}(\min(T_{\rm K}^{(1)}, T_{\rm K}^{(2)}))$, and this is not considered further.

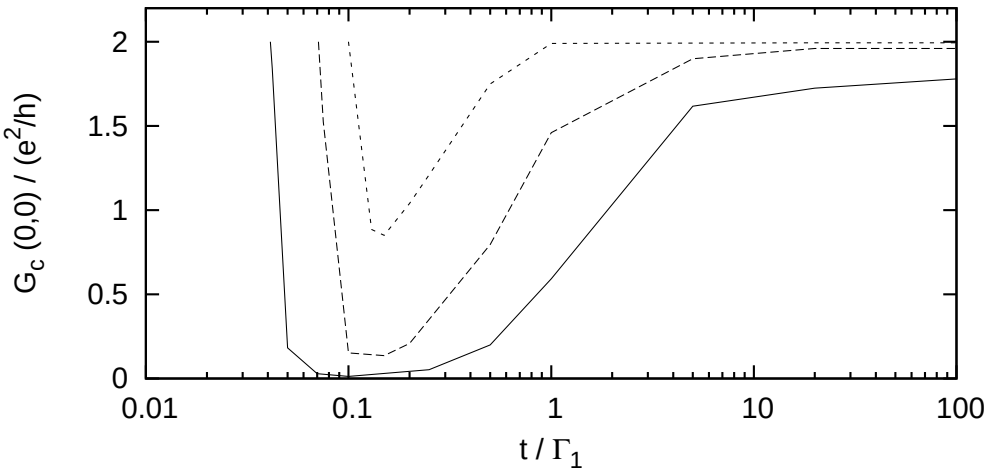


Figure 6.18: $G_c(0,0)$ as a function of t along the LS-KS crossover line (*i.e.*, with $h = h_c(t)$, see Fig. 6.17) for the ph-symmetric 2AIM with $U/\Gamma_1 = \tilde{U} = 20$ and $\Gamma_2/\Gamma_1 = \tilde{\Gamma}_2 = 0.9$ (short-dashed line), 0.75 (dashed line), 0.5 (solid line), and $t \geq t_c$. For $t = t_c$, unitary $G_c(0,0) = 2e^2/h$ arises in all cases, although the value of t_c itself varies. In the LS regime ($t_c \ll t \ll U$) the conductance is seen to decrease as LR-asymmetry increases. In the BS regime ($t \gg U$), $G_c(0,0) \simeq 2e^2/hG_0 = 2e^2/h\frac{4\Gamma_1\Gamma_2}{(\Gamma_1+\Gamma_2)^2}$. The corresponding line for $\tilde{\Gamma}_2 = 1$ is simply $G_c(0,0) = 2e^2/h$ for $t \geq t_c$.

In the LS regime ($t_c \ll t \ll U$), enhanced $G_c(0,0)$ is observed at the LS-KS crossover ($h \simeq h_c(t)$), just as in the LR-symmetric case. In this case, with $h \simeq h_c(t)$, the low-energy effective model given by Eqn. (6.22) is valid, although the unequal dot-lead couplings mean that the pseudospin is now asymmetrically coupled to the two leads. The low-energy effective model is therefore a (spin-anisotropic) 2CK model with relevant channel anisotropy and interlead, cotunneling charge-transfer [there are also $\hat{O}$ terms, but these effectively "cancel out" for $h \simeq h_c(t)$, and we therefore do not consider them in this discussion]. In the limit of large channel anisotropy, it is clear that the pseudospin will be quenched by whichever lead it is most strongly coupled to, and it will become effectively decoupled from the other lead at sufficiently low energies. The zero-bias conductance would therefore be expected to be low at zero temperature. In the other limit, in which the channel anisotropy is much smaller than the charge transfer, we would expect the channel anisotropy to be unimportant, and the zero-bias conductance at the finite-field crossover to go to $\simeq 2e^2/h$, as it is found to do in the LR-symmetric (channel-isotropic) case.

In Ref. [115] a 2CK model with small channel anisotropy and small interlead, cotunneling charge transfer was considered[9]. [Our effective model differs from this only in that the charge transfer is spin anisotropic, and there is also an additional

[9]Small in the sense that the system flows close the 2CK FP over some temperature range even in the presence of these relevant perturbations.

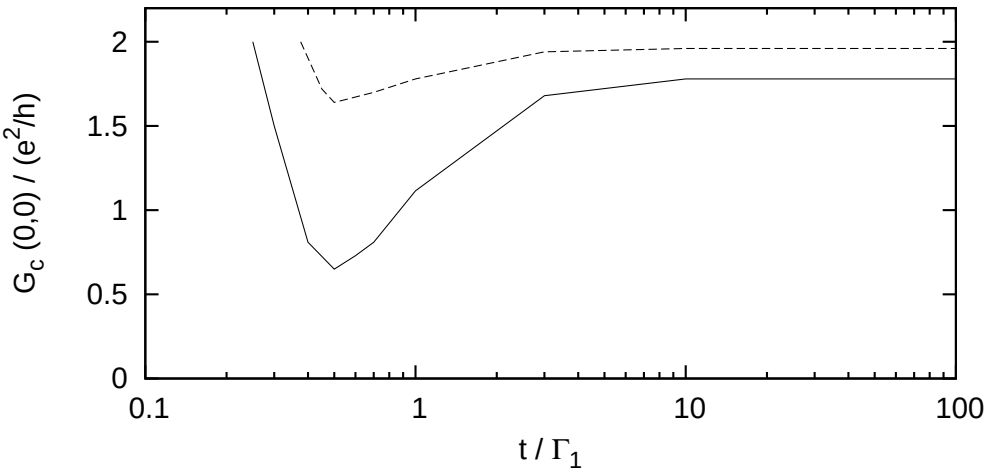


Figure 6.19: $G_c(0,0)$ as a function of t along the LS-KS crossover line (*i.e.*, with $h = h_c(t)$, see Fig. 6.17) for the ph-symmetric 2AIM with $\tilde{U} = 10$ and $\tilde{\Gamma}_2 = 0.75$ (dashed line), 0.5 (solid line), and $t \geq t_c$. For $t = t_c$, unitary $G_c(0,0) = 2e^2/h$ arises in all cases, although the value of t_c itself varies. In the LS regime ($t_c \ll t \ll U$) the conductance is seen to decrease as LR asymmetry increases, and for a given $\tilde{\Gamma}_2$ the conductance is greater for $\tilde{U} = 10$ than $\tilde{U} = 20$, cf. Fig. 6.18. In the BS regime ($t \gg U$), $G_c(0,0) \simeq 2e^2/hG_0 = 2e^2/h\frac{4\Gamma_1\Gamma_2}{(\Gamma_1+\Gamma_2)^2}$. For $\tilde{\Gamma}_2 = 0.9$, not shown, $G_c(0,0) \simeq \frac{2e^2}{h}$ for $t \geq t_c$.

direct interlead charge transfer term (given by the $\frac{1}{4}$ in Eqn. (6.22)), but intuitively one would not expect this to be important.] The two perturbations considered both cause the system to flow away from the 2CK FP on the lowest energy scales, giving rise to a crossover scale, T^*, with contributions from the channel anisotropy, T^*_δ, and the charge transfer, T^*_{LR}. The authors of Ref. [115] derive an exact expression for the **T**-matrix of the system, with the zero-temperature result [115]

$$|2\pi\rho_T T_{12;\sigma}(\omega = 0)|^2 = \frac{T^*_{LR}}{T^*} \tag{6.25}$$

and using Eqn. (3.52), it follows that (using $T^* = T^*_{LR} + T^*_\delta$)

$$G_c(0,0) = \frac{2e^2}{h}\frac{1}{1 + \frac{T^*_{LR}}{T^*_\delta}} \tag{6.26}$$

such that the zero-bias, zero-temperature conductance of the model (and therefore that of the LR-asymmetric 2AIM at the finite-field crossover) depends on the ratio of charge transfer to channel anisotropy. Although the results of Ref. [115] are valid only for sufficiently small channel anisotropy and interlead charge transfer, such that $T^* \ll T_{\rm K}^{2CK}$, this is qualitatively what we find for the 2AIM in the LS regime with $h \simeq h_c(t)$, for which this condition is not satisfied (*i.e.*, for which there is no flow in the vicinity of the 2CK FP), as we now explain.

NRG results for the zero-bias, zero-temperature conductance ($G_c(0,0)$) along the crossover line (*i.e.*, with $h = h_c(t)$, see Fig. 6.17) as a function of t (with $t \geq t_c$) are shown in Figs. 6.18 and 6.19, for two different values of $\tilde{U}$ and a number of different values of LR-asymmetry, $\Gamma_2/\Gamma_1 = \tilde{\Gamma}_2$.[10] For all values of $\tilde{U}$ and $\tilde{\Gamma}_2$, the conductance at $t = t_c$ (where the lines in the figures begin) is unitary ($G_c(0,0) = 2e^2/h$) as discussed in chapter 4; the value of t_c is of course dependent on $\tilde{U}$ and $\tilde{\Gamma}_2$. In the LR-asymmetric case, moving along the crossover line between LS and KS regimes, *i.e.*, increasing t and keeping $h \simeq h_c(t)$, causes $G_c(0,0)$ to drop sharply, to some minimum value as one moves into the LS regime ($t_c \ll t \ll U$), as seen in all cases in Figs. 6.18 and 6.19. This minimum value is dependent on the ratio of charge transfer to LR asymmetry. Decreasing $\tilde{U}$ causes charge transfer to increase and therefore increases $G_c(0,0)$ in the LS regime ($t_c \ll t \ll U$), as can be seen by comparing, for instance, the solid lines in Figs. 6.18 and 6.19, which have the same LR-asymmetry (Γ_2/Γ_1) but different $\tilde{U}$. Decreasing $\tilde{\Gamma}_2$ from unity increases LR asymmetry and therefore decreases $G_c(0,0)$ in the LS regime (see Eqn. (6.26)), as can be seen, for instance, by comparing the different lines in Fig. 6.18 for $t/\Gamma_1 = 0.2$, say – deep in the LS regime. As t is increased within the LS regime, the amount of interlead charge transfer increases, and this causes an increase in $G_c(0,0)$ for any values of $\tilde{U}$ and $\tilde{\Gamma}_2$, as seen in all cases in Figs. 6.18 and 6.19 (looking at $t_c \ll t \ll U$). Our NRG data for $G_c(0,0)$ along the finite-field crossover in the LS regime ($t_c \ll t \ll U$) are therefore qualitatively in line with the results of Ref. [115], particularly Eqn. (6.26), although we stress that this result is not strictly valid for the 2AIM, for which $T^* \not\ll T_{\rm K}^{2CK}$.

In the BS regime ($t \gg U$), the low-energy effective model at the crossover is given by Eqn. (6.23). $G_c(0,0)$ for this model is given simply by [162] $G_c(0,0) = \frac{2e^2}{h} G_0$, where $G_0 = \frac{4\Gamma_1\Gamma_2}{(\Gamma_1+\Gamma_2)^2}$ is an asymmetry factor. This is confirmed in Figs. 6.18 and 6.19, where $G_c(0,0)$ at the finite-field crossover in the limit $t \gg U$ goes to $\frac{2e^2}{h} G_0$, independently of $\tilde{U}$ (for $\tilde{\Gamma}_2 = 0.5$, $2G_0 \simeq 1.78$, for $\tilde{\Gamma}_2 = 0.75$, $2G_0 \simeq 1.96$, and for $\tilde{\Gamma}_2 = 0.9$, $2G_0 \simeq 1.99$).

6.3.2 Away from ph symmetry

We now turn our attention to the effect of applying a magnetic field to the 2AIM away from ph symmetry, considering the system with LR symmetry ($\epsilon_1 = \epsilon_2 = \epsilon$, $\Gamma_1 = \Gamma_2 = \Gamma$) for simplicity. We begin by considering the atomic-limit 2AIM in a magnetic field, for which we can trivially calculate the phase diagram, shown in Fig. 6.20. We consider only $\epsilon \geq -U/2$ as the physics of the system for $\epsilon < -U/2$ is related by ph transformation. At ph symmetry, the atomic-limit ground state

[10] In practice, we find the finite-field crossover, $h_c(t)$, as the value of h which minimises the scale on which the entropy goes to zero. This value of field also corresponds to a maximum in $G_c(0,0)$ for any given value of t.

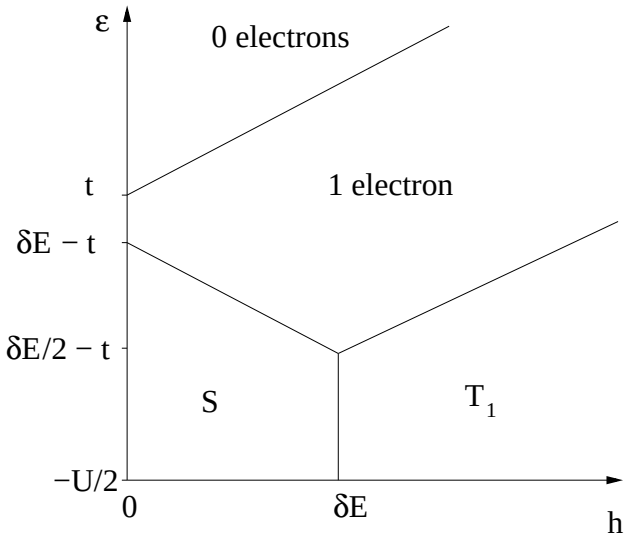


Figure 6.20: Atomic-limit phase diagram for the LR-symmetric 2AIM as a function of h and ϵ. S and T_1 represent the two-electron singlet and triplet states discussed in the text. The one-electron state has a single $\uparrow$-spin electron delocalised over the two dot levels, given by $\frac{1}{\sqrt{2}}[|\uparrow -\rangle - |- \uparrow\rangle]$. $\delta E = \frac{-U}{2} + \frac{U}{2}\sqrt{1+\frac{16t^2}{U^2}}$ is the zero-field splitting between the two-electron singlet and triplet states. Note that in the limit $t \to 0$, $\delta E \to 0$, so that the S and one-electron phases vanish. $\epsilon = -U/2$ is the ph-symmetric point of the model.

contains two-electrons regardless of field, but the ground state changes from $|S\rangle = \frac{1}{\sqrt{2}}\,[\,|\uparrow\downarrow\rangle - |\downarrow\uparrow\rangle\,]$ to $|T_1\rangle = |\uparrow\uparrow\rangle$ as the field is increased. A magnetic field also has the effect of shifting the boundaries between different charge states.

Turning now to the full lead-coupled system, we calculate the zero-bias, zero-temperature conductance, $G_c(0,0)$, via the NRG. We consider the system with a number of different values of $\tilde{t}$, beginning with the case of $t = t_c^{ph}$, which is representative of the whole $t \leq t_c^{ph}$ regime (t_c^{ph} being the crossover value of t at ph symmetry and zero field, the value of t which gives $\delta_{e\sigma} = \pi/4$ at ph symmetry and zero field). $G_c(0,0)$ as a function of $\tilde{\epsilon}$ for various values of field strength, h, for this case is shown in Fig. 6.21. For $t \leq t_c^{ph}$, at ph symmetry a magnetic field kills off the conductance on the scale of T_K, as discussed previously (see section 6.3). For $h \gg T_K$ then, the Kondo physics is destroyed, and we see Coulomb blockade structure; that is, peaks in $G_c(0,0)$ arising roughly along the lines of atomic-limit charge degeneracy shown in Fig. 6.20. These peaks have a width $\sim \mathcal{O}(\Gamma)$, but as $t/\Gamma \ll 1$, the width of the one-electron sector as a function of ϵ is $\ll \Gamma$. Therefore the two Coulomb peaks which are expected (separating two/one and one/zero electron regimes) are not distinct, so only one peak is observed. These peaks are due to sequential one-electron tunneling processes, and are relatively low; $G_c(0,0)$ is much less than the unitary limit. This can be understood physically when one considers that the interdot tunnel-coupling is relatively small ($t \ll \Gamma$), such that sequential

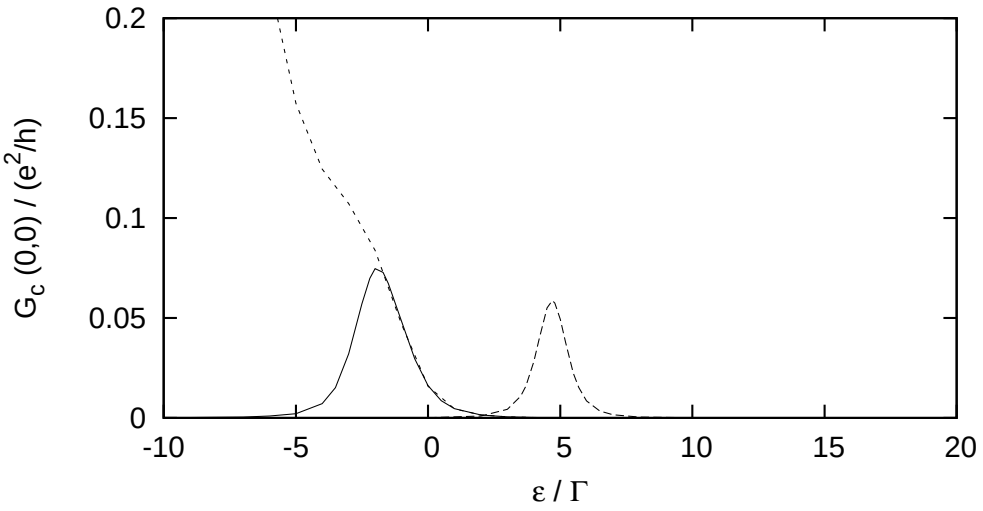


Figure 6.21: $G_c(0,0)$ vs $\tilde{\epsilon} = \epsilon/\Gamma$ for the LR-symmetric 2AIM with $\tilde{U} = 20$, $\tilde{t} \simeq \tilde{t}_c \simeq 0.123$, and $\tilde{h} = 0$ (dotted line), 0.1 (solid line) , 10 (dashed line). For even the smallest value of field strength shown here the unitary conductance arising at ph symmetry ($\tilde{\epsilon} = -10$) at zero field is destroyed. All that is seen in the finite-field data then are Coulomb blockade peaks, and these move to higher ϵ as field strength is increased. Note that because the value of $\tilde{t}$ used here is so small ($t < \Gamma$), the two Coulomb blockade peaks expected to arise (between two and one, and one and zero-electron sectors) are not distinct.

one-electron tunneling is slow.

For $t_c^{ph} \ll t \ll U$, as shown in Fig. 6.22, Kondo physics arises at zero field in the two-electron regime, giving unitary $G_c(0,0)$ for $\tilde{\epsilon} \simeq -3$ in this case. As the field strength is increased, this conductance peak moves towards ph symmetry, until for $h \simeq h_c$, unitary $G_c(0,0)$ arises at ph symmetry. As h is increased further, the Kondo physics arising in the two-electron regime dies away, and all that remains are Coulomb blockade peaks at values of ϵ for which atomic-limit charge degeneracy exists. As $t \lesssim \Gamma$ in Fig. 6.22, the one-electron sector is too small for the two Coulomb blockade peaks to be discernible, as in Fig. 6.21.

The final case we consider is the LR-symmetric 2AIM with $t \gg U$, NRG results for which are shown in Fig. 6.23. At zero field, unitary $G_c(0,0)$ arises in the one-electron sector (at $\tilde{\epsilon} \simeq 45$ in Fig. 6.23) due to a bonding Kondo effect, as discussed previously (see section 4.3). When a field of magnitude larger than the bonding Kondo scale is applied, the bonding Kondo effect is destroyed, and all that remains in the conductance is Coulomb blockade peaks, arising, as ever, for values of ϵ for which atomic-limit charge degeneracy occurs, see Fig. 6.23. As the field strength is increased, the Coulomb blockade peaks move apart, as the one-electron sector widens. Eventually $h \simeq h_c \simeq \delta E$ and unitary conductance arises at ph symmetry. As field strength is increased further (not shown), this Kondo peak dies away, and once again only the Coulomb blockade peaks remain, which vary with field in the

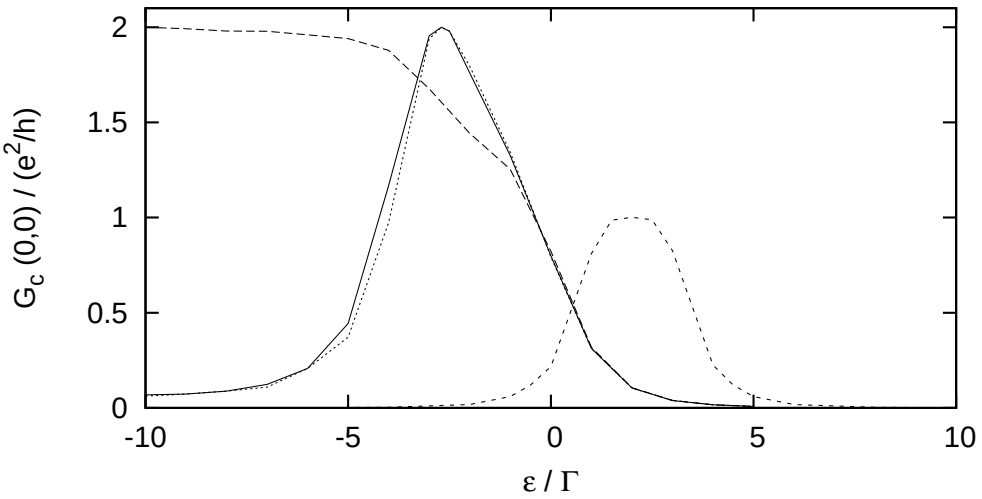


Figure 6.22: $G_c(0,0)$ vs $\tilde{\epsilon}$ for the LR-symmetric 2AIM with $\tilde{U} = 20$, $\tilde{t} = 1$, and $\tilde{h} = 0$ (dotted line), 0.1 (solid line), 0.2057 (long-dashed line), 5 (short-dashed line). The smallest field shown here is essentially identical to the zero-field case, but when the field is increased further unitary conductance arises at ph symmetry ($\tilde{\epsilon} = -10$) when $h = h_c \simeq 0.2057\Gamma$ (long-dashed line). For higher values of field strength this conductance is destroyed, and just the Coulomb blockade peaks remain (dotted line). Note that for the value of $\tilde{t}$ used here, the two Coulomb blockade peaks we expect to arise (between two and one-electron, and one and zero-electron sectors) are not distinct.

same way as the atomic-limit charge degeneracy lines in Fig. 6.20.

In addition to calculating the total $G_c(0,0)$, via the NRG we may also calculate the spin-resolved conductances, $G_{c\sigma}(0,0) = \frac{4e^2}{h}\Gamma_1\Gamma_2|G_{12;\sigma}(\omega = 0, T = 0)|^2$ (cf. Eqn. (3.54)), such that $G_c(0,0) = \sum_\sigma G_{c\sigma}(0,0)$. This is shown in Fig. 6.24 (the parameters used here are the same as those used for the long-dashed line in Fig. 6.23). As one would expect, for Coulomb blockade peaks between charge regimes which differ by addition/removal of an $\uparrow$-spin, *e.g.*, the peak between zero and one electron regimes occurring at $\tilde{\epsilon} \simeq 65$ in Fig. 6.23, $G_c(0,0)$ is dominated by $\uparrow$-spin conductance. Likewise, Coulomb blockade peaks between charge regimes which differ by addition/removal of an $\downarrow$-spin, *e.g.*, the peak between the one-electron regime and the $|S\rangle$ regime occurring at $\tilde{\epsilon} \simeq 25$ in Fig. 6.23, $G_c(0,0)$ is dominated by $\downarrow$-spin conductance. At the Coulomb blockade peaks in Fig. 6.23 then, spin-polarised currents arise upon application of a voltage bias.

Over the last three chapters we have seen that multi-impurity models, such as the 2IKM and the 2AIM, exhibit a fascinating and complex range of Kondo physics, both in the absence and presence of a magnetic field. In the next chapter we look at how this behaviour is manifest in an experimental realisation of the 2AIM in a

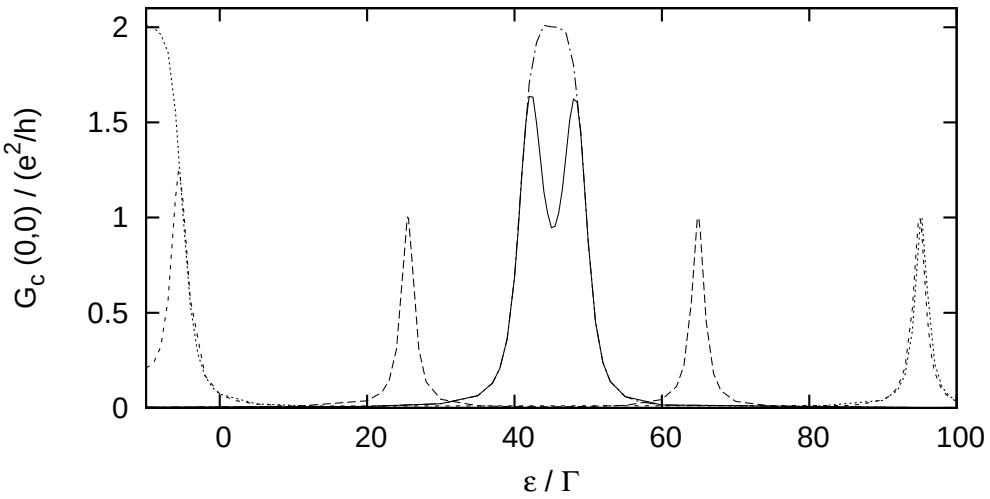


Figure 6.23: $G_c(0,0)$ vs $\tilde{\epsilon}$ for the LR-symmetric 2AIM with $\tilde{U} = 20$, $\tilde{t} = 50$, and $\tilde{h} = 0$ (dot-dashed line), 0.1 (solid line), 30 (long-dashed line), 90 (short-dashed line), and $90.53 \simeq \tilde{h}_c$ (dotted line). For the smallest value of $\tilde{h}$ shown, the bonding Kondo effect is already largely destroyed, and the Coulomb blockade peaks remain. For $h = 30, 90$ the Coulomb blockade peaks occur but their separation increases with $\tilde{h}$. When $h = h_c \simeq 90.53\Gamma$, unitary conductance arises at ph symmetry ($\tilde{\epsilon} = -10$). As field strength is increased further, this conductance is destroyed, and again, only the Coulomb blockade peaks remain (not shown, for clarity). The Coulomb blockade peaks at $\tilde{\epsilon} \simeq 95$ for $\tilde{h} = 90, 90.53$ are almost indistinguishable.

carbon nanotube TCDQD.

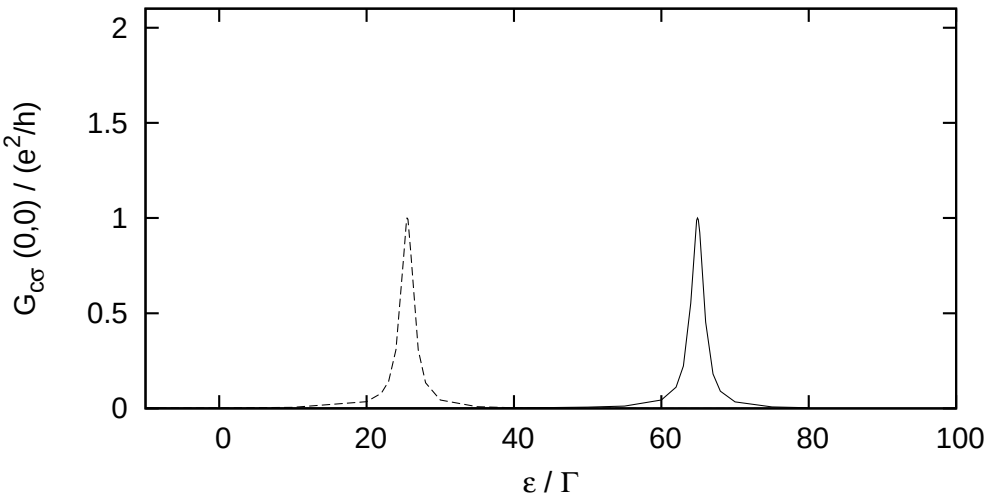


Figure 6.24: Spin-resolved zero-bias, zero-temperature conductance, $G_{c\sigma}(0,0)$, vs $\tilde{\epsilon}$ for the LR-symmetric 2AIM with $\tilde{U} = 20$, $\tilde{t} = 50$, and $\tilde{h} = 30$ for $\sigma = \uparrow$ (solid line), $\downarrow$ (dashed line). The CB peak between 0 and 1 electron regimes is dominated by up spin conductance, whereas that between 0 and 2 electron regimes is dominated by down spin conductance. The parameters used here are the same as those for the long-dashed line in Fig. 6.23.

CHAPTER 7

Experimental realisation of the 2AIM

Over the previous three chapters the Kondo physics, including the 2CK physics, arising in the 2AIM has been studied in some detail. In this chapter we apply the knowledge attained to an experimental study of a tunnel-coupled double quantum dot (TCDQD), which provides an experimental realisation of the 2AIM. We note that previous experimental work has been performed on TCDQDs in GaAs [84, 85], although without precise control over the parameters of the device or a quantitative comparison with theory. Work has also been carried out on a related scanning tunneling microscope system, which however differs from the 2AIM in that an additional direct interlead tunneling is present [86]. In this chapter we make quantitative comparison to measurements carried out by our collaborators (Dr Mark Buitelaar et al., Cavendish Laboratory, University of Cambridge) on a highly-tunable, strongly correlated carbon nanotube (CNT) DQD, in which the charge on each dot can be varied separately, such that the full range of charge regimes may be accessed. The interdot tunnel-coupling and the dot-lead tunnel-couplings can also be tuned by adjustment of gate voltages. In addition, a magnetic field may be applied to the system, allowing the behaviour discussed in chapter 6 to be probed.

In the experimental device, at the centre of the (1,1) regime (in which there is essentially one electron on each dot) the ground state of the system is a local singlet, as the effective interdot exchange coupling (J) turns out to be much greater than the dot Kondo scales ($T_{\rm K}^{(1)}, T_{\rm K}^{(2)}$). Kondo correlations are therefore suppressed at low energies. However, interlead cotunneling is restored when the applied bias (V_{sd}) is large enough to induce transitions between the atomic-limit singlet ground state and the triplet excited states, separated by J, leading to finite-bias conductance peaks. Both J and the Kondo scales can be tuned by varying the dot level energies in the (1,1) regime. The Kondo scales can also be tuned directly by varying the dot-lead couplings (Γ_1, Γ_2). The ability to tune both J and the Kondo scales allows one, in principle, to cross over from the LS to the KS regime. In our device

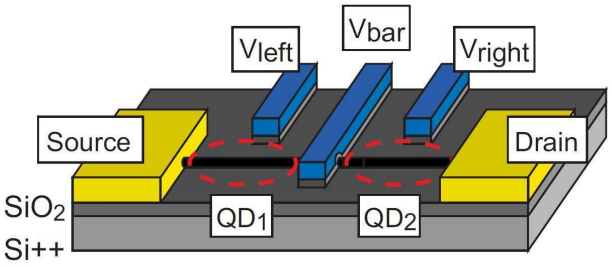


Figure 7.1: Schematic diagram of the experimental CNT DQD. The CNT (horizontal black line) sits on a SiO_2 wafer, and the two QDs are formed in series in the tube. $V_{\mathrm{left(right)}}$ are voltages applied to the left and right electrodes to control the energy levels of dot 1 (2). V_{bar} is a voltage applied to the central electrode which sits between the two dots. The two metallic leads are labeled source and drain.

the onset of charge fluctuations on the dots (as well as the inability to decrease J sufficiently) means that this crossover was not observed cleanly at zero field. However, as discussed in chapter 6, the crossover also exists at finite magnetic field. This finite-field crossover *was* observed in the experiment, manifest as an enhanced zero-bias conductance.

We are able to qualitatively reproduce all experimental results via NRG calculations. The canonical model used to describe TCDQDs is of course the 2AIM (see Eqns. (2.16) – (2.19)) [2, 40–42]. This is taken as the basic model for our NRG calculations, and supplement it with an *inter*dot Coulomb repulsion term ($\hat{H}_{U'}$, see Eqn. (2.21)), which inevitably exists in experiment, and which we find necessary to obtain good agreement between theory and the experimental "stability diagram" shown in Fig. 7.2. The electron g-factor is taken to be precisely 2 in comparing to experiment, as is common for CNTs [68], but note that a slightly smaller value ($g \sim 1.7 - 1.8$) would lead to even better agreement between experiment and theory in Fig. 7.13. In our calculations we use the parameters U, U', t and Γ_ν determined experimentally, and a temperature $T \sim 100$ mK. Experimentally, the dot level energies are controlled by two gate voltages, V_{left} and V_{right} (see Fig. 7.1). One might naively anticipate $\epsilon_1 \propto -V_{\mathrm{left}}$, $\epsilon_2 \propto -V_{\mathrm{right}}$ but, as is physically natural given the experimental set-up (Fig. 7.1), there is some 'cross talk' between the side gate voltages, and to obtain good agreement between experiment and theory it is necessary to include some dependence of ϵ_1 on V_{right} and of ϵ_2 on V_{left}. Specifically, we find

$$\epsilon_1 \propto -V_{\mathrm{left}} - aV_{\mathrm{right}}, \qquad \epsilon_2 \propto -aV_{\mathrm{left}} - V_{\mathrm{right}}, \tag{7.1}$$

with $a = 0.4$ giving the best agreement. To reduce discretisation error, we average our NRG calculations over different lead bandwidths, D (always keeping D much

greater than any other energy scale in the problem), and calculate the dot Green functions via the self-energy method (see section 3.6.3 and Ref. [135]). This enables us to work reliably with a relatively large discretisation parameter of $\Lambda = 9$.

Since the experiment was carried out at a finite temperature, the exact linear-response approach is used to calculate the zero-bias conductance (see section 3.7.3). To calculate the finite-bias conductance, we must resort to approximation, and we take the self-energies of the system to be independent of the applied bias, yielding Eqn. (3.64) (see section 3.7.4 for details). The partitioning of the applied bias is taken to be somewhat asymmetric, with $\lambda = 0.8$, this value being found to give the best agreement with the experimental data (in particular for the slopes of the Coulomb blockade peaks (in Fig. 7.7 for example), which are known to depend on λ [128, 129]).

The device we consider is a single-walled carbon nanotube on a degenerately doped Si/SiO_2 substrate contacted by Au contacts, illustrated in Fig. 7.1. A central gate, V_{bar}, is used to introduce a tunable tunnel barrier, separating the nanotube into two quantum dots, which can be individually addressed by two additional side gates, $V_{\mathrm{left}}, V_{\mathrm{right}}$. In addition, the Si wafer itself acts as a backgate [68]. The method of manufacture is as follows [67]. Carbon nanotubes were synthesized by chemical vapour deposition using a procedure similar to Ref. [163]. To form the catalyst particles, ~ 0.5 μg/cm^3 $Fe(NO_3).9H_2O$ (Sigma-Aldrich) was sonicated in isopropanol. The bare Si/SiO_2 substrate (300 nm thermal oxide) was dipped into the solution immediately after sonication and dried by air blowing. It was then heated to 900 °C in a 1" tube furnace under a hydrogen gas flow of 400 sccm, during which the iron nitrate was reduced to iron particles. Once at this temperature, 500 sccm of methane (containing natural isotope ratios) was added to the flow for 8 minutes. After the methane flow was stopped, the substrate was cooled under the same 400 sccm hydrogen flow. Alignment marks were defined by electron-beam lithography, and scanning electron microscopy and atomic force microscopy were used to locate the nanotubes in relation to these. Further steps of electron-beam lithography and evaporation contact the nanotubes with 20 nm thick, 300 nm wide gold ohmic contacts, separated by 700 nm, which also form the outer barriers of the quantum dots. The final electron-beam lithography layer writes the 100 nm wide and 100 nm spaced gates, which are made from two 1.2 nm layers of aluminum, oxidised in air and capped with a further 20 nm of titanium and 6 nm of gold. The source lead is grounded by the virtual earth of a $\times 10^7$ current to voltage preamplifier, and the drain has a small variable dc bias applied. The chip is mounted on the cold finger of a 60 mK dilution refrigerator and connected to the measurement apparatus with filtered low-frequency lines.

7.1 Stability diagram

The so-called stability diagram of the experimental device, showing the zero-bias conductance as a function of $V_{\rm left}$ and $V_{\rm right}$, the gate voltages which control the dot level energies, is shown in Fig. 7.2, top panel. The effective electron number of each charge regime is indicated by the ordered pairs (n, m). The large-small-large alternation in the stability diagram reflects the two-fold spin degeneracy of the device and allows us to unambiguously establish the parity of the electron number (even or odd). The orbital degeneracy [71, 164] of the nanotubes is broken, such that each dot has singly degenerate levels, most likely as a result of $K - K'$ mixing [165, 166]. High zero-bias conductance is observed on the boundaries of the different charge regimes. These Coulomb blockade peaks are due to strong sequential one-electron tunneling which occurs at these points, due to the fact that electrons may be added to or removed from the DQD with little energy cost. As the Coulomb blockade peaks in Fig. 7.2 reflect the atomic-limit phase diagram, we can extract the intradot repulsion $U \sim 2.5$ meV for both dots, the interdot repulsion $U' \sim 0.6$ meV and the interdot tunnel coupling $t \sim 0.4$ meV from an analysis of the stability diagram[1]. The widths of the Coulomb blockade peaks in the stability diagram allow an estimate of the coupling between the dots and the leads. In the non-interacting limit the FWHM is known to be equal to $2\Gamma_\nu$, but the peaks are broadened by a further factor of ~ 2 by many-body scattering processes [72, 167]. Bearing this in mind, we obtain $\Gamma_1 \sim 0.13$ meV and $\Gamma_2 \sim 0.23$ meV for dots 1 and 2 respectively.

We have also calculated the stability diagram via the NRG, and the result is shown in the lower panel of Fig. 7.2. Agreement between the experimental and theoretical diagrams is seen to be qualitatively good. The high conductance in the bottom left corner of the experimental stability diagram is due to a second dot level, which is not included in the model, and this feature is therefore not captured by our NRG results.

[1] In practice we calculate the atomic-limit phase diagram for a given U, U' and t and then tune these until the phase boundaries match the Coulomb blockade peaks in the experimental stability diagram. The gate voltages $V_{\rm left}, V_{\rm right}$ are related to the dot level energies by investigating the effect of a magnetic field on the Coulomb blockade peak positions, as discussed in section 7.4.

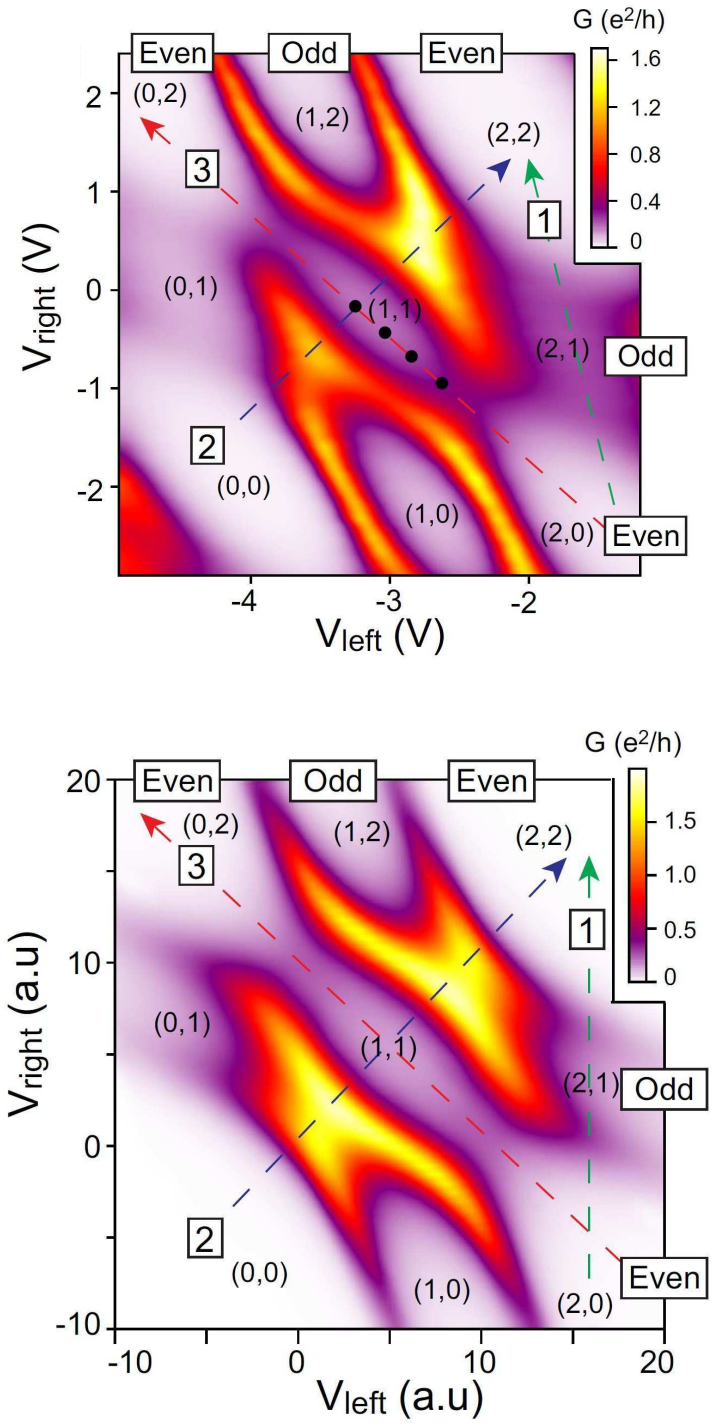


Figure 7.2: Top panel: Stability diagram of the experimental DQD measured at $T \sim 100$ mK, showing the zero-bias conductance as a colour plot as a function of V_{left} and V_{right}. The full range of charge regimes can be accessed, and high zero-bias conductance is observed at the boundaries between these. Bottom panel: NRG-calculated stability diagram. Agreement with the experimental data is seen to be qualitatively good. The lines labeled 1, 2 and 3 correspond to data shown in Fig. 7.7. The black dots in the upper panel correspond to data shown in Fig. 7.13.

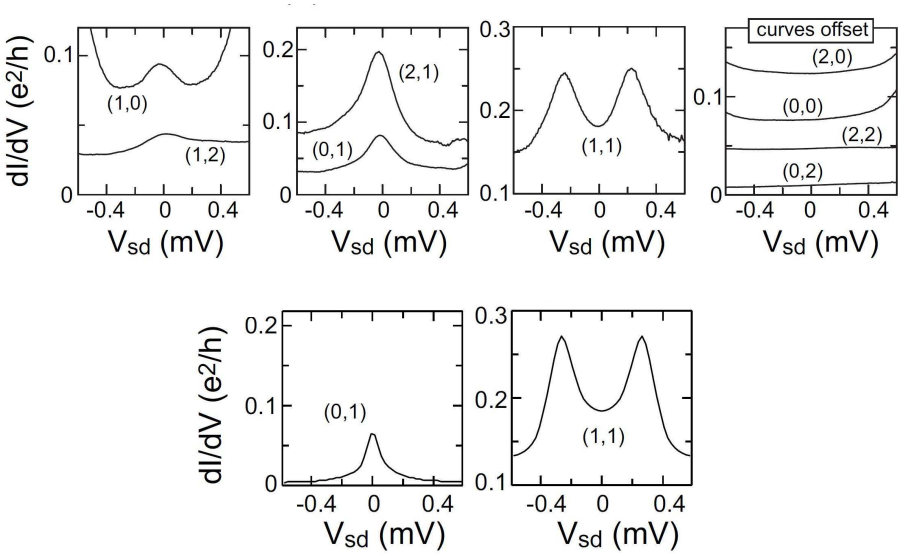


Figure 7.3: Differential conductance in the centre of the various charge regimes of Fig. 7.2 as indicated by (n, m). The top panel are experimental results, and the bottom panel are NRG results. The curves in the top rightmost panel are offset in steps of 0.03 e^2/h.

For the coupling strengths in the experiment, $U/\Gamma_\nu \sim 10$, so we might expect co-tunneling processes, and thus the Kondo effect, to be experimentally observable. To investigate the presence of Kondo correlations, the differential conductance was measured in all charge regimes, see Fig. 7.3 top panel. We also calculated the same quantity in the (0,1) and (1,1) charge regimes via the NRG, shown in Fig. 7.3, lower panel. When both dots contain an even number of electrons, the Kondo effect is inoperative, and the conductance is suppressed and featureless around $V_{sd} = 0$. On the other hand, when *one* of the quantum dots contains an odd number of electrons, we observe a pronounced zero-bias conductance peak. The characteristic appearance of a zero-bias peak when the electron number is odd is a clear indication of Kondo physics in the (0,1), (1,0), (1,2) and (2,1) charge regimes. In these regimes, the unpaired electron essentially undergoes a Kondo effect with one of the leads, the resulting Kondo singlet being only weakly perturbed by the interdot coupling.

The behaviour, however, is markedly different in the centre of the (1,1) charge regime where the electron number is odd for *both* dots. As shown in Fig. 7.3, the zero-bias conductance is suppressed and a double peak structure is observed at finite bias. This is the expected behaviour for a strongly-correlated DQD deep in the LS regime, for which $J \gg T_{\rm K}^{(1)}, T_{\rm K}^{(2)}$ $(t \gg t_c)$, as discussed in section 4.2.4. These energy scales are readily estimated using the parameters obtained above. In the centre of the (1,1) charge regime the exchange energy is approximated by $J \sim 4t^2/(U - U')$ (see section 4.2.5) which yields $J \sim 0.34$ meV. The Kondo scales can be estimated

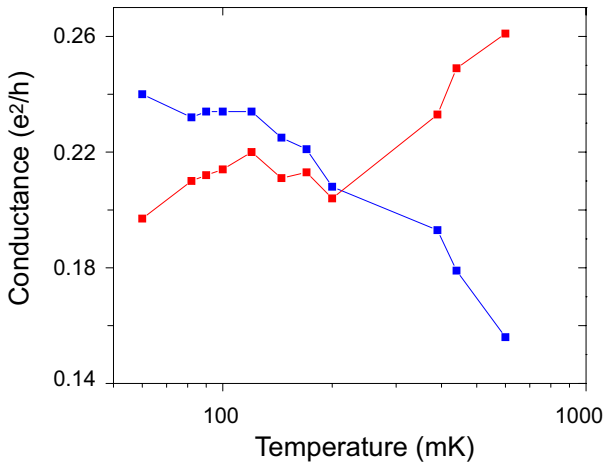


Figure 7.4: Measured temperature dependence of the zero-bias conductance in the centre of the (1,1) charge region (light-coloured line) and (2,1) charge region (dark line).

using the Haldane expression [99]:

$$T_K^{\nu} \sim \sqrt{\Gamma_\nu U}\exp[\pi\epsilon_\nu(\epsilon_\nu + U)/2\Gamma_\nu U] \ , \tag{7.2}$$

where ϵ_ν ($\nu = 1, 2$) is the level energy of dot ν relative to the zero-bias Fermi level of the leads. This yields $T_{\rm K}^{(1)} \sim 10^{-4}$ meV and $T_{\rm K}^{(2)} \sim 10^{-2}$ meV in the middle of the (1,1) charge regime, such that $J \gg T_{\rm K}^{(1)}, T_{\rm K}^{(2)}$.[2]

The above interpretation of the measurements is strengthened by our NRG study of the DQD. The calculated stability diagram, using roughly the experimental DQD parameters, see Fig. 7.2 lower panel, reproduces all of the key features of the experiment and allows for a quantitative comparison between experiment and theory. In particular the double peak structure in the (1,1) charge regime is reproduced in the calculations, see Fig. 7.3.

The pronounced conductance peaks in the (1,1) charge regime at $V_{sd} \sim 0.24$ meV in the measured data and calculations (see Fig. 7.3) can be understood physically as a non-equilibrium Kondo effect [168]. While the formation of a local singlet state suppresses Kondo correlations at zero bias, interlead spin-flip tunneling becomes possible and Kondo correlations are restored when V_{sd} is comparable to the exchange energy J that separates the atomic-limit singlet ground state from its triplet excited states.

The experimentally-measured temperature dependences of the zero-bias conductance in the centres of the (1,1) and (2,1) charge regions are shown in Fig. 7.4. They can readily be explained with reference to Fig. 7.3, noting that the dominant effect of increasing temperature is to broaden the low-energy conductance peaks. In

[2]These orders of magnitude are consistent with our NRG results.

the centre of the (1,1) region (light line) there is a gradual increase in the zero-bias conductance with temperature, corresponding to a filling-in of the conductance dip in the third panel of Fig. 7.3. This increase in zero-bias conductance with temperature at ph symmetry in the LS regime ($J \gg J_c$) was discussed in section 4.2.4. In the (2,1) region (dark line) by contrast, the broadening of the single conductance peak (see Fig. 7.3) with temperature results in a gradual decrease in the zero-bias conductance, as the Kondo effect occurring between dot 2 and lead 2 is destroyed. NRG results for similar parameters (not shown here, but see Figs. 4.10 and 4.11) display the same qualitative trends.

LR asymmetry in the stability diagram

The LR asymmetry of the experimental device, arising from $\Gamma_1 < \Gamma_2$, is apparent in the stability diagram, Fig. 7.2 upper panel (it is also captured by the NRG results shown in the lower panel). In the case of equal dot-lead couplings ($\Gamma_1 = \Gamma_2$) the (1,2) and (2,1) regimes should be identical, and therefore have identical zero-bias conductance, whereas this is seen not to be the case, with higher zero-bias conductance occurring in the (2,1) regime. There is also LR asymmetry in the Coulomb blockade peaks, with those occurring at points of charge degeneracy in dot 1 having higher zero-bias conductance than those occurring at points of charge degeneracy in dot 2.

We can understand this LR asymmetry by considering the zero-bias conductance of the system to leading order in the interdot tunnel-coupling, t (see section 3.7.4)[3]. At finite temperature, this gives the following result at zero field[4],

$$G_c(T, V_{sd} = 0) = \frac{8e^2}{h} \frac{t^2}{\Gamma_1 \Gamma_2} \int_{-\infty}^{\infty} d\omega \left[-\frac{\partial f}{\partial \omega} \right] [\pi \Gamma_1 D^{(2)}_{11;\sigma}(\omega)][\pi \Gamma_2 D^{(1)}_{22;\sigma}(\omega)] \ , \qquad (7.3)$$

with f the common Fermi function of the leads. As $T \to 0$, this reduces to (cf. Eqn. (3.70))

$$G_c(0,0) = \frac{8e^2 t^2}{h \Gamma_1 \Gamma_2} [\pi \Gamma_1 D^{(2)}_{11;\sigma}(0)][\pi \Gamma_2 D^{(1)}_{22;\sigma}(0)] \ , \qquad (7.4)$$

with $D^{(2)}_{11;\sigma}(\omega)$ the dot 1 spectrum for the $t = 0$ system. We compare first the (1,2) and (2,1) regimes. At the centre of the (1,2) regime, $\epsilon_1 \simeq -U/2 - U'$ and $\epsilon_2 \simeq -3U/2 - 3U'$. $\pi \Gamma_1 D^{(2)}_{11;\sigma}$ contains a narrow Kondo resonance of width $\sim \mathcal{O}(T_{\rm K}^{(1)})$, at zero frequency, and $\pi \Gamma_2 D^{(1)}_{22;\sigma}$ contains a Hubbard satellite peak of Lorentzian form, centred at $\omega \simeq -U/2 - U'$ with width $\sim \mathcal{O}(\Gamma_2)$. In the (2,1) regime, the two spectra are the other way around, only now the Hubbard satellite has width

[3] We have confirmed with the NRG that this leading-order approach gives reasonably accurate results for the zero-bias conductance for the 2AIM in the regimes we consider here.

[4] This result is obtained by differentiating Eqn. (D.24) with respect to bias, and then setting the Fermi functions for leads 1 and 2 to be equal ($f_1 = f_2 = f$), as is appropriate for zero bias.

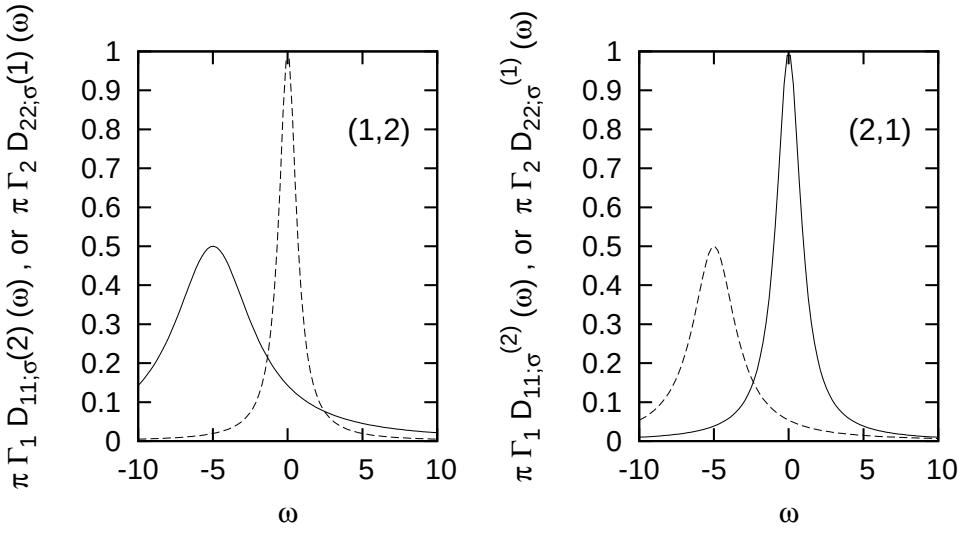


Figure 7.5: Schematic zero-temperature $t = 0$ spectra for the DQD in the (1,2) (left panel) and (2,1) (right panel) charge regimes. Frequency is plotted in arbitrary units. Solid line is $\pi\Gamma_2 D^{(1)}_{22;\sigma}(\omega)$, dashed line is $\pi\Gamma_1 D^{(2)}_{11;\sigma}(\omega)$. In both regimes one of the spectra has a Kondo resonance at zero (with width $\sim \mathcal{O}(T_{\rm K}^{(\nu)})$, which is exaggerated in these schematic graphs). The other spectra has a Hubbard satellite at $\omega \simeq -U/2 - U' \simeq -5$. In the (1,2) regime the Hubbard satellite is broader, as $\Gamma_2 > \Gamma_1$, so that the product of the spectra at zero frequency is greater, leading to higher zero-temperature, zero-bias conductance.

$\sim \mathcal{O}(\Gamma_1) < \Gamma_2$, and the Kondo resonance has a width $\sim \mathcal{O}(T_{\rm K}^{(2)}) \gg T_{\rm K}^{(1)}$. These spectra are illustrated schematically in Fig. 7.5. From Eqn. (7.4) we can see that the *zero*-temperature, zero-bias conductance ($G_c(0,0)$) depends on the product of the two $t = 0$ spectra at $\omega = 0$. The Kondo resonances that occur in these spectra have a zero frequency value of $\pi\Gamma_\nu D^{(\bar{\nu})}_{\nu\nu;\sigma}(0) = 1$. The relative $G_c(0,0)$ in the (1,2) and (2,1) regimes then depends on the zero-frequency values of the spectra which contain Hubbard satellites, *i.e.*, $\pi\Gamma_1 D^{(2)}_{11;\sigma}(0)$ in the (2,1) regime vs $\pi\Gamma_2 D^{(1)}_{22;\sigma}(0)$ in the (1,2) regime. These Hubbard satellites are both centred on $\omega \simeq -U/2 - U'$, but the Hubbard satellite in $\pi\Gamma_2 D^{(1)}_{22;\sigma}(\omega)$ in the (1,2) regime is broader than that in $\pi\Gamma_1 D^{(2)}_{11;\sigma}(\omega)$ in the (2,1) regime (the respective widths are $\sim \Gamma_2, \Gamma_1$), such that $\pi\Gamma_2 D^{(1)}_{22;\sigma}(0)$ in the (1,2) regime is greater than $\pi\Gamma_1 D^{(2)}_{11;\sigma}(0)$ in the (2,1) regime. $G_c(0,0)$ is therefore greater at the centre of the (1,2) regime than at the centre of the (2,1) regime.

This is not the trend observed in the experimental data, for which the zero-bias conductance is greater in the (2,1) regime than the (1,2) regime. The reason for this is that the experiment is of course carried out at finite temperature, and increasing the temperature from zero naturally affects the $t = 0$ spectra. The Kondo resonance in $\pi\Gamma_2 D^{(1)}_{22;\sigma}$ in the (2,1) regime dies away at $T \sim T_{\rm K}^{(2)}$, whereas the Kondo resonance in $\pi\Gamma_1 D^{(2)}_{11}$ in the (1,2) regime dies away at $T \sim T_{\rm K}^{(1)}$. The Hubbard satellites in the spectra are essentially unaffected by temperature until $T \sim \Gamma_1, \Gamma_2$. This means that

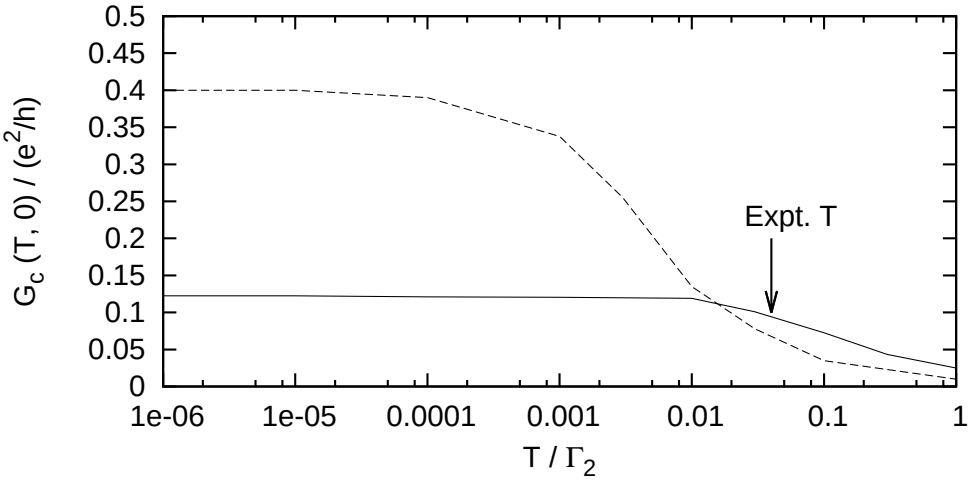


Figure 7.6: Calculated zero-bias conductance in the (2,1) (solid line) and (1,2) (dashed line) sectors as a function of temperature for the experimental parameters. The conductance in (2,1) drops off at $T \sim T_{\rm K}^{(2)} \simeq 0.04\Gamma_2$, whereas in (1,2) it drops off at $T \sim T_{\rm K}^{(1)} \simeq 4 \times 10^{-4}\Gamma_2$. At zero temperature the conductance is higher in the (1,2) regime, whereas at the experimental temperature (marked by the arrow) it is higher in the (2,1) regime.

the enhanced zero-temperature conductance will die away at $T \sim T_{\rm K}^{(1)}$ in the (1,2) sector and $T \sim T_{\rm K}^{(2)}$ in the (2,1) sector, as indeed we find from NRG calculations, shown in Fig. 7.6. At the experimental temperature ($T_{\rm K}^{(1)} \ll T \sim T_{\rm K}^{(2)}$ in the experiment), the high zero-temperature zero-bias conductance in the (1,2) sector has largely been thermally destroyed, whereas that in the (2,1) sector largely remains. The observed zero-bias conductance is therefore higher in the (2,1) sector than the (1,2) sector.

We can take a similar approach to considering the difference in zero-bias conductance between the Coulomb blockade peaks at the (1,2)/(2,2) charge regime boundary and at the (2,1)/(2,2) boundary. Considering Eqn. (7.4) in this case; at the (1,2)/(2,2) boundary (with $\epsilon_1 \simeq -U - 2U'$, $\epsilon_2 \simeq -3U/2 - 3U'$) $\pi\Gamma_2 D_{22;\sigma}^{(1)}$ contains a Hubbard satellite at $\omega \simeq -U/2 - U'$ and $\pi\Gamma_1 D_{11}^{(2)}$ contains a Hubbard satellite centred on $\omega \simeq 0$. At the (2,1)/(2,2) boundary (with $\epsilon_1 \simeq -3U/2 - 3U'$, $\epsilon_2 \simeq -U - 2U'$) it is the other way round: $\pi\Gamma_2 D_{22;\sigma}^{(1)}$ contains a Hubbard satellite at $\omega \simeq 0$ and $\pi\Gamma_1 D_{11}^{(2)}$ contains a Hubbard satellite centred on $\omega \simeq -U/2 - U'$. The widths of the Hubbard satellites are Γ_1 and Γ_2 for the dot 1 and dot 2 spectra respectively. As $\Gamma_2 > \Gamma_1$, at zero-temperature the zero-bias conductance is higher at the (1,2)/(2,2) boundary, as $\pi\Gamma_2 D_{22;\sigma}^{(1)}(0)$ is greater in this case than $\pi\Gamma_1 D_{11}^{(2)}(0)$ is at the (2,1)/(2,2) boundary. Finite temperature has little effect on these Hubbard satellites until $T \sim \Gamma_1, \Gamma_2$; much higher temperatures than in the experiment. Therefore the zero-temperature conclusions reached above remain valid for the experiment, and

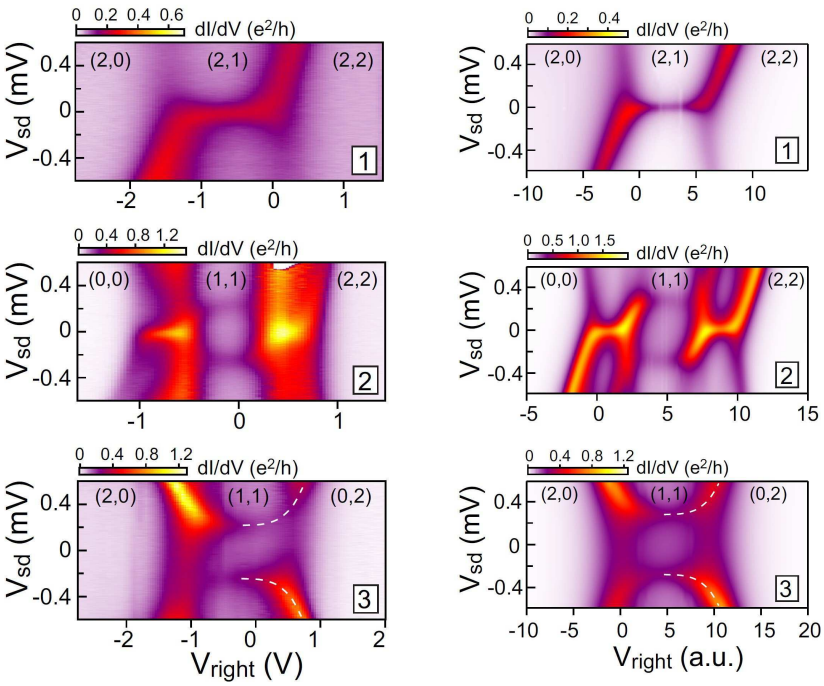


Figure 7.7: Differential conductance, $G_c(T, V)$, as a colour plot along the lines indicated in Fig. 7.2 – the left hand graphs are experimental data, the right hand graphs are NRG results. Top panel: diagonal 1, varying the charge on dot 2 – a zero-bias conductance peak arises when the charge on dot 2 is odd, indicating Kondo physics. Centre panel – varying both dot level energies equally. Finite-bias conductance peaks are observed in the (1,1) regime, indicating that the system is in the LS regime. Bottom panel – varying detuning. The splitting between the finite-bias conductance peaks in the (1,1) regime is seen to increase with detuning (shown by dashed lines).

the (1,2)/(2,2) boundary is expected to have higher zero-bias conductance than the (2,1)/(2,2) boundary, as confirmed in Fig. 7.2.

7.2 Varying dot energy levels

We now look at the effect of varying the dot energy levels in the experimental DQD, achieved by adjusting the gate voltages, $V_{\text{left}}, V_{\text{right}}$ (see Fig. 7.1). We look first at moving along diagonal 1, shown in Fig. 7.2, and corresponding to changing ϵ_2 with ϵ_1 constant. The differential conductance is shown in the top left panel of Fig. 7.7. A strong zero-bias conductance enhancement is observed in the (2,1) regime, indicative of the Kondo effect which occurs in this regime between dot 2 and lead 2. The theoretical calculation is shown in the top right panel of Fig. 7.7, and it agrees well with the experimental data. Now we discuss the behaviour along diagonal 2 in Fig. 7.2 for which the differential conductance is shown in Fig. 7.7, left middle panel.

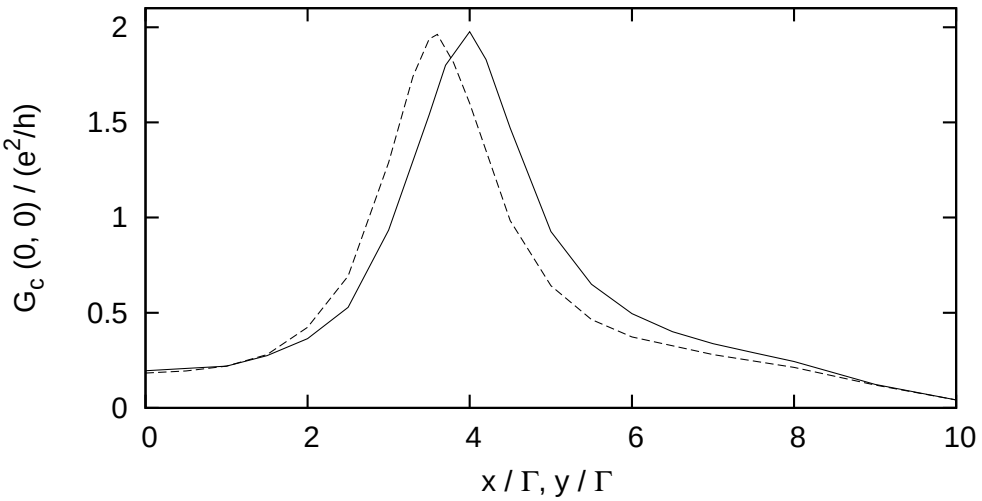


Figure 7.8: Zero-bias, zero-temperature conductance ($G_c(0,0)$) of the 2AIM with $\Gamma_1 = \Gamma_2 = \Gamma$, $\tilde{U} = 20$ and $\tilde{t} = 0.2$ ($> \tilde{t}_c$, such that the system is in the LS regime at ph symmetry), as a function of x (solid line) and y (dashed line), as defined in the text. The conductance peak, indicating the crossover between LS and KS regimes, occurs for a lower value of y than x as discussed in the text.

Along this diagonal, the dot level energies $\epsilon_{1,2}$ are decreased while their difference (or detuning) $\epsilon_1 - \epsilon_2$ remains zero. This allows the Kondo scales of the two quantum dots to be tuned (and thereby potentially allows access to the crossover from the LS regime to the KS regime) as these strongly depend on the dot level energies as expressed by, *e.g.*, Eqn. (7.2). In the centre of the (1,1) charge regime, the Kondo scales for both dots are at a minimum. Moving away from the centre, the Kondo temperatures thus increase, thereby increasing J_c, whereas J is unaltered. However, before we can access the KS regime, for which $J < J_c$, we reach the edge of the (1,1) charge regime, moving into a mixed valence regime. Here charge fluctuations are significant, and a 2IKM description of the system is no longer valid. The inability to access the KS regime this way can be understood given that for our device $J \sim \Gamma_{1,2}$, so to observe the crossover requires $T_K^{1,2} \sim \Gamma_{1,2}$, which occurs only when $|\epsilon_{1,2}| \lesssim \Gamma_{1,2}$, *i.e.*, in the mixed-valence regime. A lower J is therefore required in order to observe the crossover cleanly in this way. As we move further along the diagonal, the dot level energies become so low that the levels become essentially doubly occupied, $\epsilon_{1,2} + U \lesssim -\Gamma_{1,2} - t$. Charge fluctuations are thus suppressed, and the conductance decreases, remaining low throughout the (2,2) charge regime.

We now focus on the behaviour along diagonal 3 in Fig. 7.2 for which the differential conductance is shown in Fig. 7.7, bottom left panel (the corresponding theoretical results are shown in the bottom right panel). Along this diagonal the detuning $(\epsilon_1 - \epsilon_2)$ is varied while $\epsilon_1 + \epsilon_2$ is constant, thus fixing the number of

electrons on the DQD at $N = 2$. As indicated by the dashed white lines in Fig. 7.7 bottom panels, the peaks observed in the differential conductance move further apart as the magnitude of the detuning is increased and the conductance becomes highly asymmetric in bias. The increase in peak splitting is due to the increase of J with detuning. As detuning increases, the (1,1) singlet state becomes more strongly hybridized with the (0,2) singlet (for positive detuning). Performing a second-order SW transformation on the system with finite but small ($\ll U$) detuning yields $J \sim \frac{4t^2}{(U-U')}\left[1+2\left(\frac{\epsilon_1-\epsilon_2}{U-U'}\right)^2\right]$. The ability to tune the exchange energy is essential for spin-based quantum information processing schemes using quantum dots [169]. The present data shows that the exchange energy also plays an important role in strongly-correlated quantum dot systems.

From a second-order SW transformation, the effective dot-lead exchange couplings, J_ν, are given by (see section 4.3)

$$\rho J_\nu = \frac{2\Gamma_\nu}{\pi}\left[\frac{1}{\epsilon_\nu + U + U'} - \frac{1}{\epsilon_\nu + U'}\right] = \frac{8\Gamma_\nu}{\pi U}\left[1 + \frac{4\eta_\nu^2}{U^2} + ...\right] \tag{7.5}$$

with $\eta_\nu = \epsilon_\nu + U/2 + U'$ the difference between the dot ν level energy and its ph-symmetric value ($\epsilon_\nu = -U/2 - U'$). Increasing detuning, *i.e.*, setting $\eta_1 = -\eta_2 = x$ and increasing x from zero, then results in quadratic increases in J_ν, as well as a quadratic increase in J as discussed above. As the Kondo scales depend exponentially on J_ν, increasing detuning increases the Kondo scales much more rapidly than it increases J, such that if $J \ll T_{\rm K}^{(1)}, T_{\rm K}^{(2)}$ at ph symmetry, then the crossover cannot be accessed by increasing detuning. If on the other hand $J \gg T_{\rm K}^{(1)}, T_{\rm K}^{(2)}$ at ph symmetry, as is the case in the experiment, then it is, in principle, possible to access the crossover at finite detuning. In the experiment however we move to a mixed-valence regime before the crossover is reached, as in the case of increasing both dot level energies equally (moving along diagonal 2).

It is interesting to compare the two methods of reaching the crossover by moving away from ph symmetry (when the ph-symmetric system is in the LS regime): increasing detuning (increasing $x = \eta_1 = -\eta_2$) or increasing both energy levels equally (increasing $y = \eta_1 = \eta_2$). We concentrate in this discussion on the case of $\Gamma_1 = \Gamma_2$, merely for simplicity. The Kondo scale, $T_{\rm K}$, increases in the same fashion as either x or y is increased from zero (ph symmetry), but in the latter case J is constant whereas when detuning (x) is increased J also increases. If $J \gg T_{\rm K}$ at ph symmetry, then the crossover (occurring when $J \sim T_{\rm K}$), can in principle be accessed by increasing either x or y. A higher value of x than y is however required to reach the crossover, as increasing x increases J as well as $T_{\rm K}$, whereas increasing y merely increases $T_{\rm K}$.

This is shown in Fig. 7.8, in which we have calculated the zero-temperature,

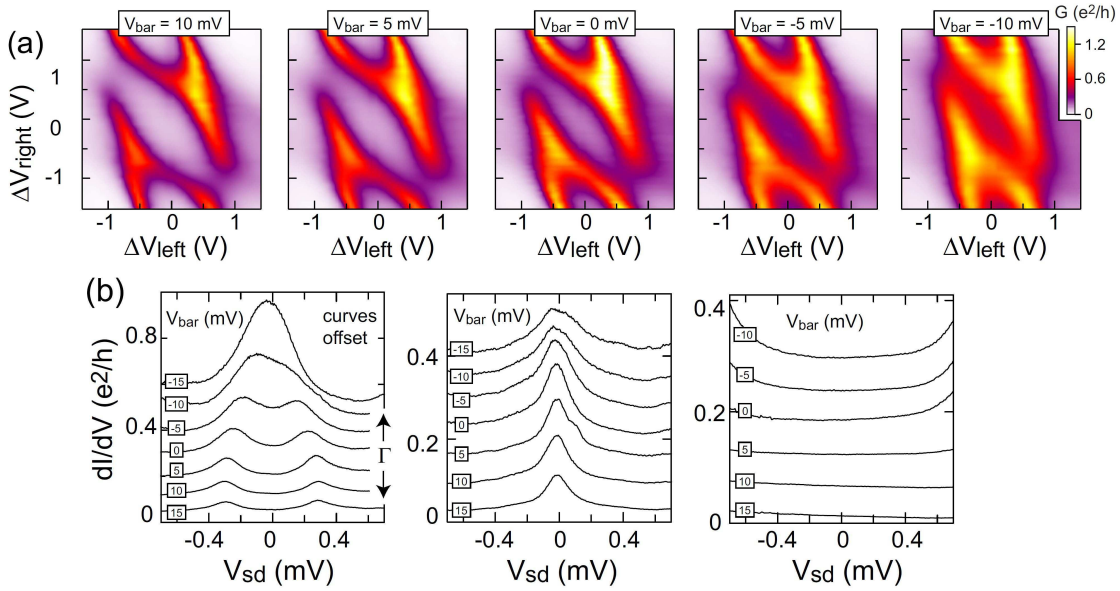


Figure 7.9: **(a)** Stability diagrams of the DQD for five different barrier gate voltages $V_{\rm bar}$. As $V_{\rm bar}$ decreases the Coulomb blockade peaks broaden and the (1,1) regime is "filled in", consonant with an increase in the dot-lead couplings. The leftmost plot ($V_{\rm bar} = 10$ mV) is the same as the upper panel of Fig. 7.2. **(b)** Differential conductance in the centre of the (1,1) charge region (left), the (2,1) charge region (middle) and (2,0) charge region (right) for a series of barrier gate voltages as indicated. Curves are offset in steps of 0.05 e^2/h in each panel. As $V_{\rm bar}$ decreases the two peaks in the (1,1) data merge into a strong zero-bias peak. In the (2,1) regime the zero-bias peak broadens as $V_{\rm bar}$ decreases, also in line with an increase in the dot-lead couplings. Varying $V_{\rm bar}$ in the (2,0) regime has little effect.

zero-bias conductance as a function of both x and y (with the other variable kept at zero) for the 2AIM which is in the LS regime ($J \gg T_{\rm K}$) at ph symmetry ($x = y = 0$). As discussed, the crossover to the KS regime can be accessed by increasing either x or y, *i.e.*, by either increasing detuning or increasing the two dot energy levels equally, and the crossover is indicated by a peak in $G_c(0,0)$. The NRG results (Fig. 7.8) confirm that the crossover is reached for a (slightly) lower value of y than x, as discussed above.

7.3 Varying dot-lead and interdot couplings

We now consider the effect of varying the barrier gate voltage, $V_{\rm bar}$, experimental results for which are shown in Fig. 7.9. By varying $V_{\rm bar}$ (see Fig. 7.1) one is able to tune both the interdot coupling (t) and the couplings between the dots and leads ($\Gamma_{1,2}$). Which of these two effects dominates varies between different experimental setups, the microscopic details of which are not presently understood. Nevertheless, within a particular experiment, the effects are highly reproducible and can be used to investigate the competition between exchange and Kondo correlations on the

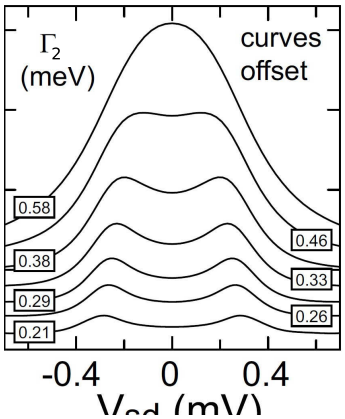


Figure 7.10: NRG-calculated differential conductance in the centre of the (1,1) charge regime for different dot-lead couplings. The curves are offset in steps of 0.05 e^2/h with the ratio $\Gamma_2/\Gamma_1 = 2$ fixed and Γ_2 as indicated. To be compared to Fig. 7.9 (b) left panel.

quantum dots.

As varying the barrier gate voltage $V_{\rm bar}$ can affect both t and $\Gamma_{1,2}$, it can thus change J and $T_{\rm K}^{(1)}, T_{\rm K}^{(2)}$. First, we discuss an example in which the main effect of $V_{\rm bar}$ is to change $\Gamma_{1,2}$. The stability diagrams for five different values of $V_{\rm bar}$ are shown in Fig. 7.9 (a). That the main effect of decreasing $V_{\rm bar}$ is an increase in the coupling to the leads is deduced from the increase in width of the Coulomb blockade peaks in the stability diagram. The increased width of the Kondo resonance observed in the (2,1) charge region, see middle panel of Fig. 7.9 (b), can also be explained as due to an increase in dot-lead couplings; the width of the peak is $\sim T_{\rm K}^{(2)}$, which increases as Γ_2 does.

For decreasing $V_{\rm bar}$, the zero-bias conductance in the centre of the (1,1) charge regime strongly increases. At the same time, as shown in Fig. 7.9 (b) left panel, the double peak structure, clearly observed at the more positive values of $V_{\rm bar}$, gradually merges into one broad peak. This can also be understood by an increase in the coupling strengths $\Gamma_{1,2}$. For our device, $J \sim \Gamma_{1,2}$, and therefore $T_{\rm K}^{(1)}, T_{\rm K}^{(2)} \sim \Gamma_{1,2}$ is required to reach the crossover, as discussed previously. However this requires $U/\Gamma_{1,2} \lesssim 1$, such that the system becomes weakly correlated before it crosses over to the KS regime. On increasing $\Gamma_{1,2}$, and hence decreasing $U/\Gamma_{1,2}$, charge fluctuations become more significant, thereby eroding and ultimately destroying the double peak structure, leading to a strong enhancement of zero-bias conductance. We have calculated NRG results for the differential conductance of the DQD in the (1,1) regime with increasing values of $\Gamma_{1,2}$, keeping the ratio Γ_1/Γ_2 fixed. The results, shown in Fig. 7.10 are in very good agreement with the experimental data (Fig. 7.9 (b), left panel) providing further evidence that the main effect of increasing $V_{\rm bar}$ in

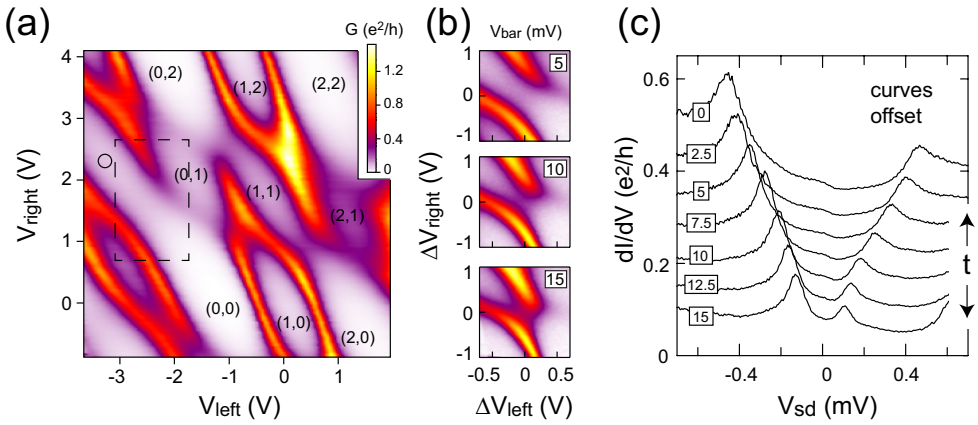


Figure 7.11: **(a)** Stability diagram of the DQD. Here the Si backgate voltage is set to $V_{bg} = -1.8$ V and $V_{\rm bar} = 0$ mV. The circle indicates the approximate centre of an effective (1,1) charge region, different from that discussed previously. **(b)** Conductance around a triple point pair for the area indicated in panel (a) by the dashed lines for three different $V_{\rm bar} = 5, 10$, and 15 mV. **(c)** Differential conductance in the centre of the leftmost (1,1) charge region, *i.e.*, position indicated by the circle in panel (a), for a series of $V_{\rm bar}$. The increase in the peak splitting correlates with an increase in the interdot coupling t, as seen theoretically in Fig. 4.24 lower panel.

this case is to increase the dot-lead couplings.

A different dependence on $V_{\rm bar}$ is observed for the neighbouring "effective" (1,1) charge region, see Fig. 7.11. As expected, a double peak structure is observed in the differential conductance (Fig. 7.11 (c)). However, in this case, the interdot coupling t is changed as $V_{\rm bar}$ is adjusted, resulting in a decrease of the exchange energy J with increasing $V_{\rm bar}$ and correspondingly smaller peak splitting, see Fig. 7.11 (c). The change in t is also evident in the stability diagram, see Fig. 7.11 (b), where it is observed as a decrease in the separation (and curvature) of the so-called triple points. In Fig. 7.11 (b) the triple points shown are those connecting effective (0,0), (1,0) and (1,1) charge regimes, and connecting effective (0,0), (0,1) and (1,1) charge regimes – from calculations of the atomic-limit stability diagram (as carried out in section 2.10) we see that both the separation and curvature of these triple points decreases as t does – as observed in Fig. 7.11 (b). The smallest peak splitting in the differential conductance was observed for $V_{\rm bar} = 15$ mV, see Fig. 7.11 (c). No further decrease in t was observed by increasing $V_{\rm bar}$ beyond this value (not shown). If t could have been decreased further, the crossover between LS and KS regimes (occurring at $J = \frac{4t^2}{U-U'} \sim T_{\rm K}^{(1)}, T_{\rm K}^{(2)}$) could have been observed in the centre of the (1,1) regime, but this was not achieved in the current experiment.

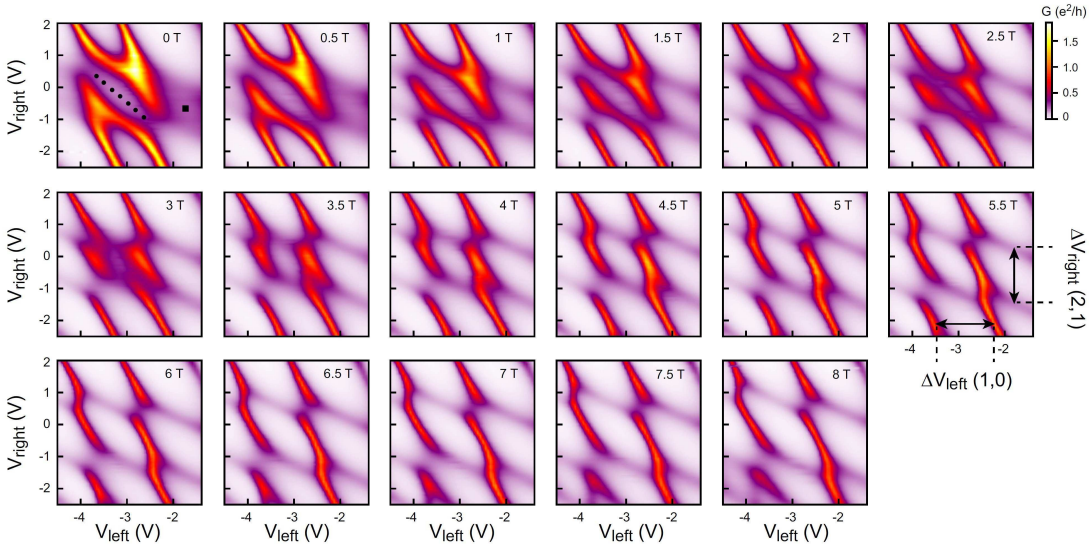


Figure 7.12: Experimental DQD stability diagrams measured at $T \sim 100$ mK. The magnetic field, B, is increased from 0 in steps of 0.5 T as indicated. The zero-bias conductance in the (1,1) regime initially increases with field and is maximal for $B \sim 3$ T.

7.4 Behaviour upon application of a magnetic field

As discussed the interdot coupling, t, could not be reduced sufficiently to reach the crossover between LS and KS regimes in the experimental DQD. However, as discussed in chapter 6, the crossover may also be reached for fixed $t > t_c$ (equivalently $J > J_c$) by application of a magnetic field, and that, as at zero field, the crossover is indicated by an enhancement of the zero-bias conductance (see section 6.3).

The stability diagrams for the experimental DQD for various values of field strength (B) are shown in Fig. 7.12. Here we see that as field strength is increased from zero, the zero-bias conductance in the (1,1) regime increases until $B \sim 3$ T. Increasing the field strength further leads to a decrease in zero-bias conductance in the (1,1) regime. The maximum in the zero-bias conductance is indicative of the crossover from the LS to the KS regime, as discussed in more detail below. Application of a magnetic field also has the effect of shifting the lines of atomic-limit charge degeneracy, along which Coulomb blockade peaks arise in the zero-bias conductance. This is evident when comparing, for instance, the zero-field and 8 T stability diagrams; in the high field case the (1,1) regime is notably larger as it has been stabilised relative to the other regimes by the field.

It is by measuring the field-induced shifts in the Coulomb blockade peaks that one can relate the gate voltages to dot level energies. Focussing on the widths of the (1,0) and (2,1) charge regimes (as marked in Fig. 7.12 rightmost middle panel);

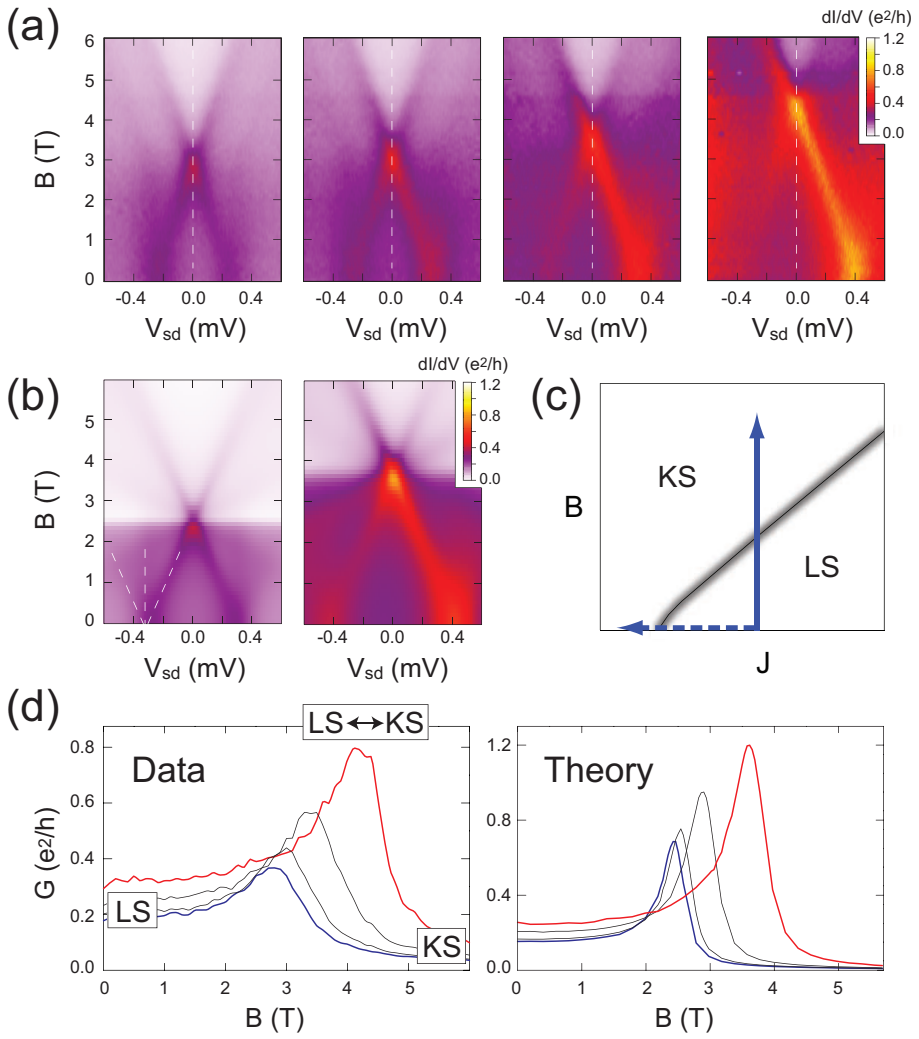


Figure 7.13: **(a)** Magnetic field dependence of the differential conductance in the (1,1) charge regime for various values of the detuning as indicated in Fig. 7.2 upper panel (black dots along line 3), with the left plot for the centre of the (1,1) regime. In each case the zero-bias conductance initially increases with field until it reached a maximum at $g\mu_B B \sim J$, with J increasing with detuning, as discussed previously. **(b)** NRG results corresponding to the left and right panels in (a), showing good agreement with the experimental data. Dashed lines show the threefold splitting of one zero-field peak. **(c)** Schematic of crossover between LS and KS regimes, see text, either by varying B (solid arrowed line) or J (dashed arrowed line). Enhanced zero-bias conductance occurs along this crossover line. **(d)** Zero-bias conductance vs B for different detuning, along dashed white lines in panel (a); both measured (left) and calculated (right). Individual curves from left to right correspond to (a) from left to right.

in the atomic limit the width of these regimes increase proportional to $g\mu_B B$ for a magnetic field applied perpendicularly to the nanotube axis, where we assume $g = 2$ for nanotubes [68]. In practice the device has a relatively strong coupling between the dot and leads, and a linear relation between the width of the regimes and B is a good approximation only in the limit of large magnetic field. Bearing this in mind,

we obtain the coupling strengths (or lever arms) between the gate electrodes and the quantum dots, *i.e.*, the relationship between the gate voltages ($V_{\rm left}$ and $V_{\rm right}$) and the dot level energies, and one can therefore estimate U, U' and t from the positions of the Coulomb blockade peaks.

We investigate the effect of application of a magnetic field to the system in the (1,1) regime further in Fig. 7.13. We consider applying a magnetic field to the system in this regime for various values of detuning, see Fig. 7.13 (a), as indicated by the black dots along line 3 in Fig. 7.2 (top panel). At finite magnetic field the observed conductance peaks split into three components (of which the innermost peaks are most easily resolved, see Figs. 7.13 (a) and (b)), consistent with a local singlet ground state and triplet excited state, separated by $\sim J$ at $B = 0$. As the magnetic field is increased, the energy difference ($\sim J - g\mu_B B$) between the singlet $|S\rangle$ and the lowest-energy triplet state $|T_1\rangle$ decreases. At some critical magnetic field strength ($B_c \sim J/g\mu_B$) these states are near degenerate. A strong zero-bias conductance peak is then observed, due to the screening of the $S - T_1$ pseudospin system [162, 170–172], here by two channels[5].

From the perspective of the 2AIM, and its experimental realisation in this device, the conductance peak is a signature of the finite-field crossover between LS (for $B \lesssim B_c$) and KS (for $B \gtrsim B_c$) regimes, which is of course a finite-field continuation of the zero-field conductance peak at $t \simeq t_c$ [94–96]. This behaviour is clearly observed in Fig. 7.13 (d). In the centre of the (1,1) regime, $J \sim 0.34$ meV (as estimated above) yields $B_c \sim J/g\mu_B \sim 2.9$ T, in very good agreement with the measured conductance peak in Fig. 7.13 (d).

As shown in Fig. 7.13 (d) the evolution of the zero-bias conductance as a function of detuning is also in good agreement with the NRG calculations. We see that the critical field required to induce the crossover ($B_c \simeq J/g\mu_B$) increases as detuning is increased, due to the fact that J increases with detuning, as discussed above. NRG calculations also confirm that the asymmetry (in bias) observed in the calculated differential conductance with increasing detuning, see Fig. 7.13 (a)/(b), requires the asymmetry $\Gamma_1 \neq \Gamma_2$. For symmetric coupling strengths, or precisely in the centre of the (1,1) charge regime, where the system is ph symmetric, no asymmetry is observed in the differential conductance.

Finally, Fig. 7.14 shows the differential conductance as a function of magnetic field in the centre of the (2,1) charge region as indicated by the square in the $B = 0$ stability diagram, Fig. 7.12 top-left panel. In contrast to the (1,1) regime, the maximum zero-bias conductance here is observed at $B = 0$. In this regime, dot

[5]We note that in this TCDQD device both the S and T_1 states arise from (1,1) configurations, in contrast to the $S - T_1$ crossings observed [69, 168, 173, 174] in single quantum dots with two "active" levels, where the relevant singlet state has a configuration with the lower dot level doubly occupied, and consequent Kondo screening arises by a single effective channel [162].

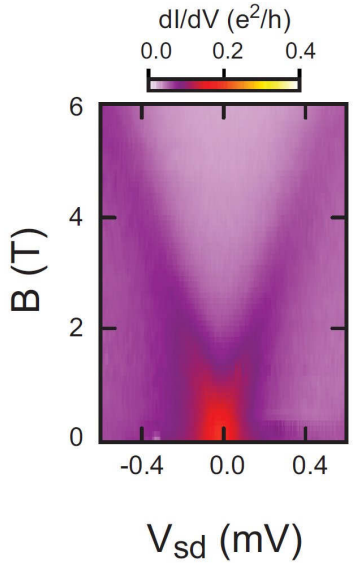


Figure 7.14: Differential conductance as a function of magnetic field in the centre of the (2,1) charge region as indicated by the closed square (■) in the $B = 0$ diagram of Fig. 7.12 top left panel.

2 effectively undergoes a Kondo effect with its lead; the effect of the field is to split the zero-bias Kondo resonance, leading to a decrease in zero-bias conductance.

In conclusion, we have studied a tunable two-impurity Kondo system in a strongly correlated carbon nanotube DQD, manufactured by our collaborators, in which the full range of charge regimes is accessible, and which amounts to a clear experimental realisation of the 2AIM. Much of the physics exhibited by the 2AIM, and discussed in chapters 4 – 6, can be accessed in this system. In the (1,1) regime, the exchange and Kondo energy scales can be varied by tuning the dot energy levels or by varying the dot-lead tunnel couplings, providing the possibility of observing the crossover between LS and KS regimes. While charge fluctuations in this device prevented observation of the crossover at zero field, we were able to observe it at finite field, indicated by enhanced zero-bias conductance. We note that these experiments are readily extended to CNT DQDs coupled to ferromagnetic [175] or superconducting [176] leads. This allows experimental access to rich phase behaviour controlled by the interplay between Kondo, exchange, and superconducting correlations, and highlights the potential of CNT DQDs to investigate correlated electron physics.

CHAPTER 8

Summary

In this thesis we have undertaken a detailed study of the two-impurity Anderson model (2AIM), looking at the system across a wide range of parameters. The conductance of the system at low temperatures was a particular focus, as this is an excellent probe of the underlying physics. The 2AIM serves as the canonical model for tunnel-coupled double quantum dots (DQDs), and as such understanding its physics is of interest to theorists and experimentalists alike. We have also studied related models, such as the two-impurity Kondo model (2IKM), as well as longer chains of impurity spins, which provide insight into the physics of quantum dot chains, looking particularly at the two-channel Kondo (2CK) effect arising at both zero and finite magnetic field. We now give a brief summary of the thesis.

After a brief introduction in chapter 1, chapter 2 began with a description of how one can model a quantum dot device. A single quantum dot (QD) is commonly modelled as a single-impurity Anderson model, which in turn is related to the simpler single-impurity Kondo model via Schrieffer-Wolff (SW) transformation. We also discussed the 2CK model, exhibiting the 2CK effect, which we studied later in the context of the 2IKM and related models. Having looked at these models, a description of the models used for a DQD was given; namely the 2AIM and the 2IKM, which are also related by second-order SW transformation. The second-order SW transformation of the 2AIM fails however to capture processes which involve charge transfer between the leads, and such processes are known to have an important effect on the low-temperature behaviour of these models. A third-order SW transformation was therefore carried out, to calculate the form of these interlead charge-transfer terms, the resulting model being the H_3 model. As a preliminary to investigating the full 2AIM, we looked at the system in two exactly soluble limits: the atomic and non-interacting limits. An understanding of the system in these special cases is very useful in understanding the full system. The results calculated in these limits also point to the rich physics accessible in the 2AIM.

Chapter 3 detailed the Numerical Renormalisation Group (NRG) technique that was used to obtain many of the results in this thesis. This non-perturbative technique is widely used to study quantum impurity problems, and has been very successful. After discussing the technique itself, we went on to explain the way in which the renormalisation group procedure can help one understand the physics of a quantum impurity system, in terms of RG flows and fixed points. This framework is crucial to understand multi-impurity systems such as the 2AIM. The full density matrix method for calculating dynamic information from the NRG was described, and we ended chapter 3 by looking at methods of calculating the conductance of quantum impurity systems from the NRG. For the 2AIM, the common method of relating the zero-bias conductance to the single-particle spectra of the system cannot be applied, but one can use a Landauer-type formula for the zero-bias conductance at zero temperature. At finite temperatures the zero-bias conductance may be calculated via a linear-response approach, which we detail. At finite bias, calculating the conductance becomes much harder, and one is forced to resort to approximations. By neglecting the bias-dependence of the self energies, an equation was derived for the conductance at finite bias, and this can be heuristically extended to finite temperature. In the limit of weak interdot tunnel-coupling, one can also derive an asymptotically-exact expression for the conductance at both finite bias and temperature via a novel perturbative approach, and this was outlined.

In the rest of the thesis we went on to apply the NRG to quantum impurity models, particularly the 2AIM and the 2IKM. In chapter 4 a general study of the Kondo physics arising in the 2AIM was carried out. We began by looking at the Green's functions of the system, deriving expressions for them in terms of the self-energies of the system. The 2AIM at particle-hole (ph) and left-right (LR) symmetry was studied, beginning with some physical ways of looking at the problem. At ph symmetry (and indeed throughout the (1,1) charge regime of the model) an interesting competition arises between the Kondo effect and the effective interdot antiferromagnetic exchange interaction, and this leads to a crossover between Kondo singlet and local singlet regimes as the interdot coupling is varied. The physical signature of this crossover is a strong enhancement in the zero-bias conductance of the system. The effect of introducing two experimentally-relevant perturbations to the standard ph and LR-symmetric 2AIM was considered; namely, an interdot repulsion and asymmetry in the dot-lead couplings. The system away from ph symmetry was investigated, at first keeping the two dot energy levels equal ($\epsilon_1 = \epsilon_2$), and it was shown that the crossover persists away from ph symmetry, but at a different critical interdot coupling. We also looked at the 2AIM with arbitrary, and in general unequal, dot energy levels, giving some representative results for the zero-bias conductance of the system. At finite temperature, Coulomb blockade structure is clearly evident in our data. Chapter 4 was concluded with a brief study of the finite-bias

conductance of the 2AIM, concentrating on the case of zero temperature, and ph and LR symmetry for simplicity. We investigated the method of calculating the finite-bias conductance to leading order in the interdot tunnel-coupling, and compared it to the bias-independent self energies approximation, showing this approximation to be inaccurate for high bias.

In chapter 5 the 2CK effect, known to arise in two-impurity models, was investigated. We began by looking at the 2IKM, which exhibits such physics for temperatures $T \lesssim T_{\rm K}$ at the quantum critical point between the local singlet and Kondo singlet phases, at which point the 2IKM is a non-Fermi liquid at low energies. The existence of interlead charge transfer, as arises in the 2AIM, is well known to destroy the pristine quantum phase transition (QPT), and also to destroy the 2CK effect on the lowest energy scales, such that the system crosses over from a non-Fermi liquid state to its Fermi liquid ground state when $T \sim T^*$. Two-channel, non-Fermi liquid physics can therefore be observed in two-impurity systems with interlead charge transfer for temperatures $T^* \ll T \ll T_{\rm K}$, provided there is a clear separation of energy scales, $T^* \ll T_{\rm K}$. For the 2AIM, a very high ratio of $U/\Gamma \gtrsim 30$ is needed in order to observe 2CK physics over an appreciable temperature window; a finding in contrast to the findings of previous work. This high ratio of U/Γ makes the $T_{\rm K}$ scale very small, of order 10^{-5} K. Two-channel Kondo physics can only be observed in a tunnel-coupled DQD, for which the 2AIM is an appropriate model, at temperatures lower than this – currently not a feasible prospect as minimum experimental temperatures are of order 10^{-2} K.

We went on to investigate whether the introduction of an interdot repulsion, asymmetry in the dot-lead couplings, or moving away from ph symmetry would be helpful in increasing the temperatures on which two-channel Kondo physics can be observed in the 2AIM. This is not however the case. Having therefore concluded that standard tunnel-coupled DQDs are not promising candidates for observing two-channel Kondo physics, we briefly discussed the prospect of observing two-channel Kondo physics in longer chains of QDs. Although we were unable to perform accurate NRG calculations on these systems, we believe that it is possible that 2CK physics could be observed in systems of three or four QDs in series at experimentally-realisable temperatures. Manufacture of such systems would however present a real challenge.

In chapter 6 the effect of applying a magnetic field to a number of quantum impurity models was considered. Beginning with the 2IKM, the zero-field QPT was found to persist at finite field, provided the system has LR symmetry, such that a phase boundary exists in the $h-J$ plane, separating Kondo singlet and local singlet phases. We derived a low-energy effective model for the 2IKM in the vicinity of this boundary, of 2CK model form, illustrating that 2CK physics occurs all the way along the phase boundary, and the system is a non-Fermi liquid on the lowest energy

scales precisely on the boundary. From consideration of the low-energy effective model it is clear that the QPT does not arise at finite uniform field if the 2IKM is LR asymmetric. However, the QPT can be restored in the LR-asymmetric system by application of a staggered magnetic field – this was explained by consideration of the low-energy effective model.

As it is known that *all* even-numbered spin chains exhibit a QPT at zero magnetic field, we went on to investigate whether these QPTs also persist at finite field. We concentrated on a system containing a chain of four spins, the four-impurity Kondo model (4IKM). In this model there are in fact two lines of QPTs as a function of field, and at both critical fields 2CK physics arises. This led us to conjecture that in a system containing a chain of $2N$ spins, there are N QPTs as a function of field. We went on to verify that this is the case for a system of six spins with $J \gg J_c$, with J_c the zero-field critical point. More work is however needed in order to fully understand the physics of a general even-numbered spin chain in a field.

The existence of interlead charge transfer destroys the pristine finite-field QPTs, just as it does the zero-field QPT. In the 2AIM therefore, a finite-field crossover is observed between local singlet and (polarised) Kondo singlet regimes. As at zero field, 2CK physics is theoretically possible in the vicinity of this finite-field crossover, but an even greater ratio U/Γ is required here, and correspondingly lower temperatures. Observing 2CK physics at finite field in a tunnel-coupled DQD is therefore unfeasible at the current time. Interesting conductance behaviour in the 2AIM at finite field does however occur, with the finite-field crossover being signaled by an enhancement in the low-temperature, zero-bias conductance.

Having discussed the low-temperature physics of the 2AIM in some detail, in chapter 7 we looked at recent experiments carried out by our collaborators on a carbon nanotube DQD, which amounts to a direct experimental realisation of the 2AIM. Many of the features of the 2AIM discussed previously appear in the experimental data, and we find good agreement between theory and experiment. These experiments illustrate the precise tunability that is possible in modern QD systems, with all charge regimes of the DQD being accessible, and control over both the interdot coupling and the dot-lead couplings achieved.

Effective single-channel Kondo physics, manifest as a zero-bias conductance peak, was observed in the charge regimes where only one of the QDs contained an odd number of electrons. In the charge regime where both dots are effectively singly occupied, the (1,1) regime, very different physics arises due to the competition between the interdot antiferromagnetic exchange coupling (J) and the Kondo effect. By varying the dot energy levels both J and the Kondo scales can be varied, allowing the possibility of reaching the crossover between local singlet and Kondo singlet regimes. The interdot coupling and the Kondo scales can also be directly tuned by varying the barrier gate voltage. In the experimental device the interdot coupling

could not be reduced sufficiently to reach the crossover, and charge fluctuations intervened upon varying the dot energy levels, so that the crossover was not reached at zero magnetic field. However, as shown in chapter 6, the crossover can also be reached by application of a magnetic field, and in the experiment this was achieved, with a strong enhancement of zero-bias conductance observed as a hallmark of the crossover.

Overall then, we have undertaken a thorough theoretical study of the 2AIM, and related models of tunnel-coupled QD systems including a comparison to recent experiments on a carbon nanotube DQD. These systems contain rich and varied physics, with a wide range of interesting parameter regimes. Recently, rapid progress in experimental techniques has allowed one to put theoretical predictions of the physics of coupled QD systems to the test, and unprecedented control over experimental parameters is now achievable. All this points to an interesting future for the study of these systems.

APPENDIX A

Outline of the third-order Schrieffer-Wolff transformation of the 2AIM

In this appendix we outline the third-order Schrieffer-Wolff (SW) transformation of the particle-hole (ph) symmetric 2AIM. We begin by partitioning the 2AIM Hamiltonian as follows:

$$\hat{H}_{\text{2AIM}} = \hat{H}_0 + \hat{H}_1 \ , \tag{A.1}$$

with

$$\hat{H}_0 = \sum_{\nu\mathbf{k}\sigma} \epsilon_{\mathbf{k}} c^\dagger_{\nu\mathbf{k}\sigma} c_{\nu\mathbf{k}\sigma} + \sum_{\nu\sigma} \epsilon_\nu \hat{n}_{\nu\sigma} + U \sum_{\nu} \hat{n}_{\nu\uparrow}\hat{n}_{\nu\downarrow} \ , \tag{A.2}$$

and

$$\begin{aligned} \hat{H}_1 &= \sum_{\nu\mathbf{k}\sigma} V_\nu \left(d^\dagger_{\nu\sigma} c_{\nu\mathbf{k}\sigma} + h.c. \right) + t \sum_{\sigma} \left(d^\dagger_{1\sigma} d_{2\sigma} + h.c. \right) \\ &= \sum_{\nu} \hat{H}_{V_\nu} + \hat{H}_t \ . \end{aligned} \tag{A.3}$$

We then carry out Brillouin-Wigner perturbation theory [98] in $\hat{H}_1$, going to third-order, projecting the Hamiltonian onto the low-energy manifold of $\hat{H}_0$ eigenstates, comprised of all the dot states with one electron on each dot. The unity operator for the low-energy manifold is therefore

$$\hat{1}' = |\uparrow\uparrow\rangle\langle\uparrow\uparrow| + |\uparrow\downarrow\rangle\langle\uparrow\downarrow| + |\downarrow\uparrow\rangle\langle\downarrow\uparrow| + |\downarrow\downarrow\rangle\langle\downarrow\downarrow| \ , \tag{A.4}$$

where $|\sigma\sigma'\rangle$ is the state with a σ-spin electron on dot 1 and a σ'-spin electron on dot 2. We define $\hat{P} = \hat{1} - \hat{1}'$ to be the projection operator that projects the system out of the low-energy manifold. Brillouin-Wigner perturbation theory [98] to third

order gives

$$\begin{aligned} E_n =&\langle n|\hat{H}_0|n\rangle + \langle n|\hat{H}_1|n\rangle + \langle n|\hat{H}_1(E_n-\hat{H}_0)^{-1}\hat{P}\hat{H}_1|n\rangle \\ &+ \langle n|\hat{H}_1(E_n-\hat{H}_0)^{-1}\hat{P}\hat{H}_1(E_n-\hat{H}_0)^{-1}\hat{P}\hat{H}_1|n\rangle \ , \end{aligned} \tag{A.5}$$

where E_n is the perturbed energy of the state $|n\rangle$ in the low-energy manifold. The first term is zeroth-order energy, the second term is the first-order correction, the third term is the second-order correction, and the final term is the third-order correction. One issue with this result is that the right hand side of the expression contains the perturbed energy, E_n, itself. However, if we wish to calculate E_n to third order in $\hat{H}_1$, then we can replace E_n with its first-order expression ($E_n = \langle n|\hat{H}_0|n\rangle + \langle n|\hat{H}_1|n\rangle$) in the second-order correction term in Eqn. (A.5), and with its zeroth-order expression ($E_n = \langle n|\hat{H}_0|n\rangle$) in the third-order correction term in Eqn. (A.5). Doing this, we still capture all terms up to third order in $\hat{H}_1$. For the 2AIM considered here, however, the first-order correction to the energy (given by $\langle n|\hat{H}_1|n\rangle$) is zero, as $\hat{H}_1$ changes the dot electron configuration, and all states in the low-energy manifold have the same (1,1) configuration. Therefore, in the right hand side of Eqn.(A.5), we may simply replace E_n with the unperturbed energy, which we denote ϵ_n. We also note that all states in the low-energy manifold have the same unperturbed energy, which we denote ϵ_0 (with $\epsilon_0 = -U$ at ph symmetry). Eqn. (A.5) then becomes

$$\begin{aligned} E_n =&\langle n|\hat{H}_0|n\rangle + \langle n|\hat{H}_1|n\rangle + \langle n|\hat{H}_1(\epsilon_0-\hat{H}_0)^{-1}P\hat{H}_1|n\rangle \\ &+ \langle n|\hat{H}_1(\epsilon_0-\hat{H}_0)^{-1}\hat{P}\hat{H}_1(\epsilon_0-\hat{H}_0)^{-1}\hat{P}\hat{H}_1|n\rangle \ . \end{aligned} \tag{A.6}$$

From the above equation we can define an effective Hamiltonian as

$$\begin{aligned} \hat{H}_{\text{eff}} =&\hat{1}'\hat{H}_0\hat{1}' + \hat{1}'\hat{H}_1\hat{1}' + \hat{1}'\hat{H}_1(\epsilon_0-\hat{H}_0)^{-1}P\hat{H}_1\hat{1}' \\ &+ \hat{1}'\hat{H}_1(\epsilon_0-\hat{H}_0)^{-1}\hat{P}\hat{H}_1(\epsilon_0-\hat{H}_0)^{-1}\hat{P}\hat{H}_1\hat{1}' \ . \end{aligned} \tag{A.7}$$

Going to second order, *i.e.*, considering the first three terms in the above expression gives rise to $\hat{H}_{\text{eff}} = \hat{H}_{\text{2IKM}}$ with $J = 4t^2/U$ and $J_\nu = 8V_\nu^2/U$ (as is well known). The third order term is

$$\hat{H}^{(3)}_{\text{eff}} = \hat{1}'\hat{H}_1(\epsilon_0-\hat{H}_0)^{-1}\hat{P}\hat{H}_1(\epsilon_0-\hat{H}_0)^{-1}\hat{P}\hat{H}_1\hat{1}' \ . \tag{A.8}$$

Calculating this term is simply a matter of putting Eqns. (A.2), (A.3) and (A.4) into the above expression and summing all possible terms. This is rather lengthy procedure, which we outline briefly below. One simplifying fact is that many of the resultant terms are easily shown to be equal to zero. For instance, only terms of order V_1V_2t are non-zero, as all other terms ($V_iV_jV_k$, t^3, tV_i^2, t^2V_i terms, with $\{i,j,k\} = \{1,2\}$) involve changes in the electron configuration of the dots.

There are four one-electron, and four three-electron, eigenstates of $\hat{H}_0$, all of which are degenerate at ph symmetry, with energy $-U/2$. The two-electron states with (0,2) and (2,0) configurations (*i.e.*, two electrons on one of the dots, and no electrons on the other) are eigenstates of $\hat{H}_0$ with energy 0. The energy factors ($(\epsilon_0 - \hat{H}_0)^{-1}$) that arise in Eqn. (A.8) are therefore all equal to either $-1/U$ or $-2/U$.

Applying the above considerations to Eqn. (A.8) yields

$$\begin{aligned}
\hat{H}^{(3)}_{\text{eff}} = \frac{2}{U^2}\hat{1}'\Big[&\hat{H}_t\hat{H}_{V_1}\hat{H}_{V_2} + \hat{H}_t\hat{H}_{V_2}\hat{H}_{V_1} + \hat{H}_{V_1}\hat{H}_{V_2}\hat{H}_t \\
&+ \hat{H}_{V_2}\hat{H}_{V_1}\hat{H}_t + 2\hat{H}_{V_1}\hat{H}_t\hat{H}_{V_2} + 2\hat{H}_{V_2}\hat{H}_t\hat{H}_{V_1}\Big]\hat{1}' \\
= \frac{2tV_1V_2}{U^2}\hat{1}' \sum_{\sigma,\sigma',\sigma''} \Big[&d^\dagger_{1\sigma}d_{2\sigma}f^\dagger_{1\sigma'}d_{1\sigma'}d^\dagger_{2\sigma''}f_{2\sigma''} + d^\dagger_{2\sigma}d_{1\sigma}d^\dagger_{1\sigma'}f_{1\sigma'}f^\dagger_{2\sigma''}d_{2\sigma''} \\
&+ d^\dagger_{1\sigma}d_{2\sigma}d^\dagger_{2\sigma'}f_{2\sigma'}f^\dagger_{1\sigma''}d_{1\sigma''} + d^\dagger_{2\sigma}d_{1\sigma}f^\dagger_{2\sigma'}d_{2\sigma'}d^\dagger_{1\sigma''}f_{1\sigma''} \\
&+ f^\dagger_{1\sigma}d_{1\sigma}d^\dagger_{2\sigma'}f_{2\sigma'}d^\dagger_{1\sigma''}d_{2\sigma''} + d^\dagger_{1\sigma}f_{1\sigma}f^\dagger_{2\sigma'}d_{2\sigma'}d^\dagger_{2\sigma''}d_{1\sigma''} \\
&+ f^\dagger_{2\sigma}d_{2\sigma}d^\dagger_{1\sigma'}f_{1\sigma'}d^\dagger_{2\sigma''}d_{1\sigma''} + d^\dagger_{2\sigma}f_{2\sigma}f^\dagger_{1\sigma'}d_{1\sigma'}d^\dagger_{1\sigma''}d_{2\sigma''} \\
&+ 2f^\dagger_{1\sigma}d_{1\sigma}d^\dagger_{1\sigma'}d_{2\sigma'}d^\dagger_{2\sigma''}f_{2\sigma''} + 2d^\dagger_{1\sigma}f_{1\sigma}d^\dagger_{2\sigma'}d_{1\sigma'}f^\dagger_{2\sigma''}d_{2\sigma''} \\
&+ 2f^\dagger_{2\sigma}d_{2\sigma}d^\dagger_{2\sigma'}d_{1\sigma'}d^\dagger_{1\sigma''}f_{1\sigma''} + 2d^\dagger_{2\sigma}f_{2\sigma}d^\dagger_{1\sigma'}d_{2\sigma'}f^\dagger_{1\sigma''}d_{1\sigma''}\Big]\hat{1}' \ .
\end{aligned} \tag{A.9}$$

Using the fermionic commutation relations to change the order of the operators in the above expression (in particular, taking all the lead (f) operators to the left, and taking dot 1 operators to the left of dot 2 operators), one can rewrite the above expression as

$$\begin{aligned}
\hat{H}^{(3)}_{\text{eff}} =&\frac{4tV_1V_2}{U^2}\sum_\sigma \Big[f^\dagger_{1\sigma}f_{2\sigma} + H.c.\Big] \\
&+\frac{8tV_1V_2}{U^2}\sum_{\sigma,\sigma',\sigma''}\Big[2f^\dagger_{1\sigma'}f_{2\sigma''}\hat{1}'d^\dagger_{1\sigma}d_{1\sigma'}d^\dagger_{2\sigma''}d_{2\sigma}\hat{1}' - f^\dagger_{1\sigma'}f_{2\sigma}\hat{1}'(d^\dagger_{1\sigma}d_{1\sigma'} + d^\dagger_{2\sigma}d_{2\sigma'})\hat{1}' + H.c.\Big] \ .
\end{aligned} \tag{A.10}$$

Defining spin operators for the dots as

$$\hat{S}^z_i = \tfrac{1}{2}\left(d^\dagger_{i\uparrow}d_{i\uparrow} - d^\dagger_{i\downarrow}d_{i\downarrow}\right) \ , \quad \hat{S}^+_i = d^\dagger_{i\uparrow}d_{i\downarrow} \ , \quad \hat{S}^-_i = d^\dagger_{i\downarrow}d_{i\uparrow} \ , \tag{A.11}$$

with $i = 1, 2$, Eqn. (A.10) can be written as

$$\hat{H}^{(3)}_{\text{eff}} = \frac{16tV_1V_2}{U^2}\hat{1}'\Big[f^\dagger_{1\uparrow}f_{2\uparrow}(\hat{S}^-_1\hat{S}^+_2 + \hat{S}^z_1\hat{S}^z_2) + f^\dagger_{1\downarrow}f_{2\downarrow}(\hat{S}^-_2\hat{S}^+_1 + \hat{S}^z_1\hat{S}^z_2) + f^\dagger_{1\uparrow}f_{2\downarrow}(\hat{S}^-_2\hat{S}^z_1 - \hat{S}^-_1\hat{S}^z_2) + f^\dagger_{1\downarrow}f_{2\uparrow}(\hat{S}^z_2\hat{S}^+_1 - \hat{S}^z_1\hat{S}^+_2)\Big]\hat{1}' + H.c. \tag{A.12}$$

A straightforward rearrangement of the above expression, as well as defining spin operators for the leads:

$$\hat{\mathbf{S}}_{\mathbf{0}\nu} = \sum_{\sigma,\sigma'} f^\dagger_{\nu\sigma}\boldsymbol{\sigma}_{\sigma\sigma'}f_{\nu\sigma'} \ , \tag{A.13}$$

yields the expression in the main text, Eqn. (2.28).

The third-order SW transformation for the 2AIM away from ph symmetry, or with a finite U', is carried out in the same way as detailed above (the U' term being taken as part of $\hat{H}_0$). In these cases the eigenstates of $\hat{H}_0$ have the same form, but different energies from the case considered above (ph symmetry and $U' = 0$). This makes the algebra slightly more "messy", but addition of ph asymmetry or interdot repulsion makes no difference to the procedure itself. The results of the third-order SW transformations carried out in these cases are given in the main text (Eqn. (5.11) for interdot repulsion, and Eqn. (5.13) for ph asymmetry), where, in the case of interdot repulsion, we have taken all the results to leading order in U'/U.

APPENDIX B

Generalised self-energy method for calculating the Green's functions of multi-impurity systems

We consider a very general system of fermions, with Hamiltonian

$$\hat{H} = \hat{H}_0 + \hat{H}_1 \ , \tag{B.1}$$

where $\hat{H}_0$ consists of all the quadratic terms, whereas $\hat{H}_1$ contains all four-fermion interaction terms. The sites of the model are labeled by indices i, j, k etc, which can be taken to be composite indices incorporating spin etc. if desired.

The equation of motion for $G_{ij}(\omega) = \langle\langle c_i ; c_j^\dagger \rangle\rangle_\omega$ is

$$\begin{aligned} zG_{ij}(\omega) + \langle\langle [\hat{H}, c_i]; c_j^\dagger \rangle\rangle_\omega &= \langle \{c_i, c_j^\dagger\} \rangle \ , \\ zG_{ij}(\omega) + \langle\langle [\hat{H}_0, c_i]; c_j^\dagger \rangle\rangle_\omega &= \delta_{ij} - \langle\langle [\hat{H}_1, c_i]; c_j^\dagger \rangle\rangle_\omega \ , \end{aligned} \tag{B.2}$$

where $z = \omega + i\eta$ with η a positive infinitesimal. Since $\hat{H}_0$ is quadratic $[\hat{H}_0, c_i] = \sum_k \alpha_{ik} c_k$ with α_{ik} depending on the details of the model[1]. Hence

$$\begin{aligned} zG_{ij}(\omega) + \sum_k \alpha_{ik} G_{kj}(\omega) &= \delta_{ij} - \langle\langle [\hat{H}_1, c_i]; c_j^\dagger \rangle\rangle_\omega \ , \\ \sum_k \left[z\delta_{ik} + \alpha_{ik} \right] G_{kj}(\omega) &= \delta_{ij} - F_{ij}(\omega) \ , \end{aligned} \tag{B.3}$$

where

$$F_{ij}(\omega) = \langle\langle [\hat{H}_1, c_i]; c_j^\dagger \rangle\rangle_\omega \ . \tag{B.4}$$

In the non-interacting limit, $\hat{H}_1 = 0$, $F_{ij}(\omega) = 0 \ \forall i, j$, or in matrix form $\mathbf{F}(\omega) = \mathbf{0}$,

[1] We assume that particle number is conserved.

so that

$$\sum_k \left[z\delta_{ik} + \alpha_{ik}\right] G^0_{kj}(\omega) = \delta_{ij} \ , \tag{B.5}$$

or in matrix form

$$\mathbf{M}(\omega)\mathbf{G^0}(\omega) = \mathbf{I} \ , \ M_{ik} = z\delta_{ik} + \alpha_{ik} \ , \tag{B.6}$$

where $\mathbf{G^0}(\omega)$ is the matrix of non-interacting Green's functions, and from which we can see $\mathbf{M}(\omega) = [\mathbf{G^0}(\omega)]^{-1}$. Using this we obtain

$$\begin{aligned} [\mathbf{G^0}(\omega)]^{-1}\mathbf{G}(\omega) &= \mathbf{I} - \mathbf{F}(\omega) \ , \\ [\mathbf{G^0}(\omega)]^{-1} &= [\mathbf{G}(\omega)]^{-1} - \mathbf{F}(\omega)[\mathbf{G}(\omega)]^{-1} \ , \end{aligned} \tag{B.7}$$

and by comparison to the Dyson equation the self-energy matrix is given by

$$\mathbf{\Sigma}(\omega) = -\mathbf{F}(\omega)[\mathbf{G}(\omega)]^{-1} \ . \tag{B.8}$$

APPENDIX C

Derivation of the linear-response formula for the finite-temperature, zero-bias conductance of the 2AIM

We begin by deriving the general linear-response equation for the expectation value of an operator. The Kubo formula approximates the expectation value of an operator to first-order in a perturbing Hamiltonian. Suppose the exact Hamiltonian for the system is of the form $\hat{H} + \hat{H}'(t)$. Then, by definition,

$$\langle A(t) \rangle = \mathrm{Tr}\left[\hat{\rho}(t)\hat{A}\right] \ , \tag{C.1}$$

where the exact density matrix $\hat{\rho}(t)$ satisfies the equation of motion

$$\dot{\rho}(t) \equiv \frac{\mathrm{d}}{\mathrm{d}t}\hat{\rho}(t) = \frac{1}{i\hbar}\left[\hat{H} + \hat{H}'(t), \hat{\rho}(t)\right] \ . \tag{C.2}$$

To derive the Kubo formula, the perturbation described by $\hat{H}'$ is given a time dependence so it may be switched on adiabatically starting at $t = -\infty$. As such, $\hat{\rho}(-\infty) = \hat{\rho}_{\mathrm{eq}}$, the *equilibrium* density matrix corresponding to $\hat{H}$ alone:

$$\hat{\rho}_{\mathrm{eq}} = \frac{e^{-\beta\hat{H}}}{\mathrm{Tr}\, e^{-\beta\hat{H}}} \ . \tag{C.3}$$

One assumes that the density matrix can then be expanded as

$$\hat{\rho}(t) \simeq \hat{\rho}_{\mathrm{eq}} + \Delta\hat{\rho}(t) \ , \tag{C.4}$$

with $\Delta\hat{\rho}(t)$ calculated to first order in $\hat{H}'$. From (C.2),

$$\dot{\rho}(t) = \frac{1}{i\hbar}\left[\hat{H} + \hat{H}'(t), \hat{\rho}_{\mathrm{eq}}\right] + \frac{1}{i\hbar}\left[\hat{H} + \hat{H}'(t), \Delta\hat{\rho}(t)\right] \tag{C.5}$$

$$= \frac{1}{i\hbar}\left[\hat{H}'(t), \hat{\rho}_{\mathrm{eq}}\right] + \frac{1}{i\hbar}\left[\hat{H}, \Delta\hat{\rho}(t)\right] \ , \tag{C.6}$$

using $[\hat{H}, \hat{\rho}_{\mathrm{eq}}] = 0$ and dropping the $[\hat{H}'(t), \Delta\hat{\rho}(t)]$ term which is at least $\mathcal{O}[(\hat{H}')^2]$. Differentiating (C.4) with respect to time (noting that $\hat{\rho}_{\mathrm{eq}}$ is time-independent) and equating to (C.6) then gives

$$\Delta\dot{\rho}(t) \equiv \frac{\mathrm{d}\Delta\hat{\rho}}{\mathrm{d}t} = \frac{1}{i\hbar}\left[\hat{H}'(t), \hat{\rho}_{\mathrm{eq}}\right] + \frac{1}{i\hbar}\left[\hat{H}, \Delta\hat{\rho}(t)\right] \ , \tag{C.7}$$

which is readily solved within the interaction representation. If $\Delta\hat{\rho}_{\mathrm{I}}(t)$ is defined by

$$\Delta\hat{\rho}(t) = e^{-i\hat{H}t/\hbar}\Delta\hat{\rho}_{\mathrm{I}}(t)e^{i\hat{H}t/\hbar} \ , \tag{C.8}$$

it is straightforward to show by differentiation that

$$\Delta\dot{\rho}(t) = \frac{1}{i\hbar}e^{-i\hat{H}t/\hbar}\left[H, \Delta\hat{\rho}_{\mathrm{I}}(t)\right]e^{i\hat{H}t/\hbar} + e^{-i\hat{H}t/\hbar}\Delta\dot{\rho}_{\mathrm{I}}(t)e^{i\hat{H}t/\hbar} \tag{C.9}$$

$$= \frac{1}{i\hbar}\left[H, \Delta\hat{\rho}(t)\right] + e^{-i\hat{H}t/\hbar}\Delta\dot{\rho}_{\mathrm{I}}(t)e^{i\hat{H}t/\hbar} \ . \tag{C.10}$$

Comparing (C.7) and (C.10), it follows that

$$e^{-i\hat{H}t/\hbar}\Delta\dot{\rho}_{\mathrm{I}}(t)e^{i\hat{H}t/\hbar} = \frac{1}{i\hbar}\left[\hat{H}'(t), \hat{\rho}_{\mathrm{eq}}\right] \ . \tag{C.11}$$

Transferring the exponentials to the right hand side, and integrating with respect to time, then gives

$$\Delta\hat{\rho}_{\mathrm{I}}(t') = \frac{1}{i\hbar}\int_{-\infty}^{t'} e^{i\hat{H}t/\hbar}\left[\hat{H}'(t), \hat{\rho}_{\mathrm{eq}}\right]e^{-i\hat{H}t/\hbar}\ \mathrm{d}t \ . \tag{C.12}$$

Using (C.8) to transform back to the Heisenberg representation, one obtains

$$\Delta\hat{\rho}(t') = \frac{1}{i\hbar}\int_{-\infty}^{t'} e^{i\hat{H}(t-t')/\hbar}\left[\hat{H}'(t), \hat{\rho}_{\mathrm{eq}}\right]e^{-i\hat{H}(t-t')/\hbar}\ \mathrm{d}t, \tag{C.13}$$

which, on swapping t and t' for convenience, becomes

$$\Delta\hat{\rho}(t) = \frac{1}{i\hbar}\int_{-\infty}^{t} e^{i\hat{H}(t'-t)/\hbar}\left[\hat{H}'(t'), \hat{\rho}_{\mathrm{eq}}\right]e^{-i\hat{H}(t'-t)/\hbar}\ \mathrm{d}t'. \tag{C.14}$$

The Kubo formula follows by substituting (C.14) into (C.1) via (C.4):

$$\langle \hat{A}(t) \rangle = \langle \hat{A} \rangle_{\rm eq} + \frac{1}{i\hbar} \, {\rm Tr} \int_{-\infty}^{t} e^{i\hat{H}(t'-t)/\hbar} \left[\hat{H}'(t'), \hat{\rho}_{\rm eq} \right] e^{-i\hat{H}(t'-t)/\hbar} \hat{A} \ {\rm d}t'. \tag{C.15}$$

The adiabatic switching-on of the perturbation can be achieved by writing

$$\hat{H}'(t') = e^{\eta t'} \hat{H}' \quad : \quad \eta = 0^{+} \tag{C.16}$$

and, assuming the system reaches a steady state, we can set $t = 0$ without loss of generality. Hence

$$\langle \hat{A} \rangle = \langle \hat{A} \rangle_{\rm eq} + \frac{1}{i\hbar} \, {\rm Tr} \int_{-\infty}^{0} e^{\eta t'} e^{i\hat{H}t'/\hbar} \left[\hat{H}', \hat{\rho}_{\rm eq} \right] e^{-i\hat{H}t'/\hbar} \hat{A} \ {\rm d}t' \ , \tag{C.17}$$

or, rather more usefully,

$$\boxed{\langle \hat{A} \rangle = \langle \hat{A} \rangle_{\rm eq} + \lim_{\omega \to 0} \frac{1}{i\hbar} \, {\rm Tr} \int_{-\infty}^{0} e^{-i(\omega + i\eta)t'} e^{i\hat{H}t'/\hbar} \left[\hat{H}', \hat{\rho}_{\rm eq} \right] e^{-i\hat{H}t'/\hbar} \hat{A} \ {\rm d}t'} \tag{C.18}$$

We now go on to apply this to finding the expectation value for the current of a two-lead quantum dot system, to leading order in bias.

General formulation

We consider a rather generic two-lead device. For now, we simply assume that the leads are non-interacting (and described by the usual operators $c^{\dagger}_{\nu k \sigma}$ with $\nu = 1, 2$), and make no assumptions about the structure of the dot(s) in between. On applying a bias across the leads, the current from 1 to 2 is given by

$$J = \langle \hat{J} \rangle = \frac{-e\langle \dot{N}_1 \rangle + e\langle \dot{N}_2 \rangle}{2} \ , \tag{C.19}$$

where e is the electron charge and $\dot{N}_\nu \equiv \frac{d}{dt}\hat{N}_\nu$ with $\hat{N}_\nu$ the *total* number of electrons on lead ν,

$$\hat{N}_\nu = \sum_{k,\sigma} c^{\dagger}_{\nu k \sigma} c_{\nu k \sigma} \ . \tag{C.20}$$

The perturbation of the system due to the applied bias is

$$\hat{H}' = \sum_{\nu} \mu_\nu \hat{N}_\nu \ , \tag{C.21}$$

(taking $\mu_1 = 0 = \mu_2$ in the equilibrium case). Using Eqn. (C.15), the expectation

values of $\dot{N}_\mu$ to leading order in $\hat{H}'$ are given by

$$\langle \dot{N}_\mu \rangle = \sum_\nu \sigma_{\mu\nu} \mu_\nu \ , \tag{C.22}$$

with $\sigma_{\mu\nu}$ the conductivity tensor

$$\sigma_{\mu\nu} = \lim_{\omega \to 0} \sigma_{\mu\nu}(\omega) \ , \tag{C.23}$$

and where the dynamical conductivity is given by

$$\sigma_{\mu\nu}(\omega) = \frac{1}{i\hbar} \operatorname{Tr} \int_{-\infty}^{0} e^{-i(\omega+i\eta)t'} e^{i\hat{H}t'/\hbar} \left[\hat{N}_\nu, \hat{\rho}_{\mathrm{eq}} \right] e^{-i\hat{H}t'/\hbar} \dot{N}_\mu \ \mathrm{d}t'. \tag{C.24}$$

Here, $\eta = 0^+$ and $\hat{\rho}_{\mathrm{eq}}$ is the equilibrium density operator

$$\hat{\rho}_{\mathrm{eq}} = \frac{e^{-\beta\hat{H}}}{\operatorname{Tr} e^{-\beta\hat{H}}} \equiv \frac{e^{-\beta\hat{H}}}{Z} \ . \tag{C.25}$$

It is difficult to calculate (C.24) directly within the NRG, as it involves the 'non-local' operator $\hat{N}_\nu$. To make progress, we apply a number of transformations. First we make the trivial change of variable $t' \to -t$:

$$\sigma_{\mu\nu}(\omega) = \frac{1}{i\hbar} \operatorname{Tr} \int_{0}^{\infty} e^{i(\omega+i\eta)t} e^{-i\hat{H}t/\hbar} \left[\hat{N}_\nu, \hat{\rho}_{\mathrm{eq}} \right] e^{i\hat{H}t/\hbar} \dot{N}_\mu \ \mathrm{d}t \ . \tag{C.26}$$

Using $\operatorname{Tr}(\hat{A}\hat{B}) = \operatorname{Tr}(\hat{B}\hat{A})$, we can shuffle the $e^{-i\hat{H}t/\hbar}$ to the end of the integrand and use

$$\dot{N}_\mu(t) = e^{i\hat{H}t/\hbar} \dot{N}_\mu e^{-i\hat{H}t/\hbar} \tag{C.27}$$

to obtain

$$\sigma_{\mu\nu}(\omega) = \frac{1}{i\hbar} \operatorname{Tr} \int_{0}^{\infty} e^{i(\omega+i\eta)t} \left[\hat{N}_\nu, \hat{\rho}_{\mathrm{eq}} \right] \dot{N}_\mu(t) \ \mathrm{d}t \ . \tag{C.28}$$

Then we note that

$$\begin{aligned} \operatorname{Tr}\left([\hat{A}, \hat{B}]\hat{C} \right) &= \operatorname{Tr}(\hat{A}\hat{B}\hat{C} - \hat{B}\hat{A}\hat{C}) \\ &= \operatorname{Tr}(\hat{B}\hat{C}\hat{A} - \hat{B}\hat{A}\hat{C}) \\ &= \operatorname{Tr}\left(\hat{B}[\hat{C}, \hat{A}] \right) \end{aligned} \tag{C.29}$$

to rewrite (C.28) as

$$\sigma_{\mu\nu}(\omega) = \frac{1}{i\hbar} \operatorname{Tr} \int_{0}^{\infty} e^{i(\omega+i\eta)t} \hat{\rho}_{\mathrm{eq}} \left[\dot{N}_\mu(t), \hat{N}_\nu \right] \ \mathrm{d}t \ . \tag{C.30}$$

By time-translational invariance,

$$\begin{aligned}\operatorname{Tr}\rho_{\mathrm{eq}}\left[\dot{N}_\mu(t),\hat{N}_\nu\right] &= \operatorname{Tr}\hat{\rho}_{\mathrm{eq}}\left[\dot{N}_\mu,\hat{N}_\nu(-t)\right] \\ &= -\int_t^\infty \frac{\mathrm{d}}{\mathrm{d}t'}\operatorname{Tr}\hat{\rho}_{\mathrm{eq}}\left[\dot{N}_\mu,\hat{N}_\nu(-t')\right]\ \mathrm{d}t' \\ &= \int_t^\infty \operatorname{Tr}\hat{\rho}_{\mathrm{eq}}\left[\dot{N}_\mu,\dot{N}_\nu(-t')\right]\ \mathrm{d}t' \\ &= \int_t^\infty \operatorname{Tr}\hat{\rho}_{\mathrm{eq}}\left[\dot{N}_\mu(t'),\dot{N}_\nu\right]\ \mathrm{d}t' \ . \end{aligned} \tag{C.31}$$

Substituting this result into (C.30) gives

$$\sigma_{\mu\nu}(\omega) = \frac{1}{i\hbar}\operatorname{Tr}\int_0^\infty \mathrm{d}t\int_t^\infty \mathrm{d}t' e^{i(\omega+i\eta)t}\hat{\rho}_{\mathrm{eq}}\left[\dot{N}_\mu(t'),\dot{N}_\nu\right]\ , \tag{C.32}$$

and, upon changing the order of integration

$$\int_0^\infty \mathrm{d}t\int_t^\infty \mathrm{d}t' \to \int_0^\infty \mathrm{d}t'\int_0^{t'} \mathrm{d}t \tag{C.33}$$

the integral over t in (C.32) can be done:

$$\begin{aligned}\sigma_{\mu\nu}(\omega) &= \frac{1}{i\hbar}\operatorname{Tr}\int_0^\infty \mathrm{d}t'\hat{\rho}_{\mathrm{eq}}\left[\dot{N}_\mu(t'),\dot{N}_\nu\right]\int_0^{t'} \mathrm{d}t\ e^{i(\omega+i\eta)t} \\ &= \frac{1}{i\hbar}\operatorname{Tr}\int_0^\infty \mathrm{d}t'\hat{\rho}_{\mathrm{eq}}\left[\dot{N}_\mu(t'),\dot{N}_\nu\right]\left(\frac{e^{i(\omega+i\eta)t'}-1}{i(\omega+i\eta)}\right)\ . \end{aligned} \tag{C.34}$$

Now, following Izumida et al. [145], we define a (Fourier-transformed) current-current correlation function by

$$K_{\mu\nu}(\omega) = \frac{1}{i\hbar}\int_0^\infty \mathrm{d}t\ e^{i(\omega+i\eta)t}\left\langle\left[\dot{N}_\mu(t),\dot{N}_\nu\right]\right\rangle\ , \tag{C.35}$$

such that (C.34) becomes

$$\sigma_{\mu\nu}(\omega) = \frac{1}{i(\omega+i\eta)}\Big(K_{\mu\nu}(\omega)-K_{\mu\nu}(0)\Big)\ . \tag{C.36}$$

The symmetries of $K_{\mu\nu}(\omega)$ can be determined by expanding the trace of (C.35) in a complete set of eigenstates of $\hat{H}$. One obtains

$$\begin{aligned}\left\langle\left[\dot{N}_\mu(t),\dot{N}_\nu\right]\right\rangle &= \sum_{n,m} e^{-i(E_n-E_m)t/\hbar}\Big[\langle n|\hat{\rho}_{\mathrm{eq}}\dot{N}_\mu|m\rangle\langle m|\dot{N}_\nu|n\rangle - \langle m|\hat{\rho}_{\mathrm{eq}}\dot{N}_\nu|n\rangle\langle n|\dot{N}_\mu|m\rangle\Big] \\ &= \frac{1}{Z}\sum_{n,m}\left(e^{-\beta E_n}-e^{-\beta E_m}\right)e^{-i(E_m-E_n)t/\hbar}\langle n|\dot{N}_\mu|m\rangle\langle m|\dot{N}_\nu|n\rangle \end{aligned} \tag{C.37}$$

and hence, from (C.35),

$$K_{\mu\nu}(\omega) = \frac{1}{Z}\sum_{n,m}\left(e^{-\beta E_n} - e^{-\beta E_m}\right)\frac{\langle n|\dot{N}_\mu|m\rangle\langle m|\dot{N}_\nu|n\rangle}{\hbar\omega - (E_m - E_n) + i\eta} \ . \tag{C.38}$$

Since $\dot{N}_\mu$ is Hermitian, $\langle n|\dot{N}_\mu|m\rangle = \langle m|\dot{N}_\mu|n\rangle$ and we see immediately that

$$K_{\mu\nu}(\omega) = K_{\nu\mu}(\omega) \ . \tag{C.39}$$

Moreover, on writing

$$K_{\mu\nu}(\omega) = K'_{\mu\nu}(\omega) + iK''_{\mu\nu}(\omega) \ , \tag{C.40}$$

it follows straightforwardly from (C.38) that

$$K'_{\mu\nu}(\omega) = K'_{\mu\nu}(-\omega) \tag{C.41a}$$
$$K''_{\mu\nu}(\omega) = -K''_{\mu\nu}(-\omega) \ . \tag{C.41b}$$

Finally, using (C.41) it follows that

$$K_{\mu\nu}(\omega) - K_{\mu\nu}(0) \sim iK''_{\mu\nu}(\omega) + \mathcal{O}(\omega^2) \ , \tag{C.42}$$

which in turn implies from (C.23) and (C.36) that

$$\sigma_{\mu\nu} = \lim_{\omega\to 0}\frac{K''_{\mu\nu}(\omega)}{\omega} \ . \tag{C.43}$$

We now go on to show how using the above, we can calculate the zero-bias conductance of a two-lead QD system.

Calculation via NRG

We write the general form of the source-drain bias as

$$\mu_1 = \lambda eV \ , \tag{C.44}$$
$$\mu_2 = -(1-\lambda)eV \ . \tag{C.45}$$

Substituting this into (C.19) and using (C.20), we get

$$J = \frac{e^2V}{2}\left[-\lambda\sigma_{11} + (1-\lambda)\sigma_{12} + \lambda\sigma_{21} - (1-\lambda)\sigma_{22}\right] \tag{C.46}$$
$$= \frac{e^2V}{2}\left[\sigma_{12} - \lambda\sigma_{11} - (1-\lambda)\sigma_{22}\right] \ , \tag{C.47}$$

where the second line follows from (C.39). Differentiation with respect to V then

gives

$$G_c(T,0) = \frac{e^2}{2}\left[\sigma_{12} - \lambda\sigma_{11} - (1-\lambda)\sigma_{22}\right] \ . \tag{C.48}$$

We will now prove a useful result:

$$\dot{N}_\nu = \frac{1}{i\hbar}\sum_i V_{i\nu}\hat{\jmath}_{\nu i} \ , \tag{C.49}$$

where

$$\hat{\jmath}_{\nu i} = \sum_\sigma \left(f^\dagger_{\nu\sigma} d_{i\sigma} - d^\dagger_{i\sigma} f_{\nu\sigma} \right) = -\hat{\jmath}^\dagger_{\nu i} \ , \tag{C.50}$$

and $V_{i\nu}$ is the (real) tunnel coupling of dot level i to the f_0 orbital of lead ν. We write the generic two-lead quantum dot model as

$$\hat{H} = \hat{H}_{\rm leads} + \hat{H}_{\rm dots} + \hat{H}_{\rm hyb} \ . \tag{C.51}$$

In the NRG basis, the only lead orbitals that couple to the dot are

$$f_{\nu\sigma} = \frac{1}{\sqrt{N}}\sum_k c_{\nu k\sigma} \ , \tag{C.52}$$

which means that

$$\hat{H}_{\rm hyb} = \sum_\sigma f^\dagger_{\nu\sigma}\left(\sum_i V_{i\nu} d_{i\sigma}\right) + \text{h.c.} \tag{C.53}$$

is the most general form for $\hat{H}_{\rm hyb}$. We can express the number operator for lead ν in terms of the f-operators:

$$\hat{N}_\nu = \sum_\sigma f^\dagger_{\nu\sigma} f_{\nu\sigma} + \sum_{n=1,\sigma}^{\infty} f^\dagger_{\nu n\sigma} f_{\nu n\sigma} \ , \tag{C.54}$$

where $f^\dagger_{\nu n\sigma}$ is the creation operator for the n-orbital of the Wilson chain for lead ν. From this it follows that

$$\begin{aligned} \dot{N}_\nu &= \frac{1}{i\hbar}\left[\hat{N}_\nu, \hat{H}\right] \\ &= \frac{1}{i\hbar}\sum_\sigma \left[f^\dagger_{\nu\sigma} f_{\nu\sigma}, \hat{H}_{\rm hyb}\right] \ . \end{aligned} \tag{C.55}$$

Simplifying (C.55) is a matter of algebra:

$$\begin{aligned}\dot{N}_\nu &= \frac{1}{i\hbar}\sum_{i,\sigma,\sigma'} V_{i\nu}\left[f^\dagger_{\nu\sigma}f_{\nu\sigma}, f^\dagger_{\nu\sigma'}d_{i\sigma'}\right] + \text{h.c} \\ &= \frac{1}{i\hbar}\sum_{i,\sigma} V_{i\nu}\left[f^\dagger_{\nu\sigma}f_{\nu\sigma}, f^\dagger_{\nu\sigma}\right] d_{i\sigma} + \text{h.c} \\ &= \frac{1}{i\hbar}\sum_{i,\sigma} V_{i\nu} f^\dagger_{\nu\sigma}d_{i\sigma} + \text{h.c} \\ &= \frac{1}{i\hbar}\sum_{i,\sigma}\left(V_{i\nu}f^\dagger_{\nu\sigma}d_{i\sigma} - V^*_{i\nu}d^\dagger_{i\sigma}f_{\nu\sigma}\right) \ . \end{aligned} \tag{C.56}$$

It is convenient to define a real operator

$$\hat{\jmath}_{\nu i} = \sum_\sigma \left(f^\dagger_{\nu\sigma}d_{i\sigma} - d^\dagger_{i\sigma}f_{\nu\sigma}\right) \ , \tag{C.57}$$

and take $V_{i\nu}$ to be pure real, to give

$$\dot{N}_\nu = \frac{1}{i\hbar}\sum_i V_{i\nu}\hat{\jmath}_{\nu i} \ , \tag{C.58}$$

as stated above. It is now convenient to define

$$iC^{ij}_{\mu\nu}(t) = \theta(t)\left\langle[\hat{\jmath}_{\mu i}(t), \hat{\jmath}_{\nu j}]\right\rangle \ , \tag{C.59}$$

with Fourier transform

$$C^{ij}_{\mu\nu}(\omega) = \int_{-\infty}^{\infty} e^{i(\omega+i\eta)t}C^{ij}_{\mu\nu}(t)\ \mathrm{d}t \ , \tag{C.60}$$

since then, from (C.35), (C.49) and (C.60) we obtain

$$K_{\mu\nu}(\omega) = \frac{-1}{\hbar^3}\sum_{i,j} V_{i\mu}V_{j\nu}C^{ij}_{\mu\nu}(\omega) \ . \tag{C.61}$$

Using (C.43) and (C.48) with (C.61), the final result follows as

$$G_c(T,0) = \frac{e^2}{h}\left[\lambda\bar{\sigma}_{11} + (1-\lambda)\bar{\sigma}_{22} - \bar{\sigma}_{12}\right] \tag{C.62}$$

with

$$\bar{\sigma}_{\mu\nu} = \frac{\pi}{\hbar^2}\sum_{i,j} V_{i\mu}V_{j\nu}\left[\lim_{\omega\to 0}\mathrm{Im}\,\frac{C^{ij}_{\mu\nu}(\omega)}{\omega}\right] \tag{C.63}$$

In the usual way, we take $\hbar = 1$ in (C.63). For the 2AIM, $V_{i\mu} = \delta_{i,\mu}V_\mu$, so we only need to calculate C^{11}_{11}, C^{22}_{22} and C^{12}_{12} (note that $C^{21}_{21} = C^{12}_{12}$).

APPENDIX D

Derivation of the current of the 2AIM to leading order in the interdot tunnel-coupling

We wish to derive an expression for the current flowing from lead 1 to lead 2 in the 2AIM upon application of a finite voltage bias, V, to leading order in the tunnel-coupling between the two dots, t.

The current is defined in Appendix C (Eqn. (C.19)) in terms of lead operators, but by considering the current flowing between the two dots (which in steady state is equal to that flowing between the two leads [147]), the current may equally be defined as (cf. Eqn. 2 in Ref. [123])

$$J = \langle \hat{J} \rangle = \frac{-iet}{\hbar} \sum_{\sigma} \langle d^{\dagger}_{2\sigma} d_{1\sigma} \rangle - \langle d^{\dagger}_{1\sigma} d_{2\sigma} \rangle \ . \tag{D.1}$$

We begin then with Eqn. (C.17), repeated here for convenience:

$$\delta A = \langle \hat{A} \rangle - \langle \hat{A} \rangle_{\mathrm{eq}} = \frac{1}{i\hbar} \mathrm{Tr} \int_{-\infty}^{0} e^{\eta t'} e^{i\hat{H}t'/\hbar} \left[\hat{H}', \hat{\rho}_{\mathrm{eq}} \right] e^{-i\hat{H}t'/\hbar} \hat{A} \ \mathrm{d}t' \ , \tag{D.2}$$

where $\hat{H}'$ is the perturbation to the equilibrium system, which itself has Hamiltonian $\hat{H}$. Making use of

$$\mathrm{Tr}([\hat{B}, \hat{C}]\hat{D}) = \mathrm{Tr}(\hat{C}[\hat{D}, \hat{B}]) \ , \tag{D.3}$$

this can be straightforwardly rearranged to give

$$\delta A = \langle \hat{A} \rangle - \langle \hat{A} \rangle_{\mathrm{eq}} = \frac{1}{i\hbar} \int_{-\infty}^{0} e^{\eta t'} \mathrm{Tr} \left(\hat{\rho}_{\mathrm{eq}} \left[\hat{A}, \hat{H}'(t') \right] \right) \ \mathrm{d}t' \ , \tag{D.4}$$

where $\hat{H}'(t)$ is the perturbing Hamiltonian in the Heisenberg picture. As we wish

to calculate the current to leading order in the tunnel-coupling between the dots, we take $\hat{H}' = \hat{H}_t = t\sum_\sigma (d^\dagger_{1\sigma} d_{2\sigma} + d^\dagger_{2\sigma} d_{1\sigma})$. Putting the current operator into this equation, and noting that the equilibrium ($t = 0$) value of current is zero, gives

$$\begin{aligned} J &= \frac{1}{i\hbar}\int_{-\infty}^{0} e^{\eta t'} \operatorname{Tr}\left(\hat{\rho}_{\mathrm{eq}}\left[\hat{J}, \hat{H}_t(t')\right]\right) \ \mathrm{d}t' \\ &= \frac{1}{i\hbar}\int_{0}^{\infty} e^{-\eta t'} \operatorname{Tr}\left(\hat{\rho}_{\mathrm{eq}}\left[\hat{J}(t'), \hat{H}_t\right]\right) \ \mathrm{d}t' \ . \end{aligned} \tag{D.5}$$

The equilibrium densitry matrix which appears here, is that for the system with $t = 0$. Using the expression for current (Eqn. (D.1)) and the expression for $\hat{H}_t$, as well as the fact that the $t = 0$ Hamiltonian, $\hat{H}$, is separable into left and right parts (*i.e.*, $\hat{H}$ consists of dot 1 and lead 1 completely decoupled from dot 2 and lead 2)[1], leads to

$$\operatorname{Tr}\left(\hat{\rho}_{\mathrm{eq}}\left[\hat{J}(t'), \hat{H}_t\right]\right) = \frac{-iet^2}{\hbar}\sum_\sigma I_\sigma(t') \ , \tag{D.6}$$

where

$$\begin{aligned} I_\sigma(t') = \ & G^<_{22;\sigma}(-t')G^>_{11;\sigma}(t') - G^>_{22;\sigma}(-t')G^<_{11;\sigma}(t') \\ & - G^>_{22}(t')G^<_{11;\sigma}(-t') + G^<_{22;\sigma}(t')G^>_{11;\sigma}(-t') \ , \end{aligned} \tag{D.7}$$

with $G^<_{ii;\sigma}(t')$ and $G^>_{ii;\sigma}(t')$ the lesser and greater Keldysh Green's functions, defined by

$$\begin{aligned} G^<_{ii;\sigma}(t') &= \ i\langle d^\dagger_{i\sigma} d_{i\sigma}(t')\rangle \ , \\ G^>_{ii;\sigma}(t') &= -i\langle d_{i\sigma}(t') d_{i\sigma}\rangle \ . \end{aligned} \tag{D.8}$$

Note that these Green's functions, and all those that follow, are those for the equilibrium ($t = 0$) system. By some straightforward manipulation, and using some simple relations between these Keldysh Green's functions and the retarded, advanced, time-ordered and anti-time-ordered Green's functions [122, 177], we get

$$\begin{aligned} I_\sigma(t') = \operatorname{Re}\Big[& \big(G^r_{11;\sigma}(t') - G^a_{11;\sigma}(t')\big)\big(G^t_{22;\sigma}(t') - G^{\tilde{t}}_{22;\sigma}(t')\big) \\ & - \big(G^r_{22;\sigma}(t') - G^a_{22;\sigma}(t')\big)\big(G^t_{11;\sigma}(t') - G^{\tilde{t}}_{11;\sigma}(t')\big)\Big] \ , \end{aligned} \tag{D.9}$$

such that (using Eqns. (D.5), (D.6) and (D.9))

$$J = \frac{-et^2}{\hbar^2}\sum_\sigma \operatorname{Re}(I_{12;\sigma} - I_{21;\sigma}) \ , \tag{D.10}$$

[1] This means that the equilibrium density matrix may be written as a product of density matrices for the left and right parts of the system. Note that this is only the case if $U' = 0$. This separability of the equilibrium Hamiltonian allows the four-point correlation functions which arise to be factorised into two-point correlation functions.

with

$$I_{12;\sigma} = \int_0^\infty dt' e^{-\eta t'} \left(G^r_{11;\sigma}(t') - G^a_{11;\sigma}(t') \right) \left(G^t_{22;\sigma}(t') - G^{\tilde{t}}_{22;\sigma}(t') \right) . \tag{D.11}$$

The retarded (superscript r), advanced (superscript a), time-ordered (superscript t) and anti-time-ordered (superscript $\tilde{t}$) Green's functions are defined as

$$\begin{aligned} G^r_{ii;\sigma}(t') &= -i\theta(t')\langle\{d_{i\sigma}(t'), d^\dagger_{i\sigma}\}\rangle , \\ G^a_{ii;\sigma}(t') &= i\theta(-t')\langle\{d_{i\sigma}(t'), d^\dagger_{i\sigma}\}\rangle , \\ G^t_{ii;\sigma}(t') &= -i\langle T(d_{i\sigma}(t'), d^\dagger_{i\sigma})\rangle , \\ G^{\tilde{t}}_{ii;\sigma}(t') &= i\langle T(d^\dagger_{i\sigma}, d_{i\sigma}(t'))\rangle , \end{aligned} \tag{D.12}$$

where T is the Wick time-ordering operator [177]. Concentrating on $I_{12;\sigma}$ now, we use the definition of the Fourier transform of the Green's functions:

$$G^x_{ii}(t) = \int_{-\infty}^\infty \frac{\mathrm{d}\omega}{2\pi} e^{-i\omega t} G^x_{ii}(\omega) , \tag{D.13}$$

with $x = r, a, t, \tilde{t}$, as well as [121, 177]

$$G^r_{ii;\sigma}(\omega) - G^a_{ii;\sigma}(\omega) = -2\pi i D_{ii;\sigma}(\omega) , \tag{D.14}$$

as well as writing the t and $\tilde{t}$ Green's functions in terms of the Keldysh Green's functions:

$$\begin{aligned} G^t_{ii;\sigma}(t') &= \theta(t')G^>_{ii;\sigma}(t') + \theta(-t')G^<_{ii;\sigma}(t') \\ G^{\tilde{t}}_{ii;\sigma}(t') &= \theta(-t')G^>_{ii;\sigma}(t') + \theta(t')G^<_{ii;\sigma}(t') , \end{aligned} \tag{D.15}$$

to get to

$$I_{12;\sigma} = -i \int_{-\infty}^\infty d\omega D_{11;\sigma}(\omega) \left[I_{1\sigma}(\omega) - I_{2\sigma}(\omega) \right] , \tag{D.16}$$

with

$$\begin{aligned} I_{1\sigma}(\omega) &= i \int_{-\infty}^0 \mathrm{d}t' \; e^{i(\omega - i\eta)t'} \; \langle d^\dagger_{2\sigma} d_{2\sigma}(t')\rangle = \int_{-\infty}^0 \mathrm{d}t' \; e^{i(\omega - i\eta)t'} \; G^<_{22;\sigma}(t') \\ I_{2\sigma}(\omega) &= i \int_{-\infty}^0 \mathrm{d}t' \; e^{i(\omega - i\eta)t'} \; \langle d_{2\sigma}(t') d^\dagger_{2\sigma}\rangle = \int_{-\infty}^0 \mathrm{d}t' \; e^{i(\omega - i\eta)t'} \; \left(-G^>_{22;\sigma}(t') \right) . \end{aligned} \tag{D.17}$$

We can now Lehmann resolve [121, 122] $I_{1\sigma}(\omega)$ and $I_{2\sigma}(\omega)$ to give

$$\begin{aligned} I_{1\sigma}(\omega) &= \frac{1}{Z}\sum_{n,\gamma}\frac{|\langle\psi_n^{N-1}|d_{2\sigma}|\psi_\gamma^N\rangle|^2 e^{-\beta E_\gamma^N}}{\omega + \frac{[E_n^{N-1}-E_\gamma^N]}{\hbar} - i\eta} \ , \\ I_{2\sigma}(\omega) &= \frac{1}{Z}\sum_{n,\gamma}\frac{|\langle\psi_n^{N+1}|d_{2\sigma}^\dagger|\psi_\gamma^N\rangle|^2 e^{-\beta E_\gamma^N}}{\omega - \frac{[E_n^{N+1}-E_\gamma^N]}{\hbar} - i\eta} \ , \end{aligned} \tag{D.18}$$

where $Z = \mathrm{Tr}\, e^{\beta\hat{H}}$ is the equilibrium partition function, such that

$$\begin{aligned} \mathrm{Re}\,[-i(I_{1\sigma}-I_{2\sigma})] &= \frac{\pi}{Z}\sum_{n,\gamma}|\langle\psi_n^{N-1}|d_{2\sigma}|\psi_\gamma^N\rangle|^2 e^{-\beta E_\gamma^N}\,\delta\left(\omega - \frac{\left[\mu_2 - (E_n^{N-1}-E_0^{N-1}) + (E_\gamma^N - E_0^N)\right]}{\hbar}\right) \\ &- \frac{\pi}{Z}\sum_{n,\gamma}|\langle\psi_n^{N+1}|d_{2\sigma}^\dagger|\psi_\gamma^N\rangle|^2 e^{-\beta E_\gamma^N}\,\delta\left(\omega - \frac{\left[\mu_2 + (E_n^{N+1}-E_0^{N+1}) - (E_\gamma^N - E_0^N)\right]}{\hbar}\right) \\ &= T_{1\sigma} - T_{2\sigma} \ , \end{aligned} \tag{D.19}$$

where μ_i is the chemical potential of lead i, $|\psi_n^N\rangle$ is the n^{th} eigenstate of the equilibrium system with N electrons, and $T_{i\sigma}$ are thus defined. By also Lehmann resolving the spectra, one can show

$$\pi D_{22;\sigma}(\omega) = T_{1\sigma} + T_{2\sigma} \ . \tag{D.20}$$

By some straightforward manipulation, and using the fact that in the thermodynamic limit we may replace $N \to N+1$, we can show that

$$T_{1\sigma} = e^{-\beta(\omega-\mu_2/\hbar)}T_{2\sigma} \ , \tag{D.21}$$

and that therefore

$$\begin{aligned} \mathrm{Re}[-i(I_{1\sigma}-I_{2\sigma})] =& \frac{e^{-\beta(\omega-\mu_2/\hbar)}-1}{e^{-\beta(\omega-\mu_2/\hbar)}+1}\pi D_{22;\sigma}(\omega) \\ =& [2f_2(\omega)-1]\pi D_{22;\sigma}(\omega) \ , \end{aligned} \tag{D.22}$$

where f_2 is the Fermi function for lead 2. This leads to, using Eqn. (D.16)

$$\mathrm{Re}\, I_{12;\sigma} = \int_{-\infty}^{\infty} \mathrm{d}\omega \ \left[2f_2(\omega)-1\right]\pi D_{11;\sigma}(\omega)D_{22;\sigma}(\omega) \ , \tag{D.23}$$

and therefore, from Eqn. (D.10),

$$\begin{aligned} J &= \frac{2\pi e t^2}{\hbar^2} \sum_\sigma \int_{-\infty}^{\infty} \mathrm{d}\omega \ [f_1(\omega) - f_2(\omega)] \, D_{11;\sigma}(\omega) D_{22;\sigma}(\omega) \ , \\ &= \frac{4et^2}{h\hbar\Gamma_1\Gamma_2} \sum_\sigma \int_{-\infty}^{\infty} \mathrm{d}\omega \ [f_1(\omega) - f_2(\omega)] \, [\pi\Gamma_1 D_{11;\sigma}(\omega)][\pi\Gamma_2 D_{22;\sigma}(\omega)] \ , \end{aligned} \tag{D.24}$$

which at zero temperature reduces to

$$J = \frac{4et^2}{h\hbar\Gamma_1\Gamma_2} \sum_\sigma \int_{\mu_1/\hbar}^{\mu_2/\hbar} \mathrm{d}\omega \ [\pi\Gamma_1 D_{11;\sigma}(\omega)][\pi\Gamma_2 D_{22;\sigma}(\omega)] \ . \tag{D.25}$$

In Eqn. (D.25) we set $\hbar = 1$ as usual. Note that the spectra appearing here are those for the $t = 0$ (equilibrium) system, denoted in the main text as $D^{(2)}_{11;\sigma}(\omega)$ and $D^{(1)}_{22;\sigma}(\omega)$.

APPENDIX E

Outline of first-order perturbation theory for the 2IKM in a field

In this appendix we outline the first-order perturbation theory of the 2IKM in a magnetic field, initially considering a uniform field, before going on to consider the effect of additionally applying a staggered field.

As discussed in Appendix A, Brillouin-Wigner perturbation theory gives an effective Hamiltonian for the 2IKM to first order, as

$$\hat{H}_{\text{eff}} = \hat{1}'\hat{H}_{2\text{IKM}}\hat{1}' = \hat{1}'(\hat{H}_0 + \hat{H}_1)\hat{1}' \ , \tag{E.1}$$

where we take

$$\begin{aligned} \hat{H}_0 &= J\hat{\mathbf{S}}_1 \cdot \hat{\mathbf{S}}_2 - h(\hat{S}_1^z + \hat{S}_2^z) + \hat{H}_{\text{leads}} \ , \\ \hat{H}_1 &= J_1\hat{\mathbf{S}}_1 \cdot \hat{\mathbf{S}}_{01} + J_2\hat{\mathbf{S}}_2 \cdot \hat{\mathbf{S}}_{02} \ , \end{aligned} \tag{E.2}$$

and $\hat{1}'$ is the unity operator for the low-energy manifold of $\hat{H}_0$ eigenstates. h is the uniform magnetic field strength, and for the 2IKM in a uniform field ($h \simeq J$), the low-energy eigenstates of $\hat{H}_0$ are $|S\rangle = \frac{1}{\sqrt{2}}(|\uparrow\downarrow\rangle - |\downarrow\uparrow\rangle)$ and $|T_1\rangle = |\uparrow\uparrow\rangle$, as discussed in section 6.1, such that $\hat{1}' = |S\rangle\langle S| + |T_1\rangle\langle T_1|$. Eqn. (E.1) therefore becomes

$$\begin{aligned} \hat{H}_{\text{eff}} =& |S\rangle\langle S|\hat{H}_{2\text{IKM}}|S\rangle\langle S| + |S\rangle\langle S|\hat{H}_{2\text{IKM}}|T_1\rangle\langle T_1| \\ &+ |T_1\rangle\langle T_1|\hat{H}_{2\text{IKM}}|S\rangle\langle S| + |T_1\rangle\langle T_1|\hat{H}_{2\text{IKM}}|T_1\rangle\langle T_1| \ . \end{aligned} \tag{E.3}$$

The matrix elements in the above equation are straightforward to calculate, and we

find:

$$\begin{aligned}
\langle S|\hat{H}_{\rm 2IKM}|S\rangle &= \frac{-3J}{4} \ , \\
\langle T_1|\hat{H}_{\rm 2IKM}|S\rangle &= \frac{-J_1}{2\sqrt{2}}\hat{S}^-_{01} + \frac{J_2}{2\sqrt{2}}\hat{S}^-_{02} \ , \\
\langle S|\hat{H}_{\rm 2IKM}|T_1\rangle &= \frac{-J_1}{2\sqrt{2}}\hat{S}^+_{01} + \frac{J_2}{2\sqrt{2}}\hat{S}^+_{02} \ , \\
\langle T_1|\hat{H}_{\rm 2IKM}|T_1\rangle &= \frac{J}{4} - h + \frac{J_1}{2}\hat{S}^z_{01} + \frac{J_2}{2}\hat{S}^z_{02} \ .
\end{aligned} \tag{E.4}$$

Defining the pseudospin operators $\hat{\tau}^z = \frac{1}{2}(|T_1\rangle\langle T_1| - |S\rangle\langle S|)$, $\hat{\tau}^+ = |T_1\rangle\langle S|$, $\hat{\tau}^- = |S\rangle\langle T_1|$, and putting the above matrix elements into Eqn. (E.3) then yields

$$\begin{aligned}
\hat{H}_{\rm eff} = &\tfrac{1}{2}J_1\left[\hat{S}^z_{01}\hat{\tau}^z - \sqrt{2}\frac{(\hat{S}^+_{01}\hat{\tau}^- + \hat{S}^-_{01}\hat{\tau}^+)}{2}\right] \\
&+ \tfrac{1}{2}J_2\left[\hat{S}^z_{02}\hat{\tau}^z + \sqrt{2}\frac{(\hat{S}^+_{02}\hat{\tau}^- + \hat{S}^-_{02}\hat{\tau}^+)}{2}\right] \\
&+ \tfrac{1}{4}J_1\hat{S}^z_{01} + \tfrac{1}{4}J_2\hat{S}^z_{02} + (J-h)\hat{\tau}^z \ ,
\end{aligned} \tag{E.5}$$

and carrying out the simple transformation, $c_{1\mathbf{k}\uparrow} \to -c_{1\mathbf{k}\uparrow}$ (corresponding to a phase shift on the up-spin electrons in lead 1), then yields the low-energy effective model given in the text, Eqns. (6.1) and (6.3).

In the presence of both staggered and uniform fields (with $h \simeq J$), as considered in section 6.1.1, $\hat{H}_0$ is now given by

$$\hat{H}_0 = J\hat{\mathbf{S}}_1 \cdot \hat{\mathbf{S}}_2 - h(\hat{S}^z_1 + \hat{S}^z_2) - h_s(\hat{S}^z_1 - \hat{S}^z_2) + \hat{H}_{\rm leads} \ , \tag{E.6}$$

with $\hat{H}_1$ as given in Eqn. (E.2). h_s is the strength of the staggered magnetic field. In this case the low-energy eigenstates of $\hat{H}_0$ are $\hat{T}_1$ and $|S'\rangle = \frac{1}{\sqrt{1+b^2}}(|S\rangle + b|T_0\rangle)$, where $|T_0\rangle = \frac{1}{\sqrt{2}}(|\uparrow\downarrow\rangle + |\downarrow\uparrow\rangle$, so that $\hat{1}' = |S'\rangle\langle S'| + |T_1\rangle\langle T_1|$. The coefficient b, found by straightforward diagonalisation of $\hat{H}_0$, is given by

$$b = \frac{2h_s}{J}\left[1 + \sqrt{1 + \frac{4h_s^2}{J^2}}\right]^{-1} \ , \tag{E.7}$$

such that $b \to h_s/J$ as $h_s/J \to 0$, and $b \to 1$ as $h_s/J \to \infty$. The low-energy effective model in the presence of both uniform and staggered fields can then be calculated via

$$\begin{aligned}
\hat{H}_{\rm eff} = &|S'\rangle\langle S'|\hat{H}_{\rm 2IKM}|S'\rangle\langle S'| + |S'\rangle\langle S'|\hat{H}_{\rm 2IKM}|T_1\rangle\langle T_1| \\
&+ |T_1\rangle\langle T_1|\hat{H}_{\rm 2IKM}|S'\rangle\langle S'| + |T_1\rangle\langle T_1|\hat{H}_{\rm 2IKM}|T_1\rangle\langle T_1| \ .
\end{aligned} \tag{E.8}$$

As in the case of a purely uniform field, we may calculate the matrix elements straightforwardly, and we define pseudospin operators: $\hat{\tau}^z = \frac{1}{2}(|T_1\rangle\langle T_1| - |S'\rangle\langle S'|)$, $\hat{\tau}^+ = |T_1\rangle\langle S'|$, $\hat{\tau}^- = |S'\rangle\langle T_1|$. Putting these matrix elements into the above equation and again carrying out the simple transformation $c_{1\mathbf{k}\uparrow} \rightarrow -c_{1\mathbf{k}\uparrow}$ the yields the low-energy effective model given in the text (Eqns. (6.9) and (6.10)).

Bibliography

[1] P. W. Anderson, Science **1770**, 393 (1972).

[2] P. W. Anderson and B. T. Matthias, Science **144**, 373 (1964).

[3] A. Hewson, *The Kondo Problem to Heavy Fermions* (Cambridge University Press, Cambridge, UK, 1993).

[4] E. Dagotto, Science **309**, 257 (2005).

[5] M. Imada, A. Fujimori, and Y. Tokura, Rev. Mod. Phys. **70**, 1039 (1998).

[6] W. de Haas, J. de Boer, and G. van den Berg, Physica **1**, 1115 (1934).

[7] J. Kondo, Prog. Theor. Phys. **32**, 37 (1964).

[8] P. W. Anderson, Phys. Rev. **124**, 41 (1961).

[9] Y. Meir, N. S. Wingreen, and P. A. Lee, Phys. Rev. Lett. **70**, 2601 (1993).

[10] F. B. Anders, Phys. Rev. Lett. **101**, 066804 (2008).

[11] H. R. Krishna-murthy, J. W. Wilkins, and K. G. Wilson, Phys. Rev. B **21**, 1003 (1980).

[12] H. R. Krishna-murthy, J. W. Wilkins, and K. G. Wilson, Phys. Rev. B **21**, 1044 (1980).

[13] K. Yosida and K. Yamada, Prog. Theor. Phys. **46**, 244 (1970).

[14] K. Yosida and K. Yamada, Prog. Theor. Phys. **53**, 970 (1975).

[15] K. Yosida and K. Yamada, Prog. Theor. Phys. **53**, 1286 (1975).

[16] J. R. Schrieffer and P. A. Wolff, Phys. Rev. **149**, 491 (1966).

[17] P. W. Anderson, Journal of Physics C: Solid State Physics **3**, 2436 (1970).

[18] K. Wilson, Rev. Mod. Phys. **47**, 773 (1975).

[19] L. D. Landau, Sov. Phys. JETP **3**, 920 (1956).

[20] L. D. Landau, Sov. Phys. JETP **135**, 101 (1957).

[21] P. Nozières, Journal of Low Temperature Physics **17**, 31 (1974).

[22] N. Andrei, K. Furuya, and J. H. Lowenstein, Rev. Mod. Phys. **55**, 331 (1983).

[23] P. B. Wiegmann and A. M. Tsvelick, Journal of Physics C: Solid State Physics **16**, 2281 (1983).

[24] R. Bulla, T. A. Costi, and T. Pruschke, Rev. Mod. Phys. **80**, 395 (2008).

[25] I. Affleck, A. W. W. Ludwig, and B. A. Jones, Phys. Rev. B **52**, 9528 (1995).

[26] D. E. Logan, M. P. Eastwood, and M. A. Tusch, Journal of Physics: Condensed Matter **10**, 2673 (1998).

[27] A. C. Hewson, Phys. Rev. Lett. **70**, 4007 (1993).

[28] A. C. Hewson, Journal of Physics: Condensed Matter **13**, 10011 (2001).

[29] R. Peters, T. Pruschke, and F. B. Anders, Phys. Rev. B **74**, 245114 (2006).

[30] A. Weichselbaum and J. von Delft, Phys. Rev. Lett. **99**, 076402 (2007).

[31] P. Nozieres and A. Blandin, J. Phys. (Paris) **193**, 41 (1980).

[32] D. L. Cox and A. Zawadowski, Adv. Phys. **47**, 599 (1998).

[33] K. Chen and C. Jayaprakash, Phys. Rev. B **57**, 5225 (1998).

[34] C. Gonzalez-Buxton and K. Ingersent, Phys. Rev. B **57**, 14254 (1998).

[35] A. K. Mitchell, T. F. Jarrold, and D. E. Logan, Phys. Rev. B **79**, 085124 (2009).

[36] A. K. Mitchell and D. E. Logan, Phys. Rev. B **81**, 075126 (2010).

[37] T. Numata, Y. Nisikawa, A. Oguri, and A. C. Hewson, Phys. Rev. B **80**, 155330 (2009).

[38] A. Oguri *et al.*, Phys. Rev. B **83**, 205304 (2011).

[39] S. Alexander and P. W. Anderson, Phys. Rev. **133**, A1594 (1964).

[40] P. Gottlieb and H. Suhl, Phys. Rev. **134**, A1586 (1964).

[41] K. Yamada, Prog. Theor. Phys. **62**, 901 (1979).

[42] C. Jayaprakash, H. R. Krishnamurthy, and J. W. Wilkins, Journal of Applied Physics **53**, 2142 (1982).

[43] C. Jayaprakash, H. R. Krishna-murthy, and J. W. Wilkins, Phys. Rev. Lett. **47**, 737 (1981).

[44] B. A. Jones and C. M. Varma, Phys. Rev. Lett. **58**, 843 (1987).

[45] B. A. Jones, C. M. Varma, and J. W. Wilkins, Phys. Rev. Lett. **61**, 125 (1988).

[46] B. A. Jones and C. M. Varma, Phys. Rev. B **40**, 324 (1989).

[47] B. A. Jones, B. G. Kotliar, and A. J. Millis, Phys. Rev. B **39**, 3415 (1989).

[48] B. A. Jones, Physica B: Condensed Matter **171**, 53 (1991).

[49] I. Affleck and A. W. W. Ludwig, Phys. Rev. Lett. **68**, 1046 (1992).

[50] J. Gan, Phys. Rev. B **51**, 8287 (1995).

[51] J. Gan, Phys. Rev. Lett. **74**, 2583 (1995).

[52] N. Andrei and C. Destri, Phys. Rev. Lett. **52**, 364 (1984).

[53] I. Affleck and A. W. W. Ludwig, Phys. Rev. Lett. **67**, 161 (1991).

[54] E. Majorana, Nuovo Cimento **14**, 171 (1937).

[55] G.-M. Zhang, A. Hewson, and R. Bulla, Solid State Communications **112**, 105 (1999).

[56] V. Mourik *et al.*, Science **336**, 1003 (2012).

[57] H. B. Pang and D. L. Cox, Phys. Rev. B **44**, 9454 (1991).

[58] M. Fabrizio, A. O. Gogolin, and P. Nozières, Phys. Rev. Lett. **74**, 4503 (1995).

[59] J. Malecki, E. Sela, and I. Affleck, Phys. Rev. B **82**, 205327 (2010).

[60] J. Malecki, E. Sela, and I. Affleck, Phys. Rev. B **84**, 159907 (2011).

[61] R. M. Potok *et al.*, Nature **446**, 167 (2007).

[62] D. Goldhaber-Gordon *et al.*, Nature **391**, 156 (1998).

[63] L. Kouwenhoven and C. Marcus, Physics World 35 (1998).

[64] A. Makarovski, L. An, J. Liu, and G. Finkelstein, Phys. Rev. B **74**, 155431 (2006).

[65] C. Stampfer *et al.*, Applied Physics Letters **92**, 012102 (2008).

[66] J. Singleton, *Band theory and eletronic properties of solids* (Oxford University Press, Oxford, UK, 2001).

[67] S. J. Chorley *et al.*, Phys. Rev. Lett. **109**, 156804 (2012).

[68] H. Ingerslev Jorgensen *et al.*, Nature Physics **4**, 536 (2008).

[69] J. Nygard, D. Cobden, and D. Lindelof, Nature **408**, 342 (2000).

[70] G. Finkelstein, Carbon Nanotube Quantum Dots, Colloquium Presentation, 2007.

[71] A. Makarovski, A. Zhukov, J. Liu, and G. Finkelstein, Phys. Rev. B **75**, 241407 (2007).

[72] F. B. Anders, D. E. Logan, M. R. Galpin, and G. Finkelstein, Phys. Rev. Lett. **100**, 086809 (2008).

[73] M. R. Galpin, F. W. Jayatilaka, D. E. Logan, and F. B. Anders, Phys. Rev. B **81**, 075437 (2010).

[74] W. G. van der Wiel *et al.*, Science **289**, 2105 (2000).

[75] R. C. Ashoori *et al.*, Phys. Rev. Lett. **71**, 613 (1993).

[76] C. W. J. Beenakker, Phys. Rev. B **44**, 1646 (1991).

[77] T. A. Fulton and G. J. Dolan, Phys. Rev. Lett. **59**, 109 (1987).

[78] U. Meirav, M. A. Kastner, and S. J. Wind, Phys. Rev. Lett. **65**, 771 (1990).

[79] M. A. Reed *et al.*, Phys. Rev. Lett. **60**, 535 (1988).

[80] B. Su, V. J. Goldman, and J. E. Cunningham, Science **255**, 313 (1992).

[81] A. M. Chang and J. C. Chen, Rep. Prog. Phys. **72**, 096501 (2009).

[82] M. R. Buitelaar *et al.*, Phys. Rev. B **77**, 245439 (2008).

[83] W. G. van der Wiel *et al.*, Rev. Mod. Phys. **75**, 1 (2003).

[84] N. J. Craig *et al.*, Science **304**, 565 (2004).

[85] H. Jeong, A. M. Chang, and M. R. Melloch, Science **293**, 2221 (2001).

[86] J. Bork *et al.*, Nature Phy **7**, 901 (2011).

[87] I. J. Hamad, L. C. Ribeiro, G. B. Martins, and E. V. Anda, arxiv 1209.3659v2 (2013).

[88] P. J. F. Harris, *Carbon Nanotube Science* (Cambridge University Press, Cambridge, UK, 2009).

[89] H. O. H. Churchill *et al.*, Nature Physics **5**, 321 (2009).

[90] S. Sapmaz *et al.*, Nano Letters **6**, 1350 (2006).

[91] O. Sakai and Y. Shimizu, J. Phys. Soc. Jap. **61**, 2333 (1992).

[92] O. Sakai, Y. Shimizu, and T. Kasuya, Solid State Communications **75**, 81 (1990).

[93] O. Sakai and Y. Shimizu, J. Phys. Soc. Jap. **61**, 2348 (1992).

[94] W. Izumida and O. Sakai, Phys. Rev. B **62**, 10260 (2000).

[95] A. Georges and Y. Meir, Phys. Rev. Lett. **82**, 3508 (1999).

[96] F. W. Jayatilaka, M. R. Galpin, and D. E. Logan, Phys. Rev. B **84**, 115111 (2011).

[97] D. E. Logan, C. J. Wright, and M. R. Galpin, Phys. Rev. B **80**, 125117 (2009).

[98] J. Ziman, *Elements of Advanced Quantum Theory* (Cambridge University Press, Cambridge, UK, 1969).

[99] F. D. M. Haldane, Phys. Rev. Lett. **40**, 416 (1978).

[100] C. J. Wright, Ph.D. thesis, University of Oxford, 2011.

[101] D. M. Cragg, P. Lloyd, and P. Nozieres, Journal of Physics C: Solid State Physics **13**, 803 (1980).

[102] I. Affleck and A. W. Ludwig, Nuclear Physics B **360**, 641 (1991).

[103] P. Sacramento and P. Schlottmann, Physics Letters A **142**, 245 (1989).

[104] N. Andrei and A. Jerez, Phys. Rev. Lett. **74**, 4507 (1995).

[105] P. Coleman and A. J. Schofield, Phys. Rev. Lett. **75**, 2184 (1995).

[106] P. Coleman, L. B. Ioffe, and A. M. Tsvelik, Phys. Rev. B **52**, 6611 (1995).

[107] G.-M. Zhang and A. C. Hewson, Phys. Rev. B **54**, 1169 (1996).

[108] R. Bulla and A. C. Hewson, Physica B **230-232**, 627 (1997).

[109] S. C. Bradley, R. Bulla, A. C. Hewson, and G.-M. Zhang, Eur. Phys. J. B **11**, 535 (1999).

[110] R. Bulla, A. C. Hewson, and G.-M. Zhang, Phys. Rev. B **56**, 11721 (1997).

[111] C. Kolf and J. Kroha, Phys. Rev. B **75**, 045129 (2007).

[112] A. Mitchell, Ph.D. thesis, University of Oxford, 2009.

[113] G. Zaránd, T. Costi, A. Jerez, and N. Andrei, Phys. Rev. B **65**, 134416 (2002).

[114] A. K. Mitchell and E. Sela, Phys. Rev. B **85**, 235127 (2012).

[115] E. Sela, A. K. Mitchell, and L. Fritz, Phys. Rev. Lett. **106**, 147202 (2011).

[116] A. K. Mitchell, E. Sela, and D. E. Logan, Phys. Rev. Lett. **108**, 086405 (2012).

[117] G. Zaránd, C.-H. Chung, P. Simon, and M. Vojta, Phys. Rev. Lett. **97**, 166802 (2006).

[118] E. Sela and I. Affleck, Phys. Rev. B **79**, 125110 (2009).

[119] E. Sela and I. Affleck, Phys. Rev. Lett. **103**, 087204 (2009).

[120] E. N. Economou, *Green's Functions in Quantum Physics* (Springer-Verlag, Berlin, 1983).

[121] D. Logan, Many-Body Theory, Lecture Notes, 2008.

[122] R. D. Mattuck, *A Guide To Feynmann Diagrams in the Many-Body Problem* (Dover Publications, New York, 1976).

[123] Y. Meir and N. S. Wingreen, Phys. Rev. Lett. **68**, 2512 (1992).

[124] L. P. Kouwenhoven *et al.*, in *Mesoscopic Electron Transport*, edited by L. P. K. L. L. Sohn and G. Schn (Kluwer Academic, ADDRESS, 1997).

[125] M. Galpin, Ph.D. thesis, University of Oxford, 2005.

[126] M. R. Galpin, D. E. Logan, and H. R. Krishnamurthy, Journal of Physics: Condensed Matter **18**, 6545 (2006).

[127] M. R. Galpin, D. E. Logan, and H. R. Krishnamurthy, Journal of Physics: Condensed Matter **18**, 6571 (2006).

[128] D. E. Logan and M. R. Galpin, The Journal of Chemical Physics **130**, 224503 (2009).

[129] C. J. Wright, M. R. Galpin, and D. E. Logan, Phys. Rev. B **84**, 115308 (2011).

[130] R. Bulla, T. A. Costi, and D. Vollhardt, Phys. Rev. B **64**, 045103 (2001).

[131] T. A. Costi, A. C. Hewson, and V. Zlatic, Journal of Physics: Condensed Matter **6**, 2519 (1994).

[132] W. Hofstetter, Phys. Rev. Lett. **85**, 1508 (2000).

[133] F. B. Anders and A. Schiller, Phys. Rev. Lett. **95**, 196801 (2005).

[134] F. B. Anders and A. Schiller, Phys. Rev. B **74**, 245113 (2006).

[135] R. Bulla, A. C. Hewson, and T. Pruschke, Journal of Physics: Condensed Matter **10**, 8365 (1998).

[136] W. C. Oliveira and L. N. Oliveira, Phys. Rev. B **49**, 11986 (1994).

[137] P. Mehta *et al.*, Phys. Rev. B **72**, 014430 (2005).

[138] D. S. Fisher and P. A. Lee, Phys. Rev. B **23**, 6851 (1981).

[139] R. Landauer, IBM Journal 223 (1957).

[140] A. Oguri, J. Phys. Soc. Jap. **66**, 1427 (1997).

[141] A. Oguri, Phys. Rev. B **59**, 12240 (1999).

[142] A. Oguri, Phys. Rev. B **63**, 115305 (2001).

[143] A. Oguri, Y. Nisikawa, and A. C. Hewson, J. Phys. Soc. Jap. **74**, 2554 (2005).

[144] R. Kubo, Journal of the Physical Society of Japan **12**, 570 (1957).

[145] W. Izumida, O. Sakai, and Y. Shimizu, J. Phys. Soc. Jap. **66**, 717 (1997).

[146] L. E. Hall, J. R. Reimers, N. S. Hush, and K. Silverbrook, Journal of Chemical Physics **112**, 1510 (2000).

[147] C. Caroli, R. Combescot, P. Nozieres, and D. Saint-James, Journal of Physics C: Solid State Physics **4**, 916 (1971).

[148] J. M. Luttinger and J. C. Ward, Phys. Rev. **118**, 1417 (1960).

[149] W. Kohn and J. M. Luttinger, Phys. Rev. **118**, 41 (1960).

[150] J. M. Luttinger, Phys. Rev. **119**, 1153 (1960).

[151] J. M. Luttinger, Phys. Rev. **121**, 942 (1961).

[152] D. C. Langreth, Phys. Rev. **150**, 516 (1966).

[153] E. Sela and I. Affleck, Phys. Rev. Lett. **102**, 047201 (2009).

[154] Y. Nishikawa, D. J. G. Crow, and A. C. Hewson, Phys. Rev. Lett. **108**, 056402 (2012).

[155] Y. Nishikawa, D. J. G. Crow, and A. C. Hewson, Phys. Rev. B **86**, 125134 (2012).

[156] Y. Nisikawa and A. Oguri, Journal of Physics: Conference Series **150**, 022066 (2009).

[157] A. K. Mitchell, D. E. Logan, and H. R. Krishnamurthy, Phys. Rev. B **84**, 035119 (2011).

[158] M. R. Gräber *et al.*, Phys. Rev. B **74**, 075427 (2006).

[159] K. Kikoin and Y. Oreg, Phys. Rev. B **76**, 085324 (2007).

[160] I. Affleck, A. W. W. Ludwig, H.-B. Pang, and D. L. Cox, Phys. Rev. B **45**, 7918 (1992).

[161] I. Affleck and A. W. W. Ludwig, Phys. Rev. B **48**, 7297 (1993).

[162] M. Pustilnik and L. I. Glazman, Phys. Rev. Lett. **85**, 2993 (2000).

[163] J. Kong, A. M. Cassell, and H. Dai, Chemical Physics Letters **292**, 567 (1998).

[164] E. D. Minot, Y. Yaish, V. Sazonova, and P. L. McEuen, Nature **428**, 536 (2004).

[165] M. R. Buitelaar *et al.*, Phys. Rev. Lett. **88**, 156801 (2002).

[166] W. Liang, M. Bockrath, and H. Park, Phys. Rev. Lett. **88**, 126801 (2002).

[167] N. E. Bickers, Rev. Mod. Phys. **59**, 845 (1987).

[168] J. Paaske *et al.*, Nat Phys **2**, 460 (2006).

[169] S. J. Chorley *et al.*, Phys. Rev. Lett. **106**, 206801 (2011).

[170] M. Pustilnik, Y. Avishai, and K. Kikoin, Phys. Rev. Lett. **84**, 1756 (2000).

[171] M. Pustilnik and L. I. Glazman, Phys. Rev. Lett. **87**, 216601 (2001).

[172] S. Florens *et al.*, Journal of Physics: Condensed Matter **23**, 243202 (2011).

[173] D. M. Zumbühl, C. M. Marcus, M. P. Hanson, and A. C. Gossard, Phys. Rev. Lett. **93**, 256801 (2004).

[174] N. Roch *et al.*, Nature **453**, 633 (2008).

[175] J. R. Hauptmann, J. Paaske, and P. E. Lindelof, Nature Physics **4**, 373 (2008).

[176] M. R. Buitelaar, T. Nussbaumer, and C. Schönenberger, Phys. Rev. Lett. **89**, 256801 (2002).

[177] A. L. Fetter and J. D. Walecka, *Quantum Theory of Many-Particle Systems* (Dover Publications, New York, 2003).